Heusler compounds for spin-orbitronics: exploration of topological effects and magnetic anisotropy engineering

Victor Palin

UNIVERSITÉ DE LORRAINE
ECOLE DOCTORALE C2MP

Thèse de doctorat

pour obtenir le titre de
Docteur de l'Université de Lorraine
dans la spécialité
Physique

Heusler compounds for spin-orbitronics: exploration of topological effects and magnetic anisotropy engineering

---

Thèse soutenue le **09 mars 2023** par

Victor Palin

devant le jury composé de :

Président du jury	**Fagot-Revurat Yannick**
Rapportrice	**Michez Lisa**
Rapporteur	**Jamet Matthieu**
Examinatrice	**Taleb Amina**
Co-Directeur	**Bertran François**
Directeur	**Andrieu Stéphane**

Instiut Jean Lamour, UMR CNRS 7198, Université de Lorraine, Nancy, France
Synchrotron SOLEIL, Gif-sur-Yvette, France

Résumé :

Spintronique et spinorbitronique

La spintronique, aussi appelée électronique de spin est un champ de recherche visant à exploiter et étudier non seulement la charge de l'électron, mais également son spin. Elle a vu le jour à la fin des années 80 avec la découverte de l'effet de magnétorésistance géante (GMR en anglais pour Giant MagnetoResistance) par Albert Fert *et al* [1]. Cet effet apparait dans des systèmes composés de l'empilement des couches suivantes : Ferromagnétique/Non Magnétique/Ferromagnétique. Ce type de système permet d'obtenir différents niveaux de résistance en fonction de l'orientation relative des aimantations portées par les deux couches ferromagnétiques. Cet effet a permis de développer un grand nombre de capteurs. Ces dispositifs GMR seront remplacés au fil des années par des jonctions tunnel magnétiques (MTJ en anglais pour magnetic tunnel junction).

Pour mieux comprendre l'enjeu de mon travail de recherche, il est intéressant de prendre l'exemple des MRAM (Magnetic Random Access Memory) qui sont des mémoires magnétiques non volatiles en développement depuis les années 1990. Cette technologie a été peu commercialisée à l'heure actuelle et les quelques modèles présents sont des MRAM basées sur le couple de transfert de spin (STT en anglais pour Spin Transfert Torque). Ces dispositifs permettent de s'affranchir de l'utilisation d'un champ magnétique extérieur réduisant la consommation d'énergie. Ce type de mémoire est basé sur un bloc élémentaire, la jonction tunnel magnétique, composée d'une barrière isolante entourée de deux couches ferromagnétiques. L'une de ses deux couches à une aimantation dite dure alors que la seconde est dite d'aimantation libre. En injectant un courant de charge dans cette structure, l'aimantation dure va permettre de polariser le courant en spin. Il y a donc un transport de moment angulaire (grâce au courant polarisé en spin) qui va pouvoir agir sur l'aimantation libre de la seconde couche magnétique et ainsi permettre son retournement. On retrouve, de la même manière qu'avec la magnétorésistance géante vue précédemment, un système binaire suivant l'orientation relative des aimantations que l'on détecte grâce à une différence de résistance entre les deux états.

De plus, lors des dernières décennies, un autre type de MRAM basé sur des effets de couplage spin-orbite a vu le jour. On parle de spinorbitronique. Elles sont appelées SOT-MRAM (SOT étant l'acronyme anglais de Spin-Orbit Torque). Pour que ce type de mémoire soit viable, il faut utiliser un matériau ayant un fort couplage spin-orbite tel qu'un métal lourd (Pt, Ta, W) ou des isolants topologiques qui vont permettre de générer de forts courants de spin. Nous reviendrons sur la façon de retourner l'aimantation après avoir décrit les principaux atouts, intérêts et propriétés physiques des isolants topologiques qui permettront une meilleure compréhension de ces dispositifs.

Cette thèse est donc divisée en deux grands axes qui visent à concevoir des matériaux et structures permettant de pérenniser l'utilisation des mémoires magnétiques décrites ci-dessus. Le premier axe utilise des matériaux émergents appelés isolants topologiques et possédant des propriétés extraordinaires qui en font de parfaits candidats pour des applications dans le domaine des mémoires magnétiques. Le second axe utilise des matériaux à forte anisotropie magnétocristalline pour permettre de réduire le courant de retournement de l'aimantation des mémoires magnétiques

et ainsi de les rendre moins énergivores.

Isolant topologique 3D

L'étude des isolants topologiques pour leurs propriétés exceptionnelles est devenue l'un des principaux axes de recherches en matière condensée lors des dernières décennies. Ce domaine, liant topologie et physique des solides, a vu le jour avec la découverte de l'effet Hall quantique en 1980 par Klauss von Klitzing (le caractère non trivial de l'effet Hall quantique trouve son origine via l'application d'un fort champ magnétique extérieur) et son interprétation par Thouless, Kohmoto, Nightingaleet den Nijs en 1982 [2] à l'aide d'invariants topologiques appelés aujourd'hui invariants TKNN. En 2005, Kane et Mele [3] ont prédit un nouveau genre d'isolant topologique. L'idée est d'utiliser des éléments lourds du tableau périodique de façon à obtenir des matériaux avec un fort couplage spin-orbite (qui va remplacer et jouer le rôle du champ magnétique extérieur). Ce fort couplage spin-orbite va permettre une inversion de bande amenant à un état topologique non trivial. On a, avec cette découverte, une généralisation à trois dimensions de l'effet Hall quantique dans le sens où les états conducteurs ne sont plus uniquement des états de bord (comme pour l'effet Hall quantique et les autres types d'isolants topologiques étudiés jusque-là), mais des états de surface.

Nous étudions ici les isolants topologiques 3D. Nous avons donc un matériau qui, lorsqu'on ne prend pas en compte le couplage spin-orbite, est isolant (c'est même en réalité plutôt un semiconducteur car les bandes de conduction et de valence sont proches l'une de l'autre). Comme dit précédemment, nous utilisons des éléments lourds du tableau périodique impliquant une forte interaction spin-orbite. Lorsque l'on prend en compte et que l'on applique cette forte interaction sur la structure de bande, cette dernière va s'inverser au niveau de Fermi et par la même occasion changer la topologie du matériau qui va devenir non trivial topologiquement. On a donc un matériau qui est toujours isolant, puisqu'il y a un gap au niveau de Fermi, et non trivial. Seulement, ce matériau a une interface avec le vide qui, lui, est de topologie triviale. Nécessairement, il doit s'opérer une transformation drastique pour assurer la continuité entre ces deux milieux. Ce changement est opéré par des états de surface métalliques qui vont connecter bande de valence et bande de conduction.

La partie intéressante de ces états de surface est qu'ils sont protégés par des considérations de symétrie et vont se matérialiser sous la forme de dispersion linéaire appelée cône de Dirac. Ils sont également pourvus d'une texture de spin particulière appelée blocage du moment de spin (spin-momentum locking en anglais). Cette texture particulière conduit à une propagation du spin dans une seule direction empêchant sa relaxation dans son état opposé grâce à la levée de dégénérescence en spin. On dit que l'on a une polarisation en spin hélicoïdale.

Effet Edelstein

L'effet Edelstein (aussi appelé effet Rashba-Edelstein) a été proposé en 1990 par Edelstein [4] lui-même et tire parti du blocage du moment de spin observé dans les isolants topologiques. Lorsqu' un courant de charge est injecté à la surface d'un isolant topologique, celui-ci va engendrer un décalage Δk de la surface de Fermi. Du fait de la texture de spin de ces systèmes, une surpopulation d'électron up (ou down) va être générée dans une région de l'espace. Le courant de charge injecté va

donc générer une accumulation de spin qui va pouvoir diffuser comme un courant de spin dans une couche adjacente à l'isolant topologique.

Un tel système dans les SOT-MRAM permettrait de retourner l'aimantation d'une couche ferromagnétique via l'injection d'un courant de charge dans l'isolant topologique puisque le pur courant de spin créé peut agir sur l'aimantation d'un coche magnétique adjacente par couplage d'échange. Il est alors possible d'obtenir deux états de résistance différente pour en faire un parfait système binaire.

L'avantage d'utiliser le retournement par couplage spin-orbite (SOT) plutôt que par couplage de transfert de spin (STT) est que le facteur de conversion entre courant de charge et courant de spin est prédit comme étant beaucoup plus important permettant de générer des couples de transfert de spins très élevés. Ceux-ci permettraient d'injecter des courants d'injection plus faible et ainsi de réduire le courant et l'énergie consommés dans ce type de système.

Les alliages d'Heusler isolants toplogiques

Les propriétés électroniques remarquables des isolants topologiques en font l'un des sujets de recherches les plus étudié actuellement. Beaucoup de prédictions théoriques ont été faites sur une grande variété de composés et la communauté scientifique s'applique actuellement à le vérifier expérimentalement. Les composés les plus étudiés sont ceux à base de Bismuth tels que Bi_2Se_3[5], Bi_2Te_3 [6] ou BiSb [7] qui ont donné des résultats plus qu'encourageants en termes d'interconversion spin/charge. Dans notre cas, l'intérêt est porté sur les alliages d'Heusler qui sont prédits isolants topologiques et qui sont, de leur côté, encore relativement peu étudiés.

Les alliages d'Heusler prédits isolants topologiques font partie de la famille des demi-Heusler d'unité formulaire XYZ. Ce sont des alliages de symétrie cubique avec un paramètre de maille de l'ordre de 6,6 Å dépendant du choix des atomes X, Y et Z. Plusieurs composés ternaires ont été identifiés théoriquement comme étant des isolants topologiques [8] dont notamment PdYBi et PtYBi qui sont les alliages d'intérêts dans notre cas. Comme expliqué précédemment, le fort couplage spin-orbite régnant dans ces composés à éléments lourds amène à une inversion de bande au niveau du point $\overline{\Gamma}$ alors que l'ordre des bandes est préservé dans les autres régions de la zone de Brillouin. Ceci devrait amener à l'observation d'états de surface topologiques à dispersion linéaire au niveau du point $\overline{\Gamma}$, des cônes de Dirac.

L'idée ici est donc de synthétiser ces différents composés par épitaxie par jet moléculaire et ensuite de les caractériser structuralement à l'aide de techniques de diffraction d'électrons (RHEED et LEED), de diffraction des rayons X et de microscopie électronique à transmission. Une fois la phase half-Heusler obtenue, le banc ARPES (Angle Resolved Photoemission Spectroscopy en anglais pour spectroscopie photoélectronique résolue en angle) du tube et des runs sur la ligne de photoémission CASSIOPEE du synchrotron SOLEIL vont permettre de vérifier la présence d'états à dispersions linéaires au niveau du point $\overline{\Gamma}$. Enfin, la réalisation de dispositifs de conversion spin/charge par lithographie UV au sein de la plateforme micro- et nanostructuration MINALOR de l'institut Jean Lamour permettra une première estimation des facteurs de conversion donnés par ces matériaux.

Résultats principaux sur les Heusler isolants topologiques

La croissance de PdYBi et PtYBi a été réalisée par épitaxie par jets moléculaires sur la MBE de l'institut Jean Lamour. Le bon déroulement des dépôts a été confirmé par de nombreuses techniques de caractérisation tel que de la diffraction électronique (RHEED, LEED), de la diffraction des rayons X (XRD, XRR), de la microscopie (TEM, STEM, STM) et de la spectroscopie (AES, EDX). Toutes ces techniques ont permis de confirmer la croissance monocristalline de nos composés. Les surfaces et leurs reconstructions ont été imagées par microscopie à effet tunnel et l'ordre chimique, étudié par microscope électronique à transmission, fait état d'un meilleur ordre chimique présent dans PtYBi comparé à PdYBi. Cette observation est de première importance puisqu'elle permet d'expliquer la structure de bande moins bien définie de PdYBi comparé à PtYBi observé en ARPES. En effet, bien que l'ordre cristallin semble meilleur dans PdYBi comparé à PtYBi (au vu des données de diffractions des rayons X et électronique), le mapping de la structure de bande, réalisé sur le banc ARPES de l'institut Jean Lamour, révèle un meilleur poids spectral dans PtYBi vis-à-vis de PdYBi ou des bandes plus diffusent sont observées. Cette disparité entre les deux composés est donc expliquée par le meilleur ordre chimique présent dans PtYBi. Néanmoins, des états à dispersion linéaire sont identifiés autour du point $\overline{\Gamma}$ de la zone de Brillouin pour les deux composés bien que leur nature triviale ou topologique n'est pas encore pleinement élucidée. Au vu des données de la littérature et des calculs *ab initio* réalisés sur PtYBi, la topologie non triviale semble se manifester bien en dessous du niveau de Fermi ou un autre croisement de bandes à dispersion linéaire est observé. Pour PdYBi, l'absence de calcul théorique est dérangeante et un parallèle avec PtYBi est réalisé puisqu'un croisement en dessous du niveau de Fermi, semblable à ce qui est observé pour PtYBi, est présent. Les mesures ARPES ne permettent pas de clairement trancher sur la nature non-triviale de nos alliages d'Heusler et les mesures de transport ont donc été entreprises avec deux objectifs précis. Le premier était d'estimer le pouvoir de conversion spin/charge de ces composés et le second de confirmer leur nature non-triviale puisque de tels états de surface se manifestent lors des mesures de transport. Malheureusement, bien qu'une conversion entre spin et charge ait été observée, il n'est toujours pas possible de clairement trancher la question sur la nature topologique de ces composés. Le principal frein rencontré réside dans la structure choisie pour les mesures de transport ou une barrière de MgO a été utilisée pour protéger la couche isolant topologique de la couche ferromagnétique utilisée comme batterie de spin. La barrière de MgO affecte probablement le transport et de nouveaux échantillons, avec une nouvelle couche séparatrice, devraient permettre de définitivement tirer une conclusion sur le potentiel de ces matériaux.

Le second axe de recherche de cette thèse porte sur les alliages d'Heusler à aimantation perpendiculaire. Pour comprendre l'intérêt d'étudier des composés avec de telles propriétées il est utile de se référer à l'équation qui suit et qui décrit les différents termes influant le retournement de l'aimantation par transfert de spin (STT):

$$J^{STT}_{retournement} = \frac{2et_F M_S}{\hbar} \cdot \frac{\alpha}{P} . H_{eff} \tag{1}$$

Avec e la charge élémentaire, t_F et M_S l'épaisseur et l'aimantation à saturation de la couche magnétique, α est le coefficient d'amortissement de Gilbert, P la polarisation en spin et H_{eff} le champ effectif qui comprend le champ magnétique appliqué, l'anisotropie magnétocristalline effective et l'anisotropie de forme.

Pour obtenir un courant de retournement de l'aimantation le plus faible possible, il est donc nécessaire, à la vue de l'équation 1, de minimiser le coefficient d'amortissement magnétique, α, et le champ magnétique effectif, H_{eff}, tout en maximisant la polarisation en spin, P. Il s'avère que les alliages d'Heusler utilisés au cours de cette thèse sont de parfaits candidats pour répondre à ces problématiques.

Faible amortissement magnétique et polarisation en spin de 100%

La polarisation en spins reflète l'alignement des spins par rapport à une direction donnée. Dans les matériaux ferromagnétiques, les électrons de conduction peuvent être polarisés et donner lieu à des courants polarisés en spin. Certains composés (les alliages d'Heusler de formule Co_2MnZ') ont été prédits comme présentant une polarisation en spin de 100% en raison d'un comportement semi-métallique (HMM pour Half-Metal Magnetism en anglais). Le HMM dans les composés Heusler a été prédit en 1983 par de Groot *et al* [9] dans NiMnSb. Cette propriété provient d'une asymétrie de la densité d'état au niveau de l'énergie de Fermi. Selon l'orientation du spin, un comportement métallique ou isolant peut être observé. Dans un composé HMM, un gap est présent pour la bande de spin minoritaire au niveau de E_F. Par conséquent, en théorie, si un courant non polarisé traverse un tel matériau, il devient alors entièrement polarisé en spin.

Le comportement HMM a des conséquences notables sur l'amortissement magnétique α (appelée constante de Gilbert) qui impactent la dynamique du spin. La constante d'amortissement provient de l'équation de Landau-Lifshitz-Gilbert qui décrit le mouvement de rotation de l'aimantation. Le terme de Gilbert caractérise la vitesse d'atténuation de la précession du moment. En effet, lorsqu'un spin tourne, un amortissement qui tente de le ramener dans sa position d'équilibre lui est appliqué. Plus α est grand, plus le mouvement de précession est amorti rapidement. Si α est faible, il permet une longue précession permettant un franchissement plus facile de la barrière pour retourner l'aimantation dans son état d'équilibre opposé. L'amortissement de Gilbert provient des mécanismes de relaxation qui sont fortement réduits avec les matériaux HMM. En effet, comme un seul canal de spin est présent en raison du comportement isolant de la bande de spin minoritaire au niveau de Fermi, il n'est donc pas facile pour les électrons de conduction de dissiper de l'énergie par retournement de spin étant donné qu'aucun état électronique n'est disponible. Le mécanisme de retournement de spin est alors fortement réduit conduisant à une faible constante α.

Plusieurs alliages d'Heusler de la famille des Co_2MnZ' ont été prédits comme HMM et donc comme ayant de très fortes polarisations en spin et de très faibles amortissements magnétique en faisant des très bons candidats pour des dispositifs de retournement de l'aimantation. Ces alliages, déjà étudiés dans de précédentes thèses dans l'équipe [10, 11], sont également utilisés dans cette thèse pour ces deux propriétés exceptionnelles.

Cependant, ces composés possèdent de faibles énergies magnéto-cristallines conduisant à une domination du champ démagnétisant du fait de la croissance sous forme de film mince. En conséquence, l'aimantation reste dans le plan de l'échantillon puisque la minimisation de l'énergie dipolaire choisit cette direction préférentielle d'aimantation et le troisième terme de l'équation donnée ci-dessus (H_{eff}) ne peut pas être minimisé par ces composés.

Comment obtenir de la PMA ?

De nos jours, une anisotropie hors du plan de croissance est une condition indispensable lorsqu'on évoque le futur du stockage de l'information. Néanmoins, en raison de leur géométrie, la position d'équilibre de l'aimantation des films minces reste la plupart du temps dans le plan de l'échantillon où le coût énergétique est plus faible en raison du champ démagnétisant. Heureusement, cette anisotropie de forme peut être contrebalancée par d'autres termes d'anisotropie magnétique qui proviennent de contributions de volumes ou interfaciales. L'anisotropie effective d'une couche mince avec deux interfaces peut être exprimée comme suit :

$$K_{eff} = K_V + \frac{K_S}{t} - \frac{1}{2}\mu_0 {M_S}^2 \tag{2}$$

Cette équation est la somme de trois termes énergétiques principaux :

- Le dernier terme est l'énergie démagnétisante également connue sous le nom d'anisotropie de forme (valable ici pour un film mince). Ce terme tend à aligner l'aimantation dans le plan du film mince en raison de la géométrie de l'échantillon qui impose cette direction préférentielle.
- L'anisotropie de surface K_S est induite par les surfaces. Elle inclut les contributions des deux interfaces. K_S est exprimée en $J.m^{-2}$.
- L'anisotropie magnéto-cristalline K_V qui représente la contribution du volume. K_V est exprimée en $J.m^{-3}$.

K_V et K_S trouvent tous deux leur origine dans l'interaction spin-orbite. L'interaction spin-orbite relie l'aimantation au réseau cristallin ce qui entraîne une déformation des orbitales des électrons. Si les orbitales sont fortement déformées dans une direction, cela peut donner lieu à une anisotropie magnétique perpendiculaire (PMA en anglais pour Perpendicular Magnetic Anisotropy). Deux possibilités peuvent être identifiées grâce à l'équation 2. D'une part, si $K_{eff} < 0$, l'anisotropie dans le plan l'emporte puisque le terme dominant est l'anisotropie de forme. D'autre part, une anisotropie hors plan peut être obtenue si $K_{eff} > 0$, grâce aux contributions de l'anisotropie de masse et/ou interfaciale.

Dans cette thèse nous nous intéressons aux matériaux possédant une forte anisotropie magnétocristalline K_V. Dans ces matériaux, la déformation des orbitales est due à

l'asymétrie du réseau cristallin qui minimise l'énergie magnétique dans une direction particulière. Une stabilité thermique élevée est plus facilement obtenue par rapport à l'anisotropie magnétique perpendiculaire d'origine interfaciale. Il s'avère que certains alliages d'Heusler présentent une forte anisotropie de volume couplée à une faible constante d'amortissement de Gilbert. Ce phénomène d'anisotropie provenant du volume est utilisé dans cette thèse pour faire de la direction hors du plan un axe de facile aimantation.

Alliages d'Heusler et aimantation perpendiculaire

Alors que la grande majorité des alliages d'Heusler sont cubiques, conduisant à une PMA nulle, certains d'entre eux peuvent cristalliser dans des structures déformées qui peuvent héberger une forte PMA. De telles distorsions sont prédites comme accueillant potentiellement d'énormes K_V, en particulier dans les alliages d'Heusler à base de Mn (famille Mn_3Z particulièrement). Différentes structures pour les alliages Mn_3Z ont été identifiées dans la littérature, les plus populaires étant la structure cubique $D0_3$, la structure hexagonale $D0_{19}$ et la structure tétragonale $D0_{22}$. Ici, les alliages d'Heusler Mn_3Z croissant dans la structure tétragonale $D0_{22}$ sont d'intérêts et plus particulièrement les deux composés Mn_3Ge et Mn_3Ga.

Mn_3Ge et Mn_3Ga ont tous deux une maille tétragonale dans leur phase $D0_{22}$. La maille élémentaire est donc allongée le long de l'axe c amenant à un ratio $\frac{c}{a}$ de l'ordre de 1.8 pour les deux composés [12, 13, 14, 15]. Plusieurs travaux ont déterminé un caractère ferrimagnétique pour les deux composés du fait de deux sites de manganèse non équivalents présents dans la maille elementaire et couplés antiferromagnétiquement [12, 16, 17]. Les mesures de l'anisotropie magnétocristalline portée par ces matériaux ont confirmé leur potentiel avec des valeurs d'anisotropie effective K_{eff} de l'ordre du $MJ.m^{-3}$ [15, 18, 19].

L'idée est donc dans un premier temps de réaliser la croissance de ces deux composés dans leur phase $D0_{22}$ avec leur axe c normal à la surface de l'échantillon et de vérifier l'obtention d'aimantation perpendiculaire. Une étude sur les variations de la stœchiométrie ($Mn_{100-x}Ga_x$ et $Mn_{100-x}Ge_x$) est faite de manière à voir son impact sur les propriétés magnétiques. Dans un second temps, des études sur des bicouches et super-réseaux composés de Mn_3Ge et d'alliages Co_2YZ' est entrepris. L'idée est de générer une anisotropie perpendiculaire dans les composés Co_2YZ' (Co_2MnGe et Co_2FeGe ici) grâce à l'alliage Mn_3Ge et sa forte anisotropie magnétocrystalline. Le but final de cette étude est donc d'obtenir une aimantation perpendiculaire dans nos structures tout en ayant un matériau possédant un gap de spin dans la couche supérieure.

Résultats principaux sur les Heusler à aimantation perpendiculaire

Les recherches faites sur les alliages d'Heusler à aimantation perpendiculaire peuvent se décomposer en deux grandes parties :

La première a consisté à déterminer le candidat idéal qui permettra de générer un axe de facile aimantation hors du plan de croissance dans des systèmes bicouches ou super-réseaux composés d'un alliage d'Heusler prédit demi-métal magnétique. Pour se faire, une première étude a été réalisée en faisant varier la stœchiométrie des alliages Mn_3Ga et Mn_3Ge. Cinq compositions pour chaque composé de la forme

$Mn_{100-x}Ga_x$ et $Mn_{100-x}Ge_x$ ont été réalisées et l'obtention d'une aimantation perpendiculaire a été observée dans toutes les compositions grâce à la stabilisation de la maille tétragonale $D0_{22}$. Néanmoins de grandes conclusions ont été tirées de cette étude. La première, la sortie de la stœchiométrie idéale que suggérent les alliages d'Heusler (ie. 3:1) affecte fortement les propriétés magnétiques et voire même le bon déroulement de la croissance pour certaines compositions. Enfin, une comparaison entre Mn_3Ge et Mn_3Ga a révélé que le premier composé présentait de meilleurs propriétés pour notre usage et a donc été choisi comme "générateur" d'aimantation perpendiculaire dans nos empilements.

La seconde partie a donc consisté en la réalisation de bicouches et de super-réseaux composés de deux alliages d'Heusler : Mn_3Ge pour apporter l'aimantation perpendiculaire et Co_2MnGe pour son faible amortissement magnétique et sa forte polarisation en spin (des études ont également été réalisées avec Co_2FeGe pour empêcher la présence du manganèse dans les deux sous-couches et ainsi faire des mesures sélectives en element tel que de l'XMCD). Que ce soit avec l'un ou l'autre des composés, en bicouches ou en super-réseaux, une croissance monocristalline dans les phases souhaitées a été obtenue tout en conservant un axe tétragonalisé (ie. l'aimantation perpendiculaire) normal à la surface de l'échantillon. Tous les échantillons réalisés présentent un axe de facile aimantation hors du plan à grand ratio de Mn_3Ge vis-à-vis du second alliage. Cet axe tend à progressivement basculer dans le plan lorsque l'épaisseur du second alliage est augmenté du fait de son comportement de film mince classique. Il est alors possible d'accorder les paramètres magnétiques du système tel que la valeur de son coercitif ou sa rémanence en jouant sur les épaisseurs des deux couches. Dans tous les cas, la croissance des systèmes a été réussie avec succès et les structures présentent un axe de facile aimantation perpendiculaire ainsi qu'une ultime couche prédite comme étant demi-métal magnétique. Ces travaux apportent de nombreuses connaissances sur la croissance et la réalisation d'hétérostructures d'alliages d'Heusler (bicouches et super-réseaux) magnétisées perpendiculairement. Les rémanences élevées mesurées pour les super-réseaux sont très prometteuses pour de futures applications mais certains travaux restent à faire tel qu'une étude plus complète de la dépendance des paramètres magnétiques vis-à-vis de l'épaisseur des deux sous couches. Une étude similaire doit être réalisée avec Co_2MnSi (qui est le matériau demi-métal magnétique le plus prometteur avec un très faible amortisesement magnétique et une polarisation en spin de 100% au niveau de Fermi) pour s'assurer que des résultats semblables soient obtenus. Ensuite, des mesures de résonance ferromagnétique doivent être effectuées pour extraire la constante d'amortissement magnétique des hétérostructures. Enfin, des mesures SR-PES (photoémission résolue en spin) doivent être effectuées afin d'estimer la polarisation en spin. Une fois la constante d'amortissement magnétique et la polarisation de spin connues, une conclusion sur leur intérêt pour des applications liées au couple de transfert de spin pourra être tirée en fonction de l'impact de la structure en bicouches et en super-réseaux sur ces deux propriétés essentielles.

Contents

Liste des Abréviations

2DEG	**2** **D**imensional **E**lectron **G**as
AES	**A**uger **E**lectron **S**pectroscopy
ANE	**A**nomalous **N**ernst **E**ffect
ARPES	**A**ngle **R**esolved **P**hoto**E**lectron **S**pectroscopy
BCC	**B**ody-**C**entered **C**ubic
EDX	**E**nergy-**D**ispersive **X**-ray
EE	**E**delstein **E**ffect
FCC	**F**ace-**C**entered **C**ubic
FFT	**F**ast **F**ourier **T**ransform
FIB	**F**ocused **I**on **B**eam
FM	**F**erro**M**agnet
FMR	**F**erro**M**agnetic **R**esonance
GMR	**G**iant **M**agneto**R**esistance
HCP	**H**exagonal **C**lose-**P**acked
HDD	**H**ard **D**rive **D**isk
HM	**H**eavy **M**etal
HMM	**H**alf-**M**etal **M**agnetism
IEE	**I**nverse **E**delstein **E**ffect
IJL	**I**nstitut **J**ean **L**amour
ISHE	**I**nverse **S**pin **H**all **E**ffect
LEED	**L**ow **E**nergy **E**lectron **D**iffraction
LSSE	**L**ongitudinal **S**pin **S**eebeck **E**ffect
MBE	**M**olecular **B**eam **E**pitaxy
MOKE	**M**agneto-**O**ptic **K**err **E**ffect
MTJ	**M**agnetic **T**unnel **J**unction
MRAM	**M**agnetic **R**andom **A**ccess **M**emory
NMR	**N**uclear **M**agnetic **R**esonance
PMA	**P**erpendicular **M**agnetic **A**nisotropy
PPMS	**P**hysical **P**roperties **M**easurement **S**ystem
QHE	**Q**uantum **H**all **E**ffect
QM	**Q**uartz **M**icrobalance
RHEED	**R**eflection **H**igh **E**nergy **E**lectron **D**iffraction
SdH	**S**hubnikov-**d**e **H**aas
SHE	**S**pin **H**all **E**ffect
SL	**S**uper**L**attice
SQUID	**S**uperconducting **Q**uantum **I**nterference **D**evice
SOC	**S**pin-**O**rbit **C**oupling
SOT	**S**pin-**O**rbit **T**orque
SP-FMR	**S**pin **P**umping – **F**erro**M**agnetic **R**esonance
SSE	**S**pin **S**eebeck **E**ffect
ST-FMR	**S**pin **T**orque – **F**erro**M**agnetic **R**esonance
STEM	**S**canning **T**ransmission **E**lectron **M**icroscopy

STEM-HAADF	**S**canning **T**ransmission **E**lectron **M**icroscopy – **H**igh-**A**ngle **A**nnular **D**ark **F**ield
STM	**S**canning **T**unneling **M**icroscopy
STT	**S**pin **T**ransfer **T**orque
TEM	**T**ransmission **E**lectron **M**icroscopy
TI	**T**opological **I**nsulator
TRS	**T**ime **R**eversal **S**ymmetry
TSS	**T**opological **S**urface **S**tate
VSM	**V**ibrating **S**ample **M**agnetometer
XAS	**X**-ray **A**bsorption **S**pectroscopy
XMCD	**X**-ray **M**agnetic **C**ircular **D**ichroism
XRD	**X**-**R**ay **D**iffraction
XRR	**X**-**R**ay **R**eflectivity

Introduction

Over the last decades, the need in computing science has shown an exponential growth behavior. This huge increase has led to a common thread to reduce device's scale, energy consumption and manufacturing cost while memories' size and information's speed has shot up. One of the representatives of this growth is without a doubt the Hard Drive Disk (HDD). HDD was born in 1957 in the IBM premises. Since its discovery, the needs have exploded with more than 260 million HDD sell in 2020. Nowadays, the information storage has to be reinvented especially with the energy crisis that the world is going through in the 21^{st} century. This introduction is thus dedicated to the progress realized in term of information storage thanks to a useful tool: the electron spin.

The birth of spintronics

Spintronics is a word made with two others, spin and electronics. It relies on the exploitation of the intrinsic spin of the electron and its magnetic moment that allow to design new kinds of magnetic storage. The birth of spintronics took place in 1988 when Albert Fert and Peter Gründberg discovered simultaneously the Giant Magnetoresistance (GMR) effect [1]. The GMR effect occurs in heterostructure composed of a non-magnetic material sandwiched by two ferromagnetic layers. The non-magnetic layer is called barrier and is thin enough to allow the conservation of the electron spin while crossing between the two ferromagnets. It is then possible to observe a perfect binary system. Depending on the relative orientation of the two magnetizations, a low resistance state (ie. both ferromagnet magnetizations pointing in the same direction) or a high resistance state (ie. both ferromagnet magnetizations pointing in opposite direction) is usually observed. This effect has led to the development of numerous sensors especially HDD's read-heads. These devices using the GMR effect have been replaced little by little by Magnetic Tunnel Junction (MTJ). MTJ was discovered in 1975 by Jullière [20]. This time, the barrier is not a non-magnetic metal anymore but an insulator. The transport is possible thanks to spin-dependent tunneling. The main interest of this junction is that the magnetoresistance effect is strongly enhanced thanks to the insulating barrier leading to much higher resistance difference[1] and therefore a higher sensitivity.

Spin transfer torque

MTJs had a second birth in 1996 with the work of Slonczewski and Berger [21] who predicted theoretically the magnetization reversal by Spin Transfer Torque (STT). This discovery has made MTJ and spin valves durable. In addition to their passive use as sensors, they can also be active by generating a polarized spin current. The heterostructure stays the same but one of the ferromagnets (FM1) has a strong

[1] Magnetoresistance effects reported in literature for MTJ is one order of magnitude higher than in heterostructure using a non-magnetic metal.

magnetization which is fixed. By injecting a charge current in FM1, the conduction electrons of the charge current can be polarized with respect to the magnetization orientation. This spin polarized current can then interact with the second ferromagnet (FM2) which hosts a soft magnetization. Spin momentum is transferred to the magnetization of FM2 that starts to precess. If the applied torque is large enough, the precession in FM2 can lead to magnetization reversal. Devices based on STT rely on switching the second ferromagnetic layer in MTJ or spin valves to obtain two resistance states according to the relative orientation of the magnetization. One of the key parameters to make this reversal suitable is to reduce the switching current (ie. the initial injected charge current) needed to reverse the magnetization of FM2. The critical current to get magnetization reversal is given by the following equation [22]:

$$J_{switch}^{STT} = \frac{2et_F M_S}{\hbar} \cdot \frac{\alpha}{P} . H_{eff} \tag{3}$$

With e the electron charge, t_F and M_S the thickness and magnetization of the soft magnetic layer, α is the Gilbert damping coefficient, P the spin polarization and H_{eff} the effective field that includes the applied magnetic field, the effective magnetocrystalline anisotropy and the shape anisotropy.

In order to understand the power of STT, one must study Magnetic Random Access Memory (MRAM). MRAM are non-volatile memory used to store data that have been developed since the mid-eighties. MTJs are used to store binary information. One of the key points of these memories is that they allow to be free from external magnetic field and replaced it by STT effect. This change in the writing of the information has drawn a lot of attention to reduce the energy consumption, minimize the bit size to enhance stockage density or increase the speed of reading/writing data compared to mechanical read-and-write heads of HDDs. STT-MRAM consists of multiple crossing lines namely word and bit lines as depicted in **figure 1**. At each cross, there is an MTJ allowing to store one bit. By sending current pulses on one line of two perpendicular arrays, the magnetization of the free layer at the crossing point can be reversed. Writing is thus realized by STT. Reading is performed by a resistance measurement between the top line and the bottom line connecting the MTJ.

Spin-orbitronics and spin-orbit torques

On top of that growing interest for STT-based electronic, another research area has attracted a lot of attention in the last two decades: spin-orbitronics. Spin-orbitronics makes use of the electron spin to generate pure spin current based on Spin-Orbit Coupling (SOC). By harnessing the transfer of orbital angular momentum from the lattice to the spin system it is possible to generate huge torques. These torques are named Spin-Orbit Torques (SOT). One of the main challenges of spin-orbitronics is to get interconversion between charge current and spin current with the highest efficiency. This interconversion can be probed by two effects namely Spin Hall Effect (SHE) [23] in the bulk of the material and Edelstein effect (EE) [4] that occurs at the surfaces/interfaces[2]. MRAM can also use SOT to reverse the magnetization of a ferromagnet and store binary states. They were identified as one of the most promising candidates for novel magnetic memories. The architecture of SOT-MRAM is slightly

[2]The reciprocal effects (ie. the generation of charge current from spin current) exist and are named Inverse Spin Hall Effect (ISHE) and Inverse Edelstein Effect (IEE).

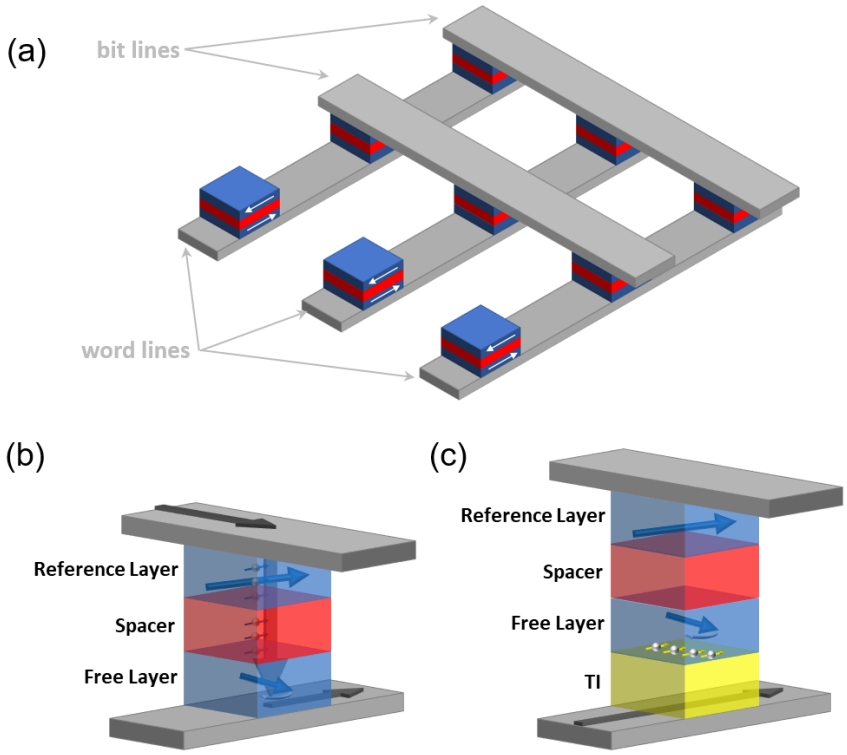

FIGURE 1: a) Sketch of a MRAM. Bit and word lines are used to write and read the bits stored in the MTJs. b) Heterostructures used for STT-MRAM. Writing is realized by injecting charge current from the top to the bottom line (black arrow). Spins are then polarized (small blue arrows) in the reference layer and act on the free layer to orient the magnetization in the desired state. Reading is realized by a measure of resistance between the top and the bottom of the MTJ. c) Heterostructures used for SOT-MRAM. The injected current only flow on the bottom line (black arrow) and is injected in the TI. The desired orientation is obtain thanks to the generated spin accumulation (yellow arrows) that acts on the magnetization of the ferromagnet. Reading process is the same than for STT-MRAM. The main advantage with SOT compared to STT is that injection and detection path are decoupled.

different from STT-MRAM as depicted in **figure 1**. On these devices, a ferromagnetic layer is in direct contact with a material hosting strong SOC. This material can be found for example in the heavy metal family (Ta, W, Pt) or in two dimensional electron gas at the surface of 3D topological insulators (Bi_2Se_3, BiSb) or at Rashba interfaces (GeTe, $SrTiO_3/LaAlO_3$) that host peculiar spin textures. By injecting a charge current in a heavy metal, a 3D transverse spin current is generated and transferred in the adjacent ferromagnet driving the magnetization dynamics. If the torque transferred by the injected spin current is high enough it can lead to a switch of magnetization. In the case of topological insulators, the situation in analogous but care must be taken with the involved densities [24]. The EE creates a non-zero 2D spin accumulation at the interface between the TI and the ferromagnet. This overpopulation of spin polarized electrons comes from the spin texture hosted by TIs and can act as a torque in the adjacent ferromagnet. In the same way than for heavy metal, the magnetization direction can be tuned to obtain the desired state. The critical switching current in the case of a heavy metal is expressed by the following equation [25]:

$$J_{switch}^{SOT} = \frac{2et_F M_S}{\hbar} \cdot \frac{\alpha}{\theta_{eff}} . H_{eff} \tag{4}$$

With θ_{eff} the conversion efficiency between spin and charge current. In the case of heavy metal θ_{eff} is named spin Hall angle which is the ratio between spin and charge currents. In the case of TI the situation is analogous but the figures of merit are not exactly the same since the involved densities in the spin to charge process are not the same [24].

Challenges of Spintronics and spin-orbitronics

First MRAMs have been in the market since 2006 but have trouble to impose themselves as recording media in our daily computers. Nowadays, HDD and SSD (Solid-State Drive) are still commonly used. Despite the huge progress made with STT- and SOT-MRAM, the needs of novel materials with better properties to make MRAM viable are still on progress. The main challenges that physicists have to overcome are listed below. For the topological insulator[3] conversion layer, the challenges are:

- A strong spin-orbit coupling to generate the band inversion and the Topological Surface State (TSS).
- A gap large enough between the conduction and valence bands to allow spin/charge conversion at room temperature.
- A simple Fermi surface is very desirable with no additional state than the TSS crossing the Fermi energy to avoid other transport contributions that can strongly affect the spin/charge conversion.
- Protection of the TSS when multilayers are realized. It was predicted that magnetic impurities can kill the TSS. It is therefore essential to protect the surface of the TI with a non-magnetic layer.
- A good spin/charge conversion to reduce the switching current needed.

For the magnetization tunable ferromagnetic layer the challenges are:

- A full spin polarization at the Fermi level. If all the electrons are either spin up or spin down then all of them are going to participate to the polarization of the current without any loss.
- A low Gilbert damping coefficient α. α is the force that wants to bring back the magnetization in its equilibrium position. It opposes to STT therefore, a low α is much needed to suppress as much as possible this restoring force.
- A high Curie temperature T_C to be able to implement the ferromagnetic layer in our daily devices.
- A magnetization perpendicular to the thin film surface. Perpendicular magnetization reduces the needed current to switch the magnetization compared to in-plane magnetization. It also allows to decrease the device size by pushing back the superparamagnetic limit. Moreover, Perpendicular Magnetic Anisotropy (PMA) thin films are perfect two-state devices.
- A small demagnetizing field. PMA allows to reduce the demagnetization field thanks to magnetocrystalline anisotropy but it is possible to go further by using compounds with low M_S like ferrimagnetic or antiferromagnetic materials.

[3]Since the spin/charge conversion is in principle much higher on TI compared to HM with the same amount of injected charge current only the TI will be discussed here.

Heusler alloys and spintronics/spin-orbitronics

The aim of this thesis is to give solutions to make the applications described above suitable for our daily life. The compounds chosen to achieve these technical challenges are Heusler alloys. Heusler alloys are a large family of compounds with a huge variety of properties. This brief introduction is thus dedicated to shine a light on the potential of Heusler alloys that fit perfectly with this research domain.

As explained previously, magnetization reversal devices by SOT have been studied a lot in the last two decades. A lot of works were realized on 4d and 5d transition metals such as W [26], Pt [26] or Ta [27]. All those elements are heavy elements hosting strong SOC that allow to generate pure spin current thanks to SHE. The growing interest in heavy metals compounds were transferred to TIs [3] that are supposed to be much more efficient to perform interconversion. Since their discovery, TIs have been a great success due to their spin texture. The surface state of a 3D-TI consists of a Dirac cone resulting in a single Fermi surface in which the spin is locked to the momentum. This property, named spin-momentum locking [28], avoids backscattering and leads to very high spin-charge current interconversion. Due to this property, TIs are perfect candidates to generate huge torques on an adjacent ferromagnet and to switch its magnetization. The most deeply studied TIs were the Bi based compounds like Bi_2Se_3 [5], Bi_2Te_3 [6] or BiSb [7] where the topological surface states (TSS) were identified and interesting spin to charge conversion realized. Some Heusler alloys were predicted to host a non-trivial nature in 2010 [8]. They come from the half-Heusler family[4] with a XYZ formula unit. By considering SOC in band structure calculations, it was shown that a band inversion can occur at the Γ point of the Brillouin zone. Similarly to what happens in HgTe [29], the Γ_8 and Γ_6 bands are inverted. Therefore, the compound has a non-trivial topology and TSS should appear. Some interesting results have already been obtained on rare-earth platinum bismuth Heusler alloys [30, 31, 32] but the observation and presence of TSS is still under debate. Moreover, most of these studies are realized in bulk materials and a lack of thin films growth allowing to tune the cell parameters are present. The first part of this thesis is thus dedicated to the study of half-Heusler compounds predicted to be topological insulator. Thin film growth is performed by Molecular Beam Epitaxy (MBE) with a particular attention paid to crystalline growth, stoichiometry and atomic disorder that can strongly affect the band structure and the electronic properties. Angle Resolved Photoemission Spectroscopy (ARPES) studies are realized to map the band structure of thin films. Finally, electronic transport measurements are done to check the spin/charge interconversion efficiency of TI Heusler alloys compared to conventional heavy metals.

The most studied magnetic Heusler alloys were probably the one predicted to be Half-Metal Magnet (HMM). In these magnetic compounds, it is possible to achieve 100% spin polarization at the Fermi energy making them perfect candidates as spin polarizers. This property comes from an asymmetry in the density of states. For one spin channel (namely majority channel), states are available at the Fermi energy while a gap is present for the other spin orientation (minority spin channel). Therefore, HMM materials are conductor for the majority spins and insulating for minority spins leading to a full spin polarization at the Fermi energy. This remarkable property was predicted in 1983 by de Groot [9] for NiMnSb. However, nowadays it is

[4] Heusler alloys are divided in two families. The full-Heusler compounds with X_2YZ formula unit and the half-Heusler compounds with XYZ formula unit.

the Co_2MnZ compounds that are all the rage with 100% spin polarization measured for example in Co_2MnSi [33, 34] by spin resolved photoemission spectroscopy measurements. Even more interesting, high spin polarization and low magnetic damping are linked together. The Gilbert coefficient is a phenomenological term of the Landau-Lifshitz-Gilbert equation [35] that describes a damping force that tends to put back the precessing magnetization in its equilibrium position. Therefore, high Gilbert damping values are not suitable to realize magnetization reversal. In HMM, due to the absence of density of states for one spin channel at the Fermi energy the spin relaxation by spin-flop mechanism is prohibited. It is then obvious that these compounds are predicted to host low magnetic damping. The damping coefficient was measured in Co_2MnSi with value of the order of 4.10^{-4} [34] which is the lowest value obtained on metallic thin films (result obtained in the spintronic group at IJL).

One of the unchecked boxes of Co_2MnZ compounds is the obtaining of Perpendicular Magnetic Anisotropy (PMA). Indeed, as in most thin films, the magnetization remains in the sample plane due to layer's geometry. This in-plane magnetization is due to the demagnetizing field that forces this configuration. Nevertheless, it is possible to overcome this shape anisotropy by playing on magnetocrystalline anisotropy in volume or generated at the surfaces/interfaces. The main problem is that Co_2MnZ compounds have low magnetocrystalline anisotropy that does not permit to switch to out-of-plane magnetization. Thankfully, other Heusler alloys host strong magnetocrystalline anisotropy that allows to overcome the demagnetizing field and get PMA. These alloys are the Mn_3Z family [36] and have attracted a lot of attention. When the growth is realized in the $D0_{22}$ structure, the unit cell has a tetragonalized shape and is elongated along the c axis with a $\frac{c}{a}$ ratio of the order of 1.8. Such unit cell allows to get an easy magnetization axis along the c direction. It is therefore possible, by choosing carefully the substrate or the buffer layer, to complete the growth along this peculiar axis and get PMA. In the second part, the objectives are to carry out the growth of Mn_3Z compounds in the $D0_{22}$ phase with an easy magnetization axis perpendicular to the sample plane. Then, the previous works performed in the team on Co_2MnZ compounds are exploited to make bilayers made of Mn_3Z for their PMA and of Co_2MnZ for their high spin polarization and ultra-low magnetic damping. The final aim is to conserve all the properties of these two compounds namely PMA, ultra-low magnetic damping and high spin polarization in the bilayers. Once again a peculiar attention is pointed out on stoichiometry and atomic disorder that can impact the damping and spin polarization values and change the layers' magnetic properties.

Chapter 1

Half-Heusler alloys topological insulators: towards spin to charge interconversion

1.1 State of art of topological insulators

1.1.1 Theoretical introduction on topological insulator

The development of Quantum Mechanics in the 20^{th} century allowed the emergence of band theory. During this period, the physicists did their best to describe the electrons motions in various kinds of potential. One should start with the nearly free electron model allowing an estimation of the shape of the density of states and of the dispersion relation which turns out to be parabolic in momentum. This model has been improved to take into account the periodic potential felt by the electron in a crystal lattice. The solutions of the Schrodinger equation in a periodic potential are given by the Bloch functions and some conclusions are revealed. Every energy band can be described in the first Brillouin zone and all the eigenvalues extracted from the resolution of the Schrödinger equation will allow to define the energy bands which form, collectively, the band structure of the solid. Electrons are authorized to occupy some of the energy bands, meanwhile, others are forbidden, the so-called gaps. From this point, it is possible to distinguish between two different phases: insulators and metals. In metals, the Fermi level lies in a band. If we apply an electric field to a metal, we can move adiabatically some states to higher momenta while the lower momenta states are depopulated. Therefore, a net current is created and the solid is conducting. In the case of an insulator, the Fermi level lies between two bands and thus in the gap. In this case, it is not possible to create a net current because there is no change of occupied states and the solid remains insulating. As you can see, insulators have trivial electronic properties but is it always true? Some phases require to take electronics interaction into account.

Quantum Hall Effect and topological invariants

The Quantum Hall effect (QHE) is a quantized version of the classical Hall effect [29]. It occurs when electrons are confined in two dimensions with a strong magnetic field applied normal to the surface. The electrons are going to precess with cyclotron frequency around the field leading to discrete energy levels, called Landau levels. The Landau levels obtained are represented in **figure 1.1**. The dispersion relation is now highly degenerated, all these levels are localized and more or less filled according to the strength of the applied magnetic field. The question is: can

this system with Landau levels be considered as an insulator? It looks like an insulator. If we take the Fermi level and we place it between two Landau levels, we are in the gap. Therefore, current does not conduct? To answer this question, physicists realized two dimensional electron gas[1] (2DEG) (GaAs, AlGaAs, graphene, ...) and patterned it into Hall bars as represented in **figure 1.1**. They applied a current along the x direction, I_{xx}, and measured the longitudinal, V_{xx}, and transverse voltage, V_{xy}. The obtained results given in **figure 1.1** are surprising. The Hall resistance presents plateaus where energy is quantized for a certain range of magnetic field and these plateaus correspond to region with zero longitudinal resistance. This system should be insulating but the non-zero Hall resistance demonstrates a conducting behavior. The second interesting thing here is that the Hall conductivity is quantized, equal to $\sigma_{xy} = \frac{Ne^2}{\hbar}$ and with an accuracy close to 10^{-10} which is unusual in condensed matter. That means despite doing the experiment on different 2DEGs with more or less defects, this quantized value of the Hall conductivity is always obtained. This is the first evidence of the topological nature of the quantum Hall state.

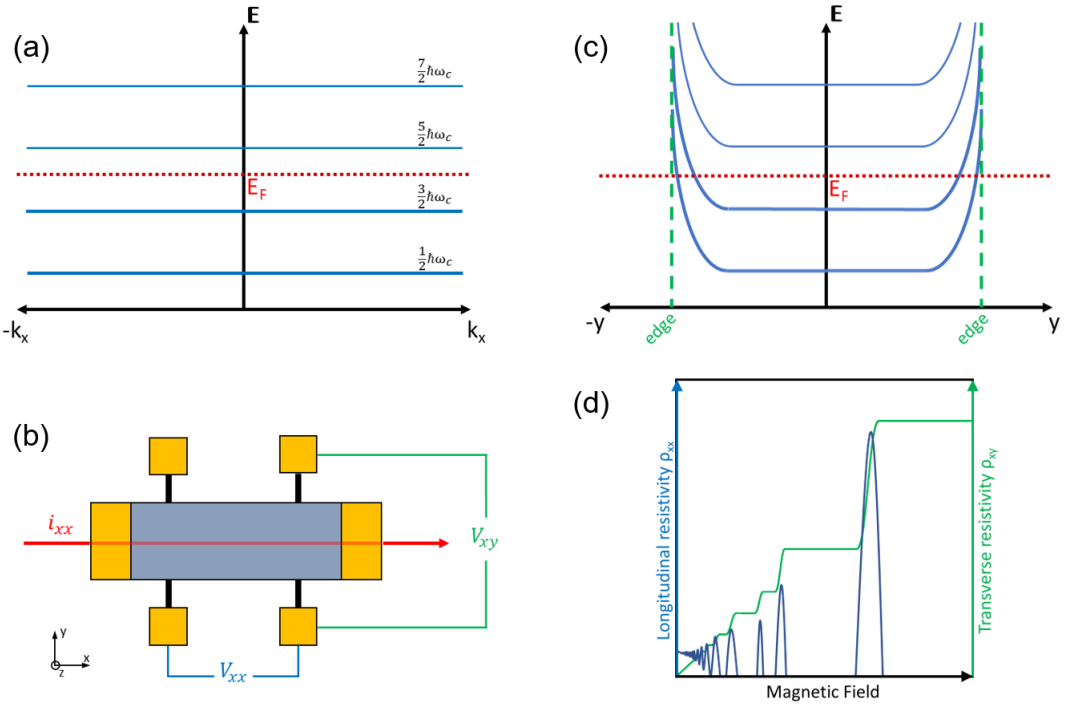

FIGURE 1.1: a) Landau levels of an infinite 2D sample. b) Hall bar geometry used to perform transverse, V_{xx}, and longitudinal, V_{xy}, resistance measurement of 2DEG. c) Shape of the Landau levels in a finite sample with edges that allow conduction at the edges while the bulk remains insulating. d) Longitudinal and transverse resistivity as a function of magnetic field.

To explain how the system is conducting, the Landau levels can be plotted in a finite sample. Due to confinement at the edges which tends to keep the electron in the sample, the Landau levels curve up at the edges as shown in **figure 1.1**. Therefore, electrons flow along the edges of the sample moving only in one direction avoiding backscattering and without any resistance. The bulk is insulating with gapless states at the edges. This new phase cannot be explained by symmetry breaking as we usually do to interpret for instance liquid to solid transition or magnetism. The answer

[1]The Quantum Hall states are predicted to occur in 2DEG.

has to come from topology.

In mathematics, topology is associated to the properties of a geometric object that are preserved under smooth and continuous deformations. This effect is often explained by saying that a torus and a mug have the same topology since it is possible to go from one to the other with no drastic transformation. On the other hand, going from a sphere to a torus implies to do a drastic change. A hole has to be drilled showing that the topology of both objects is different. The rigorous mathematic way to describe the difference between these objects is the Gauss-Bonnet theorem that links global (topology) and local (geometry) properties. The value extracted from this theorem relies on topological invariant and is named g, the genus of the surface. The integral of the Gaussian curvature is quantified and allows to classify the object. A sphere (g = 0) is different from a torus (g = 1). It turns out that a topological invariant is linked to the quantum Hall state allowing to distinguish this phase from the conventional insulating phase. This invariant is named the Chern invariant and is related to the Berry phase [37]. In order to clarify what the Berry phase is, an analogy can be done with parallel transport on a sphere. The idea is to transport a vector parallel to the surface of a sphere (**figure 1.2**). The ending point is the initial point such as a closed loop is formed. At the end of the loop the vector is not pointing in the same direction it was at the start. This angular mismatch is due to the curvature.

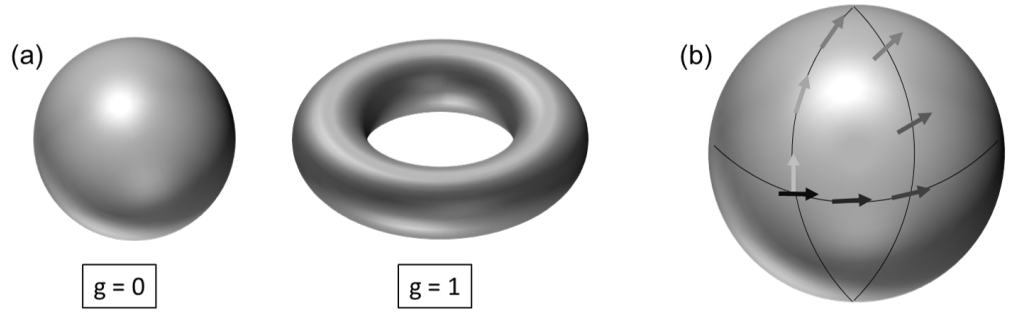

FIGURE 1.2: (a) Systems with different topology defined by their genus number g. (b) Parallel transport on a sphere. The initial vector (black arrow) is not pointing in the same direction at the end of the loop (grey arrow). It has gained a Berry phase equal to 90° here.

Similarly to parallel transport, the Berry phase depicts an additional geometrical phase on a particle wave function. Here the Brillouin zone plays the role of the surface. The Chern number relies on the Berry phase and allows to classify gapped band structure. If two materials have the same Chern invariant, therefore, they can be smoothly deformed into one another. If the Chern invariant is different, a drastic change has to be done pointing out a difference of topology. This Chern number, as demonstrated by Thouless, Kohloto, Nightingale and den Nijs [2], helps to explain the difference between the QHE and a trivial insulator.

The quantum Hall state paved the way to engineer bulk insulating material with conducting edge states. These materials need to break the Time Reversal Symmetry (TRS) to host non-trivial topology. For instance, the TRS breaker in the quantum Hall state is the applied external magnetic field. But other effects can lead to non-trivial topology as shown by Kane and Mele [3]. Indeed, they predicted in 2005 the existence of topological insulators that preserved TRS and that are characterized by the Z_2 topological invariants. This class of materials, named three-dimensional topological insulator (3D-TI), are different from QSH-like materials since they host

conductive surface states (instead of edge states) that are protected by TRS. These 3D-TIs are the compounds of interest in this work.

3D Topological insulator, spin-momentum locking and Edelstein effect

In 2006, Kane and Mele [3] proposed a new class of non-trivial insulators. The idea was to use elements with strong SOC. SOC magnitude is proportional to the gradient of the electronic potential, therefore, elements at the bottom of the periodic table are of interest here. By using these heavy elements, band inversions can occur thanks to SOC and the valence band becomes the conduction band and the other way around. The gap at the Fermi energy is still present and ensure the insulating behavior, except that, due to the band inversion, a non-trivial topology appears. The magic takes place at the interface between the non-trivial compound and the vacuum. Vacuum has a trivial topology, it can be considered as a trivial insulator. Inevitably, a drastic change has to take place to ensure the continuity between these two topological phases. Somewhere, the gap must be closed otherwise it is impossible for the topological invariant to go from one phase to the other. This change is fulfilled by metallic surface states that connect conduction and valence bands as depicted in **figure 1.3**. The key point here is that, due to the use of SOC to generate the non-trivial topology, TRS is preserved. This symmetry conservation has huge impacts on the surface states. If we look at the Kramers' theorem, all the eigenstates of a TRS Hamiltonian have to be two times degenerated. This constraint is trivial without SOC since the degeneracy is ensured by up and down spins. However, in the presence of spin-orbit interactions, states at the momenta **k** and -**k** must have spins of opposite direction. Due to symmetry considerations and SOC, the surface states exhibit a linear dispersion relation linked to an exceptional property named spin momentum locking. The spin is locked to the momentum in the way that spins rotate as the momentum moves around the Fermi surface as depicted in **figure 1.4**. These surface states are spin resolved thanks to SOC and TRS. As a consequence, back scattering is forbidden since no opposite states are available making them insensitive to non-magnetic impurities. Nevertheless, care must be taken with magnetic impurities that break the TRS and kill the TSS.

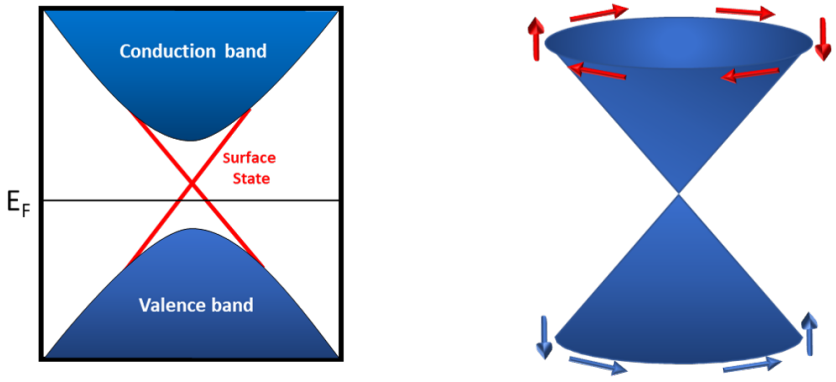

FIGURE 1.3: On the left, sketch of TI's band structure. The conduction and valence bands are separated by a gap showing the insulating bulk's behavior. These two bands are connected by a linear surface state that is conducting, the so-called Dirac cone. On the right, three dimensional representation of Dirac cone with its helical spin texture in the reciprocal space.

This peculiar helical spin texture can be harnessed by the Edelstein effect (EE) [4]. EE was predicted by Edelstein himself in 1990. The effect consists in the conversion of a bidimensional charge current into a spin accumulation. The easiest way

to understand this effect is to depict it in the reciprocal space. **Figure 1.4** represents the Fermi contour obtained with a perfect TSS. As explained before, the spins circle around the Fermi surface due to spin-momentum locking. By injecting a charge current, it is possible to generate a non-zero spin accumulation density. An injected current along the k_x direction for instance generates a variation of momentum Δk. This shift in momentum produces a spin accumulation since spin and momentum are linked together. Indeed, when the charge current flows in the TSS, it results in a different occupation of the spin-polarized branches of the Dirac cone. Therefore, an over population of down (or up) electrons is created. Because the bulk is still insulating, this charge current affects only the surface states that can generate huge spin accumulation of up or down spin depending on the applied charge current.

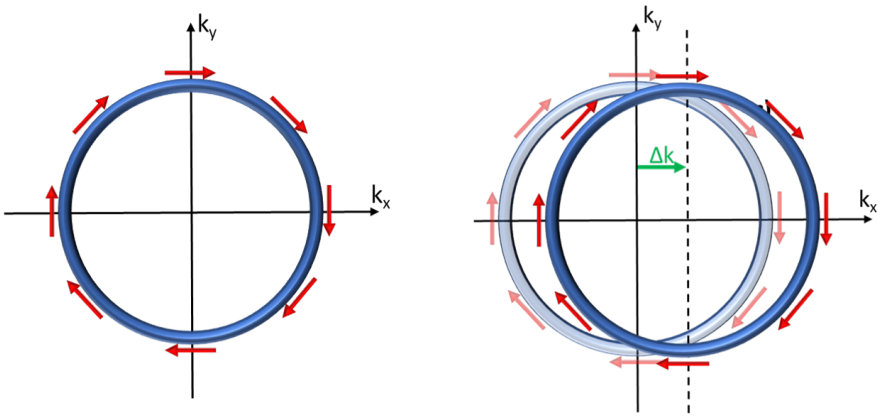

FIGURE 1.4: On the left, sketch of the Fermi contour and the spin texture in the reciprocal space. On the right, sketch of Edelstein effect. The introduced charge current generates a shift in momentum that generates non-zero spin accumulation. In this case the charge current is introduced along $+k_x$ generating an accumulation of spin $\downarrow$.

It is important to note that, similarly to Inverse spin Hall effect for spin Hall effect, the inverse effect exists. In the Inverse Edelstein Effect (IEE), a lateral spin current is injected in the TI that results in an induced lateral charge current. The spin injection in these systems is mainly realized by spin pumping. What has to be mentioned is that these spin accumulations can be harnessed to exert huge torque on the magnetization of adjacent ferromagnet. As explained in the introduction of this thesis, they provide a new way to manipulate the magnetization of ferromagnets.

1.1.2 The first topological insulators

In this section, we propose a quick outlook of the main TIs that have been studied since 2006 with the major results obtained just after their discovery. The second part will deal with the state of art of half-Heusler alloys TI from their discovery in 2010 to the realization of ARPES and transport measurements to identify the so desired TSS.

HgTe/CdTe

HgTe/CdTe are probably the compounds which paved the way for the development of topological insulator material. In 2006, Bernevig *et al.* [29] had the idea to perform mercury telluride - cadmium telluride semiconductors quantum wells. CdTe has a

common semiconductor band structure. Its conduction band has an s-like symmetry while the valence band has a p-like symmetry. CdTe is therefore a trivial band insulator. HgTe is slightly different due to the presence of a heavy element. The strong SOC lying in this compound causes a band inversion. Therefore, p levels rise above s levels. The idea of Bernevig *et al.* was to combine both telluride compounds to induce strain in the HgTe spacer (**figure 1.5**). In this heterostructure, HgTe is sandwiched between two CdTe layers. They demonstrated that for some critical thickness of HgTe (i.e higher than 6.5 nm), the band inversion occurs and the trivial insulator phase becomes a quantum spin Hall effect-like phase[2]. One year after the theoretical prediction, König *et al.* [38] managed to grow by molecular beam epitaxy HgTe/CdTe quantum well with the possibility to tune the electronic structure of the material by playing with the well size. After developing lithography, they performed transport measurements on various sizes of quantum wells by checking the conductance as a function of gate voltage. This experiment results in the first realization of a quantum spin Hall insulator material due to the observation of a quantized conductance (**figure 1.5**). Nowadays, HgTe/CdTe quantum wells are less studied due to the emergence of 3D-TIs.

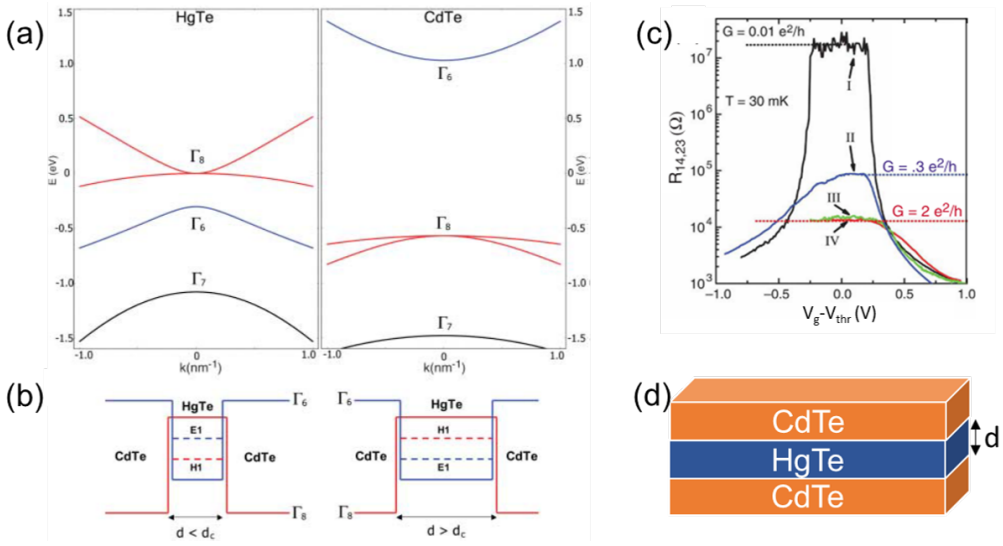

FIGURE 1.5: (a) Band structure of HgTe and CdTe with Γ_8 symmetry bands in blue and Γ_6 symmetry bands in red. (b) Quantum well in the normal regime on the left and on the inverted regime on the right. The inverted regime is the quantum spin hall insulator phase and happens above a critical thickness d_c. (c) Resistance as a function of gate voltage. Samples III and IV show quantized values of conductance demonstrating the existence of edges states in this Quantum spin Hall-like material. (d) Quantum well structure consisting of HgTe layer sandwiched by CdTe. (a), (b) and (c) taken from [29] and [38].

Alpha-Sn

In 2007, Fu and Kane [3] predicted theoretically α-Sn as a strong topological insulator. Since this prediction, a lot of physicists tried to master the α-Sn growth to confirm this theoretical prediction and checked the obtaining of linear dispersion around the Γ point, the so-called Dirac cone. But one of the main problems with α

[2]The quantum spin Hall state is the cousin of the quantum Hall state. This time no need of strong applied magnetic field since a strong SOC is present in the material. More information can be found in [28].

phase of Sn is that it is not stable at room temperature. Consequently, the deposition of the α phase took time and the first successful growth arrived in 2013 [39, 40]. Ohtsubo *et al.* [40] managed to grow α-Sn on InSb(001) substrate. The epitaxial α phase of Sn is obtained thanks to InSb substrate allowing them to stabilize α-Sn at room temperature due to a small compressive strain. They performed ARPES measurement for different sample thicknesses and confirmed the presence of a Dirac cone around the Γ point for thickness between 24 and 30 atomic monolayers. Spin-resolved photoemission spectroscopy and circular dichroism showed the presence of helical spin texture visible in the non-trivial surface states of TIs. They identified a counterclockwise spin propagation of the topological surface state with a direction almost fully in-plane. At the same time, Barfus *et al.* [39] also mastered the α-Sn growth on InSb(001) substrate by molecular beam epitaxy. They didn't observe topological surface state for pure Sn samples explained by a lower surface quality similar to some observations in Bi_2Se_3. However, with an additional Te dopant enhancing the surface quality they were able to measure linear dispersion and to tune the Fermi level position by playing with dopant concentration. They performed DFT calculations to show the origin of the TSS. Contrary to what one might think it is not based on SOC because the unstrained α-Sn is a zero gap semiconductor in which the valence band and the conduction band are already inverted (usually the role of SOC is to invert these bands) [41]. The main role here is played by the strain in the lattice that can open a gap at the Fermi energy while the band order remains unchanged which allows the emergence of the TSS. Since this discovery, some spin transport measurements have been done on α-Sn to check its efficiency [42, 43]. In 2015, Rojas-Sanchez *et al.* [42] performed spin pumping on a heterostructure composed of α-Sn layer and Fe ferromagnet separated by an Ag layer to ensure the protection of the TSS. They found an inverse Edelstein effect length higher than for conventional Rashba systems showing the efficiency of TIs for spin to charge conversion.

Bi and Sb compounds

At the same time they predicted α-Sn as a candidate to host topological phase, Fu and Kane [3] foretold bismuth-antimony alloy as a 3D-TI. One year later, Hsieh *et al.* [7] identified the first 3D-TI: $Bi_{1-x}Sb_x$. Bismuth is a semimetal and it is located at the bottom of the periodic table therefore, it hosts very strong SOC. By substituting Bi atoms with Sb ones, Hsieh *et al.* managed to generate an inversion of bands symmetry around the $\overline{T}$ point which led to the emergence of a topologically protected surface states. Thanks to ARPES measurements, they mapped the band structure of $Bi_{1-x}Sb_x$ (with $0.07 < x < 0.022$) and discovered the complex surface structure of this compound with surface bands crossing five times the Fermi level (**figure 1.6**). This odd number of crossing points confirms the presence of strong topologically protected surface states. Within the next year, Hsieh *et al.* [44] published another paper in which they performed spin-resolved photoemission spectroscopy to probe the spin polarization of the band structure and showed a strong spin polarized surface state. Another remarkable property of 3D-TIs is that they should be insensitive to non-magnetic disorder. It was for this purpose that Roushan *et al.* [45] used ARPES and scanning tunneling microscopy measurements to show that despite strong atomic scale disorder, no backscattering occurred in the TI. They concluded that backscattering between states of opposite momenta and opposite spins was absent in such material validating the robustness of these topological states. This work has launched a search for other TIs. Indeed, $Bi_{1-x}Sb_x$ has quite a complex surface structure, a narrow band gap and has been less studied than the second

generation of 3D-TIs. Nevertheless, some interesting transport measurements have emerged from this compound. For example, the recent paper from Kang *et al.* [46] shows that BiSb thin film can generate very large spin-orbit field thanks to large spin Hall angle associated to a large conductivity.

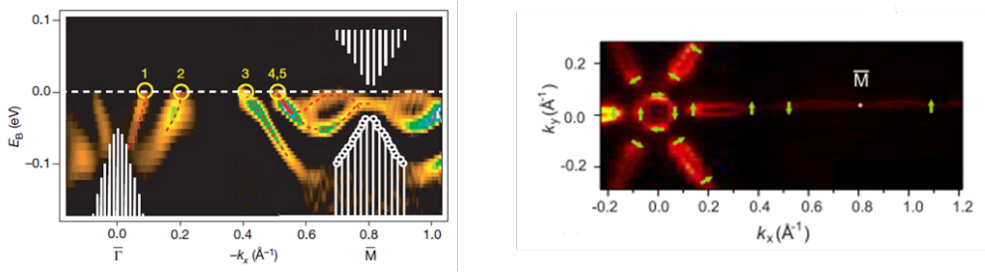

FIGURE 1.6: On the left, band structure of $Bi_{0.9}Sb_{0.1}$ obtained by [7] showing multiple band crossings at E_F. On the right, Fermi surface of $Bi_{1-x}Sb_x$ showing the complex surface of this compound.

In this research of new topological insulator with narrower band gaps and less complex band structures, some candidates were quickly identified. In 2009, Zhang *et al.* [47] performed first-principles electronic calculations on four stoichiometric compounds namely Bi_2Se_3, Bi_2Te_3, Sb_2Se_3 and Sb_2Te_3. Three of them were predicted as 3D-TIs with a single Dirac cone centered at the $\bar{\Gamma}$ point of the Brillouin zone. The most important one was without any doubt Bi_2Se_3 thanks to its large energy gap of 0.3 eV which is larger than the energy scale of room temperature. Therefore, there is no need to reach extremely low temperature to carry out experiments. It is, still nowadays, the most studied 3D-TI, this is the reason why we are going to focus on this particular one in this part. At the same time than Zhang group, Xia *et al.* [5] also performed first-principles calculations showing the same conclusions than Zhang. In addition, they also did ARPES measurements revealing the presence of a single Dirac cone lying in a bulk band gap of 0.3 eV. Starting from these results, a lot of groups have worked on Bi_2Se_3 and have confirmed the band structure observed previously. Bi_2Se_3 family compounds offers multiple advantages compared to previous $Bi_{1-x}Sb_x$ alloys. First, it is a stoichiometric compound making it easier to master a good growth with good crystallinity which is essential for ARPES measurements. Secondly, its surface band structure is much more simple than the $Bi_{1-x}Sb_x$ one and its multiple crossing points at the Fermi level. Bi_2Se_3 has only one single Dirac cone. Finally, its bulk gap is much larger than the one for $Bi_{1-x}Sb_x$ preventing the need to do ultra-low temperature measurements. Since Bi_2Se_3 is a 3D-TI, it is protected by inversion symmetry. Therefore, adding non-magnetic impurities at the surface leaves the TSS intact but can modify slightly the Fermi energy. In 2009, Hsieh *et al.* [48] were able to tune the Dirac cone position with respect to the Fermi energy by surface doping with Ca and gating control without breaking the topological order. Firstly, they were able to put the Fermi level within the bulk band gap which is not the case in undoped Bi_2Se_3. Secondly, they managed to align the Dirac point with the Fermi level. With the chemical potential lying at the Dirac point it is easy to tune the density of carriers for transport measurements just by applying a gate voltage. It is also important to notice that some works were done on doping with magnetic impurities like Fe or Mn [49, 50, 51]. Their experiments confirmed that, in presence of magnetic impurities which are time reversal breaking perturbation, a gap opens at the Dirac point.

A lot of transport measurements have been realized on Bi_2Se_3 in order to check

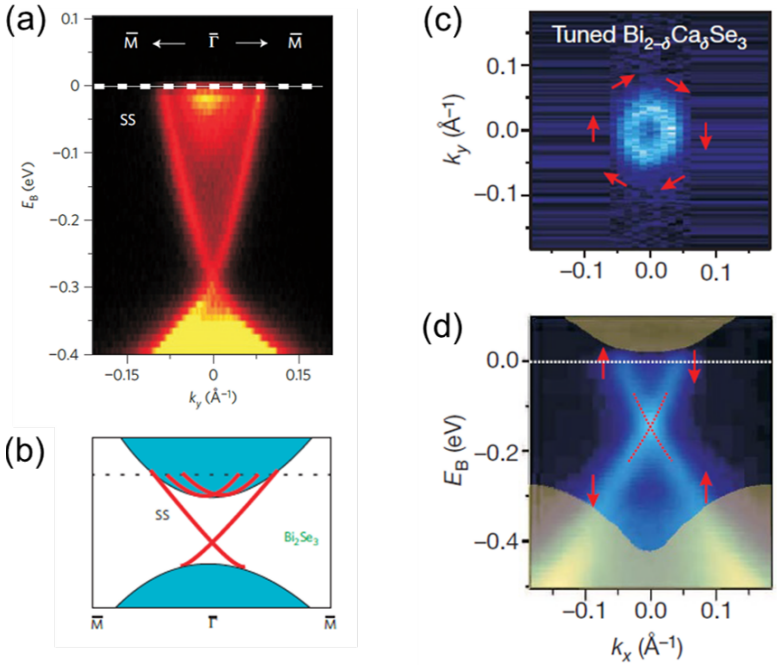

FIGURE 1.7: (a) Dirac cone identified in Bi_2Se_3. (b) Sketch of the band structure showing that bulk and surface states are present at E_F for undoped Bi_2Se_3. Fermi surface (c) and band structure (d) of Bi_2Se_3 doped with Ca to tune the position of E_F and drive away bulk states. Taken from [5] and [48].

its conversion efficiency and to perform SOT-switching [52, 53, 54, 55, 56, 57, 58, 59, 60, 61, 62]. The obtained results are one order of magnitude higher compared to classic heavy metal structures attesting to their huge potential. Nonetheless, some bottlenecks are still present with Bi_2Se_3 such as its integration in MTJ without breaking the TSS or interdiffusion between the different layers. Moreover, contributions from bulk states that can affect strongly spin transport are still under investigation since the deconvolution of bulk and surface states turn to be a complex task.

1.1.3 State of art of half-Heusler alloys 3D-topological insulators

We can divide the Heusler family in two main groups of compounds. The full-Heusler group, with a 2:1:1 stoichiometry, and the half-Heusler group, with 1:1:1 stoichiometry. This class of materials consists of more than 1500 different compounds showing a wide variety of applications and physical properties. The full-Heusler part will be discussed in the next chapter of this thesis and we are going to focus on the half-Heusler alloys here. The half-Heusler compounds have a XYZ formula unit formed by a covalent and a ionic part. Usually, X and Y atoms are transition metals and Z is a main group element. There are different nomenclature[3] in literature for Heusler alloys. Here, an order reflecting electronegativity is used. The most electropositive element is placed at the beginning of the formula while the most electronegative is placed at the end. They crystallize in a non-centrosymmetric cubic structure (space group n°216, F-43m, $C1_b$). The $C1_b$ structure, represented in **figure 1.8**, can be viewed as three interpenetrating face centered cubic (fcc) sublattices with

[3] In literature the nomenclature varies from ranking the element by electronegativity, alphabetically or randomly.

every sublattice occupied by X, Y or Z atoms. The unit cell is formed by three Wick-off positions namely 4a (0,0,0), 4b ($\frac{1}{2}$, $\frac{1}{2}$, $\frac{1}{2}$) and 4c ($\frac{1}{4}$, $\frac{1}{4}$, $\frac{1}{4}$). The atoms in position 4a and 4b form an ionic NaCl-type sublattice while atoms in position 4a and 4c form a covalent-type ZnS structure.

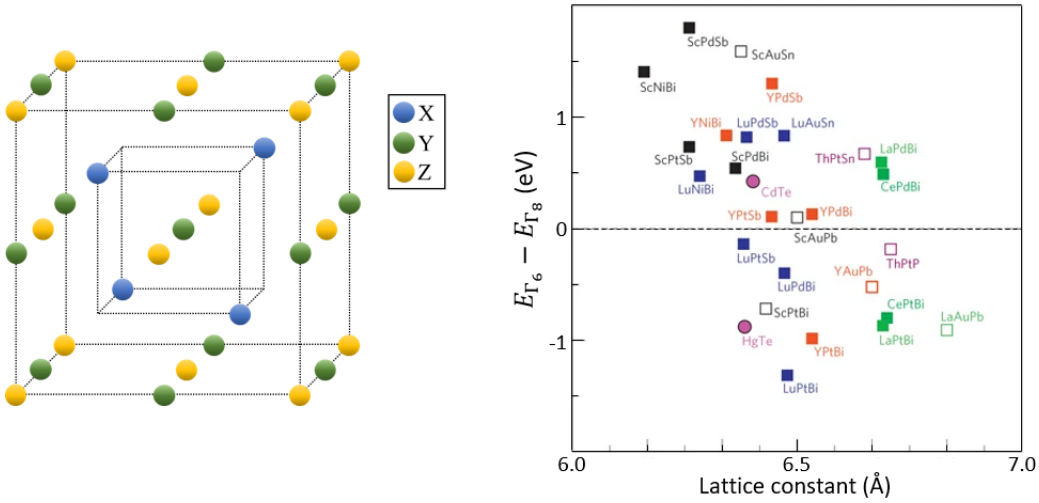

FIGURE 1.8: On the left, $C1_b$ half-Heusler structure. On the right, band inversion strength as a function of lattice constant. Compounds in the lower part of the graph are predicted to be band inverted while the upper part compounds are predicted with a trivial band structure under normal conditions. Adapted from [8].

The Heusler family is composed of more than 200 semiconductors and these mainly come from ternary compounds. This great diversity, especially compared to binary semiconductors like Bi_2Se_3, opens a wide range of compositions to design the future TI. It was demonstrated in 2010 by Chadov *et al.* [8] and Lin *et al.* [63] that around 50 Heusler alloys possess a band inversion (**figure 1.8**) similar to that of HgTe which is necessary to get a non-trivial topological phase. This large variety of compounds allows to tune the band gap thanks to the electronegativity difference of the atoms and the strain applied in the lattice. **Figure 1.9** allows to understand the band structure of half-Heusler alloys by making a comparison between the band structure of CdTe and HgTe with respectively ScPtSb and ScPtBi. To do that, attention must be given to the band with Γ_6 symmetry depicted in blue and the Γ_8 symmetry ones in red. The comparison reveals close similarity between both kinds of system. On the one hand, the normal band ordering, with Γ_6 (s-like orbital) as conduction band situated above the valence band Γ_8 (p-like orbital) is present in CdTe and ScPtSb. Both exhibit a direct gap at the Γ point of the Brillouin zone with, consequently, a trivial behavior. On the other hand, the conduction and valence bands are inverted for HgTe and ScPtBi. The Γ_6 band is now located below the Γ_8 band. This band inversion is due to the presence of heavier elements that undergo strong relativistic effects leading to a non-trivial state. Another interesting prospect is that no band cross the Fermi level except the one at the Γ point. So, no complex Fermi surface should be observed. The normal band ordering is preserved in the Brillouin zone apart from this peculiar point. Chadov *et al.* [8] published a graph listing the potential TIs candidates of the Heusler family. The graph, given in **figure 1.8**, shows the energy difference between Γ_6 and Γ_8 bands called band inversion strength. If the difference is negative, then, we are non-trivial topologically because the Γ_6 and Γ_8 band are inverted. If the difference is positive, the band order is not inverted and we are topologically trivial. But care must be taken with the Γ_8 bands that are degenerated

at the Γ point due to the high degree of crystal symmetry. Therefore, all those compounds with inverted band structure are rather non-trivial zero gap semiconductors (or non-trivial zero gap semimetals) than non-trivial insulators. However, by introducing strain in the system it is possible to change the degree of hybridization and lift the degeneracy. Then, the overlap of valence and conduction bands vanishes and a gap is open. For example, LuPtBi is predicted as a non-trivial zero gap semiconductors. Al-Sawai *et al.* [64] demonstrate that by applying a uniaxial strain along the [111] direction leading to a contraction of the lattice (3% along the lattice constant a and 4% along c) the degeneracy of the Γ_8 state is broken and a gap opens. Similar results were obtained by Chadov *et al.* [8] with YPdBi compound. As shown in **figure 1.8**, YPdBi is slightly in the positive range of the band inversion strength indicating that YPdBi is a trivial Heusler with no band inversion. They generated a small tetragonal strain along the [001] direction leading to a reduced $\frac{c}{a}$ ratio of about 3%. This uniaxial strain lifts the degeneracy which allows the transition from trivial to non-trivial state. Finally, they showed that a small change in lattice parameter can modify the band structure near the Fermi energy. They performed calculations by applying a small variation of the lattice constant ($\pm$ 3%) and showed the possibility to tune YPdBi from trivial insulator (E_{Γ_6} - E_{Γ_8} = 0.07 eV) to non-trivial insulator (E_{Γ_6} - E_{Γ_8} = -0.07 eV) with zero gap inverted structure. In summary, different ways are possible to tune the Half-Heusler compounds from trivial to non-trivial insulator or to open the gap by lifting the degeneracy of Γ_8 band. Firstly, it is possible to slightly change the lattice constant. This can be mainly done by selecting the appropriate substrate to get a constrained growth. Secondly, it is possible to construct a quantum well structure similar to what was done for HgTe/CdTe quantum-well thanks to the large variety of compounds. Some half-Heusler pair were identified like ScPdBi-ScPtBi, YPdSb-YPtSb and LuAuSn-LuPtBi. Thirdly, we can tune the band structure by elements substitutions. The alloying can be done on any atomic site providing an easy way to tune the electronegativities or the strength of SOC.

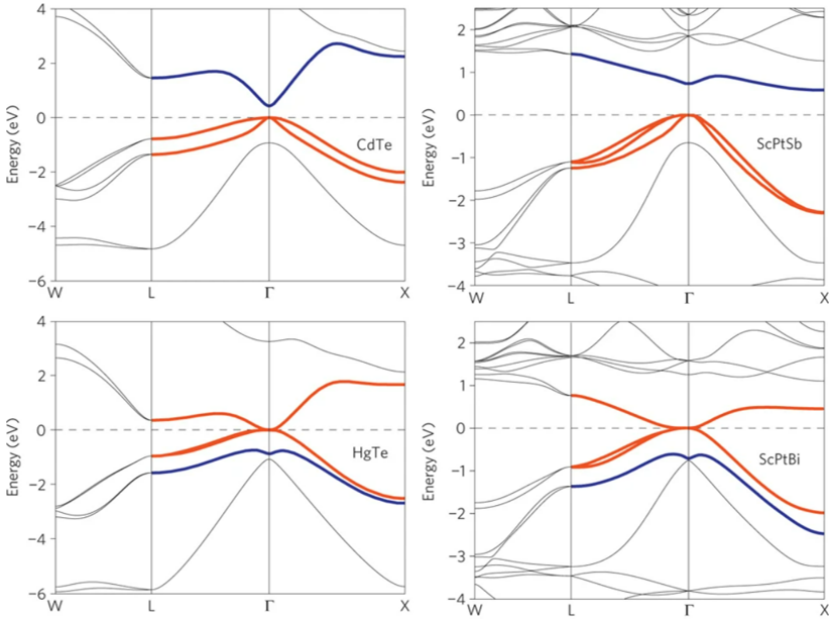

FIGURE 1.9: Comparison between the trivial band structure of CdTe and ScPtSb and between the inverted band structure of HgTe and ScPtBi showing the similarities of these compounds. Γ_6 bands are in blue and Γ_8 bands in red. Taken from [8].

Thanks to their topologically non-trivial electronic structure promising to host a wide variety of phenomena, half-Heusler have attracted attention. The next part is thus dedicated to the techniques implemented to identify the presence of a TSS. It will allow to do a non-exhaustive summary on half-Heusler compounds hosting non-trivial effects.

ARPES is probably the first technique that comes to mind to reveal TSS. In an ARPES experiment, photons are used to eject electrons from the crystal. These electrons are then collected and analyzed in term of momentum and emission angle to reconstruct the sample's band structure. The first group which performed ARPES measurements on half-Heusler alloy was Liu *et al.* [30] in 2011. They studied the metallic surface electronic state in three rare-earth Platinum Bismuth materials namely PtRBi with R = Lu, Dy, Gd. The samples were cleaved *in situ*, yielding a clean (111) surface. The Fermi surfaces, shown in **figure 1.10**, reveal a similar nature for all three compounds according to their shapes. The main difference is lying in the size of the electron pockets which are slightly different for each Heusler due to a different effective electron occupancy. Several bands cross E_F in the vicinity of $\overline{\Gamma}$ and $\overline{M}$ points. We are therefore far from the ideal case with only one crossing occurring at the center of the Brillouin zone. Multiple bands with linear dispersion that are spin-orbit split are identified as surface bands. Nonetheless, a clear estimation of the number of crossing points is not permitted. If this number is even, no contribution to the Berry curvature should be observed and these compounds should remain trivial. It is important to notice that they performed electronic calculations that are in perfect agreement with the obtained spectra. These calculations show a non-trivial topology that cannot be clearly observed experimentally due to the complexity of the band structure near the Fermi energy. In any case, this first study paved the way to further ARPES determinations of TSSs. In 2016, three other half-Heusler compounds, PtLuSb, PtLuBi and PtYBi were studied [31, 32]. These studies allowed to identify the presence of a topologically protected surface state. Logan *et al.* [31] investigated the band structure of PtLuSb and identified the presence of TSS overlapping with bulk bands. These additional bulk states generate additional spectral weight near the Fermi energy that can decrease spin transport for practical applications. However, spin-resolved photoemission spectroscopy allowed to distinguish a strong spin texture of the linear dispersion with each side carrying an opposite polarization. On their side, Liu *et al.* [32] worked on PtYBi and PtLuSb. They attested to the presence of linear dispersion protected by topology in both PtYBi and PtLuBi with a TSS lying in the bulk band gap revealing the robustness of these states. The TSS occurs at $\overline{\Gamma}$, the center of the Brillouin zone but once again, additional spectral weight is identified with multiple bands crossing the Fermi energy as shown in **figure 1.10**. Electron pockets are present at $\overline{K}$ and $\overline{M}$ points for LuPtBi and at $\overline{K}$ point for PtYBi leading to complex Fermi surfaces. *ab initio* calculations support these results with a TSS lying in the bulk bands. Finally, a recent study on PtYBi was published in 2021 by Hosen *et al.* [65]. ARPES measurements on cleaved samples and first principle calculations showed the presence of a Dirac state well below the Fermi level. In the same way than previous groups, they observed the presence of multiple Fermi surface pockets. Rashba-split bands and surface states are identified as crossing the Fermi energy in similar way than previous study except for the conclusion. According to Hansen, the linearly dispersive state that occurs below the Fermi energy is a trivial Dirac state instead of a TSS due to the absence of a band gap which should prevent a topologically non-trivial phase. At this point, the question of the non-trivial character of half Heusler is still unsettled.

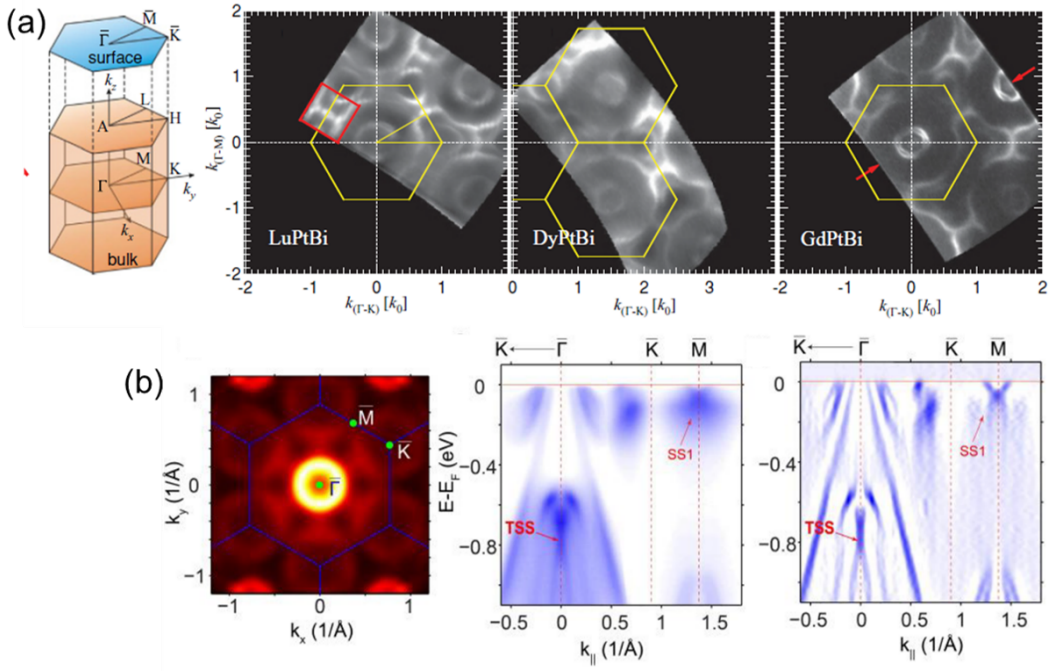

FIGURE 1.10: (a) On the left: shape of the surface and bulk Brillouin zone for the [111] direction of half-Heusler lattice. On the right: the three Fermi surfaces obtained for PtRBi compounds with R = Lu, Dy, Gd. (b) On the left: Fermi surface obtained for PtYBi sample oriented along the [111] direction. On the middle and on the right: respectively the band structure of PtYBi and its second derivative. The TSS is identified thanks to theoretical calculations. Taken from [30] and [32].

Another way to identify non-trivial state is by using transport measurements. A big part of half-Heusler alloys predicted with a non-trivial topology are hosting exciting properties such as superconductivity, antiferromagnetic order, heavy fermion behavior and so on. Mixing these properties with the topological order has attracted a lot of attention especially to achieve new topological phases like topological superconductors. This search of linked topology with superconductivity led to the realization of transport measurements to detect the presence of superconductivity. The interesting thing here is that some magneto-transport experiments have a peculiar behavior in presence of TSS. It is therefore possible to identify TSS using transport measurements but care must be taken. Magneto-transport measurements are not only surface sensitive since they probe also the sample bulk.
Platinum bismuthide and Palladium bismuthide series accompanied with a rare earth as third element have been widely studied for this superconducting property. For instance, PdYBi, PtYBi and PtLuBi are proposed as superconductor [66, 67, 68, 69]. Others like ErPdBi or HoPtBi are predicted to host superconductivity and/or antiferromagnetic order [69, 70, 71]. The superconducting transition in these compounds occurs in a range from 0.77 K to 2.2 K and all compounds exhibit the same semi-metallic-like (or metallic-like) resistivity lineshape as represented in **figure 1.11**. The antiferromagnetic transition for the second set of compounds takes place in a similar range of temperature (for instance, T_C = 1.2 K and T_N =1.1 K for ErPdBi). Their magnetic nature comes from the magnetic moment carried by the rare-earth atom. The reported charge carrier concentrations are in accordance with this semi-metallic-like behavior with low carriers concentration of the order of n $\sim 3.10^{18}$ to 10^{20} cm^{-3}. A lot of papers focus on the determination and the observation of

superconductivity and antiferromagnetic order without taking care of any demonstration of the presence of topological order jointly with those exciting properties [67, 71, 72, 73]. However, other papers deal with both aspects and try to determinate the presence of a TSS thanks to transport measurements. The main technique used is Shubnikov-de Haas (SdH) oscillations, shown in **figure 1.11**, which results in an oscillation in the conductivity of a material at low temperature with a strong applied magnetic field. SdH oscillations have been used to characterize quantum transport in materials with 2D surface states. By fitting the oscillation, a lot of physical properties can be extracted like charge carrier density, effective mass and more interestingly an estimation of the Berry phase. A non-zero Berry phase is a possible fingerprint of Dirac systems. Other physic phenomena allow to identify non-trivial topological order such as weak antilocalization or special behavior of the transverse and longitudinal magnetoresistance. In the same way than for ARPES measurement, the conclusions drawn differ from one article to another and the presence of topological surface states is still unclear. The first transport study was realized by Butch *et al.* [66] in 2011. They performed magneto-transport and Hall measurement on YPtBi that seemed to support the non-trivial topology in this compound. But one should pay attention to the strong SOC hosted by this material, the effect could come from the bulk of the sample with nothing related to TSS. In 2016, Pavlosiuk *et al.* [68] reported another study on YPtBi. Once again, they observed several features typical of a non-trivial topology namely weak antilocalization, non-saturating linear magnetoresistance and non-trivial Berry phase value extracted from SdH oscillations. The exact origin of these effects is not sure but the non-trivial Berry phase very close to the theoretical value of π for Dirac cone points strongly in their favor.

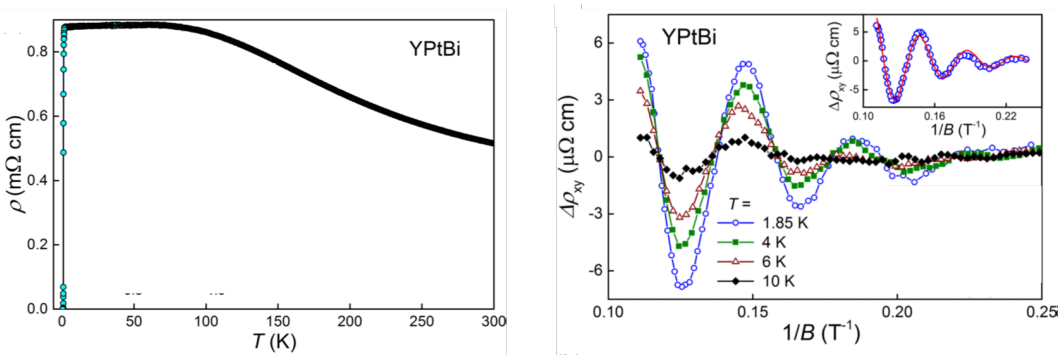

FIGURE 1.11: On the left, electrical resistivity as a function of temperature for PtYBi with a semi-metallic-like behavior. On the right, Shubnikov-de Haas oscillations obtained for PtYBi. Taken from [68].

Similar conclusions have been obtained for other Heusler alloys such as ScPtBi [74] where weak antilocalizations have been labeled as emerging from the strong spin-orbit coupling of the compound rather than from TSS. On the other hand, Bhardwak *et al.* [75] demonstrated a surface dominated transport in strained ErPdBi thin films thanks to observed 2D weak antilocalization effect and a non-trivial Berry phase.
Another compound important to mention is YPdBi. First transport study was realized in 2013 by Wang *et al.* [76] showing that SdH oscillations originate from high-mobility bulk carriers of the sample with no topological nature. However, their calculations show the presence of non-trivial Dirac states when the sample is constrained. This is what Banerjee *et al.* [75] performed in 2020. They grew YPdBi along the [110] direction using pulsed laser deposition. A MgO substrate and a seed layer of Ta induce strain that drove the emergence of topological non-triviality in YPdBi.

They identified a dominant transport contribution coming from surface states thanks to 2D weak antilocalization effect and a π Berry phase extract from SdH oscillations.

Finally, the last reported way to probe the band inversion in topologically non-trivial Heusler is Nuclear Magnetic Resonance (NMR). NMR is sensitive to the electronic band structure near the Fermi energy making it a tool to identify non-trivial behavior. Nowak *et al.* [77] and Shi *et al.* [78] studied the nuclear magnetic resonance response of Bi. By analyzing the Bi resonance shift in YPtBi and YPdBi they were able to distinguish two different behaviors. The shift difference between both compounds was attributed to the presence of spin-polarized electrons from bands near the Fermi energy in PtYBi in accordance with the band inversion predicted in this compound. On the other hand, PdYBi was confirmed as a trivial material due to the lack of shift coming from polarized surface states.

Other techniques are available to identify non-trivial behavior such as scanning tunneling microscopy and spectroscopy or bilinear magnetoresistance but none of them has been published yet in the literature for half-Heusler compounds.

1.2 Structural characterization

All the samples of this thesis were grown by molecular beam epitaxy (MBE) at the Institut Jean Lamour. The MBE quaternaire (**figure 1.12**) is made up of 24 elements that are split between three electron guns with six pockets each and six Knudsen cells. This wide variety of elements allows to perform easily ternary or quaternary Heusler compounds on numerous buffer layers. The MBE chamber is linked to the 70 meters ultra-high vacuum tube facility of the Institut Jean Lamour. Therefore, characterization experiments can be realized without breaking the vacuum such as X-ray photoelectron spectroscopy, Auger electron spectroscopy, scanning tunneling microscopy and angle resolved photoemission.

1.2.1 Determination of studied systems and growth process

MBE and RHEED

Among all the possible half-Heusler alloys candidates to be topological insulator, we chose to investigate firstly PdYBi and PtYBi. Platinum, Palladium and Yttrium elements had already been used as buffer layers or in other compounds resulting in knowledge on their deposition. Moreover, we started with Bi instead of Sb (also present in the MBE) due to the strong spin-orbit coupling hosted by this element in comparison with Sb (83 e^- against 51 e^-). Bi-based half-Heusler compounds are predicted to host more easily topological phase than the ones with Sb. Despite the lack of knowledge of Bi deposition, it was primordial to use it.

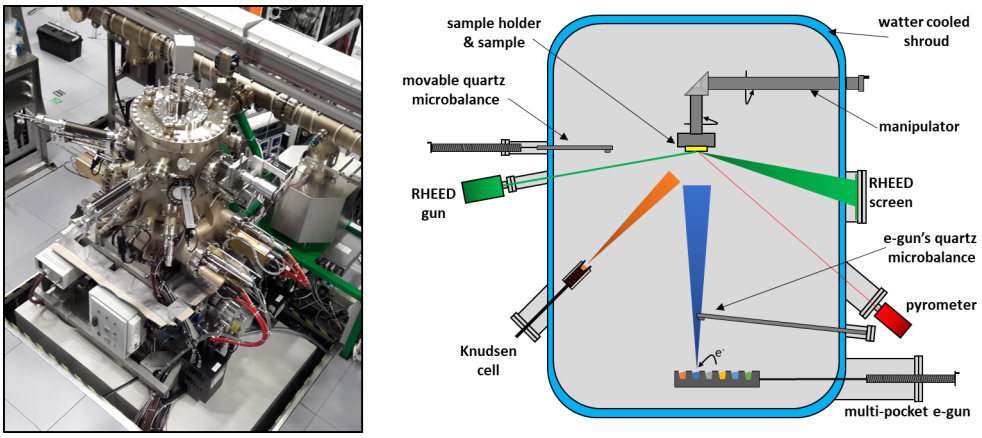

FIGURE 1.12: On the left-hand side MBE quaternaire used to grow Heusler compounds. On the right-hand side simplified sketch of the MBE quaternaire.

The growth process consisted in co-evaporating the three elements at the same-time with a base pressure equal to 3 $.10^{-11}$ Torr. Bi is evaporated using Knudsen cells while Y, Pt and Pd used e-guns. Since half-Heusler alloys rely on a 1:1:1 stoichiometry, fluxes are fixed as followed in the case of PdYBi:

$$\Phi_{Pd} = \Phi_{Y} = \Phi_{Bi} \tag{1.1}$$

For most of the deposit, Φ were fixed at 5 $.10^{13}$ at.cm^{-2}.s^{-1}. The flux is linked to the growth rate by the formula:

$$\Phi_i = v_i.n_i = v_i.\frac{\rho_i.N_A}{M_i} \tag{1.2}$$

with n the volume density (at.cm^{-3}), ρ the mass density (g.cm^{-3}), N_A the Avogadro number (at.mol^{-1}), M the molar mass (g.mol^{-1}) and v the growth rate (Å.s^{-1}). By fixing ρ to the density of the studied material, it is easy to calculate the growth rate of each element. For instance, with the chosen flux of 5.10^{13} at.cm^{-2}.s^{-1} for all elements and the fixed density of PdYBi alloy[4] which is 9.25 g.cm^{-3}, the growth rates of Pd, Y and Bi were quickly determined (see **table 1.1**) and lead to the alloy's growth rate of 0.36 Å.s^{-1}.

	Φ (at.cm^{-2}.s^{-1})	ρ (g.cm^{-3})	M (u)	v (Å.s^{-1})
Pd	5.10^{13}	9.25	106.42	0.095
Y	5.10^{13}	9.25	88.91	0.0794
Bi	5.10^{13}	9.25	208.98	0.187

TABLE 1.1: Summary of fluxes, densities, molar masses and growth rates of Pd, Y and Bi.

Quartz microbalances (QM) were used to check the growth speed and ensure the good flux rates. Evaporation rate with Knudsen cells (for instance Bi) is checked by a removable QM placed at the sample location prior to alloy deposition. The

[4]The knowledge of the alloy density is not a necessity and one can choose an arbitrary density for each element as explain in [79].

flux stability was then ensured by temperature regulation of the cell (accuracy of $\pm$ 0.2 °C) before the growth. Since cells are very stable in time, there was no need of flux control during deposition. For e-guns deposition (for instance Pd, Pt or Y) the fluxes were checked thanks to the coupled QMs on each e-gun. Before the deposition, fluxes observed at the e-gun's QM and at the sample position's QM were equalized. During the growth, the sample was located at the place of the removable QM and the e-guns' QMs ensure the good stability of the fluxes thanks to a feedback loop. E-guns are less stable compared to Knudsen cells since materials in the crucible can evolve quickly under electron radiations. This is why e-guns growth rates were checked during the deposition as shown in **figure 1.13**.

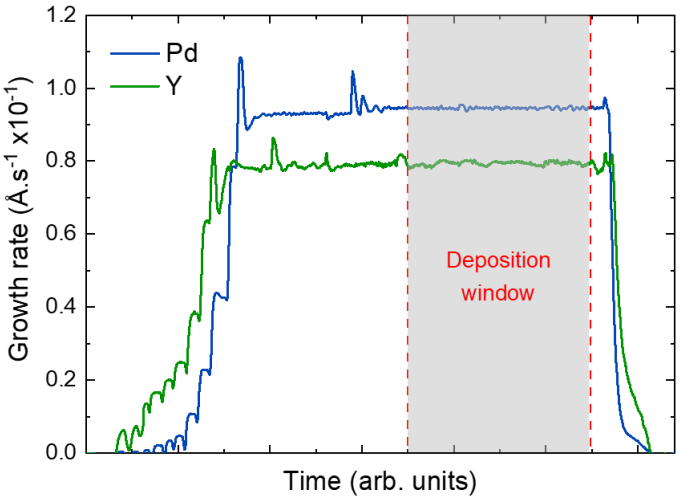

FIGURE 1.13: Recorded growth rates of Pd and Y during PdYBi deposition. Deposition window is the shaded area. The left and right part around the deposition window are respectively the e-guns ignition and stabilization and the e-guns shutdown.

In addition to the possibility to ensure the regulation fluxes thanks to e-guns' QMs, it is possible to follow the growth in real time thanks to a Reflection High Energy Electron Diffraction (RHEED) set-up coupled to the MBE that is compatible with crystal growth process. Due to the geometry of the experiment, RHEED is a surface sensitive technique since only atoms at the sample surface contribute to the diffraction pattern observed providing resolution on the atomic scale. In this set-up, electrons are accelerated by a 20 kV voltage. The glancing angle of the electron beam in regards of the sample is lower than 1°. Therefore, only a few atomic planes beneath the surface are probed. The obtained RHEED patterns are explained by the interaction between the electron beam and the atoms of the surface. According to the crystal lattice and the spacing between atoms, electrons are going to interfere constructively in some peculiar directions. A fluorescent screen allows to pick up these constructive electron waves and the obtained patterns reflect the surface crystallography.

It was with these two techniques that the growth process of half-Heusler alloys TIs began.

First growth test: MgO substrate

The first growth tests were done on MgO substrate oriented along the (001) direction. MgO substrates were outgassed *in situ* at a temperature around 950 °C (T_{pyro} ≈ 540 °C)[5]. The first attempt was done directly on MgO at a growth temperature of 450 °C (T_{pyro} ≈ 300 °C). The deposition resulted in a fiber-like texture oriented along the (111) direction. After this first test, some others were done using a buffer layer to reduce the lattice mismatch with PdYBi. Pt, V and Pd buffer layers were tested but without success especially since the use of buffer layer prevents annealing the sample otherwise interdiffusion occurs between layers. Other depositions were performed directly on MgO substrates by varying the growth temperature and the obtained fiber-like textures along the (111) direction (given in **figure 1.14**) suggest to use a suitable substrate or buffer layer to orient the growth along this direction.

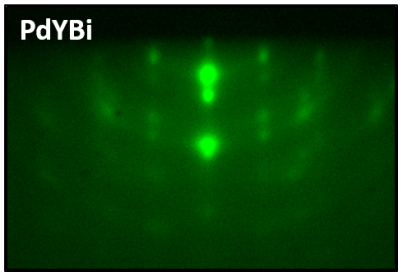

FIGURE 1.14: RHEED pattern obtained with a growth on MgO substrate showing a (111) fiber-like texture.

Second growth test: Al_2O_3 substrate

Sapphire crystallizes in a rhombohedral lattice (space group R-3ch, n°167). Therefore, sapphire substrate oriented along the c plane results in a hexagonal lattice as sketched in **figure 1.15**. Its lattice fits perfectly to the hexagonal one of our compounds and allows to reduce the misfits at the interface compared to MgO substrate. The misfit in the case of a (111) growth of PdYBi on sapphire is equal to 2%. For instance, the misfit between MgO(001) and PdYBi(111) is estimated at 10%[6]. The RHEED patterns of sapphire c-plane after outgassing at a temperature of 1000 °C (T_{pyro} ≈ 565 °C) are given in **figure 1.15**. The homogeneous streaks' intensity indicates a smooth surface and a good crystallinity. The two observed azimuths with a beam applied along [11$\bar{2}$0] and [10$\bar{1}$0] are typical of c-plane oriented sapphire[7]. Moreover, Kikuchi lines are present and are a signature of a very clean surface.

The growth of PdYBi is done on top of sapphire with a deposition temperature of 520 °C (T_{pyro} ≈ 380 °C)[8]. The growth process is Stranski - Krastanov also known as layer-plus-island growth. At the beginning, the film exhibits a 2D surface after a few seconds with nice homogeneous streaks due to a layer-by-layer-like growth. After

[5] All the temperatures given in this chapter are measured with a W/WRe thermocouple at the backside of the sample holder and with a pyrometer focalized on top of the growing surface (arbitrary emissivity of ϵ = 0.85 used for each measurement). The temperatures are always enumerated as follow $T_{thermocouple}$ = ... °C (T_{pyro} ≈ ... °C). The thermocouple is situated on the manipulator near the molyblock substrate holder therefore, the read temperature is higher than the real one.

[6] The misfit between MgO(001) and PdYBi(001) is equal to 37%.

[7] The 4-index notation is usually used for sapphire and its rhombohedral structure to distinguish similar plane rotated by 120°.

[8] The pyrometer was installed on the MBE for half-Heusler TIs growth since temperature deposition is critical.

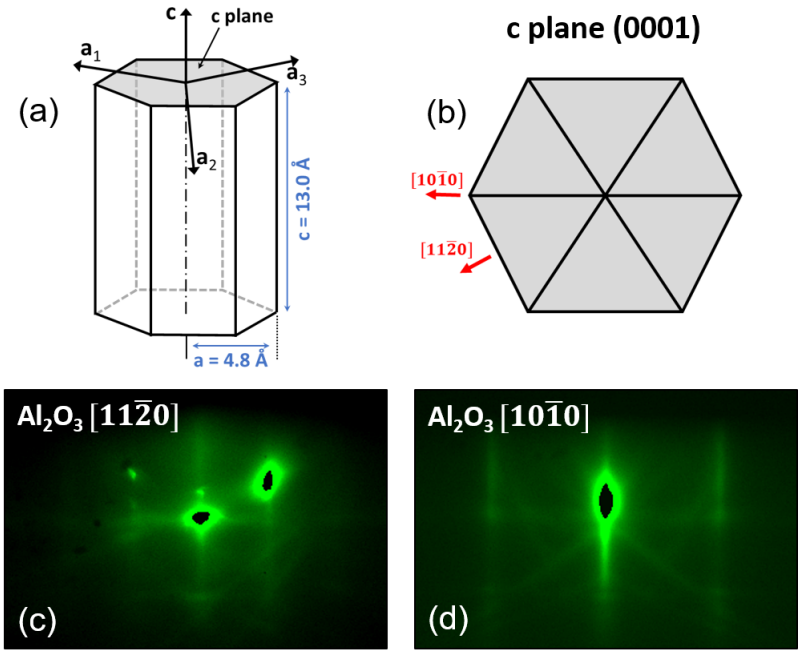

FIGURE 1.15: (a), representation of the rhombohedral structure of sapphire. (b), representation of the sapphire's c plane with the two probed azimuths. (c) and (d), RHEED patterns of c-plane Al_2O_3 substrate with the beam aligned along the directions [11$\bar{2}$0] and [10$\bar{1}$0].

a critical thickness, nucleation occurs and 3D islands growth begin. It is important to notice that, under perfect conditions, the growth stays in the Franck - van der Merwe situation with a perfect 2D surface until the end. The stoichiometry and the temperature are critical points to ensure a good deposition. The main problems to achieve this 2D growth is due to temperature variation depending on the sample's fixation[9] on the sample holder and to the amount of Bi at the sample surface. The RHEED patterns obtained in the case of the unannealed Stranski - Krastanov growth are shown in **figure 1.16a** and **1.16b** and the extracted in-plane lattice spacing is equal to 0.47 nm in agreement with the (110) PdYBi bulk distance[10]. As one can see, the streaks are not homogeneous anymore and the presence of spots shows the roughness that lies at the surface. Nonetheless, an increase of the surface's quality is possible by annealing the sample. The annealing process was realized up to 530 °C to 560 °C read with the pyrometer. Attention must be paid to annealing process since higher substrates temperatures can lead to deweting. At this stage, the surface is cleaner than before with the apparition of streaks as depicted by the **figure 1.16c** and **1.16d** RHEED patterns. The reconstructions are typical of $\sqrt{3}\times\sqrt{3}$ R30° surface superlattice with $\frac{1}{3}$; $\frac{2}{3}$ additional streaks along one azimuth. This observation will be confirmed in the STM section. The main problem with this growth process is its reproducibility which turns out to be complex since it may result in other surface reconstructions[11].

[9]Samples are held on sample holder with tungsten wire clips.

[10]The (110)PdYBi bulk distance should be $a_0 = \frac{a.\sqrt{2}}{2}$ where a is PdYBi unit cell parameter. In the case of the half-Heusler unit cell, a is expected to be 0.663 nm leading to a_0 = 0.47 nm.

[11]With this process, a $\sqrt{3}\times\sqrt{3}$ R30° reconstruction is usually observed but other complex rearrangement may occur.

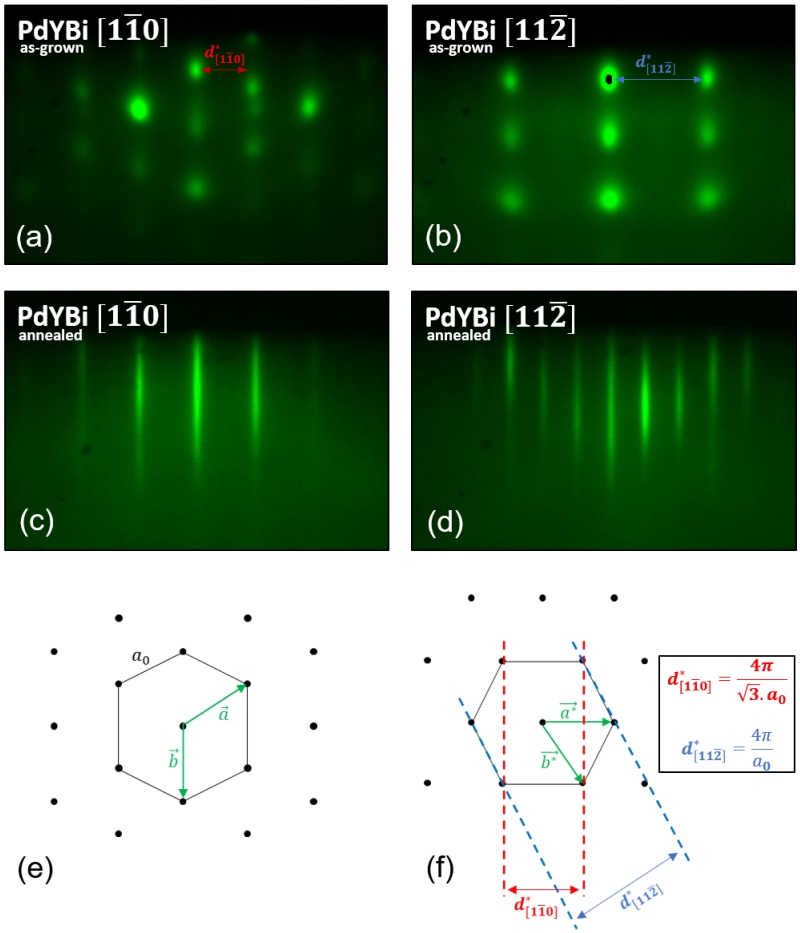

FIGURE 1.16: (a) and (b), RHEED patterns obtained with a beam applied along the [1$\bar{1}$0] and [11$\bar{2}$] azimuths on as-grown PdYBi sample. (c) and (d), RHEED patterns for annealed PdYBi with a $\sqrt{3}\times\sqrt{3}$ R30° reconstruction leading to respectively no supplementary and $\frac{1}{3}$; $\frac{2}{3}$ supplementary streaks along [1$\bar{1}$0] and [11$\bar{2}$] azimuths. (e) and (f), direct and reciprocal-space of the (111) plane of PdYBi exhibiting a hexagonal structure.

In order to obtain reproducible growth, another annealing process was used to increase the surface quality. This time the sample is annealed at the same temperature given before and an additional Bi flux is deposited at the surface that allows to obtain clean surfaces and reproducible growth. The RHEED patterns obtain with such an annealing process are given in **figure 1.17** and depict this time a 2×2-like surface

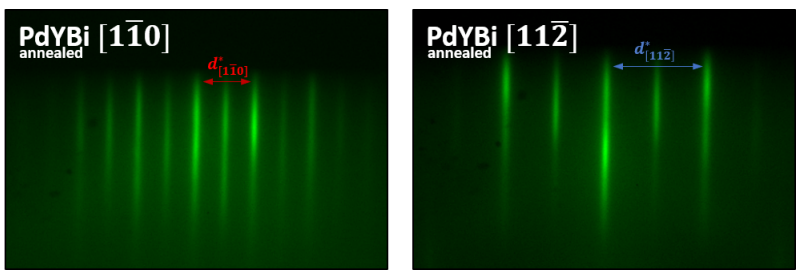

FIGURE 1.17: Typical RHEED patterns obtained with an annealing process under a Bi flux where a 2×2-like surface reconstruction is obtained. Beam applied along the [1$\bar{1}$0] and [11$\bar{2}$] azimuths.

reconstruction with $\frac{1}{2}$ supplementary streaks in both azimuths. However, more complex reconstructions are possible if supplementary Bi evaporation last for too long.

The obtained RHEED patterns allow to confirm the epitaxy relationship between sapphire and the Heusler layer. The epitaxial relation is PdYBi [1$\bar{1}$0] (111) // Al_2O_3 [11$\bar{2}$0] (0001) as shown in **figure 1.18**.

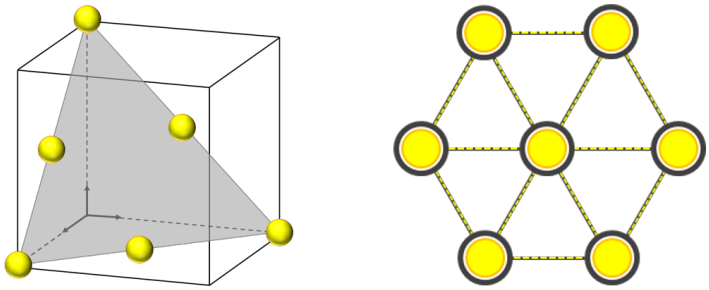

FIGURE 1.18: On the left-hand side (111) plane of PdYBi unit cell. Only the atoms that intersect with (111) plane are represented showing planes composed of a single element. On the right-hand side, epitaxial relationship between Al_2O_3 structure represented in black and PdYBi structure in yellow.

After this first successful growth the attention was drawn on PtYBi. Since both compounds are really similar, the same recipe should also fit to this second Heusler. It turns out to not be the case likely due to the Pt mobility. The temperature deposition has to be increased up to around 870 °C ($T_{pyro} \approx 540$ °C) to enhance the diffusion of atoms at the sample surface. Even with this increase of growth temperature, the surface is rough.

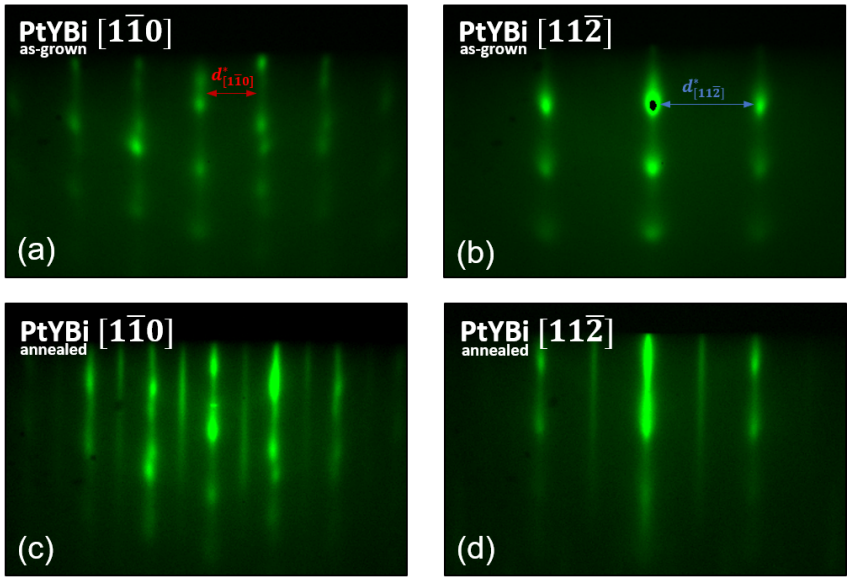

FIGURE 1.19: (a) and (b), RHEED patterns obtained with a beam applied along the [1$\bar{1}$0] and [11$\bar{2}$] on unannealed PtYBi sample. (c) and (d), RHEED patterns for annealed PtYBi.

The annealing process can be done to higher temperature without taking care of deweting[12] and PtYBi is annealed at around $T_{pyro} \approx 630$ °C but the enhancement of surface quality is not enough to be perfectly smooth and flat. At these high temperatures, Bi addition, as done for PdYBi, is not possible since no Bi atoms are absorbed. The RHEED patterns for the as-grown and after annealing PtYBi layer are given in **figure 1.19**. The spotty streaks indicate a 3D surface. Nonetheless, reconstruction along $[11\bar{2}]$ azimuth are visible indicating the presence of terraces. The surface probably consists of 3D islands with flat terraces on their top. Moreover, double spots along the $[1\bar{1}0]$ azimuth are distinguishable and indicate the presence of domains in the sample[13]. Finally, the $\frac{1}{3}$; $\frac{2}{3}$ supplementary streaks along the $[11\bar{2}]$ azimuth reveal a $\sqrt{3}\times\sqrt{3}$ R30° surface reconstruction similar to the one obtained for PdYBi (figure **1.16c** and **1.16d**) with the first annealing process. In the same way than for PdYBi other reconstructions may be observed and are related to Bi concentration at the sample surface.

After the elaboration achievement of PdYBi and PtYBi, other compounds were tested. In particular, Sb based half-Heusler were also predicted to possess topological properties [8]. An Sb Knudsen cell is present in the MBE allowing to substitute Bi with Sb atoms and perform PdYSb alloy. The epitaxy of Sb based compounds was not successful: a polycrystalline growth was systematically observed with rings in RHEED's pattern. Tests were also performed by substituting Pd/Pt with Rh, another transition metal available in the MBE. Once again, the attempt was unsuccessful without single-crystalline growth.

Finally, we succeeded in growing epitaxial PdYBi(111) and PtYBi(111) thin films. The following sections are thus dedicated to their structural characterization.

1.2.2 PdYBi

The previous part demonstrated the epitaxial growth of PdYBi on sapphire substrate. The RHEED patterns show a smooth surface and are in accordance with a growth in the $C1_b$ half-Heusler structure. Nonetheless, further characterizations have to be done to conclude on the preliminary RHEED observation. Potential contamination, structural phase, chemical order and band mapping are checked to attest PdYBi's potential.

Auger electron spectroscopy

In order to check the composition of the layers and identify possible contamination, Auger electron spectroscopy (AES) was performed. This analysis can be done without breaking the vacuum thanks to the UHV-tube facilities. AES is a surface sensitive technique that is based on the analysis of emitted electrons from a specific atom after a series of internal relaxations. These emitted electrons are element specific and do not depend on the excitation energy[14]. Typical Auger spectrum obtained for PdYBi

[12] At least in the temperature range reachable with the MBE's oven. Annealed temperatures up to 640 °C at the pyrometer with the arbitrary emissivity of $\epsilon = 0.85$ was reached.

[13] The domains are present at least at the sample surface since RHEED is surface sensitive.

[14] The excitation source can be X-rays or electrons. In this set-up, electrons are used to generate Auger transitions.

is given in **figure 1.20**. Pd_{MNN}, Y_{MNN} and Bi_{NOO} transitions were clearly observed in the 25 eV to 600 eV range. No other peak was present such as the main contaminations O (510 eV) and C (245 eV). Since quantitative analysis with AES are complex and can lead to important errors, only a qualitative study is done here[15].

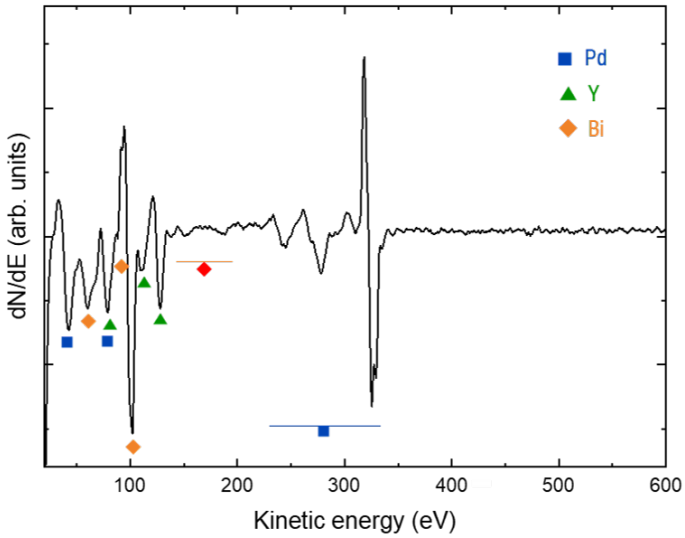

FIGURE 1.20: Typical Auger electron spectroscopy spectrum of PdYBi. Blue squares represent Pd transitions, green triangles Y transitions and orange diamonds Bi transitions.

Scanning Transmission Microscopy

Another powerful tool available on the UHV-tube of the IJL is a Scanning Tunneling Microscope (STM) which is used to image samples' surface at the atomic scale. STM was performed to have further information on the surface morphology and reconstructions.

A first approach was to look at the surface morphology recording large scales images as shown in **figure 1.21**. On the left-hand side, the scan is performed on as-grown sample (ie. before annealing). The one on the right-hand side is obtained after the annealing process. The surface of the unannealed sample presents islands explaining the spotty RHEED patterns in **figure 1.16a** and **1.16b**. The average roughness calculated on the image is of the order of 1.81 nm. On the other hand, flat and smooth terraces were observed on the sample after annealing with an average calculated roughness of 0.21 nm showing the improvement of surface morphology. The inset of **figure 1.21** shows a higher magnification of the surface with terraces' width of 40 nm. The regularity of the terraces is probably due to vicinal surfaces. Sapphire substrate used for the image on the right of **figure 1.21** was probably cut with a small deviation from the high [0001] symmetry direction leading to these periodic terraces.

[15] AES was also used to do a qualitative estimation of Bi presence at the surface under different annealing temperatures.

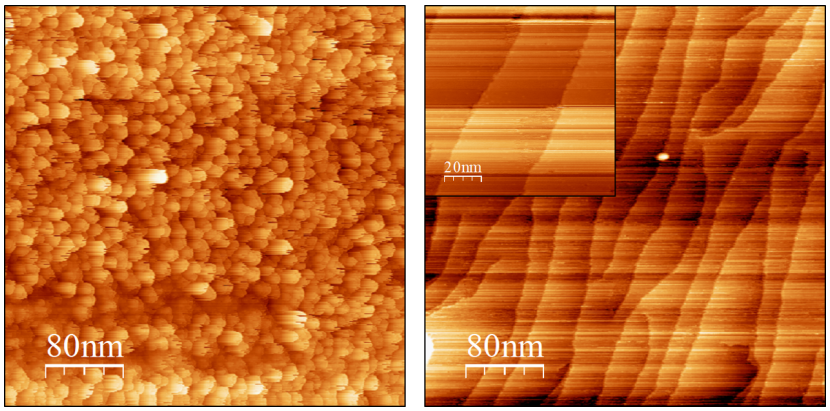

FIGURE 1.21: Typical STM images observed on as-grown PdYBi film on the left and after annealing PdYBi on the right.

Such a smooth surface allowed us to get atomic resolution on the terraces. Two PdYBi samples were grown with the two different annealing processes discussed in the growth section:

- The first one, annealed without Bi flux and whose RHEED patterns, given in **figure 1.16c** and **1.16d**, present a $\sqrt{3}\times\sqrt{3}$ R30° surface reconstruction.
- The second one, annealed under a Bi flux and whose RHEED patterns, given in **figure 1.17**, present a 2×2-like surface reconstruction.

High magnification images with atomic resolution were achieved on the $\sqrt{3}\times\sqrt{3}$ R30° surface reconstructed sample. One of these images is given in **figure 1.22** along with its FFT treatment and unveils a $\sqrt{3}\times\sqrt{3}$ R30° reconstruction. The reconstruction (lattice represented by the blue hexagon), in bright points, is turned by 30° with respect to the smaller elementary lattice (lattice represented by the white hexagon) and is perfectly in line with RHEED patterns of **figure 1.16c** and **1.16d** ($\frac{1}{3}$; $\frac{2}{3}$ streaks along the [11$\bar{2}$] azimuth and no additional streaks along [1$\bar{1}$0]).

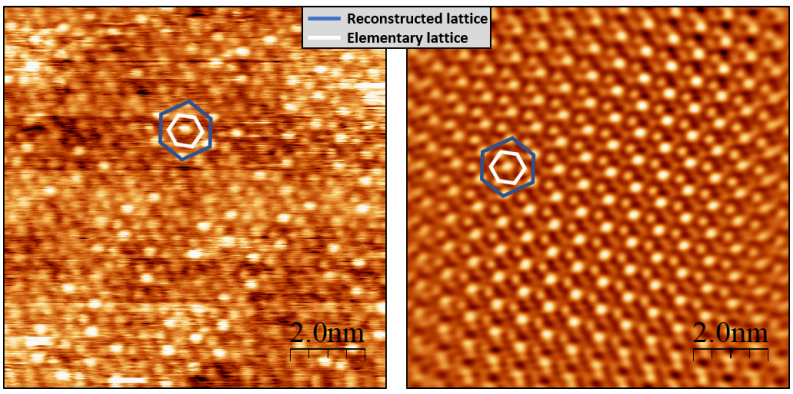

FIGURE 1.22: On the left, high magnification image with atomic resolution unveiling the $\sqrt{3}\times\sqrt{3}$ R30° reconstruction. On the right, image after data treatment.

A second sample, prepared under a Bi flux, was grown to carry out a new STM investigation. As discussed before, with such annealing process a more reproducible growth is achieved and a 2×2 surface reconstruction is obtained (**figure 1.17**). An

STM image is given in **figure 1.23** where the atomic resolution is not as clear as in **figure 1.22** but the surface lattice is visible (lattice represented by the blue hexagon) and clearly corresponds to a 2×2 surface reconstruction, in agreement with the RHEED patterns observed after the growth ($\frac{1}{2}$ additional streaks along the $[11\bar{2}]$ and $[1\bar{1}0]$ azimuths in **figure 1.17**).

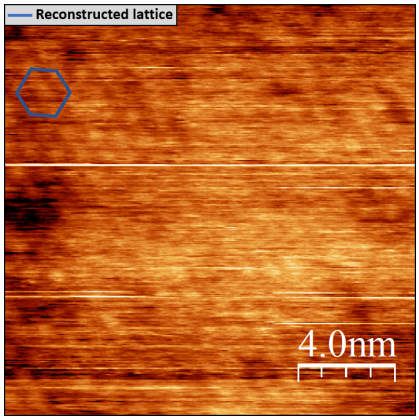

FIGURE 1.23: STM image of PdYBi sample annealed under a Bi flux. The 2×2 surface reconstruction observed in RHEED for this growth process coincides with the STM extracted inter-atomic distance.

At this stage, the smooth surface of PdYBi was imaged as well as different reconstructions occurring at the sample surface. The hexagonal shape revealed by STM (**figure 1.22** and **1.23**) agrees with the (111) growth of the $C1_b$ Heusler structure. In order to definitely confirm PdYBi's structure X-ray diffraction was carried out.

X-ray Diffraction

X-ray diffraction (XRD) permits to get bulk structural information thanks to angles and intensities of diffracted beams. It is well adapted to the study of crystalline thin films that offer a great chemical order. Unlike electrons, X-ray interaction with matter is low and thus, probes the entirety of thin films. Here, XRD are used to determine the crystal structure and its lattice parameters as well as the presence of domains in thin films. Two set-ups were used: symmetrical and non-symmetrical configurations.

Symmetrical configuration

The configuration symmetric to the sample surface uses the $\theta/2\theta$ mode. This geometry imposes diffracted planes coming from the growth axis since it involves a diffraction vector parallel to this axis according to the Bragg relation linking θ angles. Information coming from planes parallel to the surface is then obtained and allows to check the layer's crystalline phase. These measurements were carried out with a Bruker D8 advance using Cu K_α radiation with λ = 1.54056 Å allowing to perform diffraction of crystal lattices. A typical XRD spectrum of PdYBi is given in **figure 1.24**.

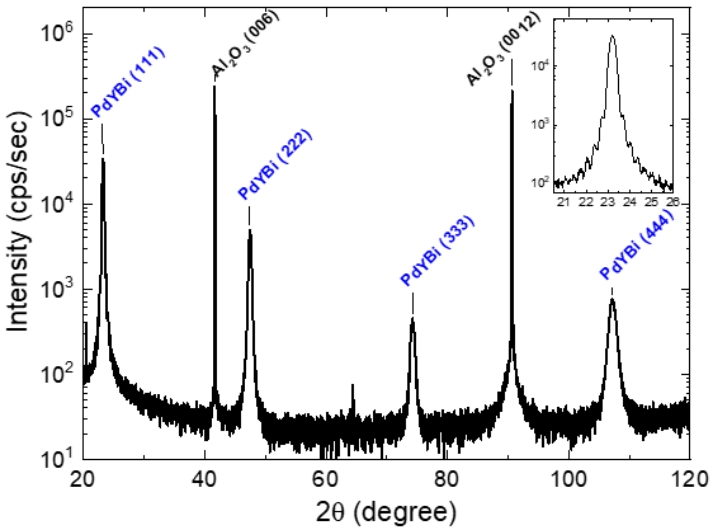

FIGURE 1.24: Typical $\theta/2\theta$ XRD scan for PdYBi. The inset on the upper part is a zoom of PdYBi (111) peak showing the presence of Kiessig fringes.

X-ray diffraction were used to probe the entire sample and to obtain global details of the structure. Therefore, peaks at 41° and 90° are labeled as Al_2O_3 substrate peaks and come from the (00l)[16] family due to substrate's orientation. The other peaks are all identified as PdYBi peaks. They all belong to the same (111) family which confirms this growth axis as previously revealed by RHEED patterns. No parasite peak is observed showing a perfect single-crystalline growth. Moreover, PdYBi peaks are sharp pointing out again the good crystallinity in the layer. The inset on the upper part of **figure 1.24** shows a zoom of the (111) peak of PdYBi unveiling the presence of Kiessig fringes as another proof of the good thin film's crystallinity. By assuming PdYBi's unit cell to be perfectly cubic (ie. a = b = c), the cell parameter can be extracted thanks to Bragg's law since θ angle is linked with inter-planar distances. The cell parameter extracted has the value a = 6.63 Å in perfect agreement with the expected $C1_b$ half-Heusler structure.

Non-symmetrical configuration

Non-symmetrical configuration allows to obtain non specular peaks thanks to the geometry of the measurement. They are performed on a PanAlytical X'Pert Pro MRD diffractometer also equipped with a Cu K_α source with λ = 1.54056 Å. The sample is placed at the rotation's center of a four-circle goniometer. The four axes allow to orientate the sample in any space position and to perform non-symmetrical measurements. In the previous part, the unit cell was obtained by assuming a perfect cubic lattice. By doing non-symmetrical measurement on new families of planes it was possible to confirm the $C1_b$ half-Heusler cubic cell[17]. Diffraction measurement on (004) and (220) family planes were performed as shown in **figure 1.25**. The data were fitted with a Voigt function to extract the 2θ positions. The determined cell parameter for the peak (004) was 6.65 Å and 6.62 Å for the peak (220). The obtained cell parameters compared to those measured with the symmetrical configuration are in the errors of the measurement and confirm the obtaining of the $C1_b$ half-Heusler

[16](00l) planes correspond to (000l) plane in the 4-index notation.

[17]Non-symmetrical configuration was also used to achieve phi-scan on oblique peaks of Al_2O_3 and PdYBi to bring another proof of the PdYBi [$1\bar{1}0$] (111) // Al_2O_3 [$11\bar{2}0$] (0001) epitaxial relationship.

structure with no obvious unit cell distortion.

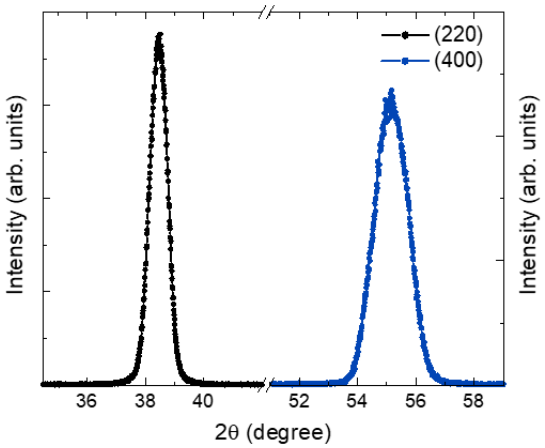

FIGURE 1.25: Non symmetrical scans of PdYBi sample. The probed peaks are from the families (220) in black and (004) in blue.

X-Ray Reflectometry

X-Ray Reflectometry (XRR) is also possible with the PanAlytical X'Pert Pro MRD diffractometer. XRR is a non-destructive technique based on the reflection of X-ray from a flat surface. The reflection intensities are picked up at an angle equal to the incidence angle and a reflectivity pattern is observed. At every interface where the electronic density varies, a part of the X-ray beam is reflected. The interferences between this partially reflected beam generate the oscillations observed in XRR measurements. The analysis of these oscillations allows to determine the thickness, the density and the roughness of the different layers. An XRR scan and its fit are given in **figure 1.26** for PdYBi.

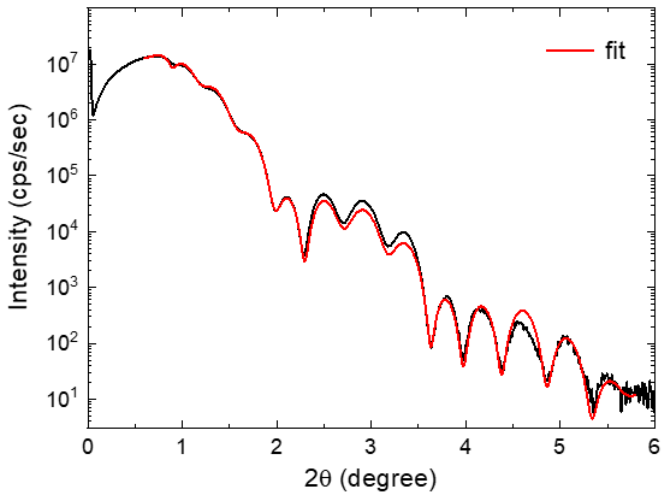

FIGURE 1.26: X-ray reflectivity scan in black and its fit in red. Measurement performed on a sample with 15.2nm of PdYBi and 5nm of Au as capping layer.

The double oscillations' period is due to PdYBi and Au layers. Thicknesses of 15.5 nm for PdYBi and 4.7 nm for Au capping are extracted from the XRR's fit. These thicknesses are in good agreement with the aimed ones respectively of 15.2 nm and 5 nm. The small deviation, especially for Au capping is attributed to the non-perfect

fit and to the roughness present at the thin film surface. For this sample, PdYBi's roughness was estimated around 0.6 nm which is slightly higher than the one obtained from STM images of the previous sample.

At this point, PdYBi deposition is controlled with a single crystalline growth along the (111) direction. RHEED, STM and XRD unveiled a good crystallinity coupled with a smooth surface. The low roughness is important for photoemission measurements since ARPES is a surface sensitive technique. Another impactful property for ARPES is the chemical ordering that can strongly reduce the photoemission signal. Transmission electron microscopy was performed to check samples' chemical ordering.

Transmission Electron Microscopy

In Transmission electron microscopy (TEM) technique, an electron beam accelerated and focused by electromagnetic lens is transmitted through a sample to construct an image. The use of electrons and the possibility to tune the acceleration beam voltage allow to get a much better resolution compared with classical microscopes. Nonetheless, to perform TEM, sample preparation has to be done. Thin films have to be thin enough to allow the transmission of the e-beam. This preparation is performed by focused ion beam etching with Ga ions and results in a film's thickness of approximately 50 nm. The interesting part with single-crystalline and well-ordered sample is that special cross section can be made to observe the atomic columns composed with only one element each. With the help of XRD, phi-scans can be performed to orientate the substrate and the thin film layer. A peculiar zone axis hosting a good atomic column arrangement can then be chosen. Here, the cut is realized along the $[1\bar{1}0]_{PdYBi}$ zone axis resulting in the pattern represented on the right side of **figure 1.27**. This expected pattern has vacant columns due to the vacancies present in the 4d site of half-Heusler structure corresponding to δ sites on **figure 1.27**.

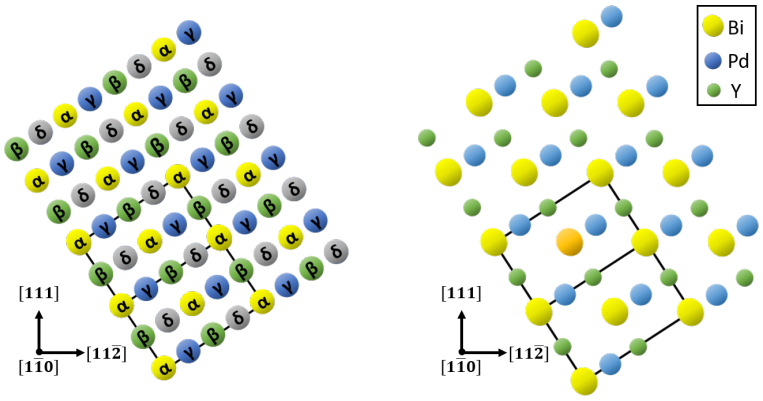

FIGURE 1.27: On the left, $[1\bar{1}0]$ zone axis atomic columns for Heusler structure where yellow, green, blue and grey circles correspond respectively to α, β, γ and δ sites. On the right, expected atomic columns arrangement of $[1\bar{1}0]_{PdYBi}$ zone axis where Bi, Pd and Y go respectively on α, β and γ sites. δ sites are empty since they are not filled in the case of the ordered half-Heusler structure. The sizes of the circles are a relative representation of the expected intensities.

TEM measurements were done on a JEM – ARM 200F Cold FEG microscope at the IJL operating with an acceleration voltage of 200 kV. Two operating modes are possible namely TEM and Scanning Transmission Electron Microscopy (STEM). In TEM imaging, a parallel electron beam is focused perpendicular to the immobile sample plane and the transmitted electrons are then imaged. TEM is useful to observe crystal defect or image bulk structure. This mode was used for low magnification images. In STEM, the beam is focused and converges at the sample surface. The focal point is then scanned across the sample to image the desired area. Here, the attention is focused on electrons scattered at high angles by using a high angular annular dark field (HAADF) detector collecting the generated electrons around the incident beam. By mapping the intensities of high-angle scattered electrons, Z-contrast images can be generated since local contrast and local mass-thickness[18] are linked. STEM-HAADF mode was used to image the atomic columns and check the chemical order of the layers. The achievable resolution on IJL's microscope is 1.2 Å in TEM mode while STEM mode can go up to 0.78 Å.

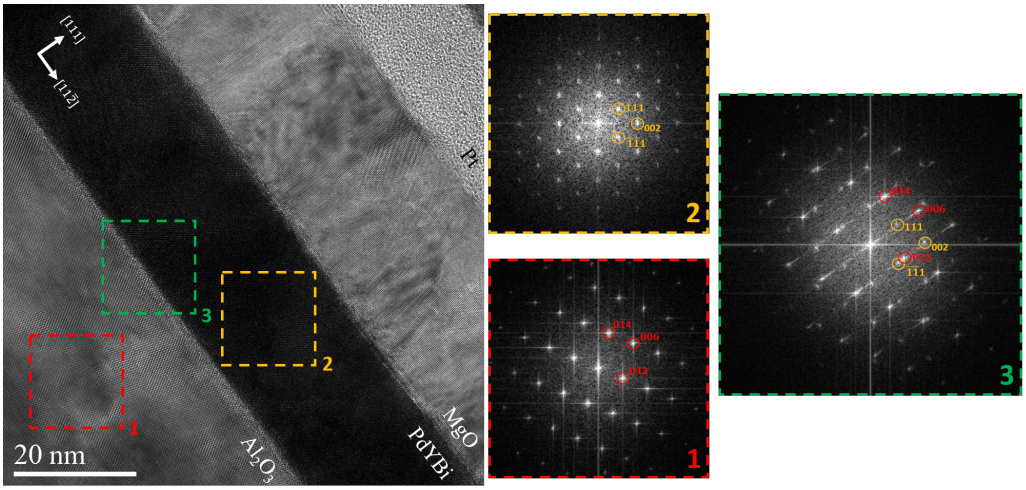

FIGURE 1.28: On the left TEM image of Al_2O_3/PdYBi/MgO. MgO is the capping layer and Pt is deposited for cross section preparation. The diffraction patterns of red, green and yellow frames are given on the right unveiling the epitaxy between sapphire substrate and PdYBi layer.

A TEM image of PdYBi is given in **figure 1.28** showing a smooth interface between sapphire substrate and PdYBi layer. PdYBi's surface is flat with low roughness as observed in RHEED. MgO was used as a capping layer to avoid contaminations and oxidation. Pt layer on the top right part of **figure 1.28** is deposited for cross section preparation. Diffraction patterns for red, green and yellow frames are given on the right side of the figure. The labeled spots (in red for sapphire and in yellow for PdYBi) allow to confirm the epitaxy between the (0001) sapphire direction with a PdYBi's layer growth along the (111) direction. The diffraction pattern of the yellow area (ie. of PdYBi alone) confirms the $[1\bar{1}0]$ zone axis. Moreover, the deposited PdYBi's thickness can be measured as 20.8 nm in good agreement with the aimed 20 nm.

In order to distinguish clearly the atomic columns, images with higher magnification were collected. A high magnification HAADF-STEM image is given in **figure 1.29**

[18]The local-mass thickness depends on the atomic number Z.

and can be processed to increase the signal to noise as shown in the inset of the image. The processed image makes possible a comparison with the expected pattern of **figure 1.27**.

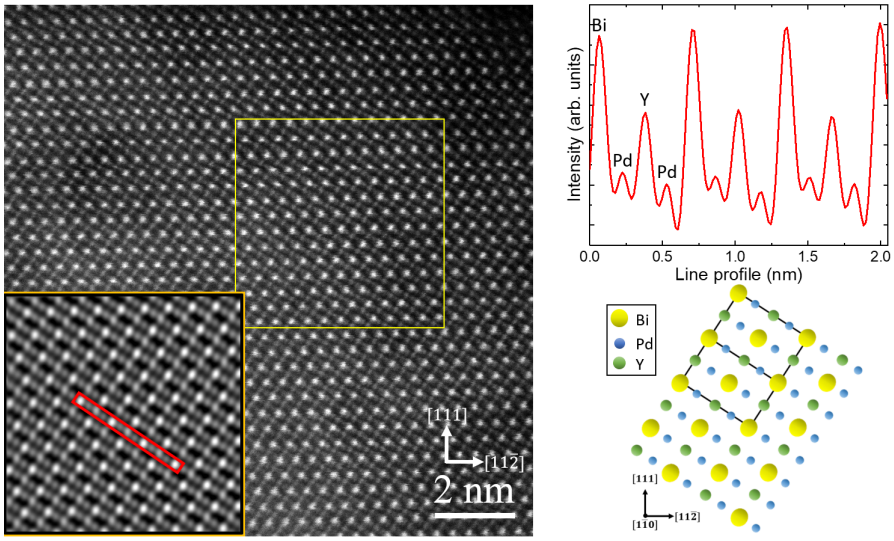

FIGURE 1.29: On the left, raw STEM-HAADF image of PdYBi. The inset is a processed image of the yellow frame in the raw image. The better signal to noise ratio allows to clearly distinguish the atomic columns and their intensities. On the top right side, intensity line profile performed on the inset's red box area. On the bottom right, sketch of the observed atomic columns pattern.

The heavier elements appear in bright while the lighter ones are darker. Therefore, Bi (Z = 83 e^-) is the brightest element then come Pd (Z = 46 e^-) and Y (Z = 39 e^-). The expected pattern, given in **figure 1.27**, does not fit to the observation as revealed by the intensity line profile. Due to the vacant site of half-Heusler, some columns should not be filled. By looking carefully at **figure 1.29**, one can say that no unfilled columns are present. There are two possible ways to explain the columns filling sketch on the bottom part of **figure 1.29**. The first one is to take into consideration domains in the sample that are turned by 180° with respect to each other. By performing simulation with two domains, the pattern is exactly the one imaged. Bi and Y atoms should stay in the same columns for both domains meanwhile, Pd atoms, depending on the domain, may fill the columns in γ or in δ positions represented in **figure 1.27**[19]. This leads to partially filled columns explaining the lower intensities for the Pd columns with respect to the Y ones. The second possibility is to take into account disorder in the unit cell. In the perfectly ordered structure Bi, Y and Pd go respectively in Wyckoff position 4a, 4b and 4c (respectively α, β and γ positions in the sketch of **figure 1.27**) but disorder could happen. If Pd goes on 4c (γ) and 4d (δ) sites, this will lead to partially filled Pd columns that come to the same pattern observed in **figure 1.29**. To decide between these two possibilities, XRD was used. By performing phi-scan on non-specular peak of PdYBi it is possible to distinguish whether domains are present or not by looking at the peak occurrence. Data are given in **figure 1.30** for the [220] peak that should have a three-fold symmetry.

[19]Here the γ and δ sites only refer to the position in the image. In the case of two domains the Pd atoms stay on the γ site and no disorder due to Pd in δ site is present.

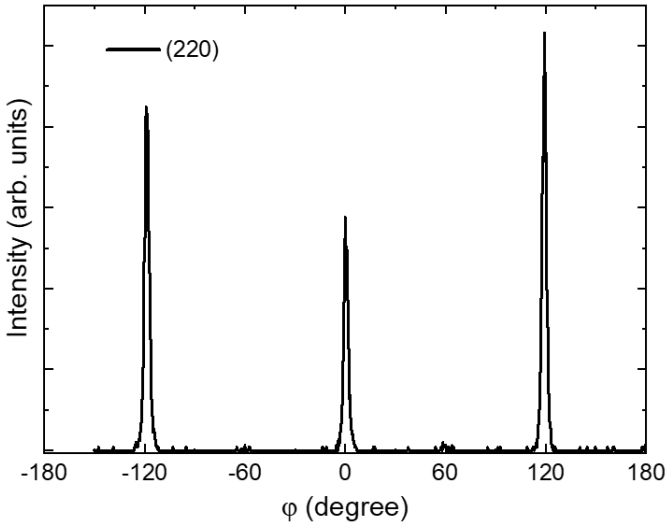

FIGURE 1.30: Phi-scan of PdYBi(220) peaks unveiling a classical three -fold symmetry.

In the presence of domain turned by 180° this symmetry should be double. As shown in the ϕ scan, this is not the case with the presence of the normal symmetry. The observed pattern may be due to disorder between two crystallographic sites in the sample. Pd atoms go on two different crystallographic sites generating partially filled columns that explained why Y appears brighter than Pd.

Energy-Dispersive X-ray

Energy-Dispersive X-ray (EDX)[20] analyses were performed on PdYBi. EDX is a spectroscopy technique used to do chemical characterization. It is based on the emission of photons excited by an electron beam focused on the sample. Since each element has a unique atomic structure with transitions well defined it is possible to perform chemical analysis by analyzing the energy of the emitted photons thanks to an energy-dispersive spectrometer. The process results in the excitation of an inner shell electron that is ejected and replaced by an outer shell electron that emitted a photon. The energy of the emitted photon is characteristic of the transition between the two shells involved and provided a signature of the probed atom. TEM was used to perform this analysis on PdYBi to ensure the good stoichiometry and to check if any interdiffusion or segregation occur in the sample. The EDX scans are given in **figure 1.31**. The area was chosen randomly on the FIB cross section and the electron beam was applied along the $[1\bar{1}0]$ direction. A homogeneous spatial distribution is observed for all elements. On the top part, Mg and O are present due to the MgO capping. On the lower part, Al and O are due to the sapphire substrate. In the middle layer, Pd, Y and Bi are present with no clear diffusion or segregation observed. The small O amount in the PdYBi layer's area can be due to a slight oxidation of the cross section during transport between ion beam etching and TEM. Nonetheless, given the numerous transitions due to the heavy elements present in the thin film an overlapping between O and another transition is also worth considering.

[20] EDX was performed instead of EELS (Electron Energy Loss Spectroscopy) since EDX is much more sensitive to heavy elements.

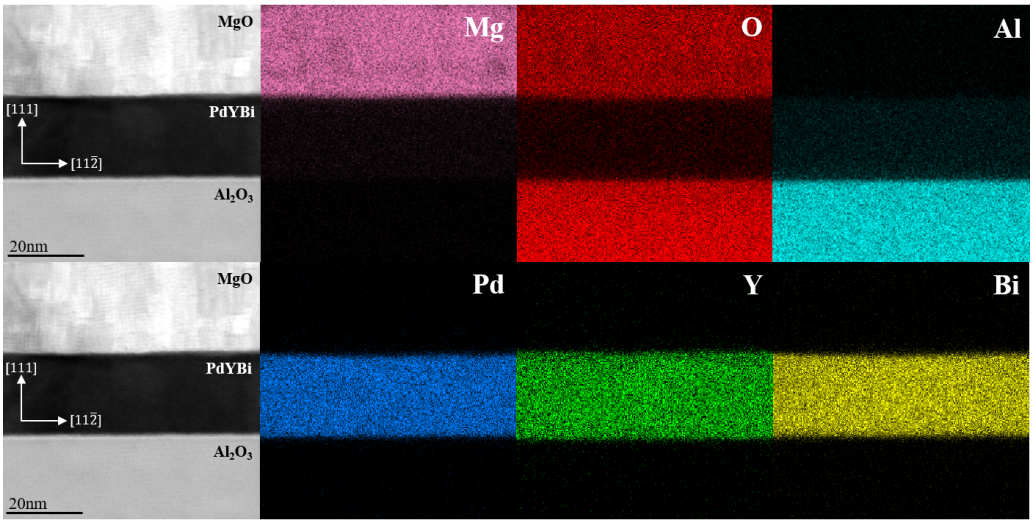

FIGURE 1.31: EDX map at the edge of Mg in pink, O in red, Al in light blue, Pd in blue, Y in green and Bi in yellow.

Angle resolved photoemission electron spectroscopy

Photoemission process

The photoelectric effect is the source of photoelectrons spectroscopy. In photoemission experiment, electrons emitted by ionizing radiations are collected in a peculiar direction and their kinetic energy is measured. This excitation phenomenon can be accurately described only in a quantum formalism established by Einstein in 1905. In this formalism, Einstein demonstrated that light is transmitted by energy quanta of hν amplitude. These energy quanta explain the frequency dependence of the photoelectric effect (and at the same time the non-dependence regarding the light intensity as a classical point of view might suggest). These works resulted on the following energy conservation equation that explains the photoelectric effect.

$$h\nu = E_k + \Phi - E_B \tag{1.3}$$

with hν the incident photon energy, E_k the kinetic energy of the emitted photoelectron, Φ the work function of the solid (ie. the minimal energy needed to extract an electron from the solid to the vacuum with a resulting kinetic energy $E_k = 0$) and E_B the binding energy of the electrons in the solid. The binding energy is defined with regards to the Fermi level and is always negative. Two photoemission regimes can be distinguished according to E_B. The first one is the spectroscopy of valence levels where the probed electrons are near the Fermi level and delocalized. In these measurements, E_B goes from a few eV to some tens of eV requiring the use of ultra-violet radiation. This technique is often called UPS for Ultra-Violet Spectroscopy and has a high sensitivity and resolution. The second family of measurements consists in probing the core electrons strongly bound to the atom with X-ray radiation[21]. The binding energies are therefore much higher. This second application is more dedicated to chemical characterization of the solid. Here, the focus is pointed on the

[21] Valence band spectroscopy can be performed with X-ray but the resolution turns to be one order of magnitude lower compared to UPS [80].

valence band's study allowing to understand the electronic properties by looking at electrons near the Fermi energy[22].

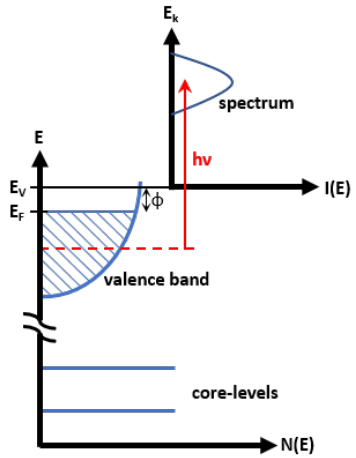

FIGURE 1.32: Sketch of the photoemission process. On the left side, simplified representation of the band structure of a solid with core-levels lying well below the Fermi level and the valence band near the Fermi energy. Electrons from the valence band have an initial energy named E_i which is their binding energy. They can be extracted by an incident photon with $h\nu$ energy to an empty state E_f. The analysis of the kinetic energy and emission angle of the emitted photoelectron allows to image the band structure of the solid. Sketch adapted from [80].

Equation 1.3 can be rewritten as a function of initial (E_i) and final (E_f) energy states with respect to the Fermi level.

$$\begin{aligned} E_i &= E_B \text{ and } E_f = E_k + \Phi \\ h\nu &= E_f - E_i \end{aligned} \tag{1.4}$$

The Hamiltonian for a resting particle is:

$$H_0 = \frac{\mathbf{p}^2}{2m} + V(\mathbf{r}) \tag{1.5}$$

If we consider the interaction of the particle with an electromagnetic wave, the minimal coupling allows to write:

$$\begin{aligned} H - q\phi &= \frac{1}{2m}(\mathbf{p} - q\mathbf{A})^2 + V(\mathbf{r}) \\ H &= \frac{1}{2m}(\mathbf{p} - q\mathbf{A})^2 + q\phi + V(\mathbf{r}) \end{aligned} \tag{1.6}$$

By developing the above expression:

[22]Since photoemission of valence band is the center of attention here, photoemission of core-levels has not been mentioned. Similar physics can be applied to core-levels and is named X-ray Photoemission Spectroscopy where high energy radiations are used to excite core-levels. The extracted information relates on chemical information.

$$H = \frac{1}{2m}(\mathbf{p}^2 - q\mathbf{p}.\mathbf{A} - q\mathbf{A}.\mathbf{p} + q^2\mathbf{A}) + q\phi + V(\mathbf{r}) = H_0 + H_{int} \tag{1.7}$$

with:

$$H_{int} = \frac{1}{2m}(-q\mathbf{p}.\mathbf{A} - q\mathbf{A}.\mathbf{p} + q^2\mathbf{A}) + q\phi \tag{1.8}$$

From here some assumptions can be done. Firstly, the term $q^2\mathbf{A}$ is a second order term and is negligible since the intensity of conventional sources are low enough. By using the Coulomb gauge $[\mathbf{p}.\mathbf{A}] = 0$ and $\phi = 0$ the equation is simplified as followed:

$$H_{int} = \frac{-q\mathbf{p}.\mathbf{A}}{m} \tag{1.9}$$

Moreover, UV and X photoemissions allow to do the dipolar electric approximation. The typical optical wavelength of UV and X-ray are much higher than the size of the electronic orbital. The vector potential is thus almost position independent so $\mathbf{A}(\mathbf{r},t) = \mathbf{A}_0(t)$.

With this simplified Hamiltonian it is now possible to express the transition probability given by the Fermi golden rule and that describes the transition rate from one energy eigenstate $|i\rangle$ to an energy eigenstate in a continuum $|f\rangle$.

$$\Gamma_{i\to f} = \frac{2\pi}{\hbar}|\langle f|H_{int}|i\rangle|^2\delta(E_f - E_i - h\nu) \tag{1.10}$$

Theoretically this expression tells that if the initial and final states are known then the photoemission spectrum can be obtained. In reality, the sample's surface changes this ideal vision with the introduction of a symmetry breaking in the direction perpendicular to the surface. A rigorous description of the process is complex and a three-step model proposed by Berglund and Spicer [81] is used here. It consists in splitting the photoemission process of a single electron into three steps. The first one is the optical excitation of a Bloch electron to an available empty state. The second step relates to the hot electron's crossing of the sample. The third step takes care of the surface crossing by the electron.

Three step model:

i. Optical excitation

An electron from the solid absorbs an ionizing photon with the energy $h\nu$. For low photon energy, as for instance in UV photoelectron spectroscopy, the photon momentum can be neglected and vertical transitions connecting directly the initial and final state are considered resulting in the following conservation equation:

$$\mathbf{k}_f = \mathbf{k}_i \tag{1.11}$$

In a periodic crystal, the momentum conservation rule is defined modulo a vector of the reciprocal lattice **G** due to the extended zone scheme, therefore:

$$\mathbf{k}_f = \mathbf{k}_i + \mathbf{G} \tag{1.12}$$

ii. Propagation process

At this stage the generated photoelectron has to cross the solid to the surface. During the crossing, the electron can be subjected to inelastic scattering due to other electrons, phonons or impurities. This results in a modified initial energy and the electron wave is damped. If the damped electron has still enough energy to escape from the solid, it will contribute to the secondary electrons that are responsible for the diffusive background observed in photoemission spectra. Only the electron that did not endure any collision will bring useful information on their initial state to reconstruct the valence band structure.

iii. Surface crossing

The last step describes the electron's surface crossing. When the electron goes from the solid to the vacuum it feels a potential barrier at the surface. As explained previously, this discontinuity has non-trivial consequences since a symmetry breaking in the perpendicular direction of the surface occurs. This symmetry breaking leads to the non-conservation of the perpendicular component of the wave vector while the parallel component is conserved. To understand this phenomenon, the components of the wave vector can be expressed with regards to the emission angle θ and ϕ of the electron. The dispersion relation in the vacuum is (free electrons):

$$E_k = \frac{\hbar^2 k^2}{2m} \tag{1.13}$$

The components of the wave vector in the three directions of space as a function of angle emission θ and ϕ can then be expressed as:

$$\begin{aligned} k_x &= \frac{\sqrt{2mE_k}}{\hbar}\sin\theta\cos\phi \\ k_y &= \frac{\sqrt{2mE_k}}{\hbar}\sin\theta\sin\phi \\ k_z &= \frac{\sqrt{2mE_k}}{\hbar}\cos\theta \end{aligned} \tag{1.14}$$

In the case of the $/\!/$ component of the wave vector, no potential is felt therefore the parallel component of the wave vector is conserved:

$$\frac{p_{/\!/}^2}{2m} = \frac{\hbar^2 k_{f,/\!/}^2}{2m} \iff k_{f,/\!/}^2 = k_x^2 + k_y^2 \iff k_{f,/\!/} = \frac{\sqrt{2mE_k}}{\hbar}\sin\theta \tag{1.15}$$

In the case of the $\perp$ component of the wave vector this time a potential barrier V_0 is present:

$$\frac{p_{\perp}^2}{2m} + V_0 = \frac{\hbar^2 k_{i,\perp}^2}{2m} \iff k_{i,\perp}^2 = k_z^2 + \frac{2mV_0}{\hbar^2} \iff k_{i,\perp} = \sqrt{\frac{2m}{\hbar^2}(E_k \cos^2\theta + V_0)} \quad (1.16)$$

The inner potential V_0 implies that the perpendicular components of the wave vector are not conserved, $k_{i,\perp} \neq k_{f,\perp}$.

Conclusions can be drawn from these formula. On the one hand, the parallel component of k_f can be probed by photoemission and moving the polar angle θ allows to map all the $k_{/\!/}$ without changing the incident energy. On the other hand, the expression of $k_\perp$ depends on the unknown V_0 that does not allow to get the normal component unless band structure calculations or assumptions are done.

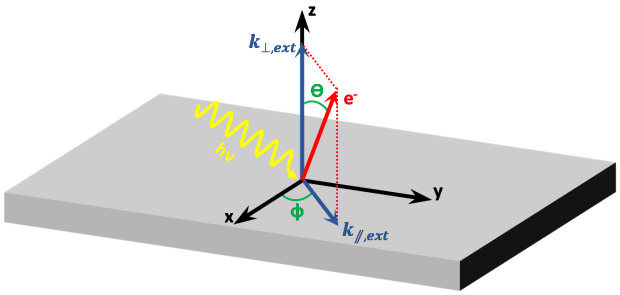

FIGURE 1.33: Sketch of the involved θ and ϕ angle in the photoemission process. The incident photon with $h\nu$ energy generated a photoelectron ejected from the solid. The photoelectron is going to be collected by the photoemission analyzer with regards to its kinetic energy E_k and its emissions angles θ and ϕ.

Low energy electron diffraction and angle resolved photoemission electron spectroscopy

All the photoemission experiments were performed at the IJL using UHV tube facilities to transfer directly samples from the MBE to the photoemission chamber without breaking the vacuum. The ARPES chamber is equipped with a DA30-L analyzer allowing a high energy (< 1 meV) and angle (< 0.1°) resolutions. The measurements were done under a high vacuum of $1 .10^{-10}$ mbar and a He-cryostat is available for ultra-low temperature measurements. The photon source used is an MBS L-1 He gas-discharge lamp. This plasma lamp allows to get high energy resolution. Different spectral lines are emitted from the He plasma lamp with mainly He_I at 21.2 eV and He_{II} at 40.8 eV. The lamp is coupled to a monochromator MBS TM-1 that allows to select the desired energy thanks to movable diffraction gratings.
A MBE chamber is directly coupled to the photoemission chamber and is equipped with a Low Energy Electron Diffraction (LEED) set-up. LEED is a technique allowing to obtain information on the surface's atomic arrangement. In LEED experiment, a low energy electron beam (typically 20 eV to 200 eV) is focused on the sample surface. The geometry differs from RHEED since the excitation beam comes normal to the surface. The penetration depth is of the order of few atomic planes regarding the mean free path curves of electrons for the considered energies. Therefore, the surface and some bulk planes are probed and the situation is intermediate between 2D and 3D diffraction for the observed reciprocal space. If the sample is single-crystalline with a smooth surface, diffracted electrons are going to form a characteristic diffraction pattern of the crystalline lattice studied. One of the advantages to perform LEED

before photoemission is that surface sensitivity in LEED and photoemission are similar allowing to do a first estimation of surface quality for ARPES measurements.

A typical LEED pattern of PdYBi is given in **figure 1.34**. The expected hexagonal symmetry for a growth along the (111) direction of a fcc unit cell is observed confirming the conclusions of previous observations. LEED can also give information on the surface's reconstructions that occur on the last atomic planes. Additional spots are clearly visible on **figure 1.34** and match with a $\sqrt{3}\times\sqrt{3}$ R30° reconstruction[23]. The LEED analysis was also used to identify the crystal orientation with regards to the sample holder (Omicron plates) which is mandatory for ARPES measurements[24]. The analyzer slit direction is represented by the white dashed line in **figure 1.34** indicating a probed direction slightly off the $\overline{\Gamma K}$ direction[25].

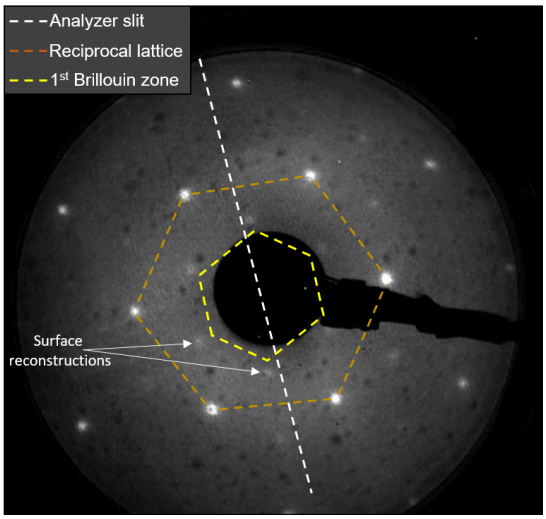

FIGURE 1.34: LEED pattern obtained for PdYBi with an excitation energy hν = 50 eV depicting the hexagonal structure of the (111) thin film's plane (in brown). The first Brillouin zone is represented in yellow. A $\sqrt{3}\times\sqrt{3}$ R30° reconstruction is present and visible with weak $\frac{1}{3}$; $\frac{2}{3}$ spots along the [11$\bar{2}$] azimuth. The white dashed line represents the slit of the ARPES analyzer.

It should be noted that surface reconstructions may impact the band structure probed by ARPES measurements as observed for numerous compounds in the literature [82, 83] unveiling additional states attributed to them. In our case, no impact on the band structure has been noticed since these surface complications are not always visible in ARPES measurements[26]. Moreover, the superlattice reflection due to the $\sqrt{3}\times\sqrt{3}$ R30° reconstruction are diffuse in our samples and suggest a partially reconstructed surface.

[23] This reconstruction for PdYBi is not surprising since this sample was not annealed under a Bi flux. As discussed in the growth section, this annealing process usually leads to a $\sqrt{3}\times\sqrt{3}$ R30° reconstruction

[24] The sample's orientation is unknown prior to LEED measurement.

[25] The probed direction can be tuned thanks to θ and ϕ angles to image the entire Brillouin zone. Nonetheless, the ARPES manipulator is made up with 5 axis which are the 3 directions of space x, y, z and the two angles θ, ϕ. No rotation in the film plane can be done and it is not possible to realign perfectly the sample in the desired direction.

[26] This statement is possible by making a comparison between our data with the literature.

Once LEED was performed, the ARPES measurements were done. Fermi surfaces spectra obtained for PdYBi are given in **figure 1.35**. The bands are not clearly defined and this can be mostly due to the chemical disorder present in the sample. The explanation of such low intensity cannot be totally due to surface quality since RHEED and LEED spectra show a well-crystallized and smooth 2D surface. Similarly, XRD spectra display a perfect growth along the (111) direction with Kiessig fringes indicating a good crystallinity. The first Brillouin zone and its hexagonal shape can be identified on constant energy contour plot at a binding energy E_B = -300 meV in **figure 1.35b**[27]. Electron pockets near $\overline{K}$ points can be identified since similar features have been observed in other Heusler compounds [32, 65]. A ring at the center of the Brillouin zone $\overline{\Gamma}$ is visible and opened while increasing the binding energy. This is a typical signature of states with linear dispersion but care must be taken since literature for other Heusler compounds labelled these states as trivial surface states.

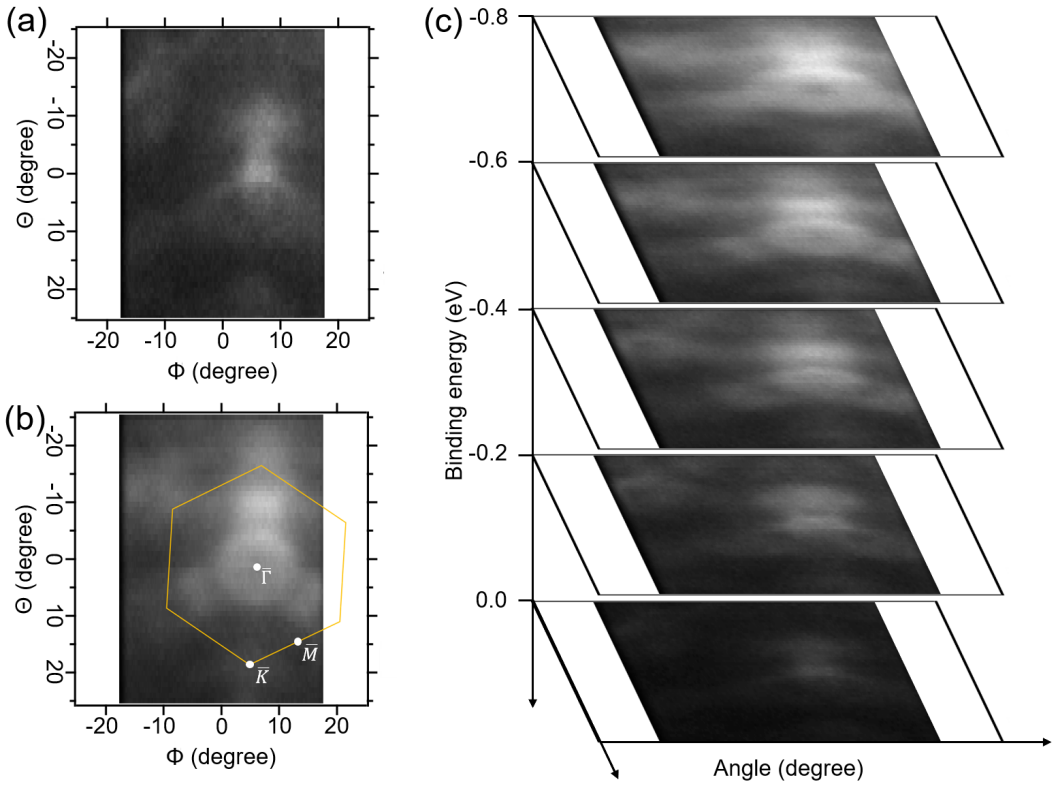

FIGURE 1.35: Fermi surface maps of PdYBi obtained at a photon energy of hν = 40.8 eV and a temperature T = 300 K. (a) and (b) are Fermi surfaces at respectively E_B = 0 eV and E_B = -0.3 eV. Saturation was modified between both images. The yellow hexagon represents the first Brillouin zone. (c) Fermi surfaces as a function of binding energy. Images' saturation is the same for the whole stack.

Bands with linear dispersion around the $\overline{\Gamma}$ point are unveiled in the band mapping given in **figure 1.36** and confirmed with the intensity profiles given on the right side of **figure 1.36**. The multiple bands with linear dispersion may originate from Kramer's pairs since similar bands have been observed in other Heusler alloys [32]. The resolution does not permit to clearly identify split channels and complementary

[27] The size and position of Brillouin zone was determined with the orientation given by LEED and the calculations of the reciprocal space vectors of PdYBi.

spin-resolved measurements have to be done to conclude on their origin. Moreover, the nature of these linear states is still unclear since no band structure calculation or energy dependence measurement have been performed. Other Heusler compounds (such as PtYBi) have an identified TSS lying in the bulk bands well below the Fermi level [32, 65]. Therefore, attention must be paid on the crossing state at approximately 1 eV below the Fermi level that also reveals a X shape. Nonetheless, once again the obtained resolution and the low spectral weight contrast do not allow to go further.

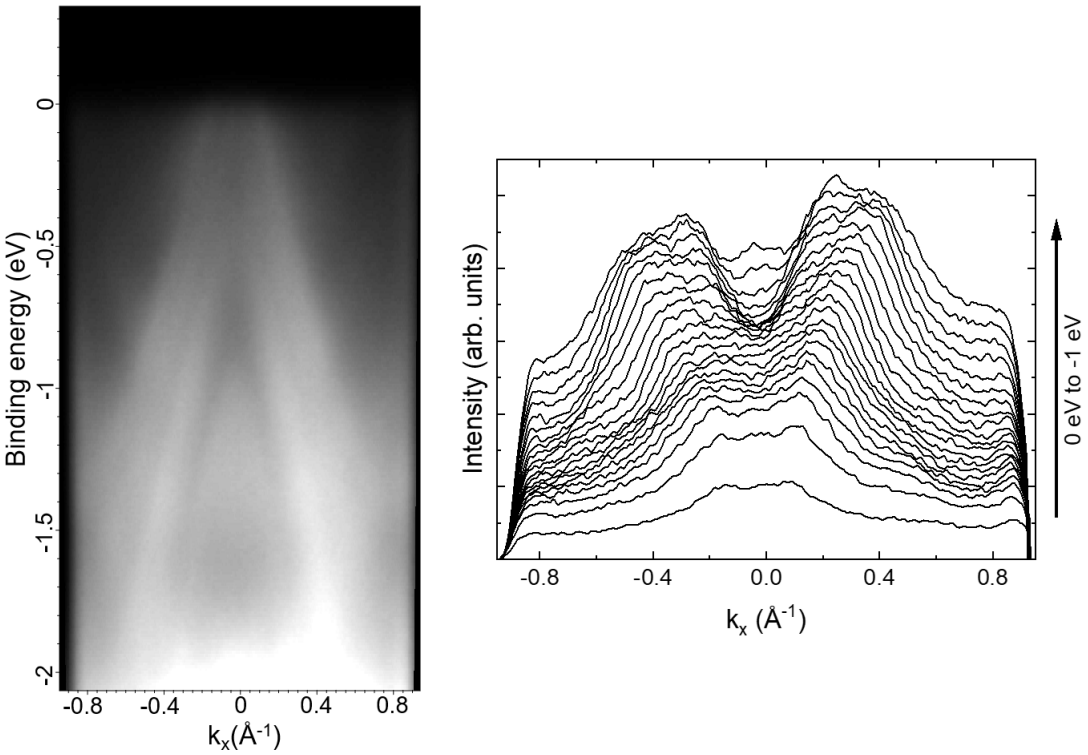

FIGURE 1.36: On the left, band mapping of PdYBi obtained at a photon energy of hν = 40.8 eV and a temperature T = 300 K. On the right, intensity profiles of the left image. Each line profile corresponds to different binding energy starting from 0 eV (at the bottom) and with a step of -0.05 eV.

To summarize, our PdYBi thin films crystalize in the $C1_b$ half-Heusler structure and smooth PdYBi's surfaces. The STEM and XRD studies highlight some Pd chemical disordering in the lattice. This explains the low spectral weight of the bands in ARPES measurements. Nonetheless, linear states are present and pave the way for transport measurements.

1.2.3 PtYBi

Similar experiments were performed on PtYBi thin films. AES, XRD, TEM, LEED and ARPES measurements are used to fully characterized them and validate the RHEED observations.

Auger electron spectroscopy

Similarly to what had been done for PdYBi, AES was performed to check the chemical composition of the sample and to detect any impurities lying at the surface. AES spectrum obtained for PtYBi samples is given in **figure 1.37**. As shown, only Auger lines of Pt_{NNN}, Y_{MNN} and Bi_{NOO} are present with no parasite peak due to O. C contamination cannot be checked since Pt transitions are present around the C ones.

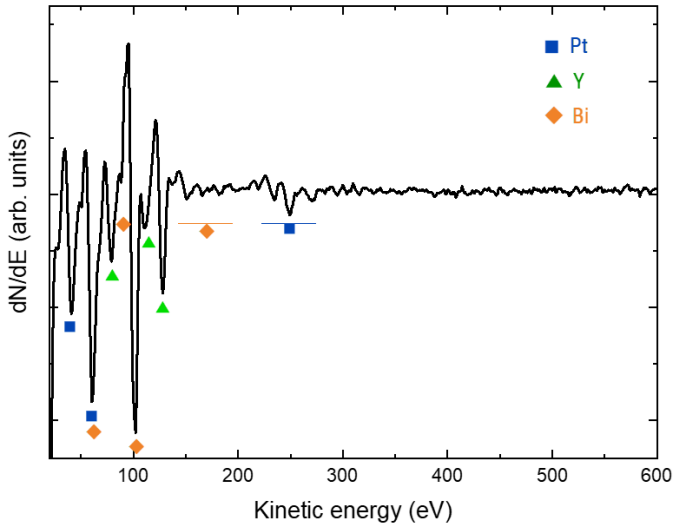

FIGURE 1.37: Typical Auger electron spectroscopy spectrum of PtYBi. Blue squares represent Pt transitions, green triangles Y transitions and orange diamonds Bi transitions.

X-ray diffraction

Symmetrical configuraion

X-ray diffraction was done and the (111) growth direction determined with RHEED was confirmed by the PtYBi's (111) peaks family of the spectrum in **figure 1.38**. No parasite peak from other PtYBi's plane families was noticed as a consequence of the good single-crystalline growth. By assuming the unit cell to be perfectly cubic, the cell parameter can be extracted from the $\theta/2\theta$ data with a determined value of a_{PtYBi} = 6.64 Å slightly higher than the one obtained for PdYBi and in good agreement with the theoretical value [8]. The inset in **figure 1.38** is a zoom of the (111) peak of PtYBi showing Kiessig fringes that are slighter compared to PdYBi ones.

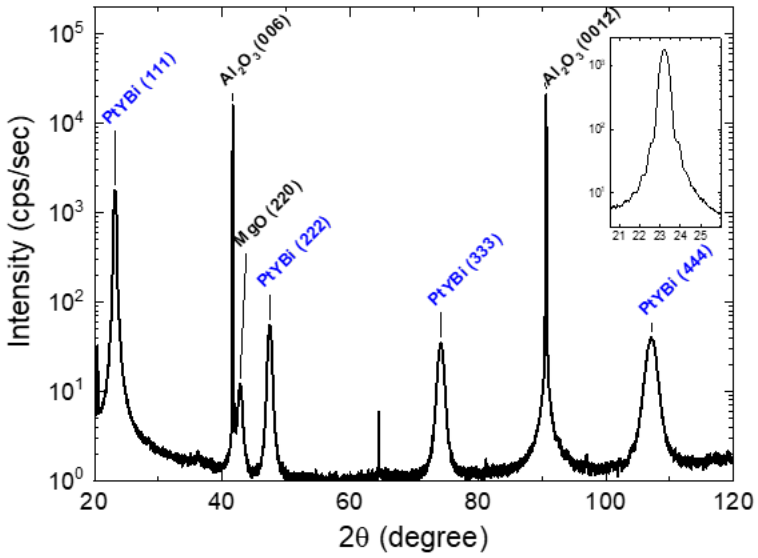

FIGURE 1.38: Typical $\theta/2\theta$ XRD scan for PtYBi. The inset on the upper part is a zoom of PtYBi(111) peak showing the presence of Kiessig fringes.

Non symmetrical configuration

Other peak families were measured thanks to non-symmetrical configuration to confirm the cubic structure. The results are given in **figure 1.39** with the (220) and (004) planes probed. The peaks were fitted with a Voigt function to extract the 2θ values. The resulting cell parameter estimations were 6.65 Å for both peaks attesting the $C1_b$ cubic phase.

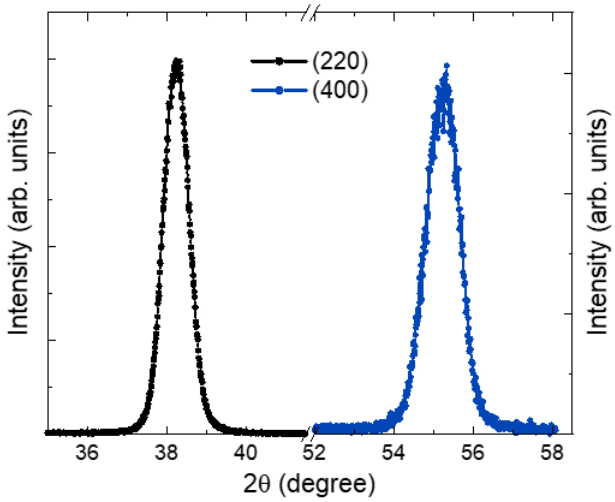

FIGURE 1.39: Non-symmetrical scans of PtYBi sample. The probed peaks are from the families (220) in black and (004) in blue.

The growth in the $C1_b$ half-Heusler structure is confirmed with no contamination detected with AES. The previous part showed the importance of chemical order that strongly impact photoemission's results. TEM study is thus done in the following in order to check the chemical ordering.

Transmission electron microscopy

Since PtYBi and PdYBi crystallize in the same $C1_b$ half-Heusler structure a cut along the same zone axis (ie. $[1\bar{1}0]_{PtYBi}$ zone axis) was done to check the atomic column arrangement. TEM spectrum is given in **figure 1.40** showing a clean interface between sapphire and PtYBi but some roughness is present at the surface of PtYBi as already revealed by the modulation in RHEED patterns. The layer above PtYBi is composed of Fe and Al. The explanation for such capping layer comes from interdiffusion. The aim of this sample was to perform transport measurements where a ferromagnetic layer was required. Fe was chosen as ferromagnetic layer and was capped with Al to avoid oxidation. Unfortunately, Fe and Al get mixed up at room temperature explaining the Fe/Al layer which was, consequently, used as capping layer. The growth direction and the epitaxial relations can be checked by performing FFT on an area at the Al_2O_3/PtYBi's interface. The diffraction pattern of the green frame in **figure 1.40** confirms the epitaxial relationship between (111) growth axis of PtYBi (spot labeled in yellow) and the (0001) direction of sapphire (spot labeled in red). Spots of the families $[11\bar{2}]_{PtYBi}$ and $[11\bar{2}0]_{Al_2O_3}$ are not visible in the FFT image but were observed by realizing FFT on separated areas consisting only of PtYBi and Al_2O_3 and attest to the epitaxial relationship PtYBi $[1\bar{1}0]$ (111) // Al_2O_3 $[11\bar{2}0]$ (0001). Moreover, PtYBi thickness was estimated around 20 ± 5 nm with the help of TEM images in the line with the desired thickness of 20 nm. This is another proof of the good control of the stoichiometry in our samples.

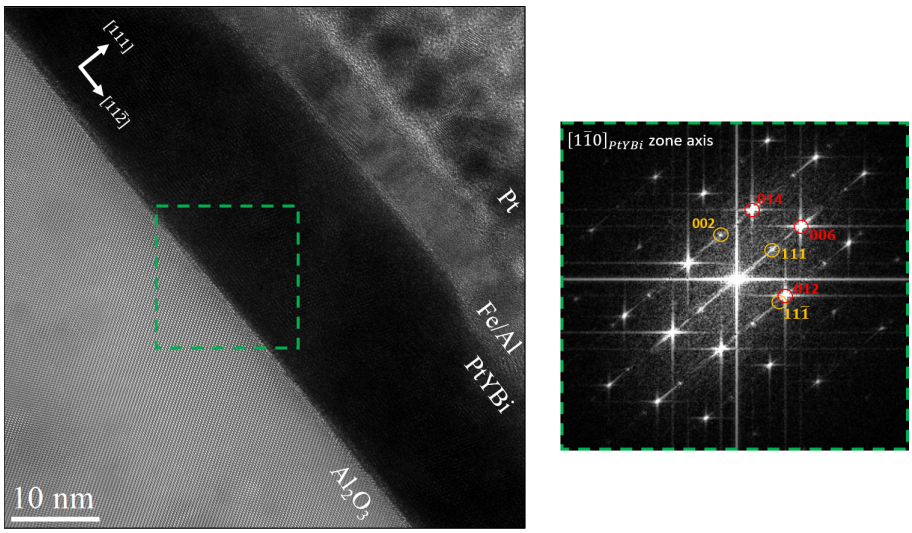

FIGURE 1.40: On the left, TEM image of Al_2O_3/PtYBi/Fe/Al. Fe and Al were used respectively as ferromagnetic layer and capping layer. Pt is deposited on top of the whole stack for cross section preparation. On the right, diffraction pattern of the green area showing the epitaxial relation between PtYBi layer and substrate. The spots labeled in yellow come from PtYBi, the ones in red are from Al_2O_3.

STEM images were also performed and one of them is given in **figure 1.41**. Despite the roughness of PtYBi's surface, the image allows to distinguish the presence of two different domains in the layer. This is even more visible by performing FFT on the blue and red frames labeled respectively 1 and 2. The diffraction pattern of the $[1\bar{1}0]$ zone axis is asymmetric and permits to distinguish the two different domains lying in the sample as shown by the FFT of both areas on the right part of **figure 1.41**.

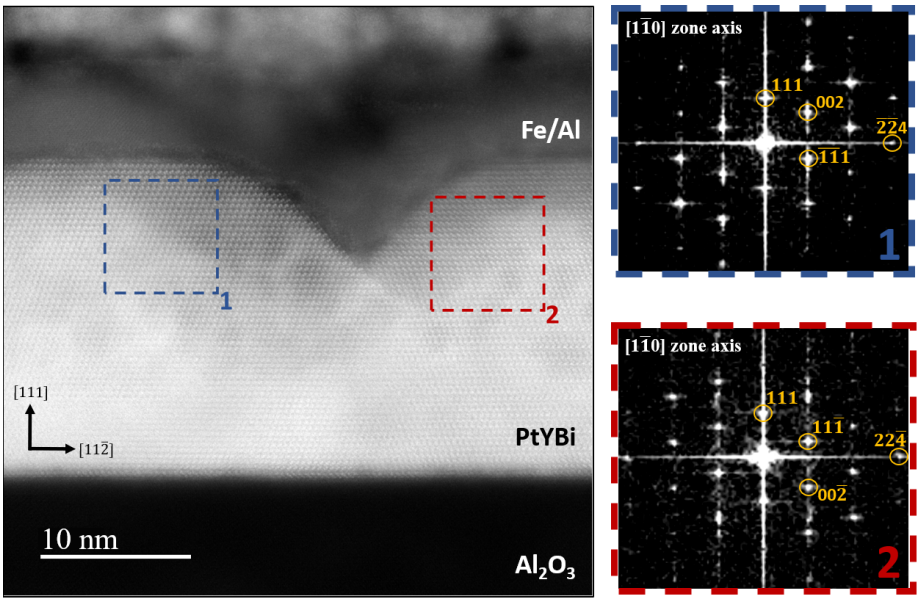

FIGURE 1.41: STEM-HAADF image of Al_2O_3/PtYBi/Fe/Al. On the right, diffraction patterns of the blue and red squared frames allowing to distinguish the presence of domains.

Chemical ordering can then be checked thanks to HAADF-STEM images. Data treatment similar to what was done for PdYBi was performed on high magnification images of PtYBi thin film to increase the signal/noise ratio. The result is given in **figure 1.42** for two areas representing both domains.

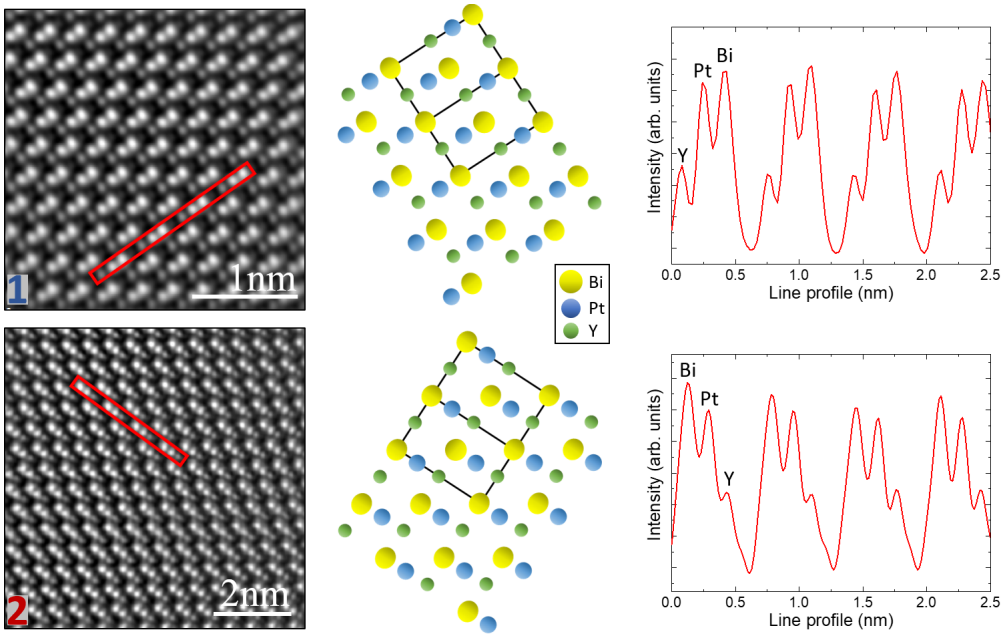

FIGURE 1.42: On the left, STEM-HAADF images of the two domains observed in the sample. 1 and 2 notations refer to the two areas of **figure 1.41**. The predicted patterns given in the middle fit perfectly well with those observed as revealed by the intensity line profiles on the right.

For each domains, the observed atomic columns arrangement fits perfectly with the expected ones assuming no chemical disordering. It is easy to identify Bi, Pt and Y columns since the intensity is linked to the number of electrons (bright for Bi, a little

less bright for Pt and dark for Y since they possess respectively 83, 78 and 39 e^-). Even if the pattern is clearly visible, intensity line profiles can be done to confirm the observed pattern. The line profiles areas are represented by red rectangles in both images and the extracted intensity lines, plotted in **figure 1.42**, are in accordance with the observed atomic arrangement.

Finally, similarly to what was done for PdYBi, XRD was used to perform phi-scan and test if the peaks symmetry is doubled or not. Phi-scan was carried out on PtYBi(220) peak. The result is given in **figure 1.43** and shows a six-fold symmetry attesting to the presence of domains. One should note that this is clearly different from PdYBi films. One of the remaining questions is, since TEM probed the entire width of the prepared sample why is there no domains superposition while both are present in the sample? A first answer can be due to the depth probed in PtYBi. Since PtYBi is composed of heavy elements, the thinnest area possible was probed by TEM reducing the possibility to observe superposed domains. The second answer is that TEM is a local measurement and only a few areas of the sample were investigated. It is likely that other areas present the domain superposition as it is slightly the case in the center of the image of **figure 1.41**. Finally, the good chemical ordering in PtYBi compared to PdYBi can be explained by the higher deposition temperature that may result in a better atomic ordering.

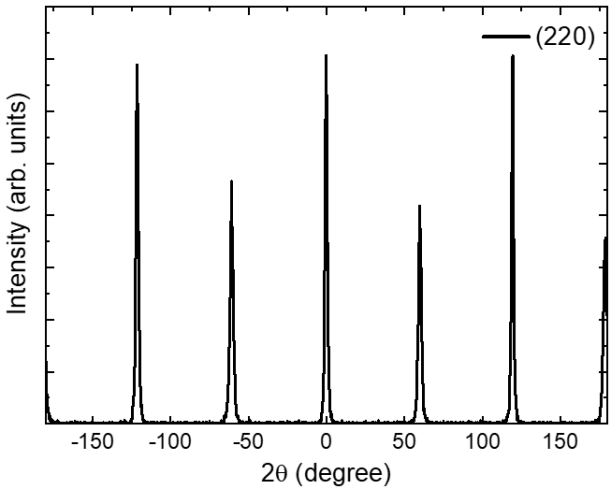

FIGURE 1.43: Phi-scan of (220) peak of PtYBi revealing a six-fold symmetry instead of a three-fold symmetry.

Energy dispersive X-ray spectroscopy

EDX was performed on PtYBi and the mapping of the different elements is given in **figure 1.44**. The capping of this sample should be Al with a Fe layer just beneath it. As said before, interdiffusion occurs between these two layers and Al oxidizes as shown by the O present in the capping layer area. Al and O are also present at the bottom of the mapping as a signature of Al_2O_3 substrate. Finally, Pt, Y and Bi unveil a homogeneous distribution. PtYBi layer is sharp with no diffusion or segregation of any element observed. The Pt detected on top of the mapping is due to Pt deposition used to build the cross section and the presence of Bi comes from an

overlapping with the Pt transitions that mislead the mapping. Finally, the small O amount located on the PtYBi area can be due to cross section oxidation during transport between focus ion beam and TEM. Nonetheless, given the numerous transitions due to the heavy elements present in the thin film an overlapping between O and another transition is also worth considering.

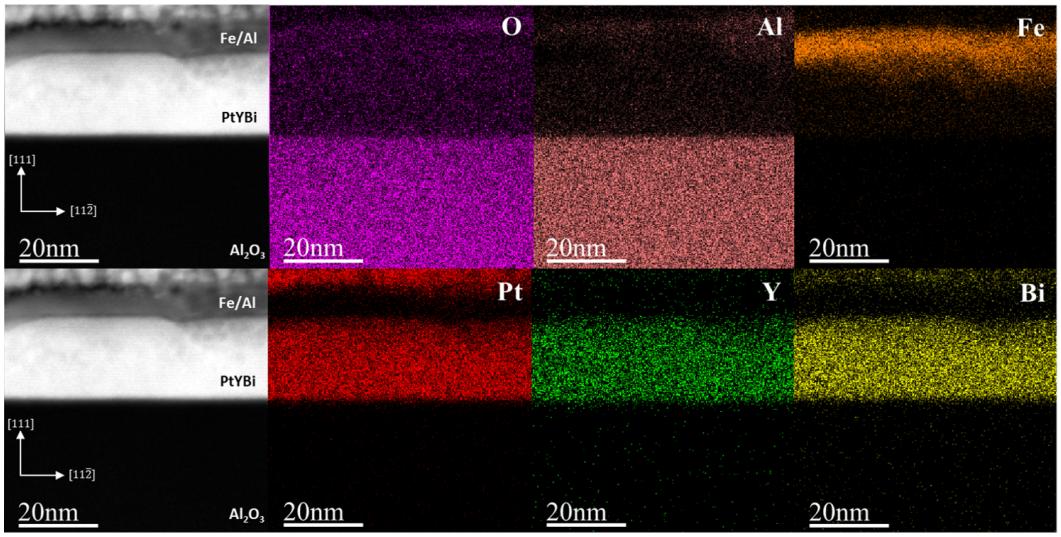

FIGURE 1.44: EDX map at the edge of O in purple, Al in brown, Fe in orange, Pt in red, Y in green and Bi in yellow.

Unlike PdYBi, PtYBi unveils a better chemical ordering. However, we never succeeded in obtaining smooth PtYBi surfaces. The good chemical order is probably linked to the higher deposition temperature for PtYBi that enhances the atomic arrangement. ARPES measurements can now be carried out to map PtYBi's band structure.

Angle resolved photoemission electron spectroscopy

Low energy electron diffraction

Typical LEED pattern of PtYBi is given in **figure 1.45** unveiling the hexagonal symmetry of the (111) growth direction of the fcc lattice. Slight additional spots, similar to PdYBi, are present and look like $\sqrt{3}\times\sqrt{3}$ R30° surface reconstructions as suggested by the RHEED patterns obtained for this sample. Nonetheless, once again the surface quality seems to be lower compared to PdYBi with spots less visible and more diffuse. Sample's orientation was done and the ARPES analyzer slit is represented by the white dashed line of **figure 1.45** suggesting a probed direction slightly off the $\overline{\Gamma M}$ direction.

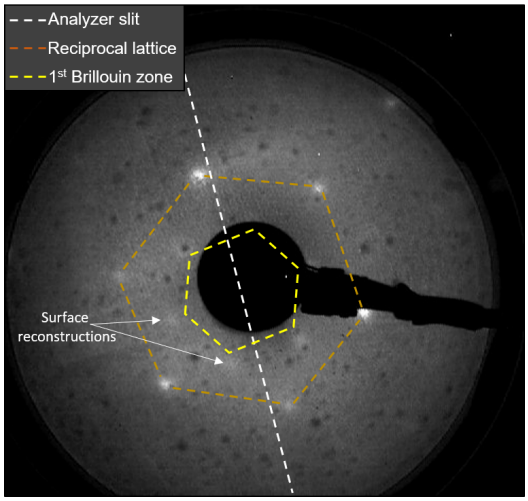

FIGURE 1.45: LEED pattern obtained for PtYBi depicting the hexagonal structure of the (111) thin film's plane (in brown). The first Brillouin zone is represented in yellow. Slight reconstructions are present and visible with weak $\frac{1}{3}$; $\frac{2}{3}$ spots along the [11$\bar{2}$] azimuth. The white dashed line represents the slit of the ARPES analyzer.

Angle resolved photoemission electron spectroscopy

In the same way than for PdYBi, ARPES measurements were performed on PtYBi to map its band structure. The constant energy contour plot is given in **figure 1.46** unveiling a better spectral weight contrast compared to PdYBi. This observation can be surprising since PtYBi surface quality is lower compared to PdYBi as revealed by RHEED, LEED or Kiessig fringes in XRD. The source of this more defined band structure in PtYBi (compared to PdYBi) certainly comes from the good chemical ordering lying in the sample. The band mapping allows us to identify the hexagonal shape of the first Brillouin zone. Numerous Fermi pockets already labeled in literature [32, 65] can be discerned around $\overline{K}$ points[28]. They also linked the spectral weight around the $\overline{\Gamma}$ point as twin hexagonal pockets that cannot be clearly identified here since the obtained resolution seems to depict a circular shape. Thanks to the tilt of both angle θ and ϕ, a second $\overline{\Gamma}$ point is visible in the constant energy contours of **figure 1.46**. An estimation of the distance between two $\overline{\Gamma}$ points is thus possible. The extracted value of $k_{//}$ = 1.54 Å^{-1} is in perfect agreement with the expected value for PtYBi and the first Brillouin zone drawn on **figure 1.46**. Finally, no additional state due to surface reconstructions is noticed since very similar ARPES band structures were published in literature [32, 65].

Band mapping of **figure 1.47** unveils multiple bands crossing the Fermi energy. Similarly to PdYBi, some of them, that are around the $\overline{\Gamma}$ point, present linear dispersion. According to the literature, these linear states crossing the Fermi energy are trivial surface states and their nature has nothing to do with topology. Nonetheless, an additional X shape band dispersing is present and lies in the bulk bands at a binding energy around E_B = -0.45 eV. Band structure calculations performed in literature [32, 65] labelled this crossing point at $\overline{\Gamma}$ as a TSS manifesting the non-trivial topology of PtYBi. Supplementary bands are discerned in the literature thanks to the high surface quality of the *in situ* cleaved bulk samples but cannot be observed here.

[28]Different ARPES works on cleaved bulk PtYBi samples have already been performed allowing the identification and comparison of the bands since the obtained band structure is very similar.

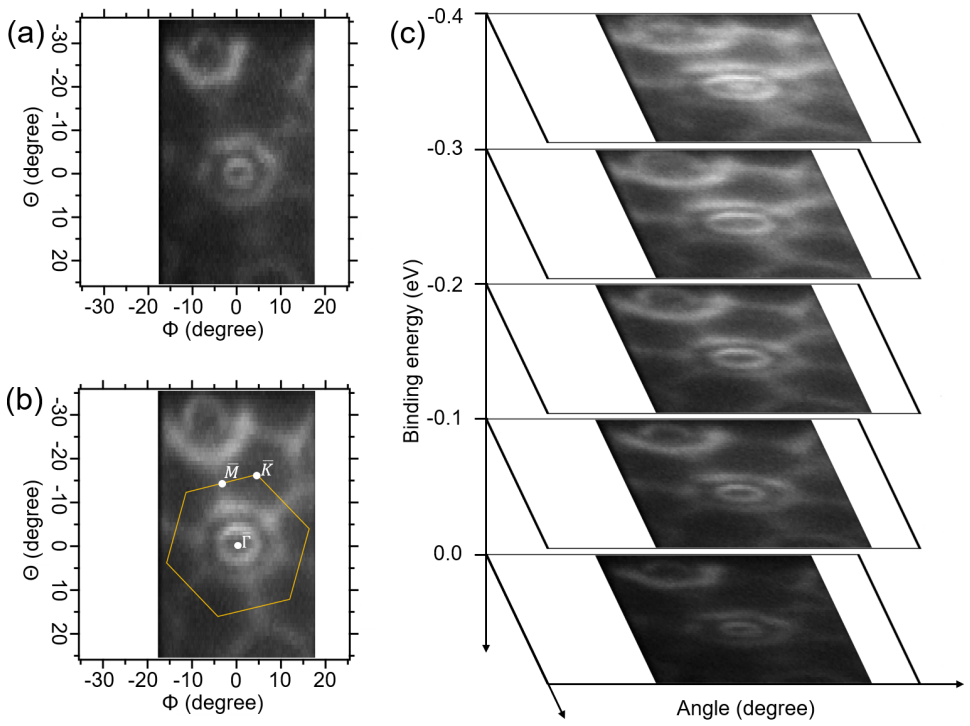

FIGURE 1.46: Fermi surface map of PtYBi obtained at a photon energy of hν = 40.8 eV and a temperature T = 90 K. (a) and (b) Fermi surfaces at respectively E_B = 0 eV and E_B = -0.3 eV. Saturation was modified between both images. The yellow hexagon represents the first Brillouin zone. (c) Fermi surfaces as a function of binding energy. Images' saturation is the same for the whole stack.

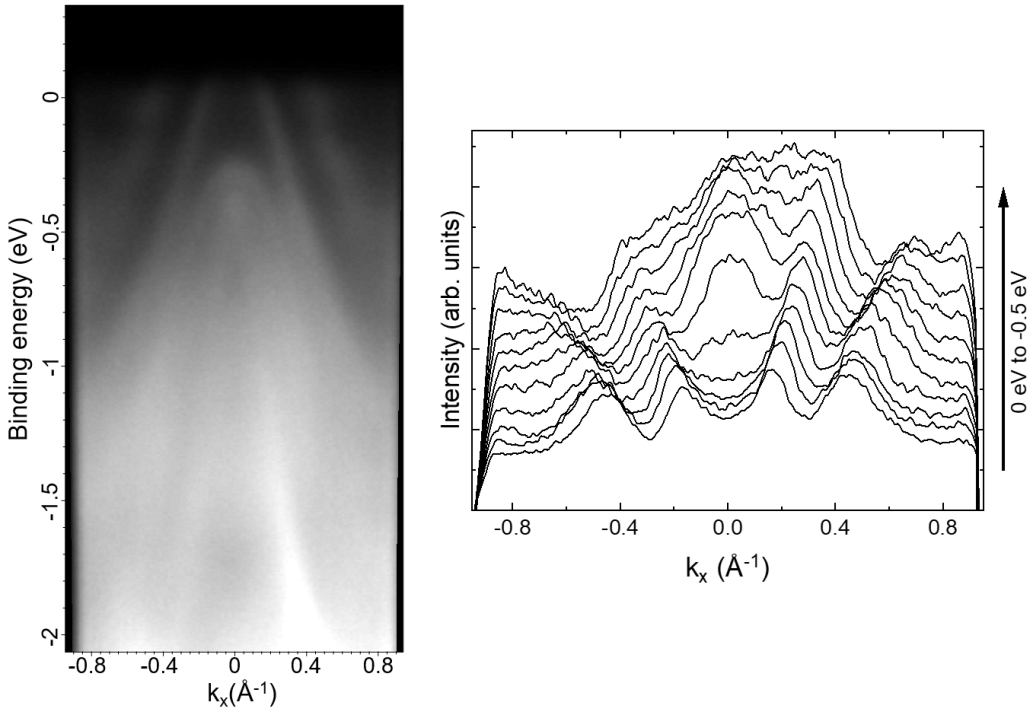

FIGURE 1.47: Band mapping of PtYBi obtained at a photon energy of hν = 40.8 eV and a temperature T = 300 K. On the left, dispersion map of PtYBi. On the right, intensity profiles performed in the left image. Each line profile corresponds to different binding energies starting from 0 eV (at the bottom) and with a step of -0.05 eV.

To summarize this chapter's section, PdYBi and PtYBi have been successfully grown by MBE in the $C1_b$ half-Heusler structure. The two thin films differ from their crystalline quality (single domain for PdYBi whereas two domains are observed for PtYBi) and their surface morphology (smooth surface for PdYBi, rough for PtYBi). STEM images also highlight a strong difference in chemical ordering in both materials: if the chemical ordering is perfect in a single PtYBi domain, it is not the case in PdYBi where Pd atoms are distributed on two sites of the $C1_b$ structure. This atomic disorder in PdYBi strongly impacts the photoemission measurements that results in a less defined band structure. Nonetheless, linear states were observed in both films. With the help of band structure calculations available for PtYBi, we found the premises of a topological signature in our PtYBi films similar to bulk samples [32]. The situation is not so clear for PdYBi since band structure calculations are not available. However, one can notice some clear similarities between PdYBi and PtYBi band structures measured by ARPES which suggest a possible topological behavior in PdYBi. These encouraging results pave the way for transport measurements to test the spin-to-charge conversion efficiency achievable with such half-Heusler compounds.

1.3 Transport measurements in half-Heusler topological insulators

The first part of this chapter was dedicated to the growth and the structural characterization of two Heusler alloys predicted to be TIs, namely PdYBi and PtYBi. The epitaxial growth was successfully achieved by MBE and characterized thanks to the large panel of tools provided by the Institut Jean Lamour. The band mapping of both compounds unveils a complex band structure where a straightforward TSS's observation turns out to be complex. On the one hand, multiple bands crossing the Fermi level are observed for PtYBi with a TSS lying well below the Fermi energy according to previous works and theoretical calculations found in literature. On the other hand, PdYBi hosts less spectral weight near the Fermi level. Bands with linear dispersion cross the Fermi energy but may be due to trivial surface states. The non-trivial topological nature may lie in the additional crossing point observed below the Fermi energy since similar features have been published for other Heusler alloys. However, the lack of band structure calculations does not allow to settle the question. Fortunately, ARPES measurements are not the unique way to identify the presence of TSSs. The second part of this chapter deals with transport measurements where the complex and unusual phenomena hosted by TIs can manifest. To do so, we engineered stacks composed of a TI and a magnetic layer to study the interconversion of charge current into spin current. In a first attempt, the chosen magnetic material was Co but the strong anisotropy and damping constant prevented to advance with the related experiments designed for this study. Fe was then chosen as magnetic material. The different systems grown are discussed in the following.

In order to carry out transport measurements and probe the potential topological nature of the samples, lithography patterning has to be done. The lithography process is explained in **appendix A** and results in four different devices, namely Hall bars, Spin Torque - FerroMagnetic Resonance (ST-FMR), Spin Pumping - FerroMagnetic Resonance (SP-FMR) and heater devices (or "spin Seebeck"). In this thesis,

Hall bars were used for conventional transport characterization. SP-FMR devices are used to evaluate the TIs spin-to-charge interconversion efficiency with the help of a ferromagnetic material at resonance. Finally, the Heater devices are used for the spin Seebeck effect where a gradient of temperature is used to estimate the spin-to-charge interconversion.

1.3.1 Samples growth for transport measurements

Now that PdYBi and PtYBi deposition has been mastered, samples growth for electrical and transport characterizations can be conducted. Two samples' batches for each compound were grown:

- The first batch consists in the following stack: Al_2O_3(substrate)/TI(Xnm)/MgO(20nm) with TI = PdYBi and PtYBi and X = 5, 10, 20 and 30 nm. PdYBi and PtYBi deposition was similar to the process described in the previous sections. The 20 nm thick MgO capping was deposited on top at room temperature to avoid samples' contamination and oxidation.
- The second batch consists in the following stack: Al_2O_3(substrate)/TI(Xnm)/MgO(barrier)/Fe(6nm)/MgO(20nm) with TI = PdYBi and PtYBi and X = 5, 10, 20 and 30 nm. PdYBi and PtYBi deposition was similar to the process described in the previous sections. The MgO barrier was 1 monolayer thick (2 monolayers thick) for PdYBi (PtYBi) samples and was used to protect the FM/TI (Ferromagnetic/Topological Insulator) interface[29]. Indeed, TIs are sensitive to magnetic impurities due to their TRS breaking nature that can strongly affect the non-trivial topological phase and kill the TSS [28, 84]. The MgO barrier task was to preserve the TRS in the TIs and was used as a shield between both layers. A 6 nm Fe ferromagnet was then deposited at room temperature to avoid interdiffusion and resulted in a polycrystalline growth. The samples were then covered by a 20 nm thick MgO capping grown at room temperature. The Fe RHEED images can be found in **appendix B** for all samples.

The two resulting stacks are sketched in **figure 1.48**.

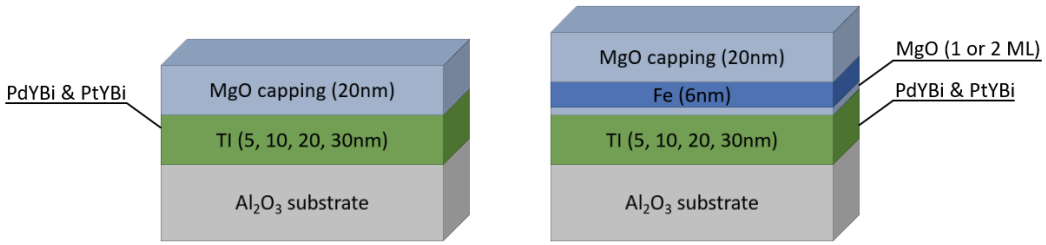

FIGURE 1.48: Sketch of the samples' stacks. Two batches were grown for both compounds. Without MgO/Fe layers on the left and with them on the right.

Additionally to these samples, a control and a reference samples were fabricated:

- A Pt control sample was grown in order to compare the spin efficiency between PdYBi and PtYBi TIs with this well-known Heavy Metal (HM). The sample composition was thus: Al_2O_3(substrate)/Pt(5nm)/MgO(barrier)/Fe(6nm)

[29]Two MgO monolayers were used for PtYBi due to the higher roughness obtained for this compound compared to PdYBi.

/MgO(20nm). The Pt layer was deposited at 950 °C ($T_{pyro} \approx 550$ °C) and covered by one monolayer of MgO. A 6 nm thick Fe layer deposition was then performed at room temperature resulting in an epitaxial growth. Finally, 20 nm of MgO were used to cap the sample. The Pt and Fe RHEED images can be found in **appendix B**.

- A Fe reference sample was deposited with the following stack: Al_2O_3(substrate) /MgO(barrier)/Fe(6 nm)/MgO(20 nm). The Fe layer was deposited at room temperature and covered with a 20 nm thick MgO capping. The Fe reference sample will be used as a Fe damping value reference for our systems. The Fe RHEED images can be found in **appendix B**.

All these samples were characterized by RHEED and XRD before patterning. Patterning was realized by standard UV lithography (see **appendix A**) for all samples resulting in four device architectures dedicated to electrical characterization and transport measurements.

1.3.2 PdYBi and PtYBi electrical characterization

All the samples were patterned into Hall bars to carry out electrical characterization (**figure 1.49**). In the following measurements, the current is always applied along the x direction (see **figure 1.49**) and the generated voltage is collected along the longitudinal direction noted V_x[30].

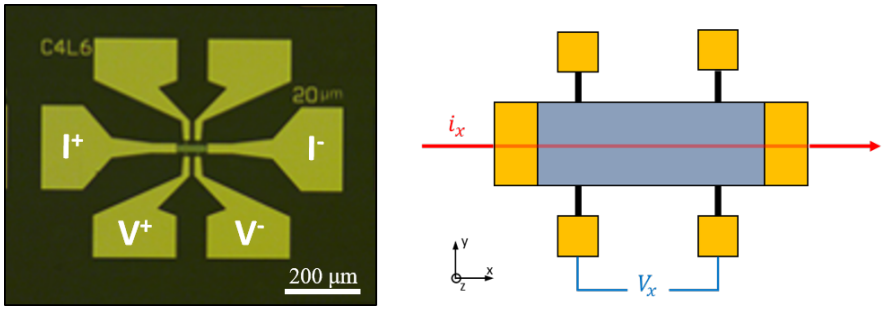

FIGURE 1.49: On the left, image of a Hall bar patterned by standard UV lithography. On the right, sketch of the Hall bar used. The current, represented in red, is applied along the x direction and the resulting voltage is picked up in the longitudinal (V_x) direction.

The longitudinal resistance was recorded while sweeping the temperature. The resulting curves are plotted in **figure 1.50** for the two compounds. First of all, two different trends were observed in the ρ_{xx} vs. T curves. For high temperature regions, the behavior is non-metallic and a negative slope is observed. For low temperature regions, a metallic-like behavior with an increasing resistivity with temperature is measured. This increasing trend has already been observed for some half-Heusler alloys such as ErPdBi [70, 71], HoPdSb [73], TbPtBi [85], HoPtBi [85] or even PtYBi [72] and PdYBi [76]. The data of **figure 1.50** are typical of semimetals or narrow-gap semiconductors. A semiconducting-like trend is observed at high temperatures and overrided at lower temperatures by a metallic-like character. According to Gofryk *et*

[30]The electrical resistivity tensor in the 2D case is given by: $\begin{bmatrix} E_x \\ E_y \end{bmatrix} = \begin{bmatrix} \rho_{xx} & \rho_{xy} \\ \rho_{yx} & \rho_{yy} \end{bmatrix} \begin{bmatrix} j_x \\ j_y \end{bmatrix}$

al. [70], this behavior is typical of doped semiconductors where the creation of acceptor or donor levels takes place due to atomic disorder, defects or off-stoichiometry compounds that result in this metallic-like shape.

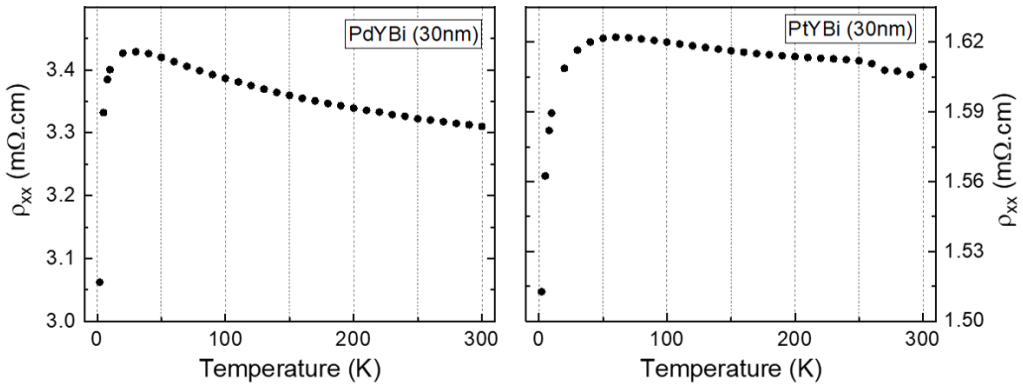

FIGURE 1.50: Temperature dependence of the electrical resistivity of the 30 nm thick PdYBi, on the left, and PtYBi, on the right, samples.

Numerous half-Heusler alloys [70, 71, 73, 75, 85] present a sharp drop in resistivity at ultra-low temperature which is attributed to the onset of superconductivity. This feature has also been observed in PdYBi and PtYBi compounds [66, 68, 72, 86, 87] but are beyond the scope of these investigations since the reported transitions temperatures are below 2 K. The superconducting transitions for PdYBi and PtYBi are expected to occur at T_C = 1.75 K [87] and T_C = 0.77 K [66, 72, 86] respectively. Finally, the resistivity values obtained are in agreement with those given in the literature which are in the mΩ.cm range for both compounds [66, 68, 76, 87]. Nonetheless, it should be noted that electrical resistivity difference is usually observed in those compounds from one sample to another due to different crystal qualities. Indeed, ρ_{xx}(T) curves for half-Heusler alloys have been demonstrated as strongly sample dependent. Defects and vacancies may drastically modify the electronic band structure leading to a change in resistivity.

The ρ_{xx} vs. T measurements are similar to the data published in literature for half-Heusler compounds but the obtained resistivities vary from one sample to the other. This significant variation is also in agreement with the results of the literature [73, 85] where they indicate that the quality of the sample, which is very difficult to reproduce or maintain during the lithography process, strongly affects the results. This dispersion will also be observed in the different magneto-transport measurements I carried out and which are presented in the following sections.

1.3.3 Spin-to-charge conversion measurements

This section is dedicated to the study of the spin-to-charge interconversion efficiency in PdYBi and PtYBi compounds. To do so, the second batch of samples (right stack of **figure 1.48**) was patterned. Two techniques were carried out, namely SP-FMR and spin Seebeck measurements, taking advantage of the Fe layer as spin battery. We generate spin accumulation at the FM/MgO interface in order to induce spin-to-charge interconversion at the MgO/TI interface, ideally purely by the inverse Edelstein effect. In the first method, a coherent spin injection is performed and a discussion about the assessment of the use of MgO as a barrier between TI and Fe is done. In a second section, our results on spin Seebeck experiments, which is an

incoherent (thermal) spin injection method, are described.

Spin Pumping – FerroMagnetic Resonance

Spin pumping - ferromagnetic resonance is a technique based on FMR. To understand an FMR experiment one must look at the LLG equation [35]:

$$\frac{d\mathbf{m}}{dt} = \gamma \times \mathbf{H}_{eff} + \alpha.\mathbf{m} \times \frac{d\mathbf{m}}{dt} \tag{1.17}$$

This equation describes the magnetization dynamics. The first term explains the magnetization's precession around the effective magnetic field, H_{eff}. The second term is a dissipative term (ie. called Gilbert damping) that tends to realign the magnetization towards its equilibrium position. It describes how fast the spin angular momentum is dissipated to the lattice and leads to a spiral motion of the magnetization. In an FMR experiment, an alternating field, h_{rf}, of constant frequency (of the order of GHz) is applied to the system and is used to excite the magnetization dynamic. At the same time, an applied dc magnetic field is swept and, when the system reaches the resonance condition, the magnetization precesses around its equilibrium position (**figure 1.51**).

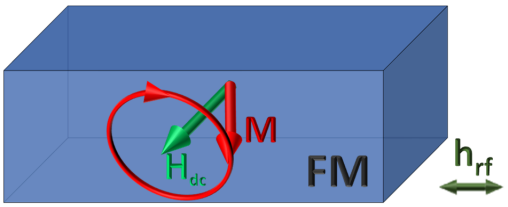

FIGURE 1.51: Sketch of the FMR principle. The magnetization dynamics is excited under the action of h_{rf} and H_{dc}. H_{dc} is swept (while h_{rf} has a fix frequency and amplitude) and, for a certain field value, the ferromagnetic resonance of the system is reached.

Therefore, when an FMR experiment is conducted, the total magnetization and field are modified owing to the injected *rf* excitation as followed: $\vec{H_{tot}} = \vec{H_{eff}} + \vec{h_{rf}}$ and $\vec{M_{tot}} = \vec{M_0} + \vec{\delta m}$. The LLG equation can be solved after linearization. It results that the FMR signal is proportional to the quantity of microwave power absorbed by the sample which is described by a change in the system's dynamic magnetic susceptibility. The dynamic magnetic susceptibility is the coefficient of proportionality between the excitation field, h_{rf}, and the response of the magnetization, δm. This demonstration is performed in numerous works [11] and allows to understand the shape of the Lorentzian-like fitting function used later on.

FMR has been widely used during the last decades to characterize ferromagnetic systems. The interesting thing is that it was demonstrated that FMR can generate pure spin currents (and spin accumulations) in hybrid nanostructures. The first heterostructures extensively studied have been the ones composed of a FM layer and a Heavy Metal (HM) [88, 89, 90]. By harnessing the spin current injected at the resonance conditions by the FM into the adjacent HM layer, a pure charge current can be produced by ISHE in the HM. This effect can be summarized by the following expression: $\mathbf{j}_C \propto \mathbf{j}_S \times \sigma$ ($\mathbf{j}_C$ and $\mathbf{j}_S$ are the charge and spin current created, σ is the spin polarization vector of the spin current whose direction is given by the applied

dc magnetic field). This spin-to-charge conversion has been used in FM/TI heterostructures [52, 55, 91, 92, 93, 94] where the charge current is generated thanks to the IEE. This spin-to-charge conversion phenomenon is described in the following.

Here, SP-FMR is performed to estimate the spin-to-charge interconversion[31]. The SP-FMR principle measurement is sketched in **figure 1.52**. As discussed above, the heterostructure is composed of a FM and a TI (or HM) layers. At the resonance conditions, the FM's magnetization precess uniformly and a pure spin current, j_S, whose spin polarization's direction is given by the equilibrium position of the magnetization, is injected in the adjacent layer [95]. If the adjacent layer hosts strong SOC and a spin texture, such as for TIs, the pure spin current will be converted in a transverse charge current by the IEE (or ISHE for HM). In other words, FMR generates a pure spin current by coherent spin pumping. It is carried by conduction electrons and is defined as a flow of spin angular momentum without any flow of charge current. This flow of angular momentum affects the LLG equation (**equation 1.17**) with a supplementary damping term:

$$\frac{d\mathbf{m}}{dt} = \gamma \times \mathbf{H}_{eff} + (\alpha + \alpha_{sp}).\mathbf{m} \times \frac{d\mathbf{m}}{dt} \tag{1.18}$$

With α_{sp} the enhancement of the magnetic damping term due to the spin pumping effect. The measured resonance is broadened and the amplitude of precession modified. Thus, it allows a direct detection of a pure spin current.

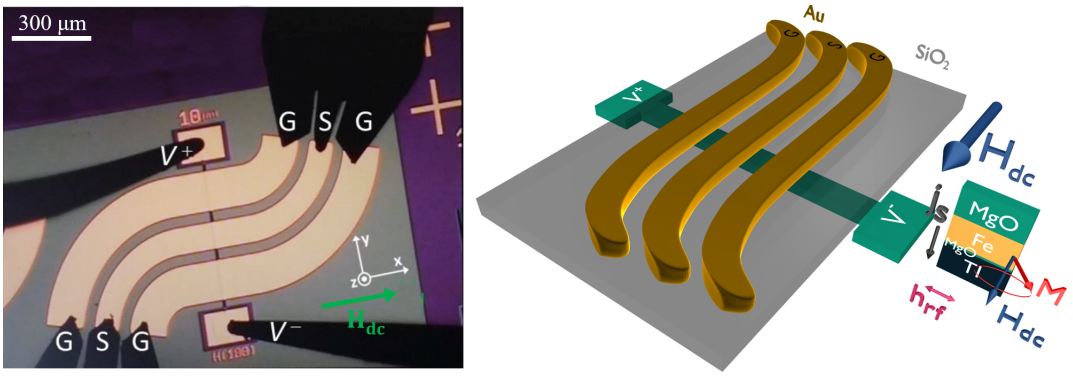

FIGURE 1.52: On the left, SP-FMR device image with *rf* (GSG) and dc connections. *rf* connections are used to inject the current in the antenna while dc connections collect the spin pumping voltage generated across the sample. On the right, sketch of the SP-FMR device and of the spin pumping mechanism. At the FMR conditions, a pure spin current, j_S, is injected from the FM to the TI interface, a transverse charge current is generated by IEE at the TI interface and is detected across the sample by the dc connections.

In summary, when one performed an SP-FMR experiments, the magnetization dynamics (ie. the precession motion of the magnetization) as well as magneto-transport (ie. the voltage created by IEE or ISHE for instance) are probed at the same time. This is resume by the Lorentzian fitting function used to fit the measured voltage:

$$V_{meas}(H) = V_{sym}\frac{\Delta H^2}{\Delta H^2 + (H - H_{res})^2} + V_{asym}\frac{\Delta H(H - H_{res})}{\Delta H^2 + (H - H_{res})^2} + V_{offset} \tag{1.19}$$

[31] All the SP-FMR experiments of this thesis were performed at 300K.

Where H_{res} is the resonance field, ΔH is the half width at half maximum and V_{sym} (V_{asym}) is the symmetric (antisymmetric) Lorentzian function's amplitude.

The V_{sym} and V_{asym} terms are directly related to magneto-transport and will be discussed later on. The two other terms, the half width at half maximum (ΔH) and the resonance field (H_{res}), are related to the magnetization dynamics. In a first approach, we are going to look only at the magnetization dynamics part and we will come back to magneto-transport.

Magnetization dynamic part:

Frequency dependence measurements can be carried out in order to determine the effective magnetization saturation M_{eff}, the inhomogeneous broadening term ΔH_0 and the damping constant α thanks to the formulas:

$$\left(\frac{2\pi f}{\gamma}\right)^2 = (H + H_K)(H + H_K + 4\pi M_{eff}) \tag{1.20}$$

$$\Delta H = \Delta H_0 + \left(\frac{2\pi f}{\gamma}\right)\alpha \tag{1.21}$$

An example of such data treatment, for the Pt control sample, is shown in **figure 1.53** where the effective magnetization saturation M_{eff}, the inhomogeneous broadening term ΔH_0 and the damping constant α values are extracted from the fits of the graphs. M_{eff} and ΔH_0 determination allow to check the quality of the Fe layer. The M_{eff} = 1371 $\pm$ 10 emu.cm^{-3} is lower than reported literature values [96, 97] and a bit low compared to the 1700 emu.cm^{-3} of bulk Fe. The frequency independent contribution ΔH_0 = 7 $\pm$ 1 mT is large and points out the presence of inhomogeneities in the FM. The damping constant, equals to α = (4.34 $\pm$ 0.08) .10^{-2}, is enhanced compared to conventional values obtained for a single Fe layer. This broadened resonance is due to the spin current pumped out of the Fe layer into the Pt layer. Nonetheless, this value is higher than the conventional damping reported in Fe/Pt systems [96, 97]. This high α value will be discussed later on.

A first figure of merit used in SP-FMR measurements is the spin mixing conductance, $g_{eff}^{\uparrow\downarrow}$, which quantifies the spin current accumulation at the FM/HM interface (ie. it characterizes the efficiency of the spin transport at the interface). Its expression is given in **equation 1.22**:

$$g_{eff}^{\uparrow\downarrow} = \frac{4\pi M_S t_{FM}}{g\mu_B}(\alpha_{FM/HM} - \alpha_{FM}) \tag{1.22}$$

With $g_{eff}^{\uparrow\downarrow}$ the effective spin mixing conductance (m^{-2}), M_S is the saturation magnetization (A.m^{-1}), $\alpha_{FM/HM}$ the total damping lying in the FM/HM bilayer and α_{FM} the damping of a reference sample.
This equation says that the linear fit's slope (ie. the damping value) of **figure 1.53** is directly related to $g_{eff}^{\uparrow\downarrow}$ since this quantity is based on $\Delta\alpha$ = $\alpha_{FM/HM}$ - α_{FM}. If one knows the damping values of the studied FM/HM structure (ie. $\alpha_{FM/HM}$) and of a

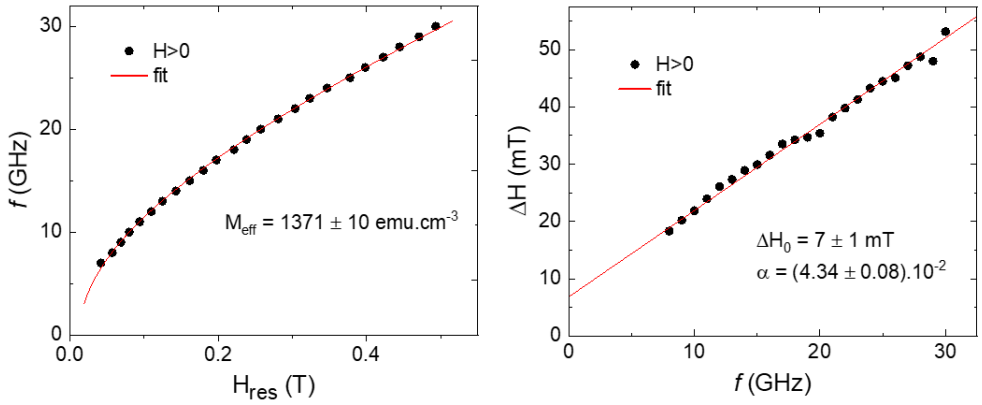

FIGURE 1.53: On the left, resonance frequency as a function of the resonant field H_{res}. The red curve is a fit to the Kittel formula. On the right, signal linewidth as a function of the resonance frequency. The red curve is a linear fit. Measurements performed on Pt(6nm)/MgO(1ML)/Fe(6nm) sample.

reference sample (ie. α_{FM}), it is possible to estimate $g_{eff}^{\uparrow\downarrow}$. The reference is a mirror sample made without the HM layer and is used to subtract the contributions that are not related to spin pumping. Indeed, the damping enhancement may originate from inhomogeneities in the FM. The subtraction of such a reference allows to suppress these contributions and characterizes only the FM/HM interface. The difficulty lies in the quality of the FM layer in the single layer and the bilayer. Ideally, both FM layers should be identical.

The Fe reference sample was measured by ferromagnetic resonance with an extracted α_{FM} value of $(2.8 \pm 0.1)\ .10^{-2}$. The high α_{FM} compared to literature values, $\approx 2\ .10^{-3}$ [96, 97], is attributed to the Fe crystalline quality. Indeed, the Fe growth is impacted by the sapphire substrate and the MgO barrier resulting in a broaden resonance. An estimation of the spin mixing conductance is done with $\Delta\alpha = 1.54\ .10^{-2}$ leading to $g_{eff}^{\uparrow\downarrow}$ =1.03 $.10^{20}$ m^{-2}. This value is in the usual 10^{18} to 10^{20} range observed for FM/HM and FM/TI structures [93] but is higher than reported values in Fe/Pt system [96, 97]. This observation is puzzling since $g_{eff}^{\uparrow\downarrow}$ quantifies the spin accumulation at the interface. In our case, the MgO barrier could reduce the $g_{eff}^{\uparrow\downarrow}$ value since a part of the spin-current pumped from the Fe layer could be reflected back. The spin mixing conductance obtained here should be seen as an upper bound. It reflects the different qualities of Fe layers obtained in the reference and Pt control samples leading to an overestimated $g_{eff}^{\uparrow\downarrow}$.

In the same way than for the Pt control sample, the damping, the effective magnetization and the inhomogeneous broadening term were extracted from the data for PdYBi and PtYBi.

Typical data obtained for PdYBi (20nm) sample are shown in **figure 1.54**. The Kittel curve allows to check the Fe layer quality with an M_{eff} value of 1405 $\pm$ 3 emu.cm^{-3} and an inhomogeneous broadening term ΔH_0 = 5 mT. An estimation of the damping constant thanks to the linear fit performed on the linewidth vs. resonant frequency graph is done with a determined value of $\alpha_{FM/TI}^{PdYBi}$ = (1.10 $\pm$ 0.02) $.10^{-2}$. The $\alpha_{FM/TI}^{PdYBi}$ value is lower than the α_{FM} determined in the reference sample

showing that the crystalline quality of the ferromagnetic layer is different in both samples. Indeed, according to spin pumping theory, a damping enhancement is expected in the FM/TI system compared to FM alone. Unfortunately, because of this too high $\alpha_{FM/TI}^{PdYBi}$, an estimation of $g_{eff}^{\uparrow\downarrow}$ was not possible.

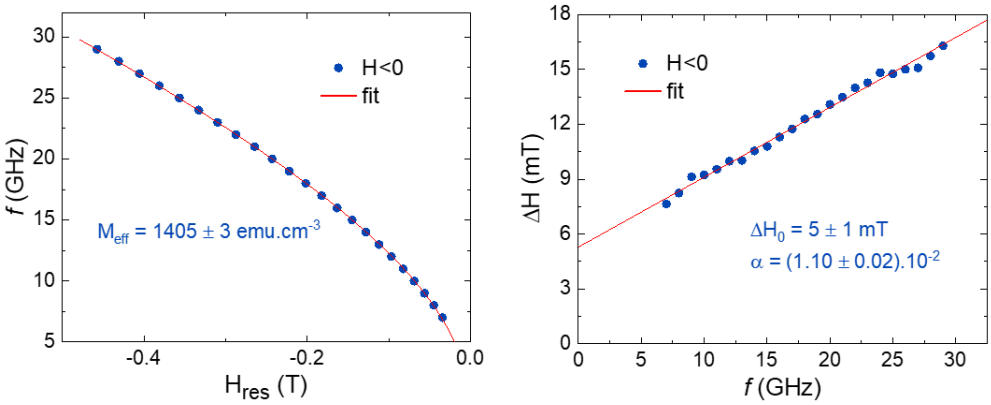

FIGURE 1.54: On the left, resonance frequency as a function of the resonant field H_{res}. The red curve is a fit to the Kittel formula. On the right, signal linewidth as a function of the resonance frequency. The red curve is a linear fit. Measurements performed on PdYBi(20nm)/MgO(1ML)/Fe(6nm) sample.

A similar trend has been observed for PtYBi samples whose data are given in **figure 1.55**. The effective magnetization and the damping constant are easily extracted and give values of M_{eff} = 1189 ± 5 emu.cm^{-3} and $\alpha_{FM/TI}^{PtYBi}$ = (2.81 ± 0.01) .10^{-2}. Here again, the damping is lower than the Fe reference and depicts a different Fe quality in both systems. This observation is checked by the lower M_{eff} extracted from the Kittel's curve where the ΔH_0 had to be fixed to zero otherwise negative values are obtained with no physical meaning. $g_{eff}^{\uparrow\downarrow}$ could not be estimated here either.

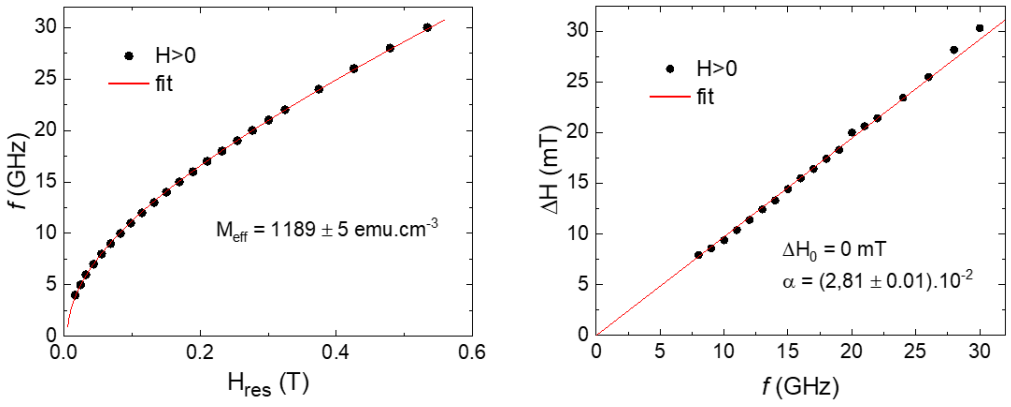

FIGURE 1.55: On the left, resonance frequency as a function of the resonant field H_{res}. The red curve is a fit to the Kittel formula. On the right, signal linewidth as a function of the resonance frequency. The red curve is a linear fit where ΔH_0 was fixed to 0 otherwise negative ΔH_0 values are obtained. Measurements performed on PtYBi(5nm)/MgO(2ML)/Fe(6nm) sample.

Magneto-transport part:

i. Spin pumping voltage and spin-to-charge interconversion formalism

Now that the magnetization dynamics data are extracted, the treatment of the magneto-transport part can be conducted. As discussed previously, the transport is included in the V_{sym} and V_{asym} terms of **equation 1.19**. In the ideal case, the voltage response should be perfectly symmetric (ie. voltage measured coming only from the spin pumping mechanism: $V_{meas} = V_{sym} = V_{SP}$) such as for the data given in **figure 1.56**. In this graph the spin pumping voltages of Ta/NiFe and Pt/NiFe samples are shown. The voltages measured for positive (H > 0) and negative (H < 0) applied magnetic field are reversed and the sign of the detected dc voltage is opposite for Ta and Pt. The results of **figure 1.56** can be easily understood with the help of the following equation : $\mathbf{j}_C \propto \theta_{SHE}\ (\mathbf{j}_S \times \sigma)$ (where $\mathbf{j}_C$ and $\mathbf{j}_S$ are the charge and spin current created, σ is the spin polarization which is aligned along the applied magnetic field in this SP-FMR experiment and θ_{SHE} is the spin Hall angle of the studied material[32]). The spin pumping theory suggests thus that the sign of the detected voltage has to reverse with the magnetic field ($\sigma \rightarrow$ -σ). Moreover, according to the negative or positive spin Hall angle of the studied material the spin pumping voltage can also be reversed. Indeed, Ta and Pt have an opposite spin Hall angle explaining the inverted sign of the detected voltage in **figure 1.56**.

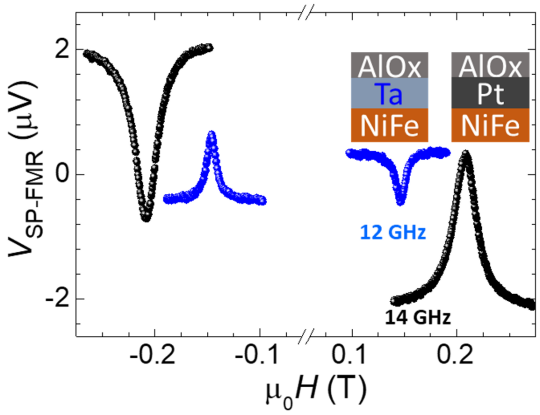

FIGURE 1.56: Raw data examples of spin pumping voltage obtained with Ta and Pt heavy metals where only symmetric curves around the resonance field are obtained. The voltage sign change upon field and sign of the spin Hall angle. Taken from [98].

This ideal vision of the spin pumping effect (ie. perfectly symmetric voltage) is usually more complex and asymmetric response may be obtained. For instance, the data given in **figure 1.56** were obtained on poly-crystalline films. The use of single-crystalline films (as in our case) may lead to asymmetric shapes. Moreover, other symmetric or antisymmetric effects may spoil the response[33] [91, 93, 98]. The first step is thus to fit the detected voltage with the help of **equation 1.19** to split the symmetric and antisymmetric components. After the obtaining of the symmetrical component of the measured voltage (ie. the one related to spin pumping), data

[32] θ_{SHE} can be viewed as the charge current to pure spin current conversion efficiency (ie. the ratio between spin and charge current). Its sign gives the sign of the interconversion.

[33] For instance, the detected voltage can contain contributions due to anisotropic magnetoresistance, planar Hall effect, anomalous Hall effect or spin Seebeck effect in addition to IEE.

treatment to estimate the spin-to-charge interconversion can begin. The process to estimate the spin-to-charge interconversion is described in the following.

As discussed previously, when one performed an SP-FMR measurement on a FM/HM or TI/HM structure a spin current is injected from the FM to the adjacent layer. The magnitude of spin current injected at the interface, j_S^{eff}, can be estimated with the **equation 1.23**[34]:

$$j_S^{eff} = \frac{g_{eff}^{\uparrow\downarrow}\gamma^2\hbar\mu_0^2 h_{rf}^2}{8\pi\alpha_{FM/TI}^2}\left[\frac{\mu_0 M_S\gamma + \sqrt{(\mu_0 M_S\gamma)^2 + 4\omega^2}}{(\mu_0 M_S\gamma)^2 + 4\omega^2}\right]\frac{2e}{\hbar} \tag{1.23}$$

With h_{rf} the *rf* field ($A.m^{-1}$)[35], M_S is the saturation magnetization ($A.m^{-1}$) and ω is the *rf* field pulsation (s^{-1}).

It should be noted that the amount of spin current injected at the interface FM/HM (ie. ISHE) is governed by the same relation than for TIs (ie. IEE). Nonetheless, attention must be paid to the conversion between charge and spin currents by spin-orbit interaction since the involved densities are not the same in ISHE and IEE. The comparison is thus not straightforward. On the one hand, conversion by ISHE involves 3D current densities: j_S injected from the FM and j_C produced in the HM layer. On the other hand, IEE involves two dimensional charge current densities produced in the TI layer owing to its surface nature even if 3D spin current are injected from the FM layer. Given these different origins, the figures of merit are not the same for both effects. The conversion by ISHE is characterized by the so-called spin Hall angle, θ_{SHE}, which is defined as the ratio between the 3D spin current density, j_S^{eff} ($A.m^{-2}$), and the 3D charge current density, j_C^{3D} ($A.m^{-2}$). It can be calculated with the following equation[36]:

$$I_C = \frac{V_{SP-ISHE}}{R} = W.\theta_{SHE}.l_{sf}^{HM}.\tanh\left(\frac{t_{HM}}{2.l_{sf}^{HM}}\right).j_S^{eff} \tag{1.24}$$

With I_C the charge current in A, $V_{SP-ISHE}$ the spin pumping voltage created by ISHE in V, R the resistance in Ω, W the sample's width in m, l_{sf}^{HM} the HM's spin diffusion length in m and t_{HM} the HM's thickness in m.

The figure of merit of the conversion is given by the ISHE length, λ_{ISHE}^*, as follows:

$$\lambda_{ISHE}^* = \theta_{SHE}.l_{sf}^{HM} \tag{1.25}$$

On the other hand, in the case of IEE, the conversion process is characterized by the λ_{IEE} coefficient:

$$\lambda_{IEE} = \frac{j_C^{2D}}{j_S^{eff}} \quad with \quad j_C^{2D} = \frac{V_{SP-IEE}}{W.R} \tag{1.26}$$

[34]Supplementary information and rigorous demonstration can be found in [98, 99, 100].
[35]In our setup, h_{rf} was estimated to be equal to 0.72 Oe for an input *rf* power of 14 dBm and 14 GHz.
[36]Supplementary information and rigorous demonstration can be found in [24].

Here j_S^{eff} is still in A.m^{-2} while j_C^{2D} is in A.m^{-1}.
The spin-to-charge conversion efficiency, with bulk (ISHE) and surface (IEE) origins, can thus be compared thanks to the figures of merit λ^*_{ISHE} and λ_{IEE}.

ii. SP-FMR data treatment

Now that the difference nature between bulk (ISHE) and surface (IEE) spin-to-charge interconversion is clarified, data treatment can be done. Typical SP-FMR data obtained for the control sample[37] made with Pt are given in **figure 1.57**. The left-hand graph shows the voltage peak generated across the sample for different frequencies and for a positive applied magnetic field. The right-hand graph of **figure 1.57** shows the raw data at 14 GHz only for the sake of clarity. As expected, the voltage is mostly symmetric around the resonance field and its sign[38] changes upon the direction of the magnetic field.

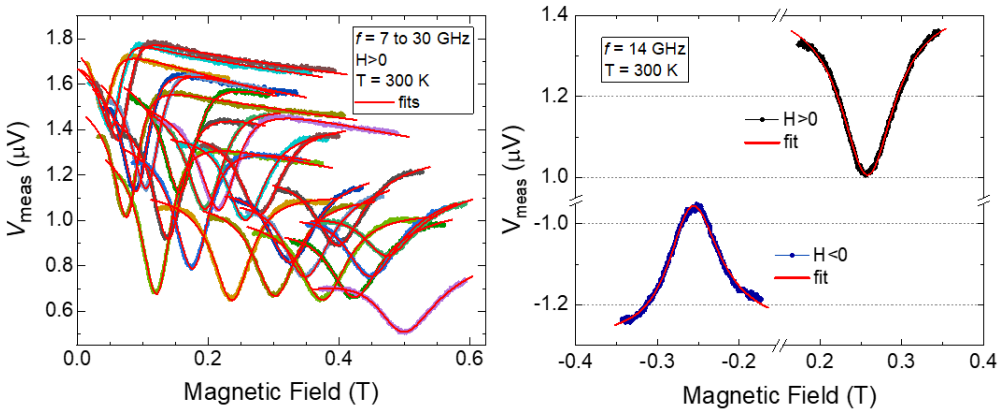

FIGURE 1.57: On the left, raw data of SP-FMR spectra of Pt(6 nm)/MgO(1 ML)/Fe(6 nm) sample measured under frequencies of 7 to 30 GHz with a positive applied magnetic field. The red curves are the fits. On the left, measured voltage signals for positive (in black) and negative (in blue) applied magnetic field (raw data). The red curves are the fits.

First, let's estimate the spin current injected at the interface, j_S^{eff}. Even if the $g_{eff}^{\uparrow\downarrow}$ determined previously for Pt/Fe is high, an estimation of j_S^{eff} can be done with the help of **equation 1.23**. By doing so, j_S^{eff} is determined to be equal to 5.34 .10^5 A.m^{-2} at f = 14 GHz.

Next, the charge current generated, I_C, can be determined. As discussed above, a transverse electric field is created by the ISHE due to the spin-orbit interaction that bends the electrons' trajectory in the Pt layer and results in a voltage detection across the sample. This voltage is fitted with the help of **equation 1.19** to split the V_{sym} and V_{asym} part. V_{sym} should be equal, in the ideal case, to $V_{SP-ISHE}$. Actually, the spin pumping contribution is mixed with the Seebeck effect contribution (both effects manifest in the V_{sym} part). Usually, in order to obtain the real $V_{SP-ISHE}$ and remove any contribution from the thermal Seebeck effect, the trick is to rectify $V_{SP-ISHE}$ as

[37] The reference sample is used to compare the spin pumping signal generated by the well-known Pt with the two TIs studied in this thesis.

[38] It should be noted that the different voltage sign observed for Pt samples given in **figure 1.56** and **figure 1.57** is due to the reverse stack order ($\mathbf{j}_S \rightarrow -\mathbf{j}_S$).

followed: $V_{SP-ISHE} = \frac{V_{sym}^{H>0} - V_{sym}^{H<0}}{2}$. This correction is possible since thermal contributions are independent of the resonance field's sign. The resulting voltage value leads to $I_C = 2.83 .10^{-10}$ A for an input *rf* power of 14 dBm and 14 GHz. By assuming l_{sf}^{Pt} = 3.4 nm [89], we determined $\theta_{SHE} = 0.025$ and $\lambda_{ISHE}^{*} = 0.085$ nm. λ_{ISHE}^{*} is lower than conventional reported values for Pt ($\lambda_{ISHE}^{*} \approx 0.2$ nm) [97]. Different factor could explain this low value. Firstly, the $g_{eff}^{\uparrow\downarrow}$ should take into account the MgO barrier and the interface quality. Nonetheless, $g_{eff}^{\uparrow\downarrow}$ is calculated with a Fe reference sample that hosts different crystalline quality misleading the obtained values. Secondly, l_{sf}^{Pt} was estimated equal to 3.4 nm from literature but the Pt and the interface qualities could be different in our system.

The SP-FMR data for PdYBi (20nm) are given in **figure 1.58**. The frequency dependence with a negative applied magnetic field shows an almost perfectly symmetrical voltage (**figure 1.58a**). This observation is highlighted by the symmetric and antisymmetric components of the fitting function given in **figure 1.58b**.

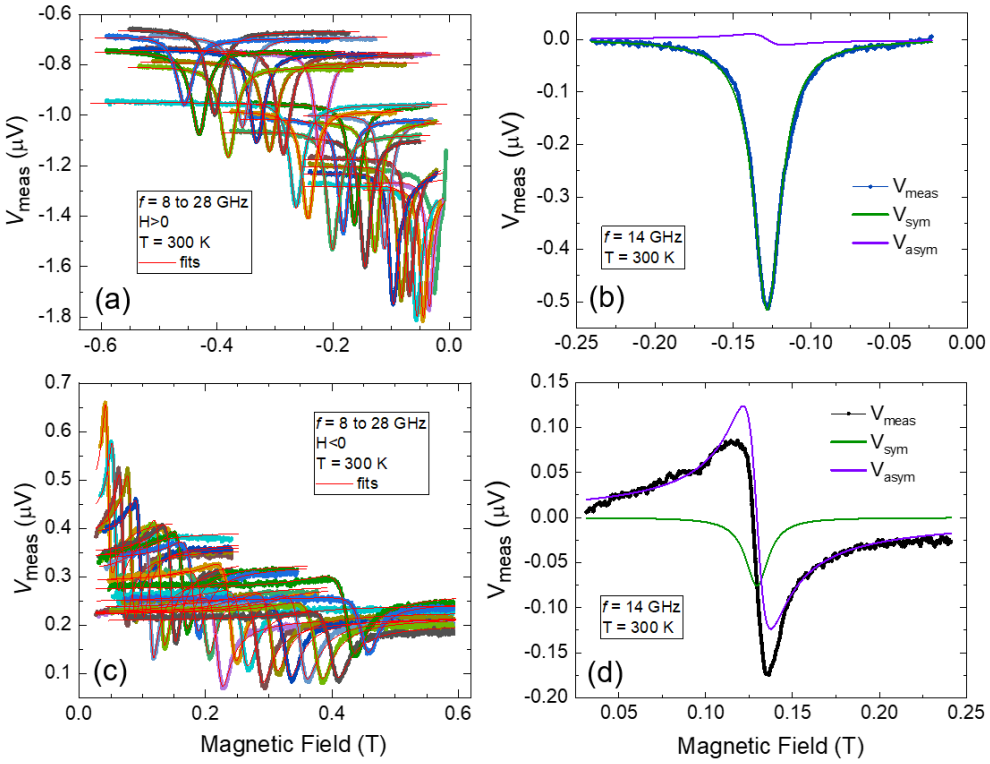

FIGURE 1.58: (a) and (c) are the SP-FMR spectra (raw data) of PdYBi(20nm)/MgO(1ML)/Fe(6nm) sample measured under frequencies of 8 to 28 GHz with respectively a negative and positive applied magnetic field. The red curves are the fits. (b) is the measured voltage signal for a negative magnetic field (V_{meas} in blue) alongside with the symmetrical (V_{sym} in green) and antisymmetric (V_{asym} in purple) components of the fitting function. (d) is the measured voltage signal for a positive magnetic field (V_{meas} in black) alongside with the symmetrical (V_{sym} in green) and antisymmetric (V_{asym} in purple) components of the fitting function.

Surprisingly, the sign of the signal does not change when the magnetic field is reversed as might be suggested by the spin pumping theory (no inversion between the detected voltages of **figure 1.58a** and **figure 1.58c**) and a strong antisymmetric

voltage is measured for positive values of the magnetic field. Moreover, the sign of the symmetric contribution is not reversed as highlighted in **figure 1.58d**. Several SP-FMR measurements were conducted on two different samples (namely PdYBi 20 nm and PdYBi 30 nm) and along different crystallographic directions (ie. voltage measured along $\overline{\Gamma K}$ and $\overline{\Gamma M}$) with similar weird results. The signal is mostly symmetric for one magnetic field sign (**figure 1.58a**) and antisymmetric for the opposite sign (**figure 1.58c**). More surprisingly, the symmetric part of the fit does not change sign between H < 0 (**figure 1.58b**) and H > 0 (**figure 1.58d**). The non-reversing voltage may be due to a strong thermal component that enhances the detected voltage for one field direction and counterbalances it for the opposite field.

Nonetheless, j_C^{2D} can be estimated (**equation 1.26**) after the thermal voltage rectification (ie. $V_{SP-IEE} = \frac{V_{sym}^{H>0} - V_{sym}^{H<0}}{2}$). By doing so, $j_C^{2D} = 7.27\ .10^{-6}$ A.m^{-1} is obtained for an input *rf* power of 14 dBm and 14 GHz. However, the lower $\alpha_{FM/TI}^{PdYBi}$ compared to α_{FM} put a stop to the determination of $g_{eff}^{\uparrow\downarrow}$ and j_S^{eff} since they rely on $\Delta\alpha = \alpha_{FM/TI}^{PdYBi} - \alpha_{FM}$. λ_{IEE} was thus not calculated.

A similar trend has been observed for PtYBi samples whose data are given in **figure 1.59**. The generated voltage for H > 0 depicts a nice symmetrical voltage for

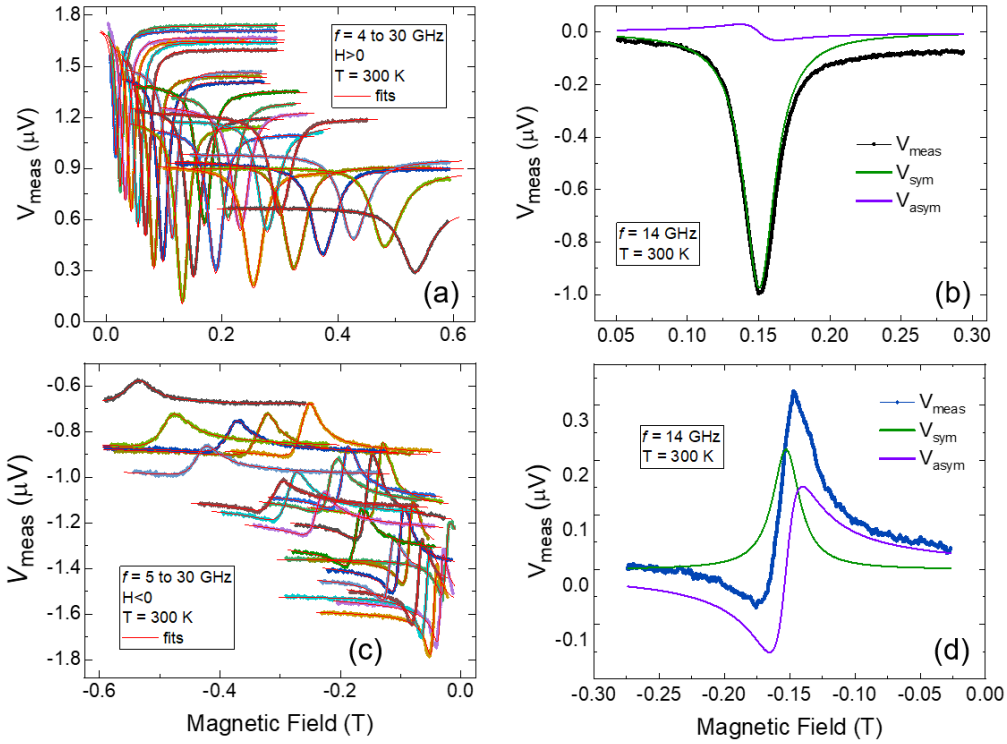

FIGURE 1.59: (a) SP-FMR spectra (raw data) on PtYBi(5nm)/MgO(2ML)/Fe(6nm) sample measured under frequencies of 4 to 30 GHz with a positive applied magnetic field. The red curves are the fits. (b) Measured voltage signal for a positive applied magnetic field (V_{meas} in black) alongside with the symmetrical (V_{sym} in green) and antisymmetric (V_{asym} in purple) components of the fitting function. (c) Resonance frequency as a function of the resonant field H_{res}. The red curve is a fit to the Kittel formula. (d) Signal linewidth as a function of the resonance frequency. The red curve is a linear fit where ΔH_0 was fixed to 0 otherwise negative ΔH_0 values are obtained.

each frequency (**figure 1.59a**). One of the fit is given in **figure 1.59b** and points out an almost perfectly symmetric response. In the same way than for PdYBi, the measured voltage for H < 0 depicts an asymmetric shape (**figure 1.59c** and **1.59d**). On this device, the symmetrical component is reversed for opposite field sign but its magnitude is lowered.

Similarly to PdYBi, j_C^{2D} = 1.05 .10^{-5} A.m^{-1} was determined after thermal rectification for an input *rf* power of 14 dBm and 14 GHz. Again we have the problem of the proper estimation of $g_{eff}^{\uparrow\downarrow}$ putting a stop to the calculation of j_S^{eff} and thus of λ_{IEE}.

Discussion: advantages and disadvantages of MgO barrier for coherent spin injection

The SP-FMR measurements performed on PdYBi and PtYBi are puzzling. The nice symmetrical response obtained for one direction of the magnetic field seems to point out a good spin-to-charge conversion. **Figure 1.60**, where the V_{meas} response for the control sample and the two TIs are plotted, confirms this tendency. Nonetheless, the persistent complex shape observed for the opposite field direction requires to be careful. Similar observations were done recently in literature [93] and attribute the absence of clear sign inversion between $V_{sym}^{H>0}$ and $V_{sym}^{H<0}$ to the lack of spin-to-charge conversion. They studied Sb_2Te_3 system in direct contact with a ferromagnetic layer and attributed the shape of the resonances and the non-reversing signal to a loss of TSS due to the direct contact between the FM and the TI. Moreover, the use of an insulating barrier between the FM and the TI remains an open issue since some works have shown that the insulating barrier may suppress the spin pumping signal [91].

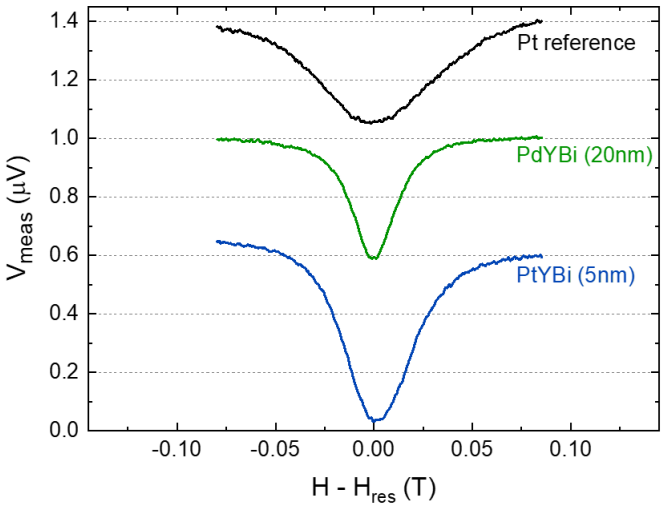

FIGURE 1.60: Raw data signals of the transverse voltage generated in the Pt control, PdYBi TI and PtYBi TI samples respectively in black, green and blue colors. Data were stacked and vertically shifted to compare them. Measurements performed with an *rf* power of 14 dBm and 14 GHz.

Clear conclusions cannot be drawn without further experiments to fully settle these questions. Additional samples must be grown in order to replace the insulating spacer by a metallic one such as Au, Ag or Al. Numerous works [42, 91, 94, 101]

using those metallic spacers revealed a nice spin-to-charge efficiency on FM/TI systems. Nonetheless, a comparison between the generated voltage and the resulting current is given in **table 1.2**.

sample	thickness	R (kΩ)	V_{SP} (μV)	I_C (A)	j_C^{2D} (A.m^{-1})
Pt/MgO/Fe	5nm/1ML/6nm	1.779	0.504	2.83 .10^{-10}	1.30 .10^{-6}
PdYBi/MgO/Fe	20nm/1ML/6nm	3.020	0.220	/	7.27 .10^{-6}
PtYBi/MgO/Fe	5nm/2ML/6nm	5.668	0.596	/	1.05 .10^{-5}

TABLE 1.2: Summary of the extracted resistances, V_{SP}, I_C and j_C^{2D} for all three systems with an *rf* power of 14 dBm and 14 GHz.

Since the λ_{IEE} figure of merit was not estimated for both TIs, the comparison with the Pt control sample is puzzling. The j_C^{2D} given in **table 1.2** for both TIs considers a perfect 2D case where all the transport comes from the interface meanwhile, in our Pt sample, the transport has a 3D origin. In order to compare the samples, we estimated a j_C^{2D} value for Pt by estimating the density of current per atomic plane. The j_C^{2D} value for the Pt sample, given in **table 1.2**, is thus determined by dividing the measured current I_C by the number of Pt atomic planes in our sample (ie. the number of planes for 5 nm of Pt) and by the width, W. By doing so, j_C^{2D} = 1.3 .10^{-6} A.m^{-1} is obtained. Obviously, this is a rough approximation since we assume that each atomic plane of Pt has an equal contribution. Nonetheless, the extracted surface density of current is much higher in our TIs than in the Pt sample.

The lack of a proper reference to subtract is problematic and puts a stop to the estimation of $g_{eff}^{\uparrow\downarrow}$ and λ_{IEE}. For instance, the $\Delta\alpha$ estimated for the Pt control sample is wrong since it does not only characterize the enhancement by spin pumping effect ($\Delta\alpha = \alpha_{SP} + \alpha_{inhomogeneities}$). The results obtained in this section allow to draw the following conclusions:

- As explained previously, a proper reference was not subtracted to only characterize the FM/TI interface. The main problem here is that the ferromagnetic layer quality is different when grown on PdYBi (or PtYBi) compared to a growth on Pt (see Fe RHEED images in **appendix B**). The Fe damping reference is thus expected to be different for the Pt control and TIs samples. The different Fe layer qualities can be solved in two different ways. Firstly, a reversed stack order should allow to obtain the same Fe crystalline quality in each system. Nonetheless, the sapphire substrate is mandatory to stabilize the epitaxial half-Heusler TIs growth. In view of the difficulties experienced in the half-Heusler TIs growth, this solution is not retained. The second possibility is to use another FM layer that would have the same crystalline quality in each stack.

- Recently, a spin pumping voltage was measured in a CoFeB/MgO structure [102]. They showed that a Rashba split state at the CoFeB/MgO interface was able to convert the spin current generated by SP-FMR into a charge current with an efficiency similar to their control CoFeB/Pt sample. In light of this, a supplementary IEE due to Rashba split states could come from our MgO/Fe interface and affect the detected voltage. Moreover, an opposite sign of this contribution would counterbalance the voltage created at the TI interface.

- The use of a MgO barrier layer to protect the TSS from the FM layer is disturbing. Results published in literature [91] for Bi_2Se_3 TI demonstrated that the insertion of an MgO interlayer (2 nm) between the TI and the FM suppresses the spin-to-charge voltage. In the same way, a partial suppression on the spin-to-charge conversion may decrease the spin pumping voltage detected in our case. Moreover, the MgO barrier deposited (1 or 2 monolayers thick) on PdYBi and PtYBi may not fully cover the surface and thus not protect efficiently the TI from the FM.

- As discussed previously, the question of the half-Heusler TIs potential will be settled by a last set of samples using a metallic spacer such as Au, Ag or Al. For instance, DC *et al.* [91] studied different sample stacks where the TI was unprotected, protected by a MgO interlayer and protected by an Ag interlayer from the FM. They concluded that the highest spin-to-charge efficiency was obtained with the Ag interlayer whereas the MgO layer tends to suppress the generated voltage. The situation was in between with no barrier layer. Other works of literature checked the spin-to-charge enhancement using a metallic spacer and validated its use [42, 91, 94, 101].

- Finally, the lithography process can severely damage the MgO layers. This especially happens with the use of water which was not avoided in the microfabrication of the different devices. To avoid this uncertainty, next lithography processes have to be performed without using water.

Spin Seebeck effect

The spin Seebeck effect (SSE) refers to the generation of a spin current, j_S, in magnetic materials as a result of a temperature gradient, ∇T. The SSE is due to thermally excited magnons that generate a magnon spin current in the FM due to the gradient of temperature. Here, the longitudinal spin Seebeck effect (LSSE) is carried out [103]. In LSSE experiment, the charge current thermally generated is parallel to the temperature gradient, $j_S \parallel \nabla T$. When a HM (or a TI) layer is in direct contact with a FM layer under a temperature gradient, the generated spin current is then transformed into an electric voltage due to spin-orbit considerations. In the same way than for

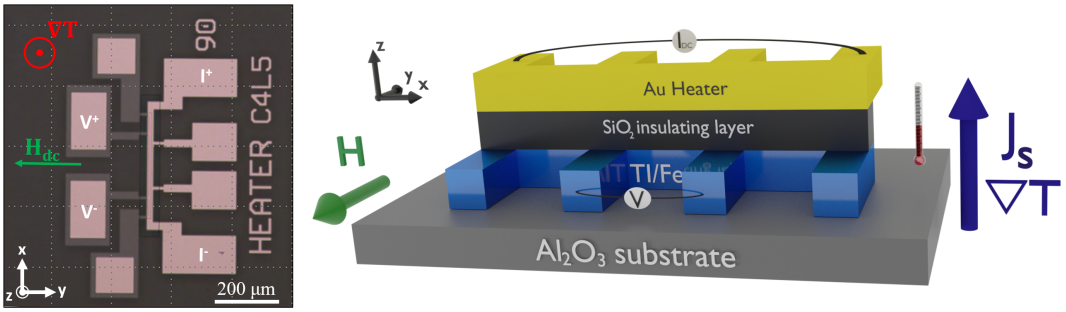

FIGURE 1.61: On the left, spin Seebeck device image. On the right, sketch of the spin Seebeck device. A temperature gradient is applied along the z direction thanks to the current injected in the Au heater and generates a spin current j_S (along the z direction) which is in turns injected at the FM/TI interface. The thermally created spin current is converted by IEE (or ISHE for HM) in a longitudinal charge current (along the x direction) which is measured by a nano-voltmeter.

SP-FMR, the transverse spin current (thermally generated now) is converted into a longitudinal charge current by ISHE in the HM or IEE in the TI. A sketch of the LSSE principle is given in **figure 1.61**. It can be summarized by the relation: $\mathbf{E}_{ISHE} \propto \mathbf{j}_C \propto \mathbf{j}_S \times \sigma$ with $\mathbf{j}_C$ the charge current created by ISHE (or IEE for TI) and detected along the x direction. $\mathbf{j}_S$ is the spatial direction of the thermally induced spin current which is perpendicular to the interface and parallel to ∇T (along the z direction). σ is the spin polarization and is parallel to the magnetization **M** (along the y direction).

In IJL's LSSE set-up, an electromagnet is used to apply an external magnetic field large enough to saturate the FM layer. A dc current is passed through the heater to generate a temperature gradient and the temperature stabilization is waited for five minutes. From here, I-V curves are performed in order to get samples and heater resistances. The thermospin voltage (ie. the raw voltage collected) is then collected by a nano-voltmeter while sweeping the magnetic field in the sample plane. LSSE measurements were conducted on PdYBi, PtYBi, Pt control and Fe reference samples[39]. Typical data obtained for a PdYBi sample are displayed in **figure 1.62**. The left graph gives the tension detected across the sample as a function of the applied magnetic field and of the injected current. Obviously, the detected $V_{thermospin}$ increases with the applied current. The amplitude of $V_{thermospin}$ can be extracted as followed $\Delta V_{thermospin} = \frac{V^{H>0}_{thermospin} - V^{H<0}_{thermospin}}{2}$ to remove any unwanted offset. The amplitude is directly related to the SSE but care must be taken since the ferromagnetic material adds a contribution coming from the Anomalous Nernst Effect (ANE)[40]. The ANE is generated according to the following relation: $\mathbf{E}_{ANE} \propto \nabla T \times \mathbf{M}$ where ∇T is along the z direction and **M** is along the applied magnetic field (along the y direction). Therefore, the ANE is proportional to the FM's magnetization and adds a supplementary detected voltage ($\mathbf{E}_{ANE}$ along the x direction) that must be corrected to obtain the real V_{SSE}.

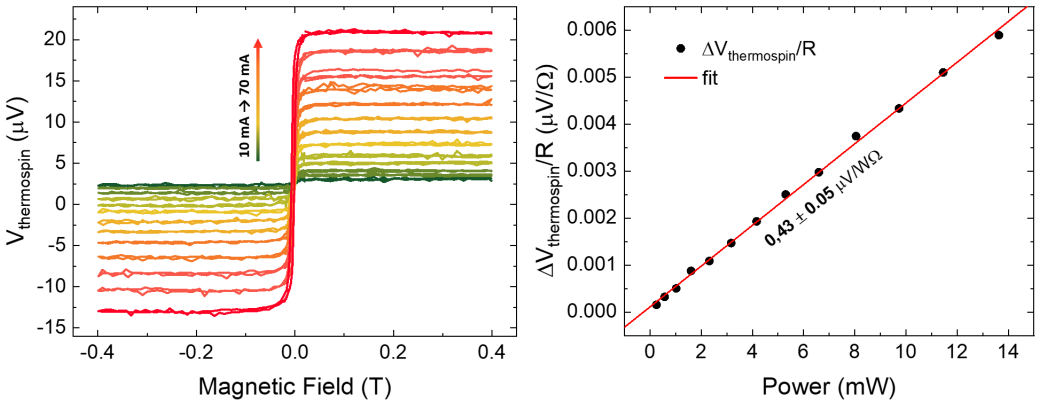

FIGURE 1.62: On the left, raw data of the $V_{thermospin}$ detected as a function of magnetic field for different heater powers. On the right, $\Delta V_{thermospin}$ as a function of the heater power. Data obtained on Al_2O_3/PdYBi(20nm)/MgO(1ML)/Fe(6nm)/MgO(20nm) sample.

The $V_{thermospin}$ detected in **figure 1.62** contains thus a mix between SSE and ANE due to the measurement's geometry. In order to solely extract the voltage generated by the SSE, a rectification must be done thanks to supplementary measurements

[39] The spin Seebeck measurements were done by Alberto Anadon Barcelona.

[40] These two effects are the two main contributions to the detected $V_{thermospin}$ since the planar Nernst effect does not contribute to the voltage in this measurement's geometry [103].

conducted on a single Fe reference sample. The absence of strong SOC material in direct contact with the FM (in the reference sample) allows to probe only the ANE contribution and to perform the ANE correction of Fe on TIs and Pt control samples afterward[41]. Indeed, by considering shunting in parallel resistance mode, Ramos *et al* [104] demonstrated that the ANE correction can be estimated according to the following equation:

$$\Delta V_{ANE}^{TI/Fe} = \frac{r}{1+r} \cdot \Delta V_{ANE}^{Fe} \quad with \quad r = \frac{\rho_{TI}.t_{FM}}{\rho_{FM}.t_{TI}} \tag{1.27}$$

Where ΔV_{ANE}^{Fe} is the voltage amplitude detected across the sample for the Fe reference sample, ρ_{FM} and t_{FM} are the resistivity and thickness of the FM layer and ρ_{TI} and t_{TI} are the resistivity and thickness of the TI (or HM) layer. ρ_i is in Ω.m and t_i in m.

The $\Delta V_{thermospin}$ detected can thus be corrected by $\Delta V_{ANE}^{TI/Fe}$ to get the overall spin-to-charge current contribution, V_{SSE}. In this case, in order to ensure a good correction, the rectification is not performed directly on the voltage but on a normalized parameter given by $\frac{\Delta V_{thermospin}}{R_{sample} \times P}$ where R_{sample} is the sample resistance and P the power injected in the heater. **Figure 1.63** gives the determined $\frac{\Delta V}{R_{sample} \times P}$ in the different samples prior and after the ANE correction. On the one hand, the ANE correction is similar in all TIs samples owing to their large resistances. On the other hand, the correction is different for the Pt control due to its lower resistance and therefore the

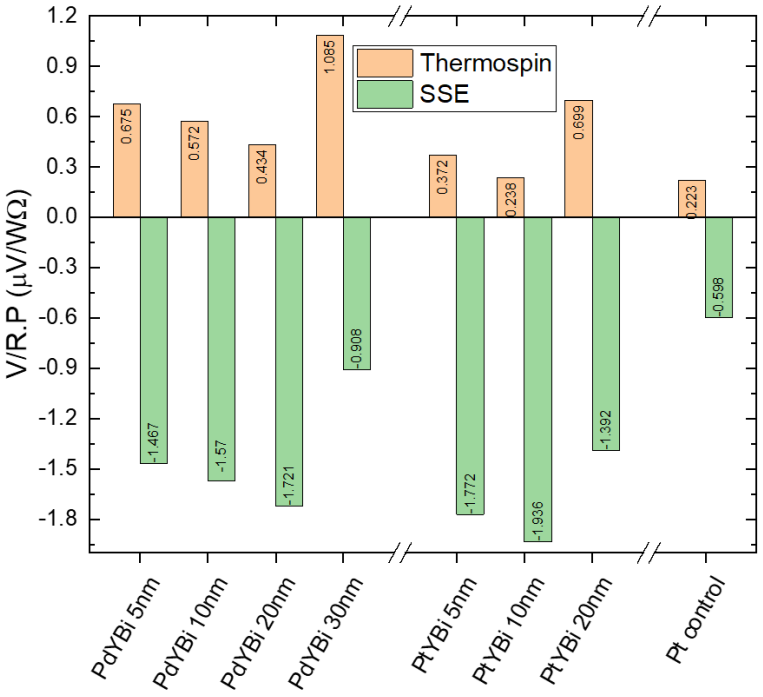

FIGURE 1.63: Summary of the voltage normalized by the product between the power injected in the heater and the sample resistance for all TIs thicknesses and Pt control sample. Orange columns are the raw voltages detected without ANE correction. The green columns are the SSE voltages (ie. thermospin voltage after ANE correction).

[41] Obviously, the voltage rectification by a Fe reference sample can be conducted only if the FM thickness remains the same in all the samples.

shunting effect of the Pt layer. Moreover, it has been shown that low Fe thickness has a negative ANE coefficient [105]. This yields to an opposite voltage than for SSE in our setup. The thermospin voltage detected, in orange bars in **figure 1.63**, is thus dominated by the ANE. Its correction, to obtain the SSE contribution in green bars, leads thus to negative voltages in ours systems. Moreover, the identical sign of V_{SSE} obtained for all samples confirms that both TIs have the same sign for spin-to-charge conversion than Pt[42].

The data given in **figure 1.63** depict a better SSE generated voltage in the TIs compared to the Pt control sample for each thickness where an overall gain two or three times higher seems to be obtained. The disparity observed in the $\frac{V_{SSE}}{R_{sample} \times P}$ values for TIs is attributed to the inhomogeneous quality of the devices from one sample to another. Moreover, ideally for TIs, the voltage should keep the same value for each thickness if the spin-to-charge conversion was purely due to TSS. Nonetheless, bulk states crossing the Fermi level were observed in ARPES measurements and contribute to the transport in our case. Finally, as in SP-FMR measurements, the MgO interlayer most likely impacts the conversion process. We suspect the spin current to be partially suppressed in the MgO barrier due to its non-magnetic and insulating nature and thus decreases the effective spin-to-charge conversion. Moreover, in the same way than for SP-FMR experiments, Rashba split states may arise at the MgO interfaces and also induce spin-to-charge conversion that could affect the measured voltages.

1.4 Conclusions

The first part of this chapter was dedicated to the structural characterization of PdYBi and PtYBi half-Heusler compounds. The growth in the $C1_b$ half-Heusler structure (in which they are predicted to potentially host a non-trivial topological state) has been mastered. Even if both compounds are very similar and crystallize along the (111) direction some differences must be noted:

- The surface quality is higher in PdYBi with a lower roughness compared to PtYBi. These observations are confirmed by RHEED and LEED studies.
- STEM study revealed that atomic disorder occurs in PdYBi meanwhile PtYBi presents a good chemical ordering. Domains were clearly imaged for PtYBi while PdYBi has a single domain structure.
- Both compounds may present different surface reconstructions that are attributed to the Bi's quantity on the surface. For PdYBi, an annealing process under a Bi flux allows to control the quantity of Bi at the surface and to obtain a reproducible 2×2 surface reconstruction. For PtYBi, the Bi addition is not possible due to the higher deposition and annealing temperatures. Therefore, two different reconstructions may be obtained, namely a 2×2 or a $\sqrt{3}\times\sqrt{3}$ R30°.
- Finally, ARPES measurements turned out to be well more defined in PtYBi compared to PdYBi. This is attributed to the chemical disorder lying in PdYBi that strongly affects the spectral weight in photoemission process. The data obtained for PtYBi are similar to literature reports and the crossing point observed below the Fermi energy is predicted to be a Dirac point. For PdYBi,

[42] It should be noted that this observation is in agreement with the SP-FMR experiments.

the lack of photoemission reports does not allow to compare our results with literature. The low spectral weight made the analysis tricky but bands with linear dispersion were observed crossing the Fermi level. Furthermore, similarly to PtYBi, a crossing point below the Fermi level is present and could be the signature of the non-trivial topology.

PdYBi and PtYBi have been grown in the desired structure and photoemission unveils the presence of states with linear dispersion. Nonetheless, the question of their topological nature cannot be fully settled and transport measurements were conducted to bring further information on their potential non-trivial nature.

- SP-FMR measurements were conducted on PdYBi and PtYBi. Unfortunately, a full data analysis was not possible due to the different Fe layer qualities present in the TIs and the reference samples. Nonetheless, the analysis performed on a Pt control sample revealed that the MgO interlayer probably strongly impacts the spin-to-charge conversion.
- In the same way than for SP-FMR, spin Seebeck measurements were carried out on TIs and Pt control samples. The generated SSE voltage is two to three times higher in both TIs compared to the Pt control sample. This gain is an overall gain since some dispersions are observed between the different thicknesses of the TIs. This discrepancy is attributed to the quality of the lithography patterning and to the additional bulk states present at the Fermi energy that add supplementary contributions to transport. However, despite having a good TI but not optimally integrated with the FM layer, we clearly see that the TIs we have developed show a spin-to-charge current conversion advantage over the Pt. This advantage goes up to a factor of 3.6. In an optimized system, this gain should be higher.
- Both experiments show clearly, beyond the limitations by the samples' quality, that the sign of spin-to-charge current conversion in the two TIs is the same as for Pt.

Chapter 2

Perpendicular magnetic anisotropy in Heusler thin films

This section is dedicated to the study of PMA in Heusler thin-films. As explained in the introduction and with regards to **equation 1.2** and **4**, STT and SOT switching still needs emerging materials to implement them in everyday life. This part is based on previous works done in the team [10, 11] on Co_2MnZ'[1] compounds that show ultra-low magnetic damping constant and very high spin polarization which fit perfectly to STT and SOT applications. A short introduction is thus first dedicated to these compounds. However, these previous works were done on rather thick films, for which, the in-plane magnetization was not the best magnetic configuration for applications such as STT. Here, we explore possible PMA in such films by using a second Heusler alloy coming from the Mn_3Z family. Indeed, some Mn_3Z compounds can be grown in a tetragonal structure and thus host a strong magnetocrystalline anisotropy thanks to an elongated unit cell along one axis. A literature review of Mn_3Z compounds is done in the next pages. Finally, some works have been done on Mn_3Z/Co_2MnZ' bilayers and superlattices (SLs) and will be discussed in the last part of this state of art.

2.1 Literature review on Mn_3Z and Co_2MnZ' compounds

2.1.1 Co_2MnZ' compounds

Co_2MnZ' compounds have been widely studied in literature owing to their theoretically predicted and proved experimentally high Curie temperature [106, 107], high spin polarization [33, 34, 108, 109, 110, 111, 112, 113], low magnetic damping [33, 34, 112, 113, 114, 115, 116] and control over disorder [106, 113, 114, 116] or interface [117].

Co_2MnZ' compounds crystallize in the full-Heusler structure (space group n°216, F-43m, $L2_1$) with a X_2YZ formula unit leading to a 2:1:1 stoichiometry. In opposite to half-Heusler structure, all the crystallographic sites are occupied and the compounds are centrosymmetric. Usually, X and Y are transition metals and Z is a main group element. The structure is represented in **figure 2.1** and can be viewed as four interpenetrating fcc sublattices composed of one element each. For instance, here α and β sites are occupied by Co atoms, γ sites by Mn atoms and δ sites by Z' atoms.

[1] Z' is used instead of Z just to differentiate the atoms present in Mn_3Z and Co_2MnZ' compounds.

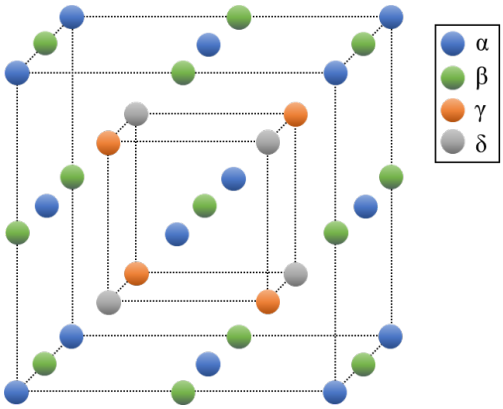

FIGURE 2.1: Sketch of the full-Heusler (X_2YZ formula unit) structure unit cell. In the ordered full-Heusler structure X goes in α and β sites, Y in γ site and Z in δ site.

Spin current polarization and Gilbert damping

Spin polarization reflects the alignment of spins with respect to a given direction. In ferromagnetic materials, the conduction electrons can be polarized and give rise to spin-polarized currents. Some Co_2MnZ' compounds were predicted as hosting 100% spin polarization due to Half-Metal Magnetism (HMM) behavior. HMM in Heusler compounds was predicted in 1983 by de Groot *et al.* [9] in NiMnSb. This property comes from an asymmetry of the density of state at the Fermi energy as shown in the sketch of **figure 2.2**. Depending on the spin orientation, a metallic or an insulating behavior can be observed. In HMM, a gap is present for the minority spin band at E_F. Therefore, theoretically, if a non-polarized current goes through a half-metal, it is then fully spin polarized.

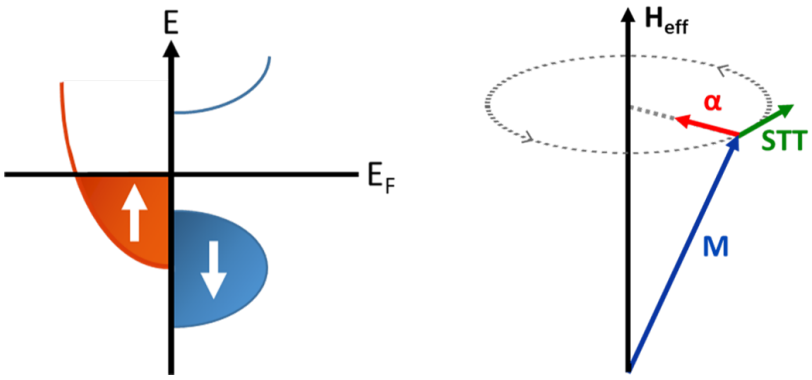

FIGURE 2.2: On the left, sketch of the density of states of a half-metal magnet unveiling the gap for one spin channel at the Fermi energy. On the right, sketch of the different terms of the Landau-Lifshitz-Gilbert equation. The magnetization dynamic of **M** in blue is governed by the precession term in green and the damping term in red.

HMM has notable consequences on the Gilbert damping constant α that impact the spin dynamic. The Gilbert damping comes from the Landau-Lifshitz-Gilbert equation that described the rotational motion of magnetization. The Gilbert term characterizes the attenuation speed of the moment precession. Indeed, when a spin rotates, a damping is applied to it and tries to bring it back in its equilibrium position as shown in **figure 2.2**. The bigger α is, the faster the precession motion is damped. If α is low, it allows a long precession enabling an easier overcome of the

barrier to switch the magnetization. Gilbert damping arises from relaxation mechanisms that are strongly reduced with HMM materials. Indeed, since only one spin channel is present due to the insulating behavior of the minority spin band at the Fermi level, it is therefore not easy for conduction electrons to dissipate energy by spin flipping because no electronic states are available. Spin-flip mechanism is then strongly reduced leading to low α constants.

Co_2MnZ' (Z' = Ge, Si) state of art

The first electronic band structure calculations unveiling the HMM behavior of Co_2MnSi and Co_2MnGe was performed in 1995 by Ishida *et al.* [108] showing a spin gap in the minority spin band. Later, theoretical works [109, 111] showed similar results and predicted spin gaps close to 0.8 eV and 0.6 eV for respectively Co_2MnSi and Co_2MnGe. Experimental evidences of this character have been obtained for both compounds [33, 34, 112]. With the help of spin-resolved photoemission spectroscopy, direct evidence of Fermi levels lying in half-metallic gaps were obtained for Co_2MnSi and Co_2MnGe. Ultra-low Gilbert damping linked to the half-metallic behavior was also checked with record values of $\alpha_{Co_2MnSi} = 4.6\ 10^{-4}$ and $\alpha_{Co_2MnGe} = 5.3\ 10^{-4}$ obtained by Guillemard *et al.* in 2019 [34]. The Gilbert damping measured for Co_2MnSi is still nowadays the lowest α value measured in a conductive thin film. Moreover, Co_2MnSi and Co_2MnGe have also a very high Curie temperature which is very desired for implementations in devices. Webster *et al.* [106] determined a T_C of respectively 985 K and 905 K for Co_2MnSi and Co_2MnGe. Both compounds follow the Slater-Pauling rule that allows to estimate the magnetic moment of the 3d elements and their binary alloys by considering band filling with a resulting moment of 5 μ_B/f.u. A more exhaustive literature review on Co_2MnGe and Co_2MnSi alloys can be found on the previous PhD thesis done in the team [10, 11].

2.1.2 Mn_3Z compounds

How to obtain PMA in thin films?

Nowadays, information storage is achieved by harnessing the magnetization orientation of small magnetic domains, the so-called bits. The binary storage imposes a design allowing two stable and distinct states at the material's magnetic remanence. This is provided by uniaxial magnetic anisotropy and its two states with opposite magnetization orientation. One of the main challenging parts of data storage is due to the surge in data quantities that computing has endured since the last decades. To increase data storage capacities, bits densities must enlarge and the grain sizes[2] have to be reduced. This size reduction generates concerns on the grain's magnetization stability and therefore the information storage. To switch from one state to the other, the magnetization has to overcome an energy barrier ΔE that can be expressed as:

$$\Delta E = K_u.V \tag{2.1}$$

With K_u the anisotropy energy and V the grain size's volume. As shown by **equation 2.1** a decrease in grain size leads to a lower volume. Therefore, materials with higher K_u are needed to compensate the lost grain size's volume and to stabilize the information stored. The two stable states must have a sufficient magnetic energy

[2]Nowadays grain sizes is of the order of 7 nm with densities in storage media close to 1 Tbit/in^2.

difference to avoid any unwanted switching by thermal fluctuation[3]. According to Dieny *et al.* [118] to get a ten years stable information, one should have $\Delta E = K_u.V > 45\ k_BT$. Over the last years, this challenge was achieved by minimizing the impact of shape anisotropy of thin films by replacing in-plane by out-of-plane magnetization.

Out-of-plane anisotropy is then a prerequisite for future data storage. Nonetheless, due to thin films geometry, the equilibrium magnetization's position remains most of the time in the sample's plane where the energy cost is smaller due to the demagnetizing field. Fortunately, this shape anisotropy can be counterbalanced by other magnetic anisotropy terms that arise from bulk or interfacial contributions. The effective anisotropy of a thin layer with two interfaces can be expressed as:

$$K_{eff} = K_V + \frac{K_S}{t} - \frac{1}{2}\mu_0 {M_S}^2 \tag{2.2}$$

This equation is the sum of three main energy terms:

- The last term is the demagnetizing energy also known as shape anisotropy (valid here for a thin film). This term tends to align the magnetization within the plane of the thin films due to sample geometry that imposes this easy-plane anisotropy.
- The surface anisotropy K_S induced by surfaces. It includes contributions from both interfaces. K_S is expressed in $J.m^{-2}$.
- The magneto-crystalline anisotropy K_V which represents the volume contribution. K_V is expressed in $J.m^{-3}$.

Both K_V and K_S have spin-orbit interaction origins. Spin-orbit interaction links the magnetization with the crystallographic lattice resulting in warp electrons' orbitals. If the orbitals are strongly deformed in one direction, it can give rise to PMA. Two possibilities[4] can be identified thanks to **equation 2.2**. On the one hand, if $K_{eff} < 0$, in-plane anisotropy wins since the dominant term is the shape anisotropy. On the other hand, out-of-plane anisotropy can be obtained if $K_{eff} > 0$, thanks to bulk and/or interfacial anisotropy contributions.

Two different origins of PMA can be labeled with regard to **equation 2.2**. The interfacial PMA, coming from the K_S term of **equation 2.2**, is due to the breaking periodicity at the interface. This discontinuity generates orbitals' deformation. In the past decades, physicists have made notable improvement on interface induced PMA such as the well-known CoFeB/MgO [119], Co-based multilayers [120] or even predicted in some Heusler alloys SLs [121]. Nonetheless, interfacial PMA has several disadvantages. Since its origin arises from interfaces, roughness is critical and can strongly reduce or even kill any PMA effect. Film thickness is also of prime importance. Indeed, interface effects have to overcome bulk effects that tend to impose an in-plane anisotropy and thin layers are needed to reduce the bulk contribution. The growth of smooth and continuous surfaces is then harder. Finally, another reported drawback is the increase of Gilbert damping constant while decreasing the thickness. As explained before, an increase in damping generates the need of a higher

[3] K_u has been increased so much to ensure stability that the field produced by conventional HDD's write-heads is now insufficient to overcome the energy barrier ΔE.

[4] In reality, a third possibility with $K_{eff} = 0$ can happen with no anisotropy in this case.

switching current to reverse the magnetization of grains. In order to overcome these difficulties, new materials have to be engineered.

The second way to counterbalance the demagnetizing energy is to play with bulk magnetic anisotropy contributions (K_V term of **equation 2.2**). This time the orbitals deformation is due to the asymmetry of the crystal lattice that minimizes the magnetic energy in a peculiar direction. High thermal stability is more easily obtained compared to interfacial PMA. It turns out that, some Heusler alloys host strong bulk anisotropy coupled with low Gilbert damping constant. This bulk induced anisotropy phenomena is used in this thesis to make the out-of-plane direction as an easy axis of magnetization.

The weak magneto-crystalline energies of Co_2MnSi and Co_2MnGe lead to a domination of the demagnetizing field. As a result, the magnetization remains in the sample plane since the minimization of dipolar energy chooses this preferential direction of magnetization. Therefore, materials with high magnetocrystalline anisotropy K_V are desirable and growing interest has been recently observed for tetragonal Mn-based Heusler alloys that are predicted to host very strong K_V. They are the compounds of interest in this part and an overview of the literature is done below.

Mn_3Z state of art

While the big majority of Heusler alloys are cubic leading to zero PMA, some of them can crystallize in distorted structures that may host strong PMA. Such distortion are predicted to potentially host huge K_V, especially in Mn-based Heusler alloys (Mn_3Z family). Different structures for Mn_3Z alloys have been identified in literature with the most popular ones being the cubic $D0_3$ structure, the hexagonal $D0_{19}$ structure and the tetragonal $D0_{22}$ structure. Two of them are represented in **figure 2.3**. As one can see, full-Heusler compounds contain two different magnetic sublattices coming from the different chemical environment felt by atoms in both sublattices. This can lead to peculiar spin arrangement as for instance ferromagnetism, antiferromagnetism or ferrimagnetism.

The $D0_3$ structure is a classical cubic structure. Usually, $D0_3$ phase is observed when disorder between X and Y atoms occurs in Heusler unit cell. Here, since X and Y atoms are Mn atoms, $D0_3$ structure corresponds to an ordered structure and this nomenclature is only due to the presence of Mn in three different crystallographic sites. The studies performed on $D0_3$ Mn_3Z compounds aim to get half-metal compensated ferrimagnets. The $D0_3$ structure is predicted to possibly generate a moment compensation of Mn atoms on their different crystallographic sites. In 2006, Wurmehl *et al.* [122] predicted a half-metallic compensated ferrimagnetic behavior in $D0_3$ Mn_3Ga. In addition to a half-metallicity, such compounds do not have any stray field and the impact of an external magnetic field is minimized making them very promising for future applications. Unfortunately, no property of magneto-crystalline anisotropy has been determined on this structure yet and it turned out that $D0_3$ Mn_3Ga phase is not stable. The hexagonal $D0_{19}$ ($P6_3/mmm$, space group n°194) structure has also been investigated by physicists for its non collinear antiferromagnetic phase with a triangular spin configuration. This antiferromagnetic

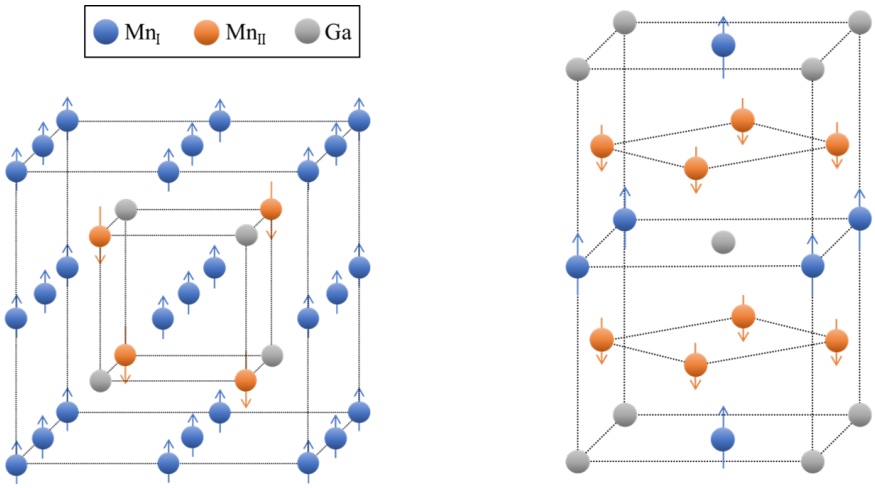

FIGURE 2.3: $D0_3$ cubic structure on the left and $D0_{22}$ tetragonal structure on the right of Mn_3Z compounds. In the $D0_{22}$ structure, Ga, Mn_I and Mn_{II} are respectively in Wyckoff positions 2a → (0,0,0), 2b → ($\frac{1}{2}$,0,0) and 4d → ($\frac{1}{2}$,0,$\frac{1}{4}$), (0,$\frac{1}{2}$,$\frac{1}{4}$).

order has been predicted by first-principles density-functional theory [123] and experimentally observed in Mn_3Ga [124], Mn_3Ge [125] and Mn_3Sn [126].

The $D0_{22}$ structure (I4/mmm, space group n°139) is a tetragonalized version of the $D0_3$ structure with basis vector turned by 45° as shown in **figure 2.3**. It can be viewed as a cubic phase with a distortion along the z axis that produces an easy anisotropy direction for magnetic moments along this direction (ie: along the unit cell's c axis). The growing interest on material with strong bulk magnetic anisotropy has led to several density functional calculations on various Mn-based Heusler alloys [15, 36, 123, 127, 128]. A lot of Mn_3Z alloys have been identified to potentially grow in distorted phases[5] but only a few of them have been reported experimentally, namely Mn_3Ga [12, 13, 14, 16, 129, 130, 131], Mn_3Ge [15, 125, 132, 133, 134, 135, 136, 137] and Mn_3Sn [138] since the stabilization of tetragonal phase can be complex as explained by Zhang *et al.* [123] for Mn_3Sn. Moreover, chemical ordering turns out to be very important to keep the interesting properties. The most attractive tetragonal compounds are Mn_3Ga and Mn_3Ge since they host for instance high PMA, high Curie temperature or low saturation magnetization. In light of these exceptional properties, Mn_3Ga and Mn_3Ge are the distorted Heusler alloys studied in this thesis and a literature overview of both compounds is done below.

Mn_3Ga compounds

As said before, density functional calculations [36, 123, 127, 128] have been performed on Mn_3Ga compound to unveil its outstanding properties. Among them, a ferrimagnetic behavior and a strong PMA very suitable in storage devices to minimize the switching current, enlarge switching speed and increase storage density. Its experimental study has begun in 1970 with the work of Kren *et al.* [12] who investigated the growth of $Mn_{2.85}Ga_{1.15}$. First of all, they obtained the hexagonal $D0_{19}$ phase with a weak ferromagnetic behavior. Then, by annealing it at 750 K, they got the tetragonal $D0_{22}$ Heusler structure with a $\frac{c}{a}$ ratio of 1.824. Thanks to

[5] Some Mn_2YZ Heusler alloys have also been identified but are not the compounds of interest here.

neutron diffraction, they measured a ferrimagnetic order coming from the two non-equivalent Mn sites which results in Mn_I moment of -2.8 $\pm$ 0.2 μ_B and Mn_{II} moment of 1.6 $\pm$ 0.2 μ_B. The $D0_{22}$ structure is made of two inequivalent Mn crystallographic sites with Mn_I and Mn_{II} respectively in Wyckoff position 2b and 4d. Ga goes in 2a position. The Mn in 2b and 4d positions are coupled antiferromagnetically resulting in an overall ferrimagnetic structure as sketched in **figure 2.3**. The alternating planes of up and down moments are expected to be collinear and aligned along the z direction.

Many years later, Balke *et al.* [13] showed with theoretical calculations and experiments that the $D0_{22}$ phase presents a ferrimagnetic order coming from partially compensated moments in accordance with previous works. Moreover, they found theoretical moments on Mn_I and Mn_{II} sites of respectively -2.896 μ_B and 2.355 μ_B which give rise to a total moment of M_{tot} = 1.77 μ_B. Thanks to electronic structure calculations, they predicted a nearly half-metallic ferrimagnet with 88 % of spin polarization at the Fermi energy and experimental results gave a Curie temperature of 762 K. Finally, they showed moment tunability from 0 to 1 μ_B by changing Mn ratio from Mn_3Ga to $Mn_{2.85}Ga$. The work of Balke *et al.* was confirmed by the publication of Winterlik *et al.* [14], which goes further. They studied $Mn_{3-x}Ga$ with x varying from 0 to 1. Every compound crystallized in $D0_{22}$ structure. Furthermore, volume and $\frac{c}{a}$ ratio increased with Mn contents while moments decreased from 0.47 μ_B to 0.26 μ_B and were lower than the theoretical values determined by Balke *et al.* [13]. Both works showed a high magneto-crystalline anisotropy when Mn_3Ga grows in $D0_{22}$ Heusler phase. This property comes from the highly tetragonal structure with a $\frac{c}{a}$ ratio around 1.8 [12, 13, 14] leading to K_{eff} values of the order of 1 to 3 MJ.m^{-3} [18, 19].

The collinear arrangements between the two Mn sublattices are still under debate. In 2013, Rode *et al.* [16] published a paper focusing on the magnetic moments and especially the magnetic structure of tetragonal $D0_{22}$ Mn_3Ga. They labeled the origin of the strong magnetic anisotropy to the Mn 4d-site and observed for some samples a soft intrinsic in-plane component resulting in a non-collinear structure and coming from Mn 2b-site. This non-collinear structure is explained by the 2b-sites's in-plane anisotropy and by the competing Mn-Mn interactions. Nowadays, the exact magnetic structure of Mn_3Ga is still unclear. Substrate and buffer layers play an important role on thin film constrain and chemical ordering lying in the sample are probably of primary interest to explain the different results given in literature.

Despite this complex magnetic behavior, many papers have reported the growth of $D0_{22}$ Mn_3Ga on numerous substrates or buffer layers such as MgO [16, 129, 130], $SrTiO_3$ [16], GaAs [131], Pt [129], Cr [18, 19, 129]. All of them state the presence of a tetragonalized structure with a $\frac{c}{a}$ ratio of the order of 1.8. All the samples present an out-of-plane easy axis of magnetization with a strong uniaxial magnetocrystalline anisotropy always estimated on the vicinity of MJ.m^{-3}. Typical values for magnetocrystalline anisotropy and saturation magnetization are: $K_u \approx$ 1 to 1.5 MJ.m^{-3}, $M_S \approx$ 200 to 600 emu.cm^{-3} depending on alloy stoichiometry. Hysteresis loops performed on Mn_3Ga do not present a perfectly squared shape but a strong perpendicular easy axis is always observed. This strong easy axis in magnetization results in difficulties to reach saturation with an in-plane applied magnetic field as shown in **figure 2.4**.

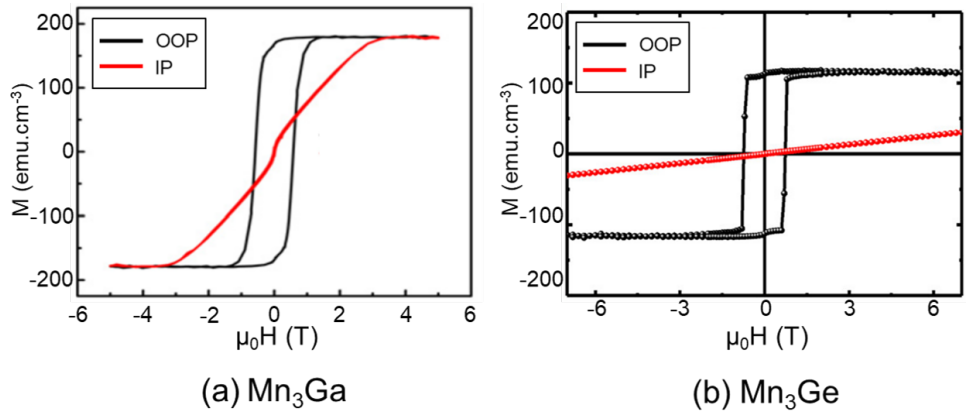

FIGURE 2.4: In-plane in red and out-of-plane in black hysteresis loops of Mn_3Ga (a) and Mn_3Ge (b) grown on Cr buffer layers unveiling the strong out-of-plane easy magnetization axis of these compounds. The correction applied to the in-plane Mn_3Ga curve is probably incorrect since a saturation field around 4 T was assumed. Both graphs are adapted from [131] and [137].

Mn_3Ge compounds

Similarly to Mn-Ga, Mn-Ge binary compounds possess a manifold of stable phases [139] but only the $D0_{22}$ structure is of interest here. $D0_{22}$ Mn_3Ge is isomorphic to $D0_{22}$ Mn_3Ga but has been less investigated despite similar properties. The first reported paper on the tetragonal version of Mn_3Ge dates back to 1961 [140] and the first magnetic study was performed by Krén *et al.* [17] in 1971 unveiling the presence of the two different Mn moments with respectively $Mn_I = 2.8 \pm 0.3\ \mu_B$ and $Mn_{II} = 1.6 \pm 0.2\ \mu_B$. The structure is organized as followed. Ge goes on 2a site while Mn goes on 2b and 4d Wyckoff positions leading to a ferrimagnetic order due to the two antiferromagnetically coupled magnetic sublattices. The first studies conducted to make use of the strong magnetocrystalline anisotropy of $D0_{22}$ Mn_3Ge arrived during the 2010s [15, 123, 132, 133, 135, 136, 137, 141]. The group of Kurt [15] was the first to investigate tetragonal Mn_3Ge for its potential applications on nanoscale spin valve or MTJ. They mastered Mn_3Ge growth on $SrTiO_3$ substrate with a $\frac{c}{a}$ ratio of 1.866 in accordance with the $D0_{22}$ structure. Magnetization measurement confirms the out-of-plane easy magnetization axis with a huge coercivity $\mu_0.H_c = 2.3$ T and a resulting anisotropy constant $K_u = 0.91$ MJ.m^{-3}. Magnetic measurement with the field applied parallel to the surface unveils a small in-plane component that may be a consequence of frustration of some of the exchange bonds. They measured the spin polarization at the Fermi level by point contact Andreev reflection with a resulting value of 46 % well below the theoretical value of 75 % obtained by density functional calculations. After this first investigation, other groups tried to control the $D0_{22}$ Mn_3Ge growth on various types of substrate or buffer layers such as MgO [141], Cr [132, 133, 135, 137] or Ru [136] studying particularly stochiometric and off-stochiometric $Mn_{3-x}Ge$ alloys to investigate the robustness of the $D0_{22}$ phase and the impact of stoichiometry on the relevant properties [132, 133, 141]. The most important effect for STT and SOT applications revealed by Sugihara *et al.* [132] is the non-square shape obtained for off-stoichiometry samples. It must be noted that non-square shapes are also obtained for stoichiometric Mn_3Ge sample grown on $SrTiO_3$ [15], MgO [141] and Ru

[136] seed layer. Nonetheless, magnetocrystalline anisotropy K_u, saturation magnetization M_S and $\frac{c}{a}$ ratio stay in the same range[6]. As a summary, the main experimental properties values extracted from literature [15, 123, 132, 133, 135, 136, 137, 141] for stochiometric $D0_{22}$ Mn_3Ge are: $K_u \approx 2$ MJ.m^{-3}, $M_S \approx 100$ emu.cm^{-3}, P = 46 % and a T_C above 800 K. Theoretical papers attest to the good properties of Mn_3Ge [15, 36, 128, 141]. Theoretical K_u, M_s and P values are always higher than the experimental ones. For instance, Mizukami *et al.* [141] calculated an anisotropy value of $K_u = 2.3$ MJ.m^{-3}, a net magnetization of $M_S = 180$ emu.cm^{-3} and a spin polarization at the Fermi energy of P = 77 %. The mismatch between theory and experience is not yet fully understood but off-stoichiometry and chemical order may influence these properties. Moreover, they predicted a low damping value of $\alpha = 9 .10^{-4}$ with an identified fully spin-polarized Δ_1 band at the Fermi level that makes Mn_3Ge even more promising than Mn_3Ga as MTJs electrodes with a tunneling barrier, such as MgO.

2.1.3 Mn_3Z/Co_2MnZ' bilayers and superlattices

Preliminary results on MTJ or SOT-effect using Mn_3Ga have been published over the years [131, 137, 142] but our attention focuses on Mn_3Z/Co_2MnZ' compounds here. Few articles dealing with Heusler compounds' bilayers or SLs growth are present in literature. The group of Ranjbar published a series of papers [143, 144, 145, 146] on Heusler bilayers. They grew $D0_{22}$ Mn_3Ga/ Co_2FeAl [144, 145, 146], Co_2FeSi [144, 145, 146], Co_2MnSi [143, 145, 146], Co_2MnAl [145, 146] and managed to obtain out-of-plane magnetized bilayers with a perfect growth of Mn_3Ga along its c axis. Hysteresis loops unveil a non-square shape with a two-step switching. This two-step switching is explained by an antiferromagnetic exchange coupling at the Mn_3Ga/Co_2YZ' interface as shown in **figure 2.5** for Mn_3Ga/Co_2MnSi bilayer. In the case of Co_2MnSi, the strength of the interfacial exchange coupling was estimated as J_{ex} = -3.2 erg.cm^{-2}.

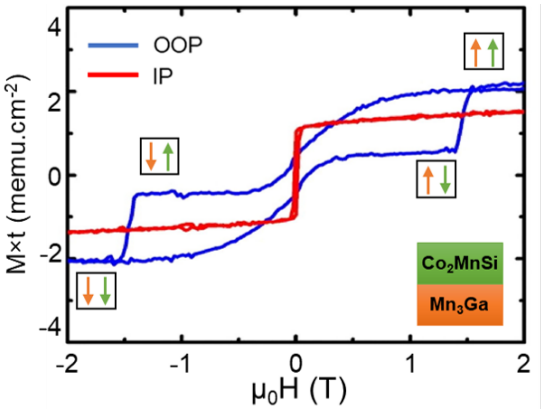

FIGURE 2.5: In-plane and out-of-plane hysteresis loops obtained for Mn_3Ga/Co_2MnSi bilayer. The orange and green arrows represent the magnetization orientation of Mn_3Ga and Co_2MnSi respectively and unveil the antiferromagnetic coupling between both layers. Adapted from [145].

[6]It should be noted that the highest K_u value is obtained for the stochiometric Mn_3Ge sample.

Similar behavior was observed for Mn_3Ga/Co_2MnSi heterostructures [147]. Since the lattice mismatch and surface energy difference between Mn_3Ga and MgO do not allow to get well crystalline Mn_3Ga layer, Mao *et al.* [147] built Mn_3Ga-based perpendicular-MTJ with the help of Co_2MnSi alloy. The $Mn_{3.1}Ga/Co_2MnSi/MgO/Co_2MnSi/Mn_{2.9}Ga$ structure was investigated and a strong antiferromagnetic coupling in Mn_3Ga/Co_2MnSi was observed with an interfacial exchange coupling of J_{ex} = -5 erg.cm^{-2}. It can be noticed that a TMR ratio up to 65 % was achieved at 5 K. Finally, Ma *et al.* [148] engineered a Heusler ferrimagnetic SL composed of two Heusler alloys namely $Mn_{62}Ga_{38}$ and Co_2FeAl. $Mn_{62}Ga_{38}$ crystallizes in the $L1_0$ phase which is a cousin of the $D0_{22}$ phase since both of them derive from classical Heusler structure and are tetragonalized. The SL is formed of a $[Mn_{62}Ga_{38}/Co_2FeAl]$ repetition with each unit exhibiting an antiferromagnetic coupling between both layers. This result is in agreement with the antiferromagnetic exchange coupling observed in the works of Ranjbar [143, 144, 145, 146] and Mao [147] with the $D0_{22}$ phase.

2.1.4 Our strategy to obtained PMA Heusler compatible with spintronic needs

One of the prerequisites of this study is to grow Mn_3Z along the elongated c direction resulting in an easy axis of magnetization normal to the sample surface. First, MgO(001) substrate was used since many layers can be epitaxially grown on it. Mn_3Z growth attempts [128] were directly performed on MgO substrate but were not successful and resulted in large 3D island growth. We thus decided to grow Mn_3Z on buffer layers and 3 materials were tested: Pd(001), V(001) and Cr(001). A V buffer layer was tested due to its resistance to interdiffusion with many elements up to quite large substrate temperatures. However, it was quickly set aside because Mn_3Ga grow on it in its cubic structure [11]. On the contrary, Pd(001) and Cr(001) buffer layers allow to stabilize the $D0_{22}$ phase. In theory, a Pd buffer layer is ideal since its cell parameter (fcc - a_{Pd} (001) = 3.89 Å) fits perfectly to in-plane Mn_3Ga one. Cr is also a good candidate (bcc - a_{Cr} (011) = 4.01 Å). The first part of our study was thus dedicated to the magnetic properties of Mn_3Ga and Mn_3Ge thick films grown on such buffer layers.

These compounds are not known to host a spin gap on the contrary to Co_2MnSi or Co_2MnGe [10, 11]. The idea was thus to grow these HMM Heusler on top of Mn_3Ga (or Mn_3Ge) and try to keep the PMA in the whole stack. To test this persistence of the PMA different magnetic characterizations means were used, namely:

- Macroscopic magnetization measurement (SQUID and/or VSM), sensitive to the whole sample, including the MgO substrate (diamagnetic in theory, but slightly paramagnetic due to some impurities included to stabilize the MgO structure).
- X-Ray Magnetic Circular Dichroism (XMCD), interesting owing to its element specific sensitivity that allows, in principle, to look separately at the magnetic properties of Mn_3Z and the X_2YZ full-Heusler grown on it. (see **appendix C** for XMCD basics).

- Magneto-Optical Kerr Effect (MOKE), sensitive to the top film and not to the substrate. For this, the new *in situ* MOKE set-up available on the tube was used (see **appendix D** for its description).

The final goal of this study is to get square magnetic hysteresis loop with an easy magnetization axis normal to the sample surface and along with a spin gap in the top layer. Such properties will ensure a full spin polarization injection as well as ultra-low magnetic damping.

This goal was however constrained by many experimental limits. First, the basic Mn_3Z / X_2YZ block useful for XMCD eliminates the choice of Co_2MnZ compounds since Mn is in both layers. We consequently choose the Mn_3Z/Co_2FeGe block for XMCD studies. Second, if a Mn_3Z/Co_2FeGe bilayer is pertinent for XMCD studies, the amount of materials is thus too small for MOKE measurements. Superlattices (with 5 repetitions) were thus grown for this later technique[7]. All these constraints lead to the following samples:

- Mn_3Ga and Mn_3Ge thin films grown on Pd or Cr buffer layers, analyzed by VSM and XMCD.
- Mn_3Ge/Co_2FeGe bilayers especially dedicated for XMCD and VSM.
- Mn_3Ge/Co_2FeGe superlattices to compare XMCD and MOKE measurements.
- Mn_3Ge/Co_2MnGe superlattices for MOKE measurements.

These different layers stacks are presented in the following, with a first description of the growth and structural properties and a second description of the resulting magnetic behavior. The first section is dedicated to Mn_3Ga-based stacks, the second one to Mn_3Ge ones, and the third one to discussion.

2.2 Perpendicular magnetic anisotropy in Mn_3Ga-based stacks

2.2.1 $Mn_{100-x}Ga_x$ study on Pd buffer layer

The reported magnetic properties of Mn_3Ga slightly vary from one work to another in literature. Since this variation may result from chemical order and stoichiometry, a first study was done on different $Mn_{100-x}Ga_x$ stoichiometries with x equal respectively to x = 15, 20, 25, 30, 35. The aim was to check if the $D0_{22}$ phase is always achieved and how the off-stochiometric impacts the magnetic properties.

[7] Moreover, multilayers have been proved to act on the heterostructures' remanence and coercive field [149] making them tunable.

Growth and structural properties

MgO substrate was outgassed *in situ* at a temperature around 950 °C ($T_{pyro} \approx 540$ °C)[8] to clean the surface. Straight after, a 10 nm thick MgO layer was deposited around 880 °C ($T_{pyro} \approx 510$ °C) to bury the potential contamination and smooth the surface. Typical RHEED patterns obtained are given in **figure 2.6**. Nice homogeneous intensity streaks unveil a smooth surface with a good crystallinity. The two patterns imaged by applying the electron beam along [100] and [110] azimuths are in accordance with the (001) orientation of the MgO's fcc lattice (Fm-3m, space group n°225). The 10 nm thick Pd buffer is grown at room temperature on top of MgO and then annealed at 550 °C ($T_{pyro} \approx 350$ °C) to flatten the surface. Obtained RHEED patterns, given in **figure 2.6**, show a smooth surface with a perfect single-crystalline growth[9]. The misfit between a_{Pd} = 3.89 Å and a_{Mn_3Ga} = 3.9 Å is lower than 1% and should allow to stabilize the $D0_{22}$ $Mn_{100-x}Ga_x$ growth with an elongated direction normal to the sample surface. The epitaxy relationship is expected to be $Mn_{100-x}Ga_x$ [100](001)$/\!/$Pd [100](001)$/\!/$MgO [100](001).

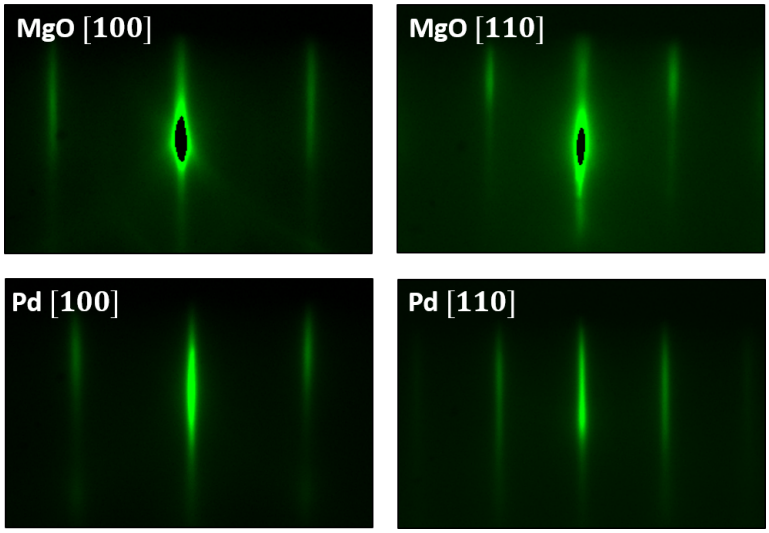

FIGURE 2.6: RHEED patterns with a beam applied along the $[100]_{MgO}$ and $[110]_{MgO}$ azimuths for MgO and Pd.

Mn and Ga were both evaporated using Knudsen cells and the fluxes were regulated with respect to $\Phi_{Mn} = 3.\Phi_{Ga} = 1.5\ .10^{14}$ at.cm^{-2}.s^{-1} in the case of $Mn_{75}Ga_{25}$. Fluxes were adapted to get the correct stoichiometry for the other $Mn_{100-x}Ga_x$ compounds and the density was fixed to the alloy density of ρ_{Mn_3Ga} = 7.4 g.cm^{-3} with an aimed thickness of 50 nm for each sample. The deposition was performed at a temperature around 260 °C ($T_{pyro} \approx 210$ °C) and no annealing process was done to avoid any interdiffusion with Pd buffer layer. This results in a single-crystalline growth with a smooth surface as revealed by the RHEED patterns given in **figure 2.7** for the $Mn_{100-x}Ga_x$ series.

[8] All the temperatures given in this chapter are measured at the thermocouple and with a pyrometer (arbitrary emissivity of $\epsilon = 0.85$ used for each measurement). The temperatures are always enumerated as follow $T_{thermocouple}$ = … °C (T_{pyro} = … °C).

[9] All the RHEED images given in this chapter are labeled according to MgO azimuths.

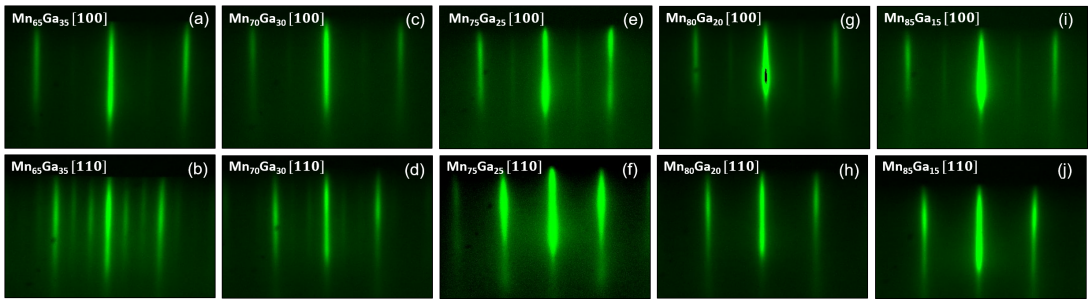

FIGURE 2.7: RHEED patterns with a beam applied along the $[100]_{MgO}$ and $[110]_{MgO}$ azimuths for $Mn_{65}Ga_{35}$ (a) and (b), $Mn_{70}Ga_{30}$ (c) and (d), $Mn_{75}Ga_{25}$ (e) and (f), $Mn_{80}Ga_{20}$ (g) and (h), $Mn_{85}Ga_{15}$ (i) and (j).

RHEED oscillations were performed during the growth on the $Mn_{100-x}Ga_x$ series and one of them is given in **figure 2.8** for $Mn_{75}Ga_{25}$. The deposition begins around 20 sec and the streaks intensity starts to oscillate. The Fourier transform (inset of **figure 8**) leads to a frequency $f_{oscill} = 0.1475 \pm 0.0030$ s^{-1} resulting in an accomplished atomic plane in $T^{exp}_{1ML} = 6.78 \pm 0.14$ s. This experimental value can be checked by an estimation of the growth rate according to the total flux used. The atomic density of one (001) plane of $Mn_{75}Ga_{25}$ is $\frac{2}{(a_{Mn_{75}Ga_{25}})^2} = 1.335\ .10^{15}$ at.cm^{-2} and the total flux is given by the sum of Mn and Ga fluxes: $\Phi_{tot} = \Phi_{Mn} + \Phi_{Ga} = 2\ .10^{14}$ at.cm^{-2}.s^{-1}. Therefore, the growth rate is expected to be $T^{th}_{1ML} = \frac{1.315\ .10^{15}}{\Phi_{tot}} = 6.68$ s. These results confirm the good fluxes calibration performed before deposition in addition with a good stoichiometry.

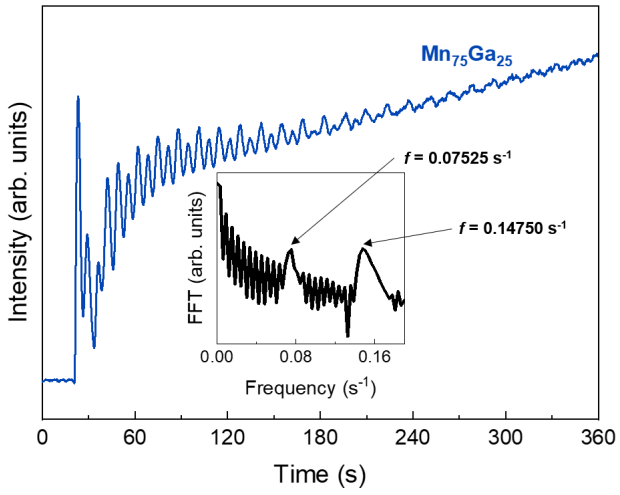

FIGURE 2.8: RHEED oscillations intensity vs. time of (00) $Mn_{75}Ga_{25}$ streak. The Fourier transform of the blue curve is given on the inset where two oscillation frequencies are extracted.

Furthermore, a second frequency is visible at $f_{oscill} = 0.0752 \pm 0.0030$ s^{-1} in the Fourier transform graph. The period of the oscillations in this case is $T^{exp}_{2ML} = 13.29 \pm 0.51$ s and corresponds to a bilayer deposition mode. A competition between layer-by-layer and bilayer-by-bilayer growth is present here. This bilayer behavior has already been reported in literature for MBE-grown semiconductors [150] and has

also been observed for Heusler alloys [79]. It relies on the covalent tetrahedrons stability that occurs in zinc blend structure[10] and is a proof of a good chemical ordering.

In parallel with RHEED oscillations, X-ray reflectivity was also performed (**figure 2.9**) to check the thicknesses of $Mn_{100-x}Ga_x$ samples and, as a consequence, the control of the stoichiometry. The fits in red allow to extract densities, roughness and thicknesses for all samples that are given in **table 2.1**. All the thicknesses are in perfect agreement with the expected 50 nm aimed before deposition and typical roughness around 3.5 Å is determined for all samples.

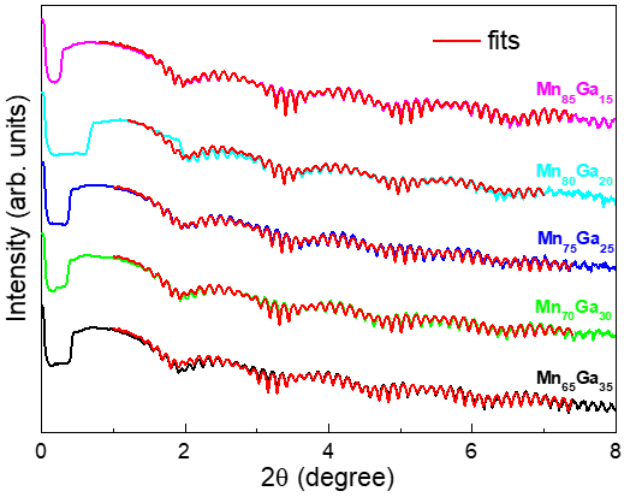

FIGURE 2.9: X-ray reflectivity spectra of the $Mn_{100-x}Ga_x$ series with x = 15, 20, 25, 30 and 35 respectively in pink, light blue, blue, green and black colors.

	density (g.cm^{-3})	thickness (nm)	roughness (nm)
$Mn_{65}Ga_{35}$	7.5 ± 0.3	50.7 ± 0.1	0.35 ± 0.04
$Mn_{70}Ga_{30}$	7.2 ± 0.4	50.5 ± 0.1	0.36 ± 0.05
$Mn_{75}Ga_{25}$	6.8 ± 0.4	50.0 ± 0.1	0.48 ± 0.07
$Mn_{80}Ga_{20}$	7.2 ± 0.6	49.5 ± 0.2	0.37 ± 0.05
$Mn_{85}Ga_{15}$	7.2 ± 0.3	49.1 ± 0.1	0.26 ± 0.03

TABLE 2.1: Summary of densities, thicknesses and roughness extracted from the XRR fits of the $Mn_{100-x}Ga_x$ series.

Finally, $\theta/2\theta$ X-ray diffraction scans are given in **figure 2.10**. $Mn_{100-x}Ga_x$ diffracted planes only come from the (001) families revealing the single-crystalline growth with c axis normal to the surface. Only peaks with even (hkl) values are observed due to the fcc nature of the unit cell. The extracted cell parameter gives an out-of-plane parameter value around c = 7.17 Å for every composition. This c value is in perfect agreement with the $D0_{22}$ phase of $Mn_{100-x}Ga_x$ observed in literature [13, 130, 131]. Moreover, the Pd(001) growth is also checked even if some small (111) peaks are observed (probably due to an over-annealed buffer layer). The Pd(002) peak fit results in a cell parameter of a_{Pd} = 3.88 Å which validates its fcc phase growth. In all

[10] Heusler alloy can be described by a zinc blende-type sublattice [151].

samples, the capping used was 5 nm of Au as shown by (111) peaks for $Mn_{85}Ga_{15}$ and $Mn_{70}Ga_{30}$. For the three remaining compositions, Au was grown along the (001) direction, the Au peak is therefore hidden by MgO(002) and Pd(002). The peaks' intensity is proportional to the structure factor that, in the case of $Mn_{100-x}Ga_x$, leads to higher intensities for h+k+l = 4n peaks compared to h+k+l = 4n+2 ones. Furthermore, the intensity of $Mn_{100-x}Ga_x$(002) peak clearly decreases when Mn content increases. This behavior is also explained by the structure factor since Ga atoms are replaced by Mn ones resulting in a decrease of the peak intensity.

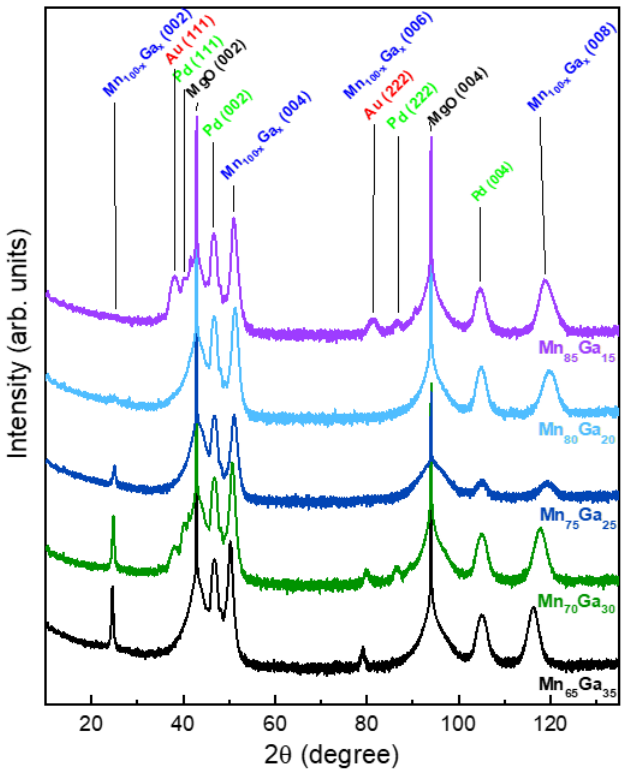

FIGURE 2.10: $\theta/2\theta$ X-ray diffraction spectra of the $Mn_{100-x}Ga_x$ series with x = 15, 20, 25, 30 and 35 respectively in pink, light blue, blue, green and black colors.

The graph of **figure 2.11a** gives the c parameters extracted for each stoichiometry of $Mn_{100-x}Ga_x$[11]. When Mn concentration is low the out-of-plane parameter is higher and decreases while increasing the Mn content. Interestingly, the c parameter increases again when the Mn concentration reaches 85 %. Since at this stoichiometry we are in the vicinity of pure Mn, this behavior can be explained by $Mn_{85}Ga_{15}$ that comes closer to pure Mn resulting in an increase of the c parameter. Nonetheless, all the out-of-plane lattice constants are in good agreement with the $D0_{22}$ phase. Non-symmetrical measurements were also performed to extract the in-plane parameters and confirm the $D0_{22}$ structure. The peaks and the obtained a parameter are given in **figure 2.11c** and **2.11d**. All the in-plane values are of the order of a = 3.87 Å in good conformity with the $D0_{22}$ structure. The a parameter's increasing trend with Mn contents seems to point out a lower in-plane frustration of $Mn_{100-x}Ga_x$ by the Pd buffer leading to lower c values. The extracted a value for $Mn_{70}Ga_{30}$ is puzzling

[11]The reported Mn_3Ga values for a, c and c/a are only indicative. No growth report with a Pd buffer layer is present in literature and the use of different substrate or buffer layer strongly impact the cell parameter values.

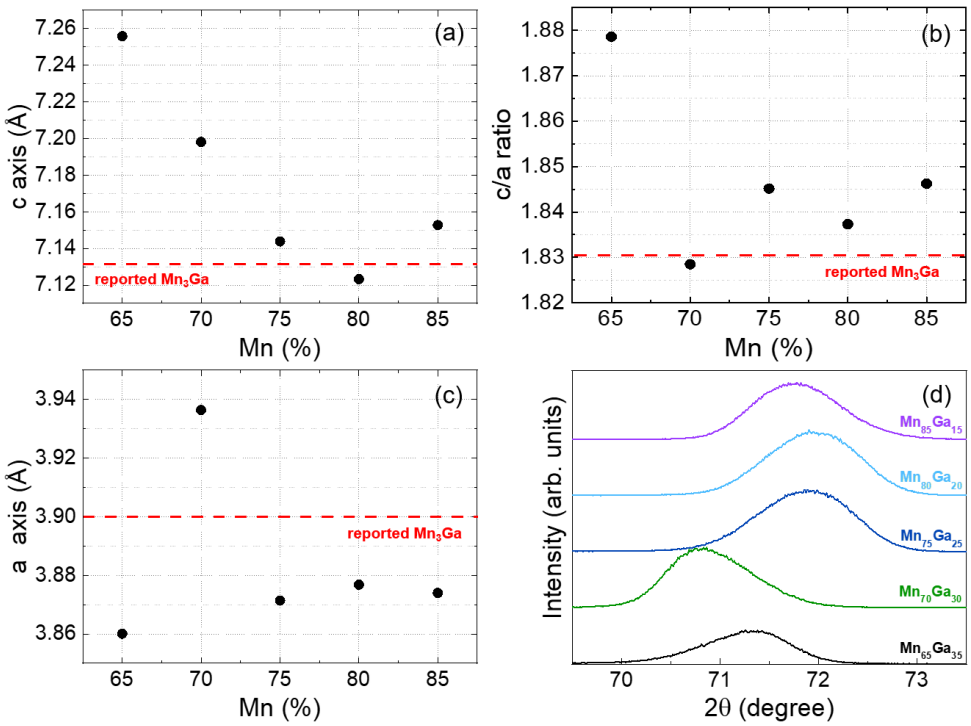

FIGURE 2.11: (a) and (c), c- and a-axis values as a function of composition with the resulting $\frac{c}{a}$ ratio (b). a parameters are extracted from the non-symmetrical (204) peaks (d).

and is attributed to an artefact during non-symmetrical measurements. This wrong a value also misleads the $\frac{c}{a}$ ratio and must thus not be considered.

Magnetic properties

In order to have a preliminary overview of the magnetic behavior of the $Mn_{100-x}Ga_x$ series, vibrating sample magnetometry study was performed. The measurements were done on a PPMS-VSM (Physical Properties Measurement System - Vibrating Sample Magnetometer) from Quantum Design allowing to apply a magnetic field up to 9 T with a moment sensitivity lower than 10^{-6} emu. This set-up probes the entire sample and the diamagnetic contribution coming from MgO is included. A slope correction was thus done assuming fully saturated $Mn_{100-x}Ga_x$ at high field. The measured magnetic curves are given in **figure 2.12** for x = 20, 25, 30 and 35[12] with an in-plane and out-of-plane applied magnetic field. First of all, each composition shows a clear cycle opening in the out-of-plane direction as a result of PMA. Nonetheless, the cycles do not exhibit a square shape and are bent as seen in literature. Moreover, most of them are probably not fully saturated especially in the in-plane direction where the saturation field values shoot up due to the strong out-of-plane magnetic anisotropy. This non-reach saturation for in-plane measurements is confirmed by the magnetization saturations for x = 25 and 30 that do not match the out-of-plane ones. More interestingly, the in-plane curves (for x = 25, 30 and 35) present a soft in-plane component that may be related to a non collinear arrangement of the two different Mn moments hosted by the $D0_{22}$ structure. This observation has already been done by Rode *et al.* [16] and is attributed to a canted moment carried

[12]The sample $Mn_{85}Ga_{15}$ is not shown here since extremely noisy curves were obtained due to a very low sample moment.

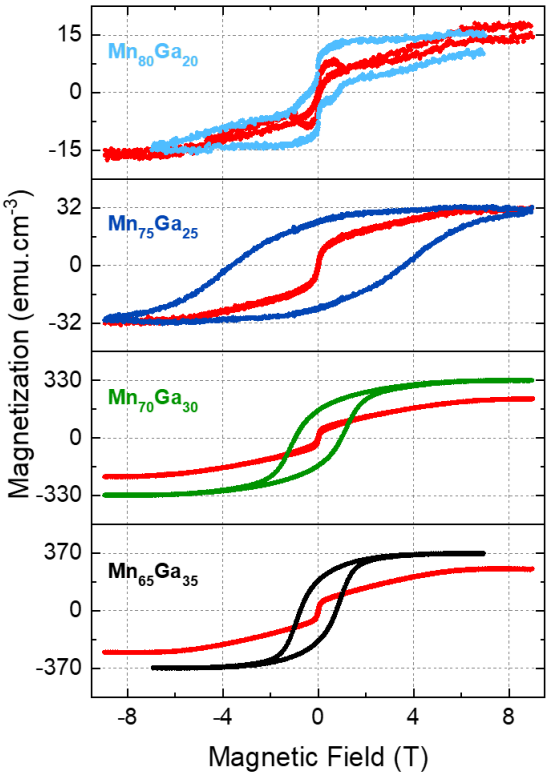

FIGURE 2.12: Hysteresis loops measured using a PPMS-VSM with an out-of-plane applied magnetic field for the $Mn_{100-x}Ga_x$ series with x = 20, 25, 30 and 35 respectively in black, green, blue and light blue. The curves with an in-plane applied magnetic field are given in red. Measurements performed at 300 K.

by one of the Mn sublattice.

The extracted magnetic information, namely coercive field H_c, remanence moment M_R and magnetization values, are summarized in **figure 2.13**.

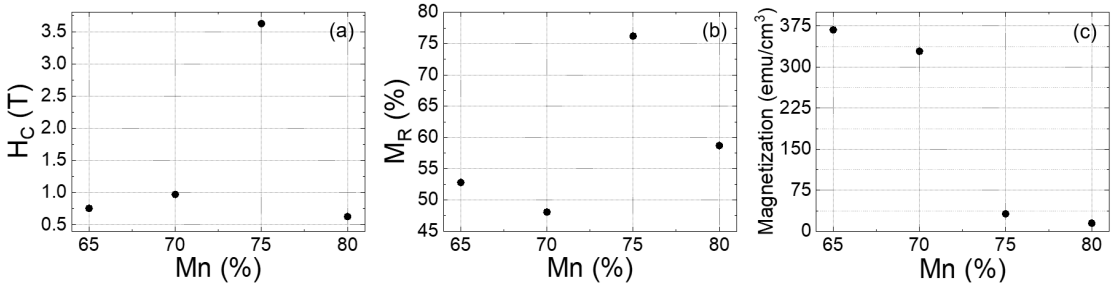

FIGURE 2.13: Summary of the extracted coercive field H_c, magnetization remanence M_R and magnetization as a function of Mn content.

No clear tendency is observed but the magnetization seems to decrease while increasing Mn content and the very noisy curve obtained for x = 15 (not shown here) confirms this vanishing magnetization behavior. On the other hand, maximum remanence and coercive fields are obtained for $Mn_{75}Ga_{25}$ and deviation from 3 to 1 stoichiometry strongly influenced them.

To go further, X-ray magnetic circular dichroism experiments were carried out on the $Mn_{75}Ga_{25}$ sample (with a 5 nm thick Au capping). The absorption spectra were

measured using the total electron yield mode at a temperature of 4 K. The resulting absorption (XAS) and dichroic (XMCD) signals are given in **figure 2.14**. The XAS signal exhibits some kinks from both edges. This multiplet behavior has already been observed for $D0_{22}$ compounds [16, 152, 153] and is attributed to the Mn_I and Mn_{II} components with opposite sign. Because of the two Mn sublattices of opposite direction, the XMCD signal is lowered. This observation was also done by Okabayashi *et al.* [153] with the study of $Mn_{3-x}Ga$ (x = 0, 1, 2) where the XMCD signal loses intensity while decreasing x since more antiparallel components are present. Nonetheless, even if the XMCD signal is small and noisy, it is clear that the shape of the L_3 edge unveils a ferrimagnetic signature. This result confirms the presence of the two Mn sites with a non collinear arrangement. Unfortunately, the too low dichroic signal did not allow to perform hysteresis cycle.

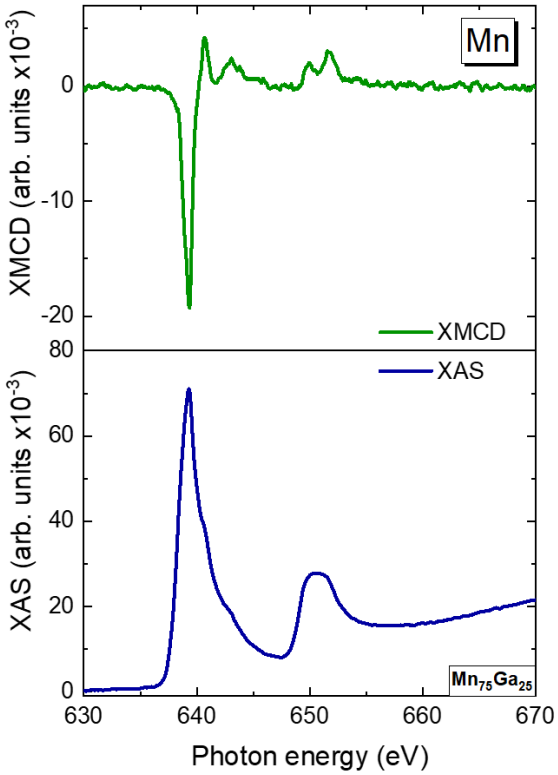

FIGURE 2.14: XAS (in blue) and XMCD (in green) signals measured at L_3 and L_2 Mn edges for $Mn_{75}Ga_{25}$. Measurements performed at 4 K with an applied magnetic field of 6 T.

$Mn_{75}Ga_{25}$ alloy pointed out as the best composition of the series to obtain strong PMA but the non-squareness of the hysteresis loop is puzzling. The ferrimagnetic behavior, confirmed by XMCD results, may not be perfectly collinear with a tilted moment for one of the Mn sites. Moreover, chemical order can strongly impact the magnetic properties and increases the hysteresis loop bending.

2.2.2 Mn_3Ga/Co_2MnSi superlattices

In order to fully settle on the potential of $Mn_{75}Ga_{25}$ alloy, a SL was grown and measured by Magneto-Optical Kerr Effect (MOKE). The advantage of MOKE is that the measurement can be performed *in situ* since MOKE and MBE are coupled thanks

to the UHV-tube[13]. Moreover, it provides information only on the SL since the substrate is not probed. No diamagnetic correction due to MgO substrate and Pd buffer has to be taken into account resulting in a hysteresis loop characterizing only the desired layer. The MOKE data for $[Mn_{75}Ga_{25}(3\text{ u.c})/Co_2MnSi(5\text{ u.c})]_{\times 5}$ SL are given in **figure 2.15**.

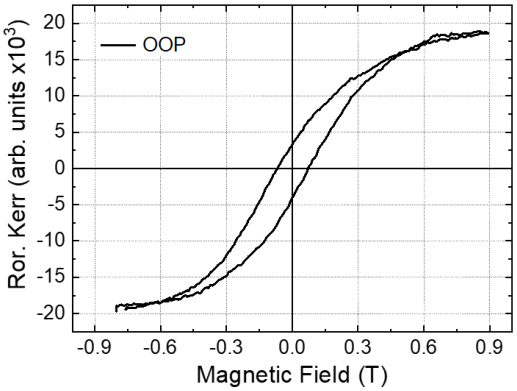

FIGURE 2.15: Out-of-plane hysteresis loop obtained for $[Mn_{75}Ga_{25}(3\text{ u.c})/Co_2MnSi(5\text{ u.c})]_{\times 5}$ sample by MOKE measurement.

The open cycle confirms that the SL is perpendicularly magnetized. Nonetheless, the cycle is stretched and curved. As a consequence, a very low magnetic remanence (of the order of 18%) is obtained pointing out that Mn-Ga alloys are not good candidates to build perpendicularly magnetized devices for spintronic.

2.3 Perpendicular magnetic anisotropy in Mn_3Ge-based stacks

As the magnetic properties of Mn_3Ga do not fulfilled the criteria for an optimal use in spintronic devices, we decided to move to Mn_3Ge. The experimental method was similar to the one performed in Mn_3Ga. However, a more complete XMCD analysis was done on Mn_3Ge-based stacks.

2.3.1 $Mn_{100-x}Ge_x$ study on Pd buffer layer

Growth and structural properties

Similarly to $Mn_{100-x}Ga_x$ series, $Mn_{100-x}Ge_x$ samples were grown on a Pd buffer layer. Mn was evaporated with Knudsen cell while Ge evaporation was done with e-gun. The fluxes were calibrated as follow in the case of $Mn_{75}Ge_{25}$: $\Phi_{Mn} = 3.\Phi_{Ge} = 1.5\ .10^{14}$ at.cm^{-2}.s^{-1} and were adapted for the four other stoichiometries. The density was fixed at the material density ($\rho_{Mn_3Ge} = 7.5$ g.cm^{-3}) and the growth was performed at a temperature around 260 °C ($T_{pyro} \approx 210$ °C) with no annealing process. The resulting RHEED patterns are given in **figure 2.16** for the whole $Mn_{100-x}Ge_x$ series. On the contrary to Mn-Ga alloys, two epitaxial regimes were observed depending on the Mn/Ge concentrations. For $x < 25$ %, RHEED patterns are typical of

[13]See **appendix D** for a description of the MOKE set-up.

the $D0_{22}$ structure. Nonetheless, the epitaxial process completely changes for high Ge concentration. This observation is not surprising since other compounds such as Mn_5Ge_3 (x = 37.5) or Mn_2Ge (x = 33) are stable [139].

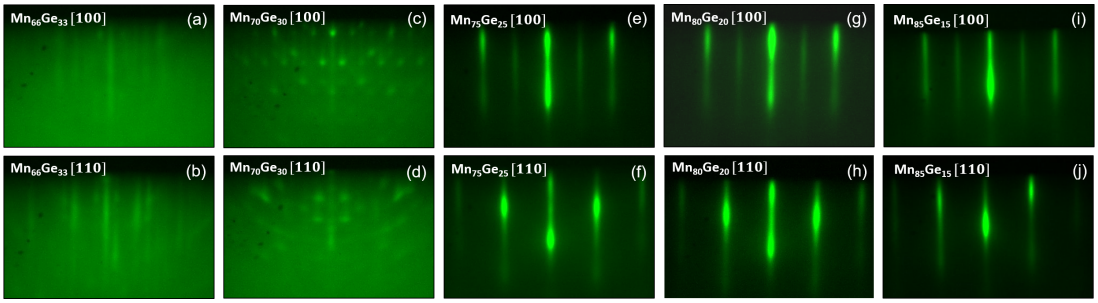

FIGURE 2.16: RHEED patterns with a beam applied along the $[100]_{MgO}$ and $[110]_{MgO}$ azimuths for $Mn_{66}Ge_{33}$ (a) and (b), $Mn_{70}Ge_{30}$ (c) and (d), $Mn_{75}Ge_{25}$ (e) and (f), $Mn_{80}Ge_{20}$ (g) and (h), $Mn_{85}Ge_{15}$ (i) and (j).

RHEED oscillations were also observed and are shown in **figure 2.17** for $Mn_{75}Ge_{25}$. The Fourier transform gives a frequency f_{oscill} = 0.0745 $\pm$ 0.0063 s^{-1} corresponding to a double period of T^{exp}_{2ML} = 13.42 $\pm$ 1.03 s. This experimental period is found equal to T^{th}_{2ML} = 13.67 s (using $\Phi_{tot} = \Phi_{Mn} + \Phi_{Ga}$ = 2 .10^{14} at.cm^{-2}.s^{-1}). This leads to a 2 % difference which is in the error bars of the measurements. Again, this demonstrates the good control of the stoichiometry using our calibration process. It should be noted however that a layer-by-layer deposition mode is also observed at the beginning of the growth like in Mn_3Ga. However, it rapidly disappears to let the bilayer mode taking place. This double period, associated to a bilayer-by-bilayer mode, is a fingerprint of the good chemical ordering occurring at the very beginning of the growth.

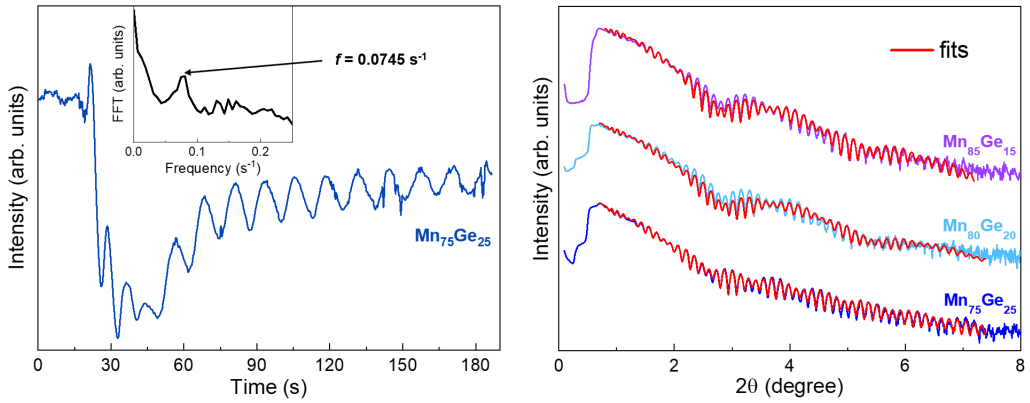

FIGURE 2.17: On the left, RHEED oscillations intensity vs. time of (00) $Mn_{75}Ge_{25}$ streak. The Fourier transform is given on the inset. On the right, X-ray reflectivity spectra of the $Mn_{100-x}Ge_x$ series with x = 15, 20, 25 respectively in pink, light blue and blue colors.

This nice control of the fluxes and stoichiometry was also checked by X-ray reflectometry. The data and fits are given in **figure 2.17** for the samples with x = 15, 20 and 25 since the roughness for x = 30 and 33 was too high to obtain good XRR spectra enabling a fit. The resulting densities, thicknesses and roughness are shown in the following **table 2.2**. Low roughness was identified for all three samples and a

slight difference between aimed and deposited thicknesses is observed.

	density (g.cm^{-3})	thickness (nm)	roughness (nm)
$Mn_{75}Ge_{25}$	7.6 ± 0.2	48.2 ± 0.1	0.72 ± 0.11
$Mn_{80}Ge_{20}$	7.7 ± 0.8	48.6 ± 0.3	0.43 ± 0.10
$Mn_{85}Ge_{15}$	7.0 ± 0.6	47.0 ± 0.2	0.52 ± 0.08

TABLE 2.2: Summary of fluxes, densities, molar masses and growth rates of Pd, Y and Bi.

XRD measurements are plotted in **figure 2.18** for the $Mn_{100-x}Ge_x$ series. It unveils a growth along the (001) direction for all samples. Nonetheless, additional peaks are visible for the curve with x = 30 and 33 and are assimilated to the presence of other phases in the films. This unknown peaks are indexed with black diamonds in the curve of $Mn_{66}Ge_{33}$. These results are in agreement with the RHEED observations (**figure 2.16**). We thus focused our analysis on samples with x = 15, 20 and 25 for which the $D0_{22}$ structure takes place as in $Mn_{100-x}Ga_x$.

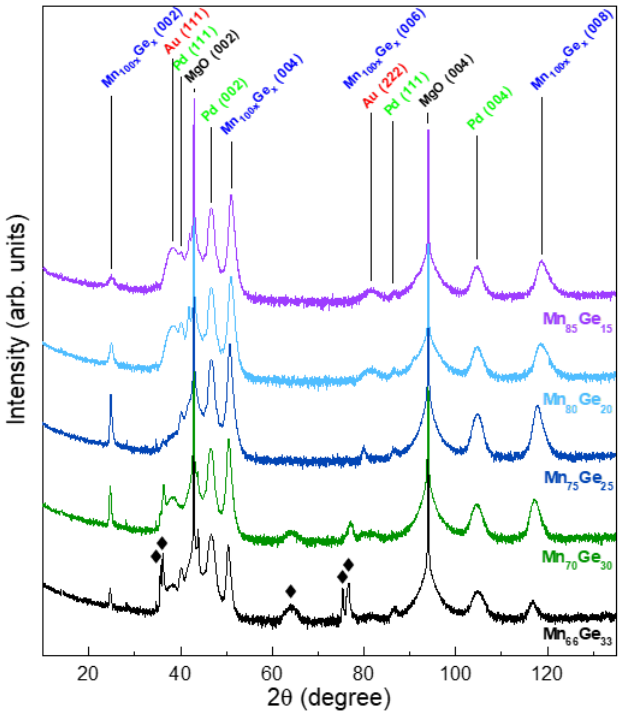

FIGURE 2.18: $\theta/2\theta$ X-ray diffraction spectra of the $Mn_{100-x}Ge_x$ series with x = 15, 20, 25, 30 and 33 respectively in pink, light blue, blue, green and black colors. The black diamonds in $Mn_{66}Ge_{33}$ scan identify the peaks position from other Mn-Ge phases.

We report in **figure 2.19** the extracted c, $\frac{c}{a}$ and a parameters along with the data obtained on the $Mn_{100-x}Ga_x$ series. A similar trend between both series is observed. The c parameter and $\frac{c}{a}$ ratio reduce when the Mn content is higher since the in-plane distance tends to increase. Here again, the a values are in good agreement with a growth in the $D0_{22}$ structure.

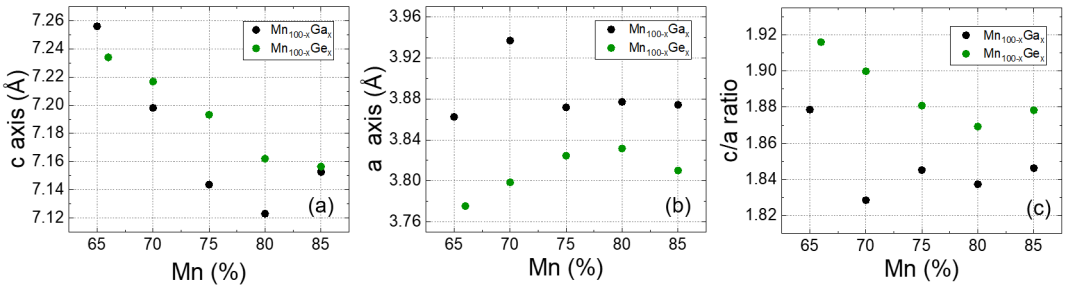

FIGURE 2.19: Comparison of the c parameter (a), a parameter (b) and $\frac{c}{a}$ ratio (c) extracted as a function of Mn content between $Mn_{100-x}Ga_x$ (in black) and $Mn_{100-x}Ge_x$ (in green) series.

Magnetic properties

PPMS-VSM measurements are shown in **figure 2.20** and all stochiometries exhibit an out-of-plane easy magnetization axis. Unlike $Mn_{100-x}Ga_x$ samples, the Mn-Ge alloys display a clear different hysteresis shape with regards to Mn content. For high Mn concentration, namely x = 15 and 20, it looks like the easy magnetization axis starts to switch within the film plane.

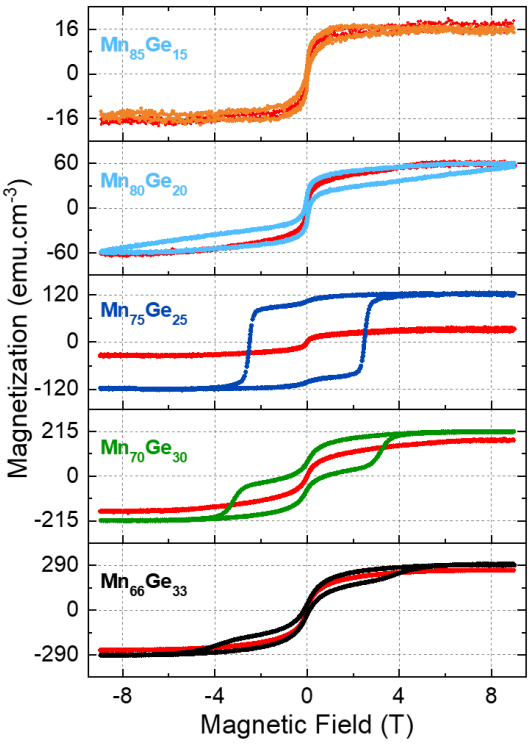

FIGURE 2.20: Hysteresis loops measured using PPMS-VSM with an out-of-plane applied magnetic field for the $Mn_{100-x}Ge_x$ series with x = 15. 20, 25, 30 and 33 respectively in black, green, blue, light blue and orange. The curves with an in-plane applied magnetic field are given in red. Measurements performed at 300 K.

As expected, the 3 to 1 stochiometric sample (ie. 75:25) unveils the best hysteresis loop with high remanence and high coercive field. It displays the squarest cycle but a two-step switching is present. These two steps are more pronounced when increasing x and their origin, at least for x = 30 and 35, is another proof of different phases' mixing highlighted by RHEED and XRD analyses.

A summary of the extracted magnetic values is presented in **figure 2.21**. The saturation magnetization depicts a clear decreasing behavior similar to the tendency observed for $Mn_{100-x}Ga_x$ samples. Once again, the 3:1 stochiometric sample exhibits the squarest shape resulting in the higher magnetization remanence. In comparison to $Mn_{75}Ga_{25}$, $Mn_{75}Ge_{25}$ has a lower coercive field which will prove to be very useful to carried out magnetic measurements where the applied magnetic field are limited. More importantly, the remanence turns out to be higher with Ge as a result of the squarer cycle. These two observations make $Mn_{75}Ge_{25}$ (ie. Mn_3Ge) a more suitable candidate to induce PMA in Mn_3Z-based stacks.

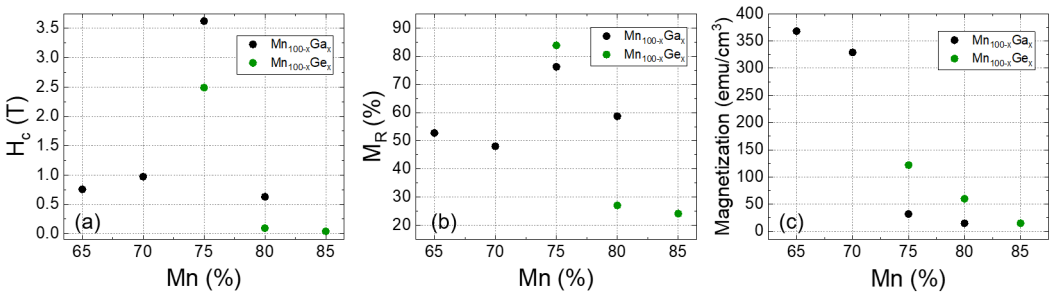

FIGURE 2.21: Comparison of the coercive field (a), magnetization remanence (b) and magnetization (c) extracted as a function of Mn content between $Mn_{100-x}Ga_x$ (in black) and $Mn_{100-x}Ge_x$ (in green) series.

XMCD measurements were performed on these alloys and were recorded at the L_2 and L_3 Mn edges. XAS and XMCD signals for $Mn_{75}Ge_{25}$ compound are given in **figure 2.22**. In the same way than for $Mn_{75}Ga_{25}$, the XAS signal exhibits a multiplet behavior coming from the different chemical environment felt by the two different types of Mn atoms. The XMCD signal shows a clear ferrimagnetic behavior that

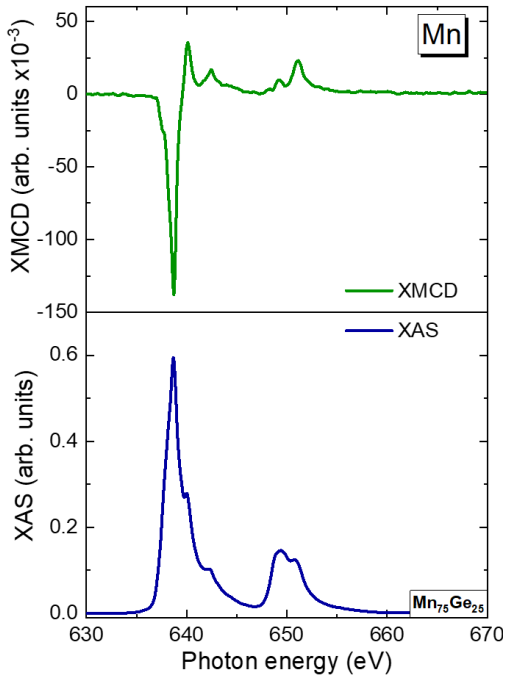

FIGURE 2.22: XAS (in blue) and XMCD (in green) signals measured at L_3 and L_2 Mn edges for $Mn_{75}Ge_{25}$. Measurements performed at 4 K with an applied magnetic field of 6 T.

validate the non collinear arrangement of the two Mn sublattices. Similarly to $Mn_{75}Ga_{25}$, no hysteresis cycle was performed due to the too low dichroic signal.

2.3.2 Mn_3Ge on Cr buffer layer

It should be noted that the coercive fields are still very high in Mn_3Ge on Pd buffer layers. In the literature much lower coercive fields were observed using Cr instead of Pd. Lower coercive fields are needed for our MOKE study since the maximum applied magnetic field for out-of-plane measurements is 0.9 T.

Structural properties

Similarly to Pd, Cr buffer layer was grown on MgO(001) at room temperature and annealed at a temperature of 730 °C ($T_{pyro} \approx 430$ °C) to get a smooth surface as revealed by RHEED in **figure 2.23**. The epitaxial relationship, checked by RHEED, is Cr [110](001) // MgO [100](001). Mn_3Ge layer (5 nm) is then deposited at a temperature of 450 °C ($T_{pyro} \approx 390$ °C) with $\Phi_{Mn} = 3.\Phi_{Ge} = 1.5 .10^{14}$ at.cm^{-2}.s^{-1}. No annealing process was done afterward to avoid interdiffusion. The resulting RHEED patterns are given in **figure 2.23**. The lattice mismatch between Cr and Mn_3Ge is higher than the one for a growth on Pd. Therefore, RHEED oscillations were observed only on the first planes and quickly disappears, probably due to the appearance of misfit dislocations. As we go along, in-plane Mn_3Ge stress relaxes and the surface quality increases as shown by the RHEED images of Mn_3Ge. $\frac{1}{2}$ streaks along the $[110]_{MgO}$ azimuth are a first indicator of a good chemical ordering. Once again, RHEED confirms the expected epitaxial relationship between Cr and Mn_3Ge which is Mn_3Ge [100](001) // Cr [110](001) since $\sqrt{2}.a_{Cr} \approx a_{Mn_3Ge}$. The sample was then capped with a 2 nm thick Au layer for XMCD measurements. The corresponding $\theta/2\theta$ X-ray diffraction scan is shown in **figure 2.23** and displays a perfect growth along the (001) direction for Cr and Mn_3Ge. The extracted out-of-plane cell parameter from Mn_3Ge (004) peak is c = 7.12 Å in good agreement with the $D0_{22}$ structure. As expected, the out-of-plane value is lower than the ones obtained with Pd buffer layers since the Mn_3Ge layer slightly relaxes to fit the Cr buffer in-plane lattice. These data fit with the RHEED observation and confirm the growth in the $D0_{22}$ structure.

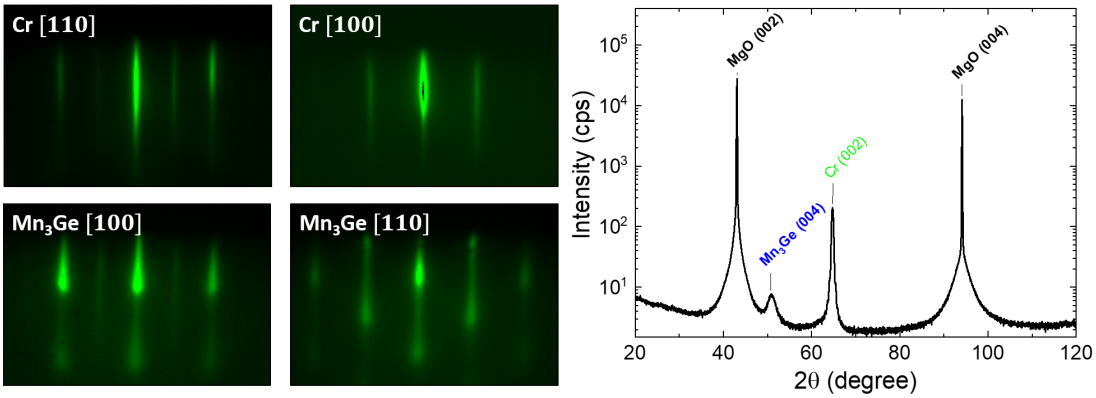

FIGURE 2.23: On the left, RHEED patterns with a beam applied along the $[100]_{MgO}$ and $[110]_{MgO}$ azimuths for Cr at the top and Mn_3Ge at the bottom. On the right, $\theta/2\theta$ XRD spectra of the Cr/Mn_3Ge/Au sample.

Magnetic properties

The sample was measured at the Mn $L_{2,3}$ edges and the resulting data are given in **figure 2.24**. As in the previous Mn_3Z measurements, multiplet fine structure is observed in the absorption spectrum (**figure 2.24b**). However, the XMCD spectrum differs from that observed in previous Mn_3Z : one can note two features at the L_3 edge dichroic signal (noted A and B in **figure 2.24a**) that were not observed previously. We consequently recorded hysteresis loops[14] at the two photon energies corresponding to A and B (**figure 2.24c**). A square loop with a large coercive field is observed for A. This means that the growth direction is a strong magnetic anisotropy axis as expected. The second feature leads to a very different magnetic behavior. Similar experiments performed on samples with different Mn_3Ge thicknesses showed that this B contribution does not depends on the film thickness (on the contrary to A). This feature thus comes from interfacial effects. A possible explanation is that the 2 nm Au capping is not sufficient to protect the film and some oxidation close to the Au capping layer occurred. This hypothesis will be confirmed later.

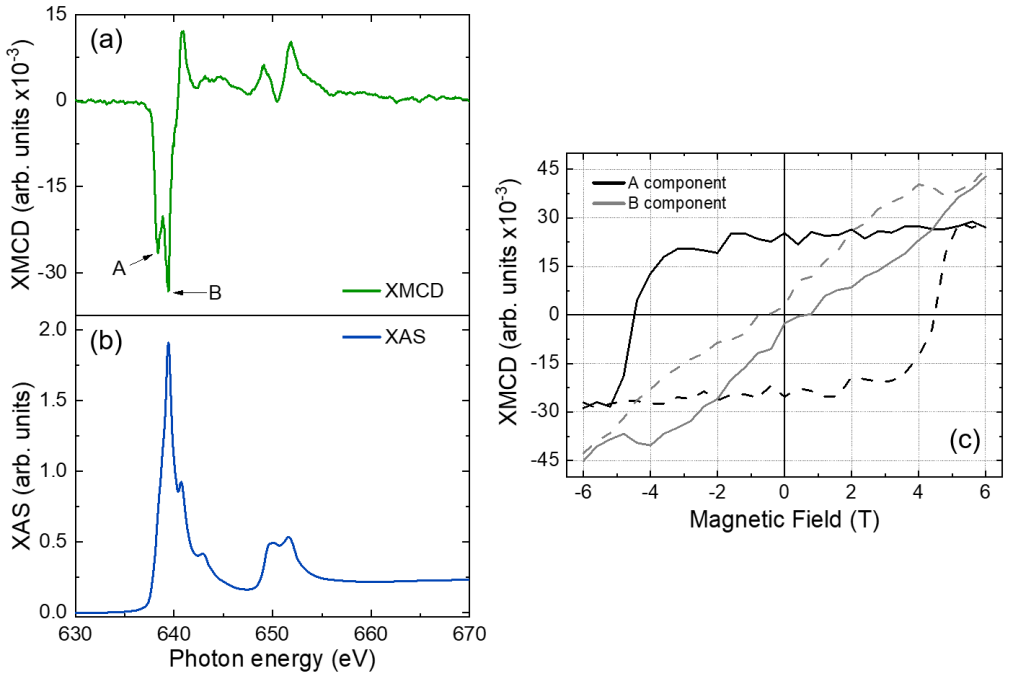

FIGURE 2.24: XMCD (a) and XAS (b) spectra measured at the Mn $L_{2,3}$ edges of Mn_3Ge. (c) Mn_3Ge hysteresis loops measured at the L_3 edge of Mn by XMCD with an out-of-plane applied magnetic field. Black and grey curves correspond respectively to the A and B components identified on the XMCD spectrum (a). Measurement performed at 300 K.

The results obtained in this section unveil that, similarly to Pd buffer, the growth of Mn_3Ge on Cr buffer leads to the stabilization of the $D0_{22}$ structure with a strong perpendicular magnetic anisotropy. However, the magnetic behavior seems a little bit different from Mn_3Ga and Mn_3Ge measured in the previous sections. It is suspected to come from an inefficient Au capping as will be confirmed in the following.

[14]Because of the too low Mn_3Ge dichroic signal, the standard way to measure an XMCD loop (by following the variation of the dichroic signal while swiping the magnetic field) is not possible. Therefore, multiple XMCD scans were performed at different magnetic field values resulting in a XMCD vs. B mapping.

2.3.3 Mn_3Ge/Co_2FeGe bilayers capped with Au

Structural properties

Cr and Mn_3Ge growth process is identical to the one described in the previous section. The Co_2FeGe layer is deposited on top of them and is expected to have a unit cell turned by 45° with respect to the above layer since $\sqrt{2}.a_{Mn_3Ge} \approx a_{Co_2FeGe}$. The fluxes are fixed as $\Phi_{Co} = 2.\Phi_{Fe} = 2.\Phi_{Ge} = 1\ .10^{14}$ at.cm^{-2}.s^{-1} and the temperature deposition is set at 260 °C ($T_{pyro} \approx 210$ °C) to avoid interdiffusion. The resulting RHEED patterns for Cr, Mn_3Ge and Co_2FeGe are given in **figure 2.25** and confirm the Co_2FeGe [110](001)//Mn_3Ge [100](001)//Cr [110](001)//MgO [100](001) epitaxial relationship. Cr and Mn_3Ge RHEED patterns are in accordance with the ones observed in the previous section. For Co_2FeGe, a single-crystalline surface with some roughness is obtained and the $\frac{1}{2}$ supplementary streaks are a first fingerprint of chemical order in the layer. Five samples were grown with a fixed 5 nm thick Mn_3Ge and a varying Co_2FeGe thickness from 2 to 6 nm. The Au capping thickness was fixed to 2 nm for XMCD needs. The X-ray diffraction spectra obtained on these stacks are shown in **figure 2.25**. All the samples exhibit a perfect single-crystalline growth of Mn_3Ge and Co_2FeGe along the (001) direction and the extracted Mn_3Ge c value is $c_{Mn_3Ge} = 7.14$ Å in perfect agreement with the $D0_{22}$ structure.

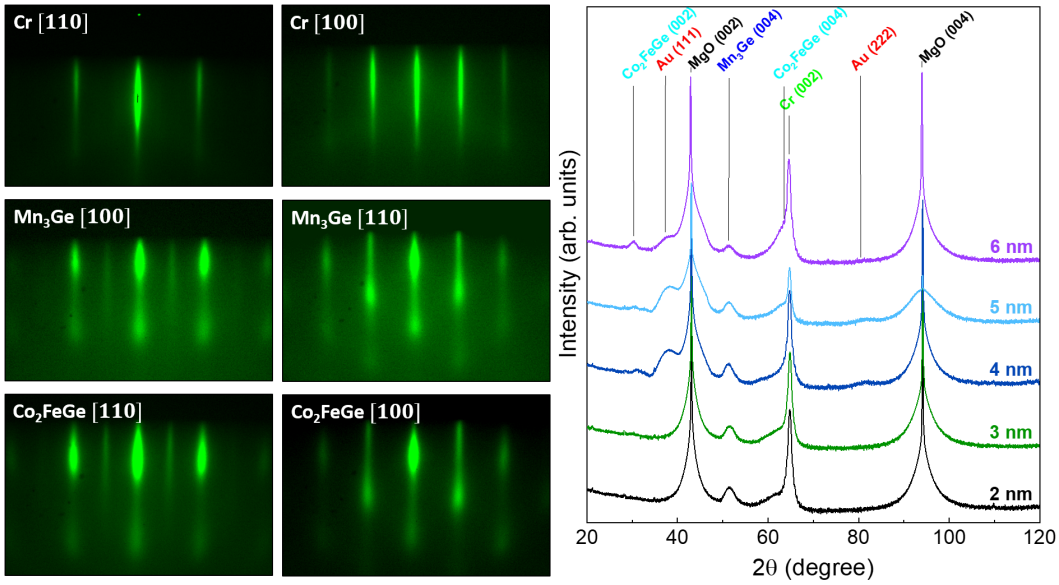

FIGURE 2.25: On the left, RHEED patterns with a beam applied along the $[100]_{MgO}$ and $[110]_{MgO}$ azimuths for Cr at the top, Mn_3Ge in the middle and Co_2FeGe at the bottom. Images obtained for the sample Cr(20 nm)/Mn_3Ge(5 nm)/Co_2FeGe(2 nm). On the right, $\theta/2\theta$ X-ray diffraction spectra of the Mn_3Ge(5 nm)/Co_2FeGe(X nm) series with X = 2, 3, 4, 5 and 6 nm respectively in black, green, blue, light blue and pink colors.

In order to distinguish both layers and get local information, transmission electron microscopy was performed. A Mn_3Ge/Co_2FeGe cross section was built by focused ion beam etching with the $[110]_{Co_2FeGe}$ zone axis (ie. $[100]_{Mn_3Ge}$ zone axis). With this peculiar direction, atomic columns made of a unique element can be observed in the presence of chemical order. Cross section's low magnification image is given on the left of **figure 2.26** and a zoom in STEM mode is given on the right side.

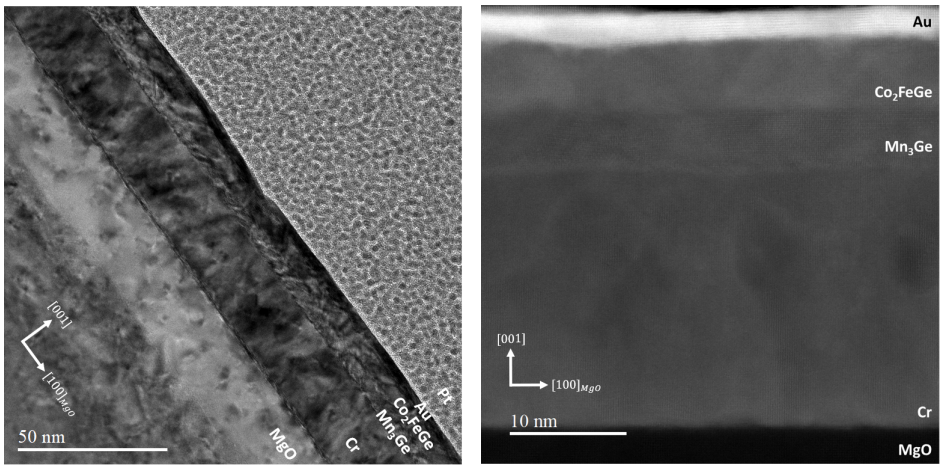

FIGURE 2.26: On the left, large TEM cross section image of MgO/Cr/Mn_3Ge/Co_2FeGe/Au sample. On the right STEM-HAADF image unveiling the different layers thanks to Z contrast.

All the layers depict a smooth surface with a slight roughness already observed in RHEED. Even if the contrast between Mn_3Ge and Co_2FeGe is weak, both layers are already distinguishable and well separated. A higher magnification STEM-HAADF image of Mn_3Ge is given in **figure 2.27**. The columns intensity modulation is already visible to the naked eye since Mn (Z = 25 e^-) and Ge (Z = 32 e^-) generate a good contrast. The expected pattern for a perfectly ordered structure with a cut along the $[100]_{Mn_3Ge}$ zone axis is given at the top of **figure 2.27**. Line profiles are performed on the rectangular areas marked in red, green and blue allowing to clearly attest to the good chemical ordering in Mn_3Ge layers. The resulting intensity line profiles performed on the treated STEM-HAADF image of **figure 2.27** are perfectly in agreement with the ordered Mn_3Ge structure sketched on top of the figure.

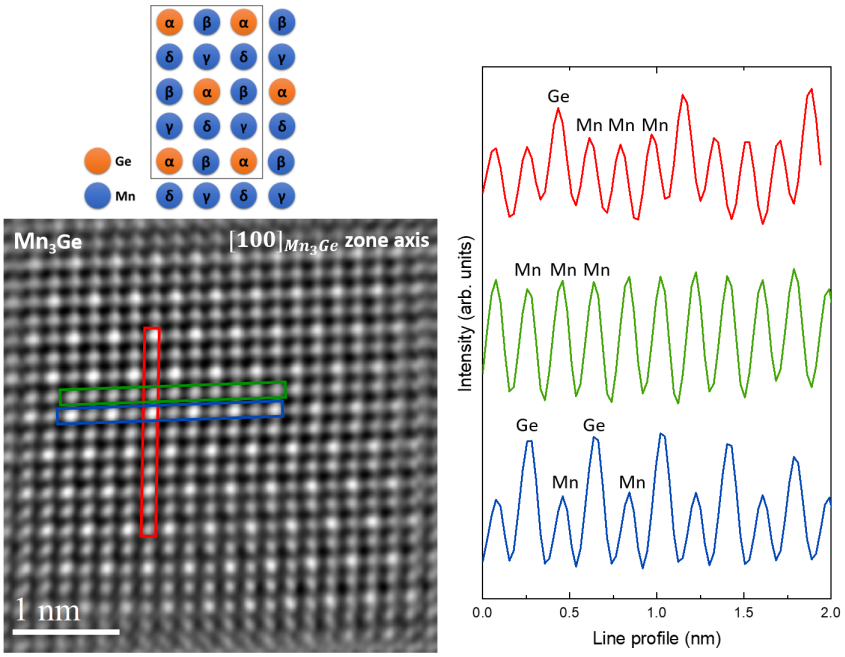

FIGURE 2.27: Inverse FFT of STEM-HAADF Mn_3Ge image with the corresponding line profile performed on red, green and blue areas. The expected atomic column arrangement is given on the upper part.

Similar data treatment was done for the Co_2FeGe layer as shown by the zoomed image of **figure 2.28**. The expected pattern for the $L2_1$ phase (ie. the perfectly ordered full-Heusler phase) and line profiles for the red, green and blue areas are shown. This time, an observation to the naked eye is harder since Co, Fe and Ge have close atomic numbers but the intensity line profiles confirm the $L2_1$ phase since their intensity modulations suit with the prediction given on the top left part of the figure.

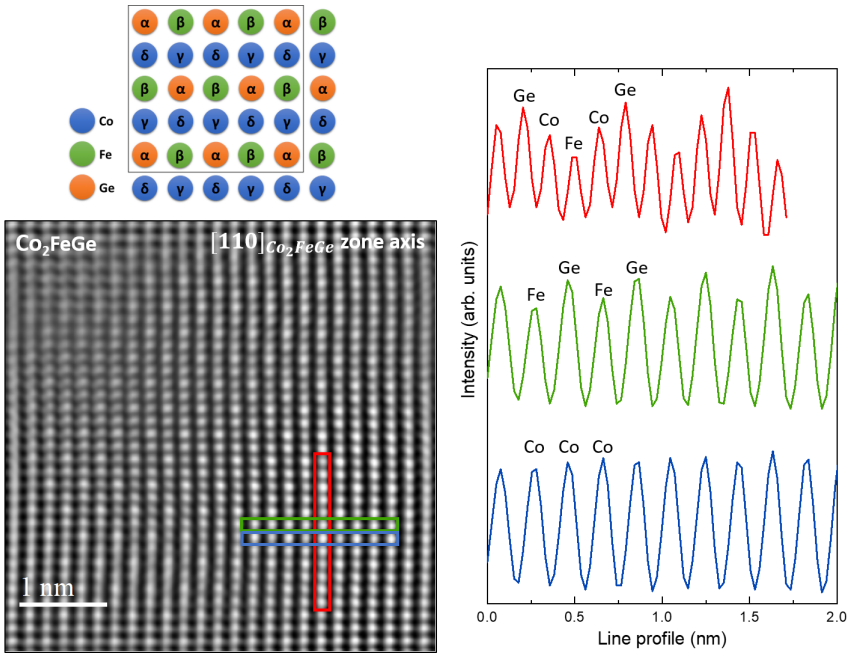

FIGURE 2.28: Inverse FFT of STEM-HAADF Co_2FeGe image with the corresponding line profile performed on red, green and blue area. The expected atomic column arrangement is given on the upper part.

Finally, EDX was performed to ensure that no interdiffusion occurred between the layers. EDX mapping is given in **figure 2.29** for O (K edge), Cr (L edge), Mn (L edge), Ge (L edge), Co (L edge), Fe (L edge) and Au (M edge). All the layers are well separated with no interdiffusion. In addition to the elements present in the stack, we also checked a potential O contamination, at least in Mn_3Ge, Co_2FeGe and Au capping (not in the Cr layer since O K edge and Cr L edge are too close in energy. The detection of O in the Cr layer is thus an artefact).

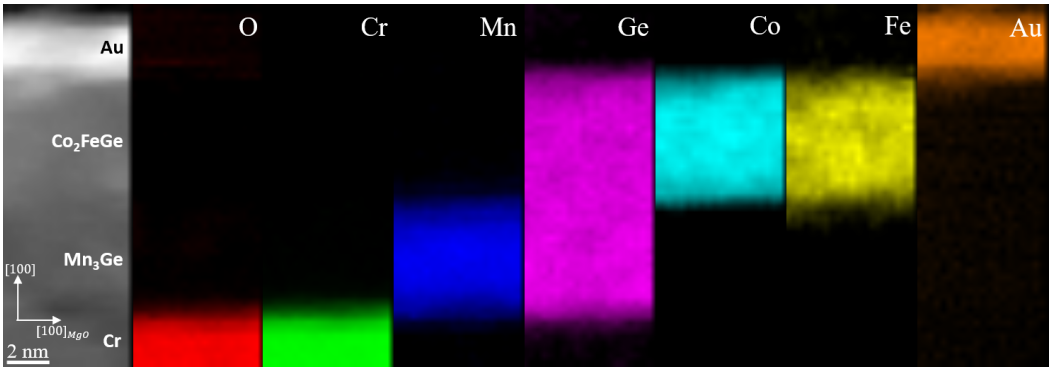

FIGURE 2.29: EDX mapping of the MgO/Cr/Mn_3Ge/Co_2FeGe/Au sample. The mapped area is shown on the left and the probed edges are K edge of O, L edges of Cr, Mn, Ge, Co, Fe and M edge of Au.

Magnetic properties

SQUID-VSM measurements were first performed for the different Co_2FeGe thicknesses as shown in **figure 2.30** and all of them display PMA. As expected, the increase in Co_2FeGe thickness leads to a weaker PMA since the higher Co_2FeGe magnetic volume tends to align the magnetization in the sample plane due to its classical thin film behavior. On the other hand, the strong magnetocrystalline magnetic anisotropy of Mn_3Ge tries to keep an out-of-plane easy axis of magnetization. The resulting loop is thus a competition between these two contributions explaining the loss of square shape for higher values of t_{Co_2FeGe}. Indeed, the curved shape for the thicker samples is explained by an easy axis of anisotropy that tends to switch within the film plane.

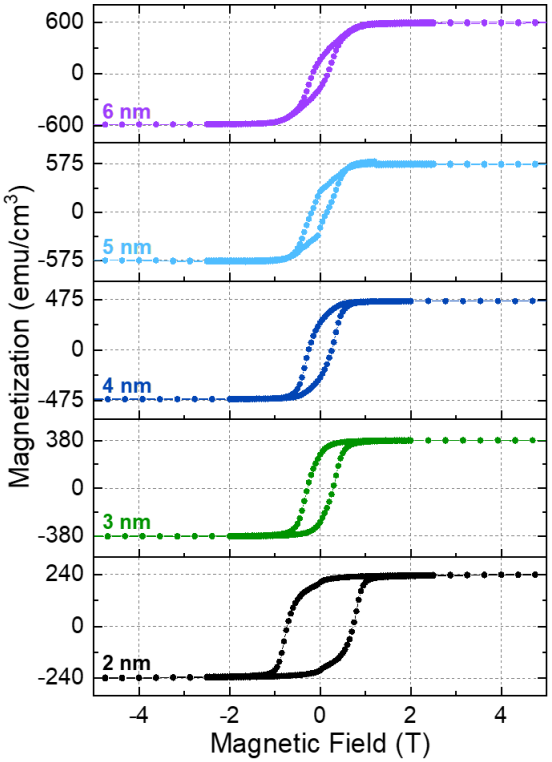

FIGURE 2.30: SQUID-VSM hysteresis loops measured with an out-of-plane in black applied magnetic field for the Mn_3Ge(5 nm)/Co_2FeGe(X nm) series with X = 2, 3, 4, 5 and 6 nm. Measurements performed at 300 K with an applied magnetic field up to 7 T.

The extracted values of moments at remanence and coercive fields, given in **figure 2.31a** and **2.31b**, are another proof of the transition from out-of-plane to in-plane magnetization when increasing the Co_2FeGe thickness. On its side, the saturation magnetization (**figure 2.31c**) increases linearly with the Co_2FeGe thickness due to a higher magnetic volume.

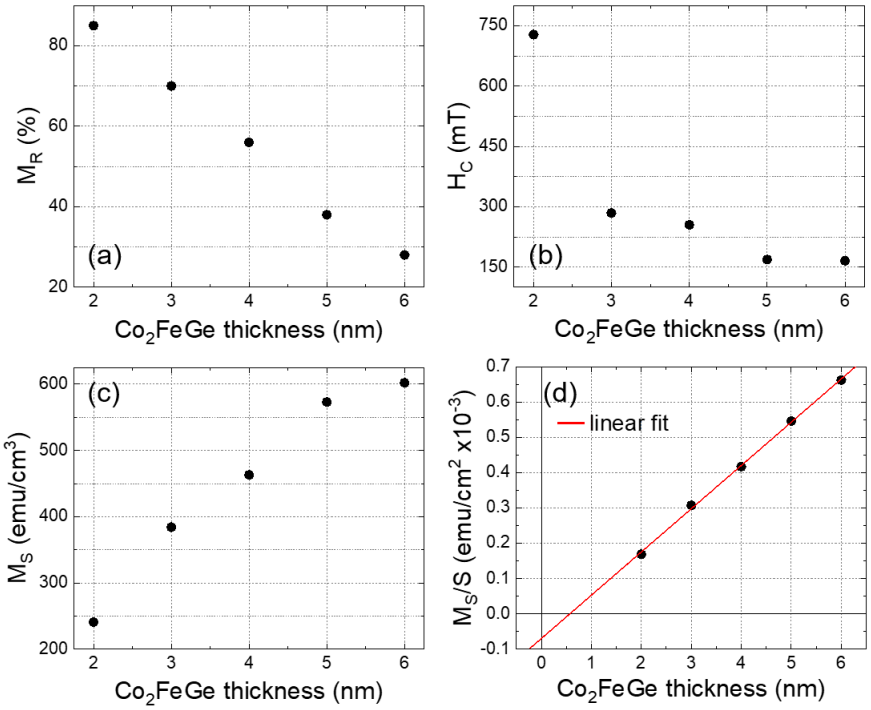

FIGURE 2.31: Summary of the extracted magnetization remanence M_R (a), coercive field H_c (b) and saturation magnetization M_S (c). (d), saturation magnetization per surface unit $\frac{M_S}{S}$ as a function of Co_2FeGe thickness.

Thanks to the Co_2FeGe thickness dependency series it is possible to plot the magnetization per surface unit as a function of Co_2FeGe thickness to obtain information on the magnetic state of Mn_3Ge and Co_2FeGe separately by assuming the following relationship:

$$\frac{M_S}{S} = M_{Mn_3Ge}.t_{Mn_3Ge} + M_{Co_2FeGe}.t_{Co_2FeGe} \tag{2.3}$$

With M_S the saturation magnetization (emu), S the magnetic surface (cm^2), M_i and t_i are respectively the magnetization (emu.cm^{-3}) and the thickness (cm) of Mn_3Ge and Co_2FeGe. The magnetization per surface unit vs. Co_2FeGe thickness graph is given in **figure 2.31**. The linear fit in red checks an essential information since the ordinate intercept is negative.

This result may be explained in two ways :

i. The magnetization of Mn_3Ge and Co_2FeGe are antiferromagnetically coupled.

ii. The Co_2FeGe magnetic moment is lower at the interface with Mn_3Ge.

Moreover, the magnetization value of Co_2FeGe can be determined by the slope's value of the fit. By doing so, M_{Co_2FeGe} is determined to be 1226 $\pm$ 23 emu.cm^{-3} in good agreement with values reported for Co_2FeGe thin films [154].

To address the question of magnetic coupling, XMCD experiments were performed at Mn, Fe and Co L edges on all five samples : MgO/Cr(20 nm)/Mn_3Ge(5 nm)/Co_2FeGe(X)/Au(2 nm) with X = 2, 3, 4, 5, 6 nm. The results are shown in **figure 2.32**. XMCD depicts a negative signal at the L_3 edge and a positive one at the L_2 edge

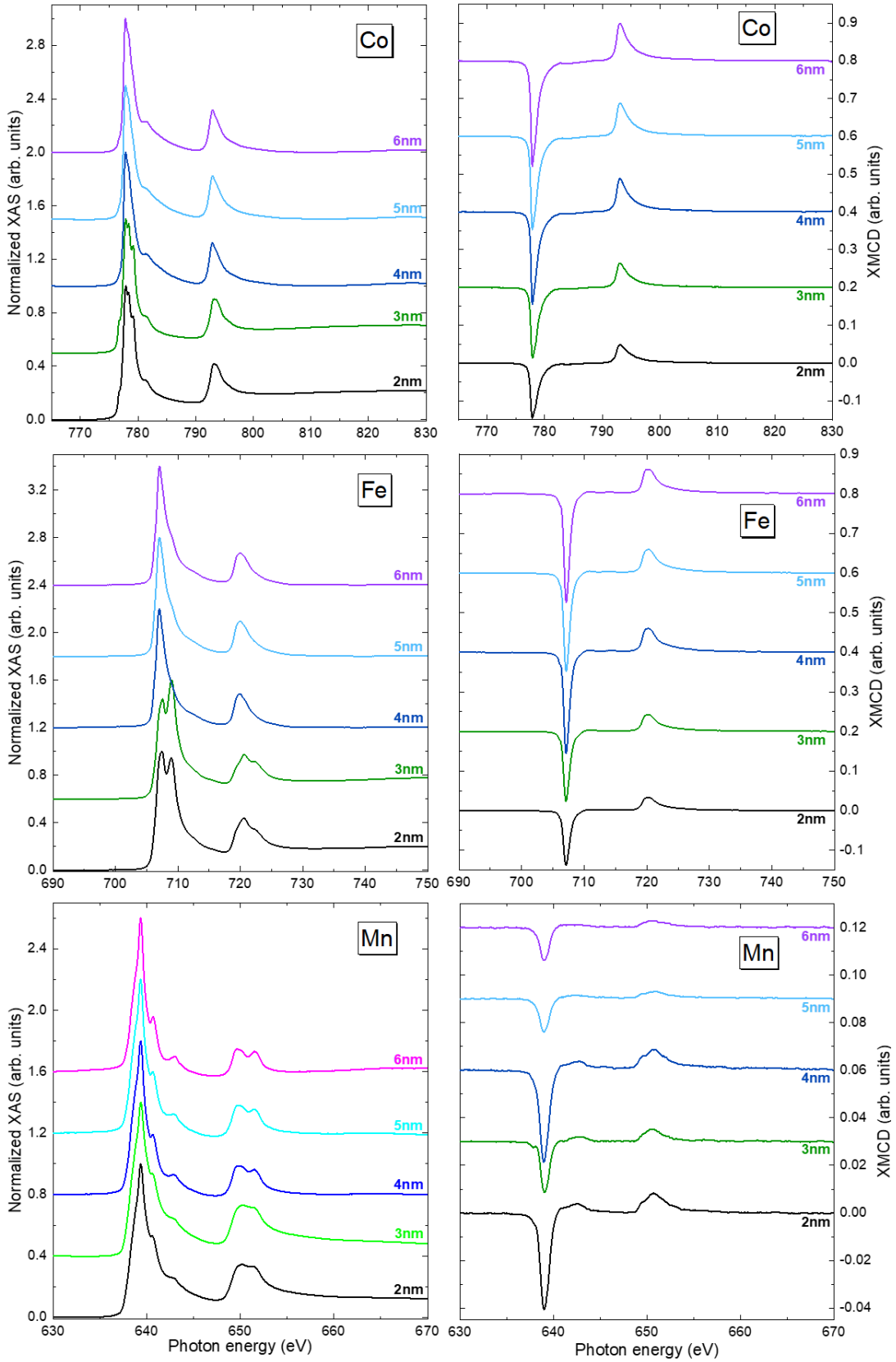

FIGURE 2.32: XAS (on the left) and XMCD (on the right) spectra measured at $L_{2,3}$ edges of Co, Fe and Mn. The thicknesses reported on the right of the curves stand for Co_2FeGe layer thickness. All the curves are for Au capped samples. Measurement performed at 300 K under a 6 T magnetic field.

unveiling a ferromagnetic coupling between all the elements. The layers are thus ferromagnetically coupled showing a different behavior compared to literature reports on similar bilayer structures [143, 144, 145, 146, 147] where an antiferromagnetic coupling is observed. We should keep in mind that a change of bilayer structure may change the magnetic coupling.

To go further, one should note that the Mn-edge multiplet features typical of Mn_3Ge is still observed for X = 4 to 6 nm, but XAS spectra for X = 2 and 3 nm are now different. One should suspect some oxidation due to some inefficiency of the Au capping. This is actually confirmed by looking at the Co and Fe edges for the 2 and 3 nm thick Co_2FeGe samples. To get a full set of experimental results with X varying from to 2 to 6 nm, we thus prepared the same X = 2 and 3 nm stacks but capped with V (4 nm). The results are shown in **figure 2.33**.

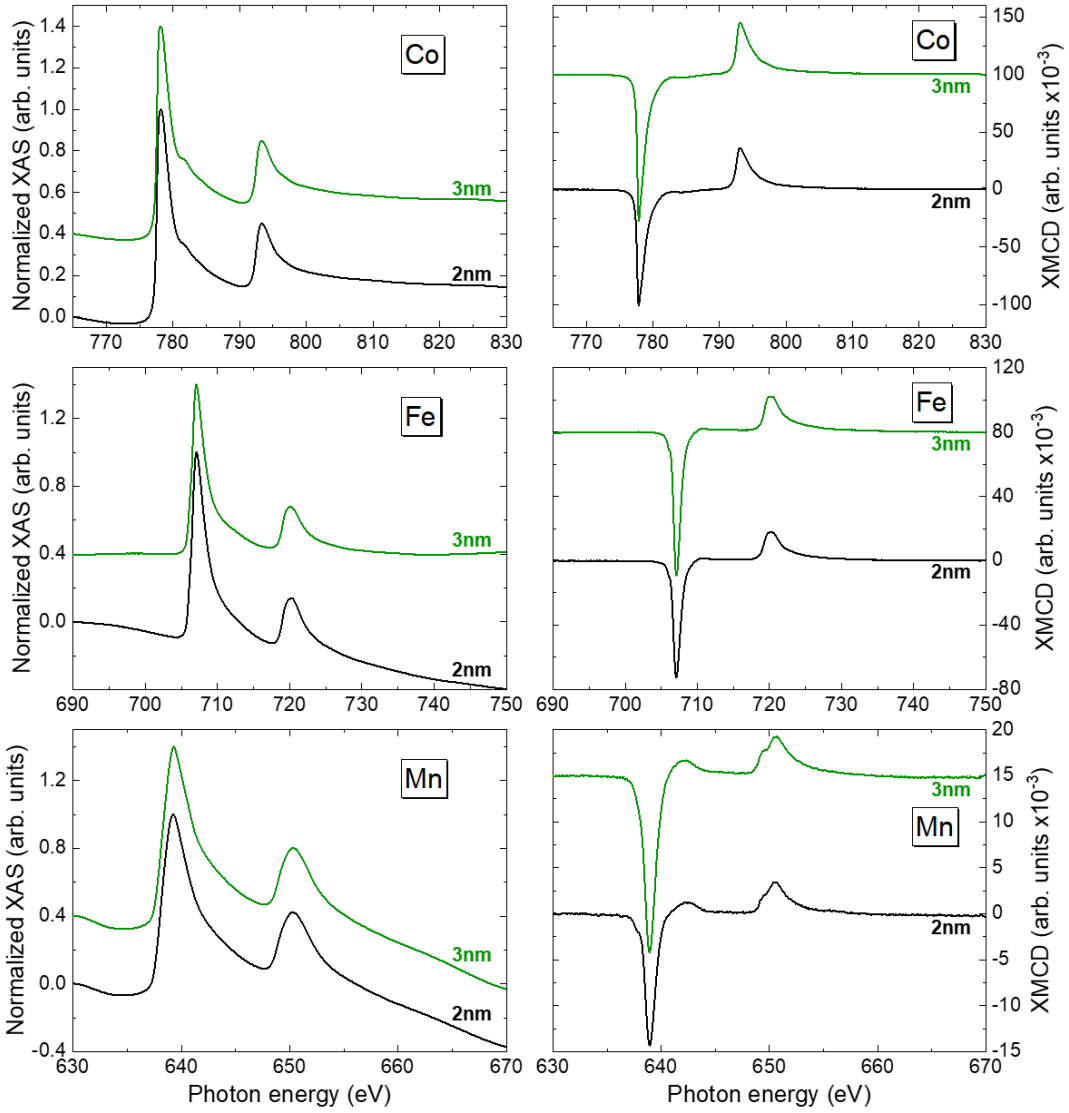

FIGURE 2.33: XAS (on the left) and XMCD (on the right) spectra measured at $L_{2,3}$ edges of Co, Fe and Mn for Mn_3Ge(5 nm)/Co_2FeGe(X nm) samples capped with V with X = 2 nm in black and X = 3 nm in green. Measurement performed at 300 K under a 6 T magnetic field.

Now all the absorption spectra do not show any O contamination but very surprisingly, we lost the multiplet behavior in Mn XAS edge. We will discuss this surprising result further.

Finally, the orbital, spin and total magnetic moments for Co and Fe were extracted from XMCD spectra using the sum rules analysis (see **appendix C**) for the Au capped and V capped samples (**figure 2.34**). Firstly, the impact of oxidation on the two thinnest samples covered with Au is visible with low calculated moment. The calculated moment is more reliable on the two samples capped with V. Secondly, the total moment of Co and Fe are close to the theoretical values for the highest Co_2FeGe thicknesses. On the other hand, the two thinner samples, especially for Fe, displayed a reduced moment. This behavior, added to the ferromagnetic coupling between Mn_3Ge and Co_2FeGe, allows us to choose the scenario (ii) of the previous discussion on the $\frac{M_S}{S} = f(t_{Co_2FeGe})$ curve.

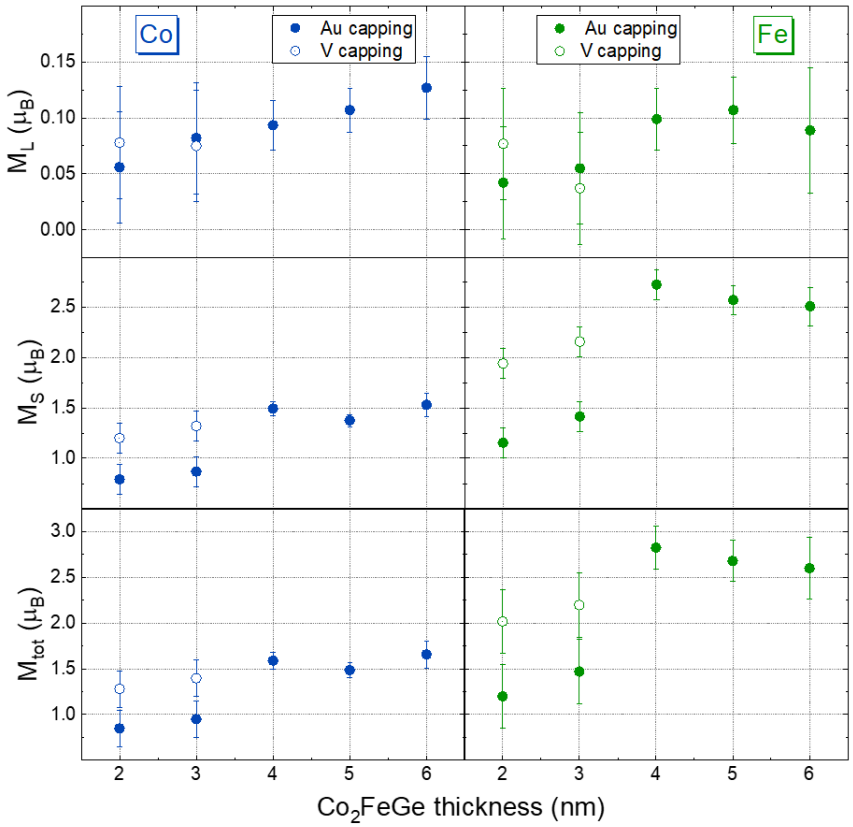

FIGURE 2.34: From top to bottom, extracted values of orbital, spin and total magnetic moments for Co (left) and Fe (right). Solid circles are for Au capped samples, hollow circles are for V capped samples. Theoretical values in red dashed lines taken from [111].

XMCD hysteresis loops were recorded at Fe and Mn edges with a magnetic field normal to the sample surface (**figure 2.35**[15]) and are in perfect agreement with the SQUID-VSM data with a clear cycle opening for each thickness. As expected, a clear decreasing tendency of the out-of-plane magnetic anisotropy is observed while increasing Co_2FeGe thickness. The magnetization gradually switches in the sample

[15]Only the loops performed at Fe and Mn edges are shown since Co loops are similar. Fe loops were chosen instead of Co ones since the XMCD signal is much higher for Fe than Co.

plane because of the higher Co_2FeGe volume that enhances the demagnetization energy and counterbalances the volume anisotropy of Mn_3Ge. Nonetheless, hysteresis loops obtained for low Co_2FeGe thickness show a good remanence with slightly bent cycles and are very promising.

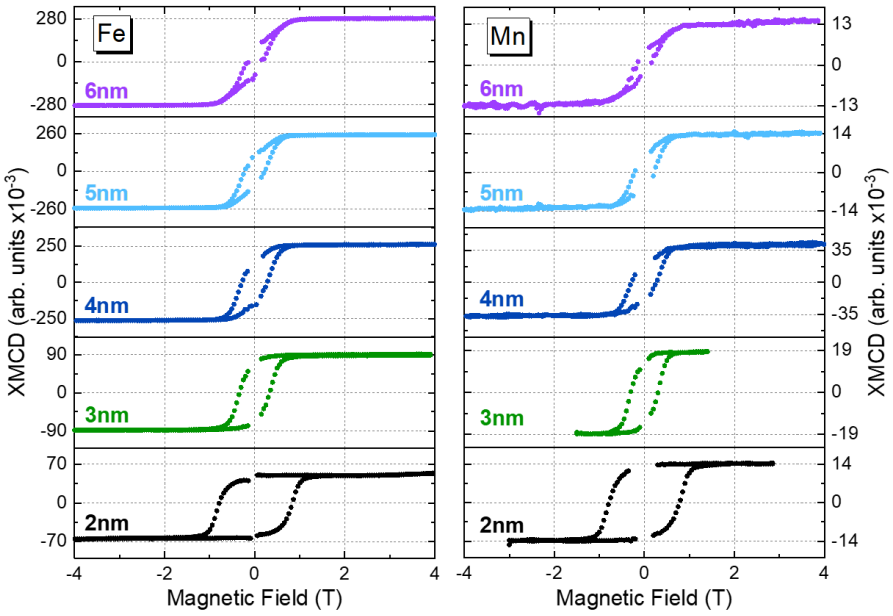

FIGURE 2.35: XMCD hysteresis loops obtained at the Fe (on the left) and Mn (on the right) L_3 edges with an out-of-plane applied magnetic field. From bottom to top, Co_2FeGe thickness from 2 nm to 6 nm. Measurements performed at 300 K.

Finally, **figure 2.36** displays the normalized hysteresis loops performed at the L_3 edges of each atom (namely Co, Fe and Mn) for the sample Mn_3Ge(5nm)/Co_2FeGe(3nm). All the curves unveil the same switching shape. This is a clear proof that the stack behaves as a unique ferromagnetic layer and eliminates any exotic magnetic arrangement from one layer to the other.

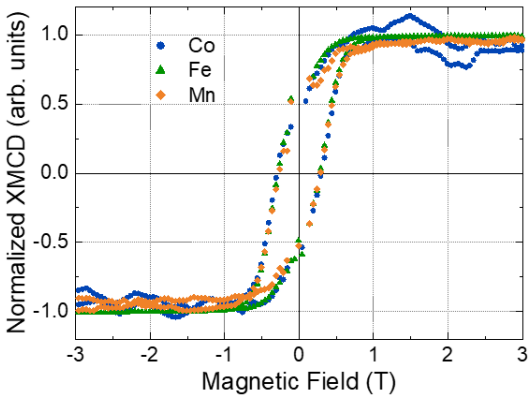

FIGURE 2.36: Normalized Mn_3Ge(5 nm)/Co_2FeGe(3 nm) XMCD hysteresis loops measured at the L_3 edges of Co (blue circles), Fe (green triangles) and Mn (orange diamonds) with an out-of-plane applied magnetic field. Measurements performed at 300 K.

This part was dedicated to bilayers structure composed of two Heusler alloys, namely Mn_3Ge and Co_2FeGe. The growth of Mn_3Ge/Co_2FeGe samples was successfully done in the desired structures for both compounds. Transmission electron microscopy has revealed a significant chemical order in both samples. This observation is of prime importance since chemical disorder can strongly impact the physical properties of Heusler alloys. Perpendicularly magnetized bilayers were obtained and XMCD revealed a ferromagnetic coupling between both layers for every thickness. The hysteresis loops measured for the thinnest bilayers are promising thanks to their good remanences. Nonetheless, the magnetic remanence quickly decreases for higher Co_2FeGe thicknesses where the cycles tend to bend. One of the solutions may be to use SLs to straighten up the loops and increase the magnetic remanence.

2.3.4 Influence of the capping layer

Since the capping layer was observed to strongly affect the Mn XAS L edge, 5 nm thick Mn_3Ge films were prepared with different capping, namely Au(2 nm), V(2nm) and MgO(1 nm)/Ti(1.5 nm). All the curves shown in this paragraph are labeled according to the capping layer to distinguish the three samples. The XAS are shown in **figure 2.37**. Again, the Mn multiplet is present with Au capping and vanishes with V as in the previous section. This situation is in between with MgO/Ti capping: the multiplet is now present compared to the V capping but is less pronounced than with Au capping.

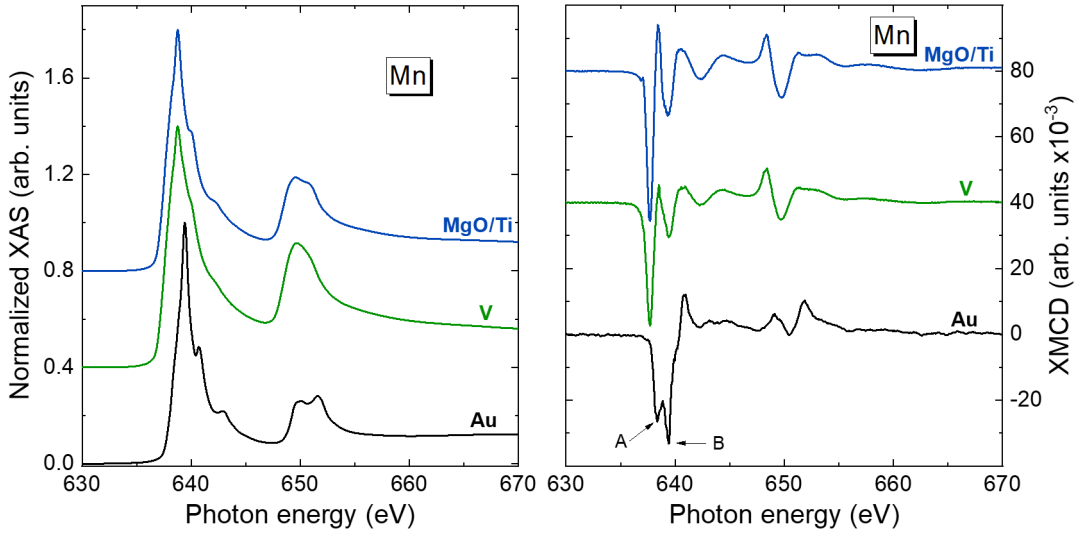

FIGURE 2.37: XAS (on the left) and XMCD (on the right) spectra measured at the Mn $L_{2,3}$ edges of Mn_3Ge. Samples with Au, V and MgO/Ti capping are respectively plotted in black, green and blue colors. Measurement performed at 300 K.

The XMCD hysteresis loops were thus recorded and compared in **figure 2.38** for Au and V capping. The Au capped sample differs from the V one by the supplementary magnetic contribution in the XMCD signal. Indeed, the hysteresis loops observed for the V capped sample present a unique contribution. On the one hand, the double contribution of the Au capped sample is probably related to an oxidation of the

Mn_3Ge layer. On the other hand, the metallic-like shape of the Mn XAS with V capping may be explained by some interdiffusion, but we never observed it (at least under UHV just after the layer preparation). Furthermore, TEM measurements validate that no interdiffusion occurred. At this stage of the investigations, we have no explanation for these different Mn L edges shapes.

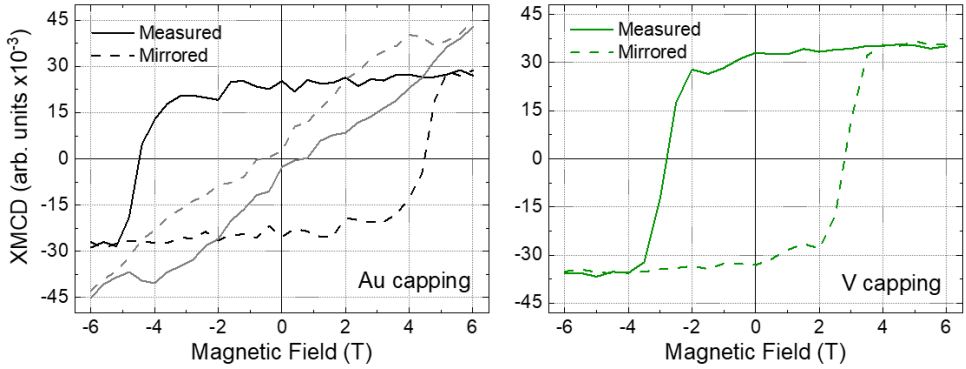

FIGURE 2.38: Mn_3Ge hysteresis loops measured at the L_3 edge of Mn by XMCD with an out-of-plane applied magnetic field for Au capping on the left and V capping on the right. The black and grey loops for Au capping come respectively from the A and B components of the Mn L_3 edges. Measurement performed at 300 K.

To summarize, the choice of the capping layer seems to be of crucial importance for these materials and stacks. However, one should keep in mind that very small thicknesses were used to cap the stacks, a constraint imposed by the XMCD analysis. This should not be a problem for devices since thicker capping were usually used. Indeed, as revealed by the sum rules analysis, the shape's change of the XAS signal does not seem to impact the magnetic properties since the extracted moments in the previous section with different capping layers seem reliable and consistent.

2.3.5 Mn_3Ge/Co_2FeGe superlattices

The next step of this study was to look at the magnetic properties evolution when repeating the Mn_3Ge/Co_2FeGe bilayer. It is well-known that repetitions usually affect the coercive field, the remanence, and the total magnetic anisotropy of the systems [149]. Moreover, the higher magnetic volume will allow us to characterize the films by MOKE measurements. These are the goals of this section, still done with Co_2FeGe to get separated XMCD information of the two layers.

Sample architecture and growth

The growth process is similar to the one explained in the previous section. This time the Cr buffer was 10 nm thick for the whole series. Mn_3Ge and Co_2FeGe were both deposited at around 240 °C ($T_{pyro} \approx 220$ °C) to avoid interdiffusion between layers. The SLs consist in five repetitions of the [Mn_3Ge/Co_2FeGe] elementary block[16]. Finally, we chose the MgO/Ti capping discussed before. A sketch of the SL is drawn in **figure 2.39**. In this study, five samples were grown with the following composition: MgO/Cr(10 nm)/[Mn_3Ge(3 nm)/Co_2FeGe(X nm)]$_{\times 5}$/MgO(1)/Ti(1.5) with X = 1, 2, 3, 4 and 5 nm. Since in this series only the Co_2FeGe thickness varies, most of the graphs plotted below use it to distinguish the samples. The RHEED patterns all over the stack growth were similar to what was observed before.

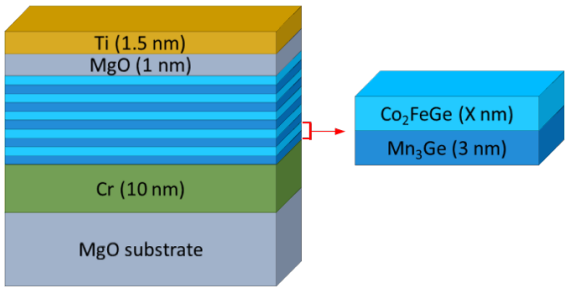

FIGURE 2.39: On the left, sketch of the SLs. On the right, representation of the elementary block of the SLs.

Magnetic properties

The magnetic properties were investigated by using on the one hand XMCD and *in situ* MOKE (see **appendix D** for details on the set-up) on the other hand. The XAS and XMCD spectra for the whole series measured at the $L_{2,3}$ edges of Co, Fe and Mn are given in **figure 2.40**. Co and Fe transitions are similar to the one observed in the previous section for V capped samples. First, no oxidation is observed on Co and Fe. Second, the Mn XAS are different to what has been observed on Au capped samples, but are similar to those observed on samples capped with V or MgO/Ti. On their side, the dichroic signals depict a similar form to those obtained for Mn_3Ge/Co_2FeGe bilayers.
The identical XMCD signs present at the L_3 (negative) and L_2 (positive) edges of Co, Fe and Mn attest to the ferromagnetic exchange between the elements and layers.

[16] In this thesis, the number of repetitions will be indexed using a subscript such as [Mn_3Ge/Co_2FeGe]$_{\times 5}$.

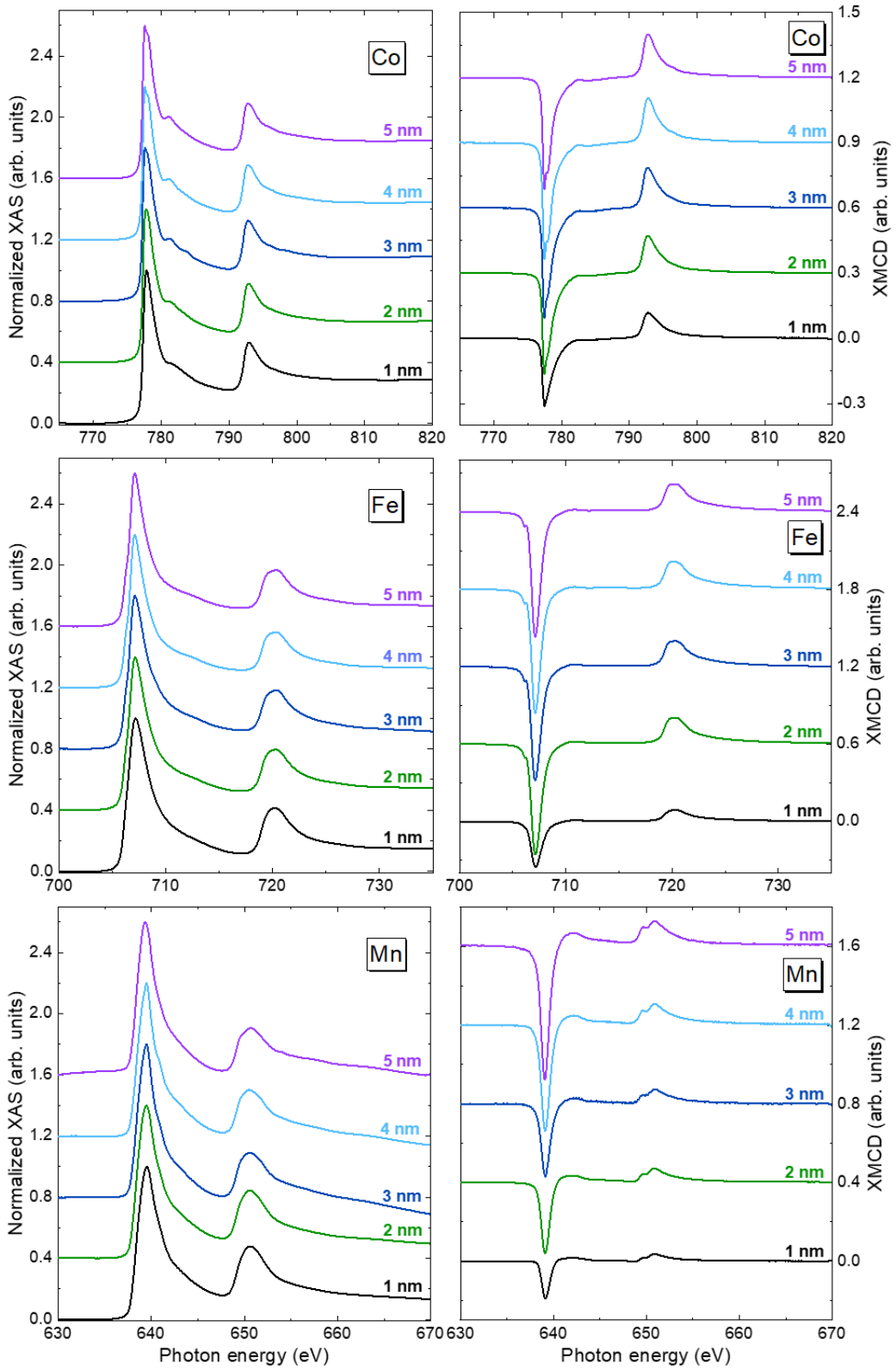

FIGURE 2.40: XAS (on the left) and XMCD (on the right) spectra measured at $L_{2,3}$ edges of Co, Fe and Mn. The thicknesses reported on the right of the curves stand for Co_2FeGe layer thickness. Measurement performed at 300 K under a 6 T magnetic field.

Hysteresis loops were performed using in-plane and out-of-plane applied magnetic field[17]. The resulting data measured at the Fe edge are given in **figure 2.41**. First, samples with t_{Co_2FeGe} = 1 and 2 nm are clearly perpendicularly magnetized and the loops are sharper than for the bilayers of the previous chapter with 100 % of remanence[18]. For higher Co_2FeGe thicknesses, the magnetization starts to switch within the film plane. The loops measured in grazing incidence confirm this behavior with an obvious easy axis toggling in the film plane for the thicker samples. A cycle opening is present for the grazing incidence curves of t_{Co_2FeGe} = 1 and 2 nm and is attributed to the fact that the real in-plane direction is not probed but only a direction between the in- and out-of-plane axis.

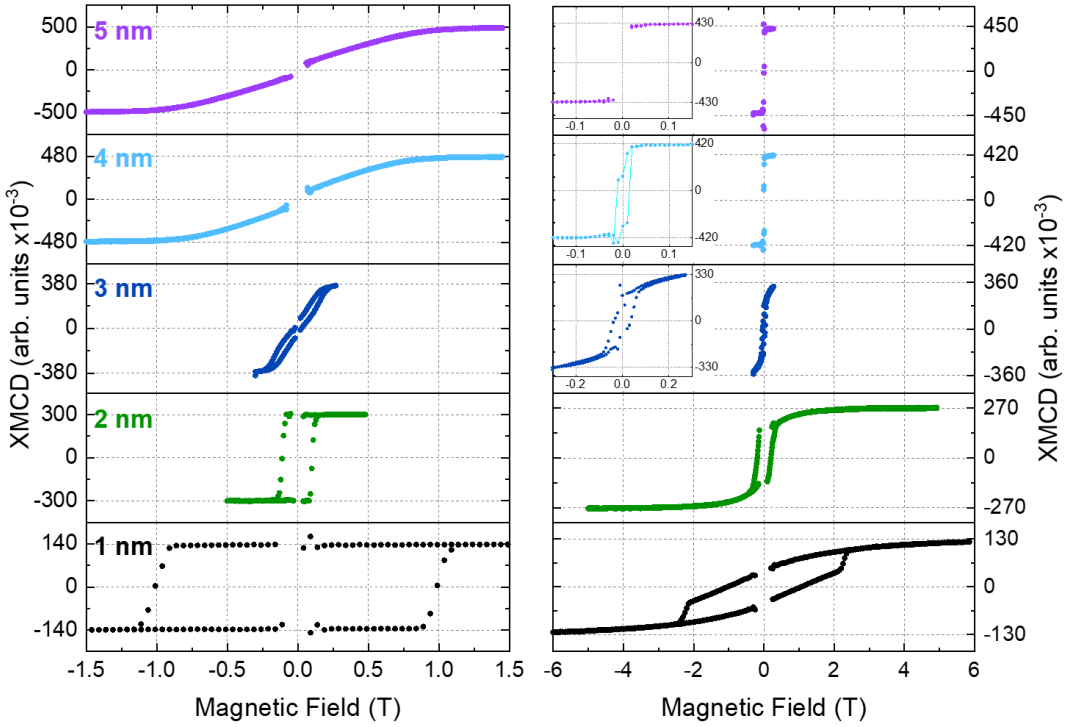

FIGURE 2.41: XMCD hysteresis loops obtained at the Fe L_3 edge with a beam applied normal to the sample surface (on the left) and applied with a beam applied in grazing incidence (on the right). From bottom to top, increase of the Co_2FeGe thickness from 2 nm to 5 nm. The inset graphs are zooms of the loops. Measurements performed at 300 K.

Finally, spin, orbital and total magnetic moments were extracted using the sum rules (**figure 2.42**). Similarly to bilayers, the thinner sample depicts magnetic moments values lower than in the bulk. This is explained by the only 1 nm thick Co_2FeGe that has still not reached its bulk values.

[17] Actually, the magnetic field stays fixed during the experiment. An XMCD measurement gives access to the magnetization projection along the propagation axis of the X-ray beam. Therefore, the sample is tilted instead of the magnetic field to probe other directions.

[18] Supplementary measurements were performed at 0 T after saturation of the samples. The nearly 100 % of remanence were checked by making a comparison between both XMCD amplitudes as followed: Remanence = $\frac{max_{XMCD}(0T)}{max_{XMCD}(6T)} \times 100$.

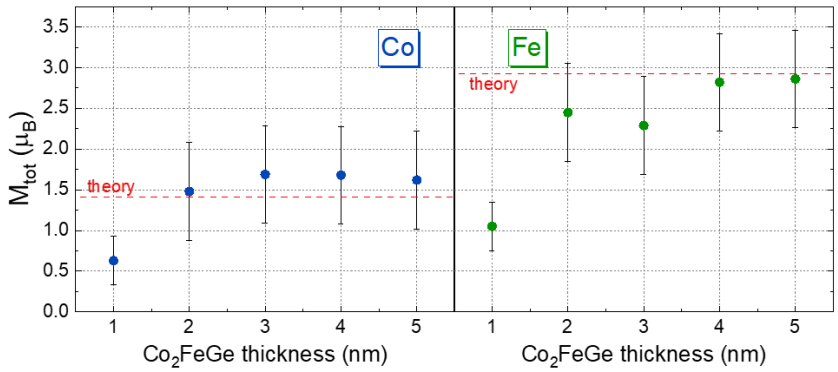

FIGURE 2.42: Extracted values of the total magnetic moments for Co (on the left) and Fe (on the right). The theoretical values, represented in red dashed lines are taken from [111].

This kind of samples fully characterized using XMCD were chosen to test the new Magneto-Optical Kerr Effect (MOKE) set-up installed on the IJL's UHV tube (at least in polar configuration, that is for an applied magnetic field perpendicular to the film plane). The growth was performed on the MBE and samples were then transferred to the MOKE chamber all under UHV. The sample was placed at the center of an electromagnet that allows to apply a magnetic field up to 0.9 T in the direction normal to the sample's surface. There are at least three main advantages of using this technique here:

- The measurement is sensitive to the thin film and not to the substrate (contrary to VSM/ SQUID measurements).
- The film is measured immediately after the growth process.
- No capping is needed. This allows us the possibility to see any influence of the capping on the magnetic properties of the underneath magnetic layer.

Five samples with the following stack MgO/Cr(10nm)/[Mn_3Ge(3nm)/Co_2FeGe(X nm)]$_{\times 5}$ with X = 0.5, 1, 2, 3 and 5 nm were characterized with the MOKE setup. The resulting curves are given in **figure 2.43**. The first observation that jumps out is the signal inversion occurring between samples with 1 and 2 nm of Co_2FeGe. This inversion is attributed to the different sign of Kerr rotation hosted by Mn_3Ge and Co_2FeGe. For low Co_2FeGe thicknesses, the loop is inverted due to dominant Mn_3Ge layers. As far as the Co_2FeGe thickness increases, the signal vanishes and the null Kerr angle is reached between t_{Co_2FeGe} = 1 and 2 nm. This behavior is clearly supported by the right graph of **figure 2.43** where a linear dependence of the Kerr amplitude with Co_2FeGe thickness is observed. An additional sample, made with only a Co_2FeGe layer, was measured and unveiled a classical Kerr rotation sign (ie. sign observed for t_{Co_2FeGe} = 2, 3 and 5 nm in **figure 2.43**) attesting to the inverse Mn_3Ge Kerr rotation[19].

[19]Unfortunately, the maximum applied magnetic field is 0.9 T. MOKE measurements on Mn_3Ge alone are then not possible since the saturation magnetization cannot be reached. The inverse Kerr rotation of Mn_3Ge cannot be directly imaged by MOKE measurements.

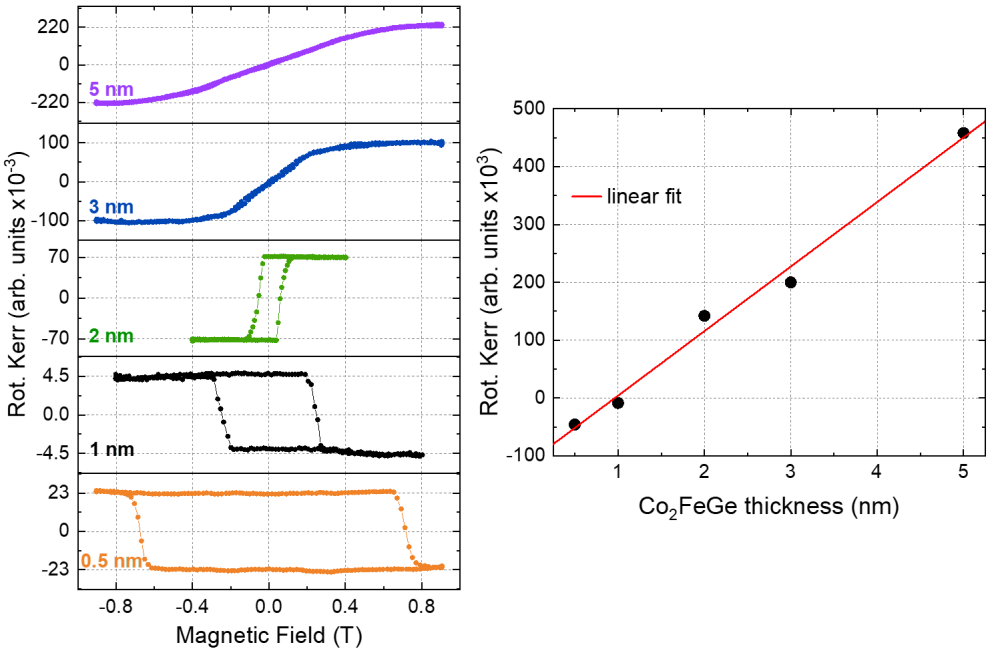

FIGURE 2.43: On the left, MOKE hysteresis loops obtained with an out-of-plane applied magnetic field. From bottom to top, increase of the Co_2FeGe thickness from 0.5 nm to 5 nm. Measurements performed at 300 K. On the right, Rotation Kerr amplitude as a function of Co_2FeGe thickness.

The comparison between XMCD (**figure 2.41**) and MOKE (**figure 2.43**) results is puzzling but care must be taken since the samples are from two different batches. For instance, the loops obtained for t_{Co_2FeGe} = 1 nm depict a quite different coercive field but one should keep in mind that domain wall pinning can strongly vary from one sample to the other especially in strained films (which is the case here). Moreover, an impact of the capping layer on the coercive field is also possible. Apart from this, a similar trend is observed with a magnetization toggling within the plane from t_{Co_2FeGe} = 3 nm. The samples perpendicularly magnetized have 100 % of remanence and confirm the XMCD data. All this study paves the way to grow and analyze a stack with a true Half-Metal-Magnet Heusler compounds using MOKE. The best ones are Co_2MnSi and Co_2MnGe since the spin gap is large (0.6 and 0.4 eV respectively [34]. We focused our work on Co_2MnGe which is close to Co_2FeGe in composition.

2.3.6 Mn_3Ge/Co_2MnGe superlattices

The growth process is very similar to the ones already described above. A 10 nm thick Cr buffer is deposited on top of a MgO substrate. The growth of the first Mn_3Ge layer is performed in the same condition given in the previous section. Co_2MnGe is then deposited with the following flux regulation $\Phi_{Co} = 2.\Phi_{Mn} = 2.\Phi_{Ge} = 1\ .10^{14}$ at.cm^{-2}.s^{-1} at a temperature around 240 °C ($T_{pyro} \approx 250$ °C) (Mn_3Ge and Co_2MnGe are deposited at the same temperature) with no annealing process done afterward to avoid interdiffusion. Four samples were grown with a 2 u.c. (u.c. stands for unit cell) fixed thickness for Mn_3Ge while Co_2MnGe thickness varies from 1 to 4 u.c.[20]. The resulting stack is then: MgO/Cr(10 nm)/[Mn_3Ge(2 u.c.)/ Co_2MnGe(X u.c)]$_{x5}$

[20] 1 u.c. of Mn_3Ge and Co_2FeGe is equivalent to 7.14 Å and 5.74 Å.

with X = 1, 2, 3 and 4 u.c.. The RHEED patterns observed all along the growth are similar to what we observed in the stacks shown in previous section.

These samples were thus measured by using the polar MOKE just after the growth. The hysteresis loops are shown in **figure 2.44**. Similarly to the observation done in the previous section for [Mn_3Ge/Co_2FeGe] SLs, the signal is gradually decreasing while increasing the Co_2MnGe thickness. This time, the Kerr null point is not reached but the sample with t_{Co_2FeGe} = 4 u.c. is close to the compensation point with an almost canceled signal. In the same way than Co_2FeGe, Co_2MnGe has a classical Kerr rotation that counterbalances the inverted one of Mn_3Ge. A linear relationship is also observed in the Rotation Kerr amplitude vs. Co_2MnGe thickness graph of **figure 2.44** even if more points are needed to properly describe the trend. Nevertheless, we finally reach one of our main goal : growing a PMA stack finishing by a HMM layer with a remanence of 100 %.

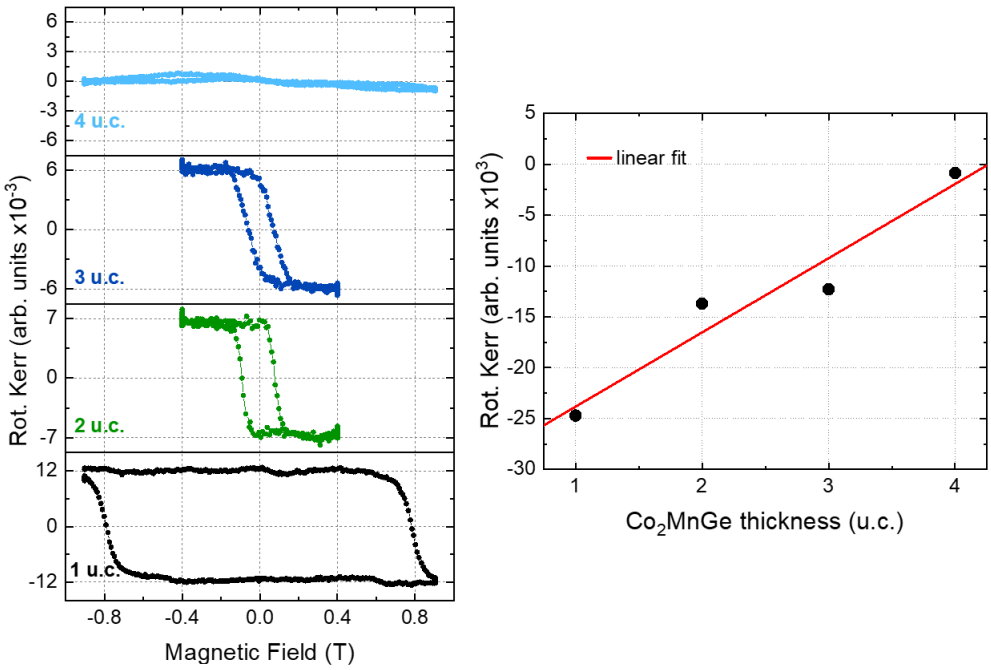

FIGURE 2.44: On the left, MOKE hysteresis loops obtained with an out-of-plane applied magnetic field. The thicknesses on the inset of the graphs stand for the Co_2MnGe thickness. Measurements performed at 300 K. On the right, rotation Kerr amplitude as a function of Co_2MnGe thickness.

2.4 Conclusions

We have seen in this chapter that PMA can be induced in Heusler bilayers and SLs thanks to the strong magnetocrystalline anisotropy carried by Mn_3Ga and Mn_3Ge grown in the $D0_{22}$ Heusler phase thanks to appropriate buffer layers, here Pd and Cr(001). This analysis leads to important conclusions:

- We clearly observed in $Mn_{100-x}Ga_x$ and $Mn_{100-x}Ge_x$ alloys that the standard 3:1 stoichiometry is the best one to get the largest perpendicular magnetic anisotropy.

- The comparison between both Mn_3Ge and Mn_3Ga compounds quickly enables us to make a choice between the two. Indeed, Mn_3Ga investigation showed a complex magnetic behavior leading to bent hysteresis loops with small magnetic remanences. This puzzling shape is not present for Mn_3Ge alloy.

In light of these results, Mn_3Ge was picked for growing the HMM Heusler on it. The tests using different buffer layers lead to the following conclusions:

- The PMA in $D0_{22}$ Mn_3Ge is large enough to keep this easy axis of magnetization when growing a Co-based full Heusler compounds on top of it (up to a critical thickness of course).
- We clearly observe that the PMA in bilayers is larger when using a Pd buffer layer compared to Cr. This is due to the misfit between the Mn_3Ge layer and the buffer layer. The misfit is close to zero with Pd whereas it is equal to -4 % with Cr.
- The Cr buffer layer leads to squarer hysteresis loops with high magnetic remanences compared to Pd.

In view of these conclusions, Mn_3Ge grown on a Cr buffer layer was chosen to carry on the study.

To investigate in details the magnetic behavior of Mn_3Ge/Co-based Heusler bilayers basic block, XMCD experiments were chosen because of their chemical selectivity that allowed us to get separate information on both layers. The main observations are the following:

- We systematically observed a ferromagnetic coupling between the Mn_3Ge layer and Co_2FeGe on top of it, whereas an antiferromagnetic coupling was observed many times in the literature (but with different systems such as Mn_3Ga/Co_2MnSi [143, 145]). We should keep in mind in the future that this coupling may change when replacing Co_2FeGe by another Heusler like Co_2MnSi. Moreover, the magnetic coupling may also depend on the thicknesses use in the stack.
- The Mn X-ray absorption L edge is observed to be affected by the capping, although the Mn_3Ge layer is not in contact with it.
- The whole stack behaves as a unique ferromagnetic layer (similar hysteresis loops measured at Mn, Co and Fe L edges) in the thicknesses range used.
- Large coercive fields associated with 100 % remanence are achievable.

The growth of desired Heusler compounds on top of the Mn_3Ge layer (here Co_2FeGe and Co_2MnGe) was under control, with a clear evidence of the chemical ordering as shown by RHEED during the growth and STEM. Nevertheless, one should note that an annealing up to 450 °C is necessary to improve the chemical ordering of Co_2Mn-based Heuslers. In our PMA stacks, such annealing temperatures are too high and lead to intermixing. One should keep in mind that this limited annealing temperature (around 220 °C) may have some impact on the spin polarization and magnetic damping.

Conclusions and perspectives

In the first chapter of this thesis we studied two Heusler alloys predicted to be topological insulator and we achieved the following point:

- The epitaxial growth of PdYBi and PtYBi in the desired $C1_b$ structure (the one predicted to potentially host a non trivial topology) was successfully mastered. The single-crystalline growth was checked by means of X-ray and electronic diffractions and the surface morphology as well as the reconstructions imaged by scanning tunneling microscopy. Finally, the presence of atomic ordering was checked by scanning transmission electron microscopy where a different behavior was observed in both compounds. PtYBi turned out to be well ordered meanwhile atomic disorder was observed in PdYBi. This observation is of prime importance since it allows to explain the quality of the band mapping obtained in angle resolved photoemission spectroscopy.
- Angle resolved photoemission spectroscopy experiments were conducted on the ARPES set-up connected to the IJL's UHV tube. Linear states were identified in both compounds even if their trivial or non-trivial nature is still under debate. PtYBi's band structure is well more defined than PdYBi's one owing to the better chemical ordering lying in this alloy. Strong similarities with literature's band structure of PtYBi allowed us to identify the manifestation of the non-trivial topology well below the Fermi level where an additional crossing point is distinguishable. For PdYBi, the low spectral weight combined with the lack of band structure reports made the analysis though. Nonetheless, similarities with PtYBi band structure were noted and the non-trivial topology could manifest in a crossing point distinguishable below the Fermi level and around the $\overline{\Gamma}$ point as for PtYBi.
- Finally, transport measurements (namely SP-FMR and spin Seebeck measurements), where the non-trivial topology is supposed to manifest due to the spin texture of such materials, were performed. Unfortunately, the results are only preliminary and do not allow to draw conclusions on the nature of the transport even if some spin-to-charge interconversion was measured.

In view of these results, additional experiments have to be carried on to finally settle on the half-Heusler TIs' potential:

- The surface reconstructions imaged by RHEED and STM probably influence the transport measurements even if no additional state were observed by ARPES. Other growth studies have to be done to stabilize different surface reconstructions and evaluate their impact in transport measurements. Obviously, STM and ARPES studies have to be conducted in parallel.
- As already discussed, the MgO barrier is suspected to strongly influence the transport measurements, mostly in a negative way. This assumption is strengthened by literature works where the use of an MgO barrier leads to a reduction

of the generated voltage in SP-FMR measurements. Moreover, the only one monolayer thick (two monolayers for PtYBi) MgO barrier may not fully cover the surface. A direct contact between the TI and the FM layer may occur and killed the TSS.

- In view of the questions about the MgO barrier and the literature reports on TI/FM systems, a new batch of samples should be grown using a metallic interlayer instead of the insulating MgO barrier. Metallic interlayers, such as Au, Ag or Al, were used recently by physicists as interlayer between the TI and the FM and the resulting spin-to-charge conversion validates their use. Moreover, the interfaces quality could be increased by a metallic interlayer since MgO probably affects it.

- Finally, the Fe layer quality turned out to be different in each of our samples. The usual correction by the FM reference subtraction is thus incorrect. A reverse stack order (ie. FM/TI instead of TI/FM) is not worth considering since the $Al_2O_3(0001)$ substrate is mandatory for the half-Heusler growth. The use of another FM material instead of Fe has to be studied in order to get a homogeneous FM quality in TIs, control and reference samples.

The second chapter of this thesis dealt with Heusler alloys hosting perpendicular magnetic anisotropy. The results obtained can be divided in the two following part:

- The first part consisted in the study of $D0_{22}$ Mn-Ga and Mn-Ge alloys and how the off-stoichiometry impacts their magnetic properties. Two series of five samples with different stoichiometries were done for both compounds ($Mn_{100-x}Ga_x$ and $Mn_{100-x}Ge_x$). We managed to stabilize the $D0_{22}$ structure for all compounds and to obtain an easy axis of magnetization perpendicular to the sample's surface. Nonetheless, we showed that the off-stoichiometry (away from the ideal 3:1 stoichiometry suggested by the full-Heusler structure) strongly impacts the magnetic properties. Moreover, Mn_3Ga and its complex magnetic behavior turned out to be a less good candidate for our purpose than Mn_3Ge. We thus decided to carry on the investigation with Mn_3Ge.

- The second part dealt with the engineering of bilayer and supperlattice structure perpendiculary magnetized thank's to Mn_3Ge and its strong magnetocrystalline anisotropy. To do so, bilayer and supperlattice composed of Mn_3Ge and a second Heusler alloy (Co_2MnGe or Co_2FeGe) were grown. The epitaxial growth was mastered with an elongated c axis of Mn_3Ge along the growth axis resulting in an overall PMA in the stacks. The magnetic properties of the systems are dependant of the thicknesses used for both sublayers allowing to tune the coercive and remanence of the stacks. In conclusion, we successfully grew perpendicularly magnetized structures terminated with a half-metal magnet.

This work brings a lot of knowledge on the realization of perpendicularly magnetized bilayers and SLs heterostructures made of Heusler alloys. The high remanences measured for the SLs are very promising for future applications but some works still have to be done:

- Firstly, a more complete thickness dependence studies (of both Mn_3Ge and Co_2MnGe) has to be done to determine the most suitable thicknesses. A similar investigation has to be done with Co_2MnSi (the best half-metal magnet of the Heusler family) to ensure that similar results are obtained.
- Secondly, ferromagnetic resonance measurements must be carried out to extract the magnetic damping constant of the heterostructures.
- Finally, SR-PES measurements have to be performed in order to estimate the spin polarization.

Once the magnetic damping constant and the spin polarization known, one would be able to draw a conclusion on their interest in spin transfer applications according to the impact of the SL structures on these two essential properties.

Finally, to conclude this thesis one must think to merge the two chapters presented to engineered future materials fully based on Heusler alloys. As already discussed during this work, the material studied here are pioneering to develop today's data storage. It should be possible to build a stack composed of a topological insulator (PdYBi or PtYBi) with a fully spin polarized and perpendicularly magnetized structure on top of it (such as Mn_3Ge/Co_2MnSi). Such a structure should host all the convenient physical properties to improve the conventional magnetic memories. Obviously, further investigations are needed in both studies to improve their properties at their best. Nonetheless, this thesis paves the way to further investigations on such heterostructures.

Appendix A

Lithography process

In order to perform transport measurements on TIs samples, multiple devices were patterned by standard UV lithography. The used lithography process is explained in the following.

All the lithographed samples were grown on the MBE of the Institut Jean Lamour and MgO capping layers were deposited to avoid oxidation. UV lithography is commonly used in integrated circuit manufacturing to pattern devices. In such process, a light-sensitive chemical layer is exposed to UV radiations. In a first step, the sample is coated with a UV sensitive photoresist. A geometrical pattern is obtained with the help of an optical mask inserted between the sensitive layer and the UV source. The mask blocks light in some areas whereas others let it pass. The unhidden areas let the UV light go through the mask and the photoresist beneath those gaps is changing chemically. Thanks to this local chemical transformation, a step, named development, can be carried out to only remove the exposed areas. To do that, the sample is drowned in a developer, the exposed areas are removed while the unexposed ones remain intact and are used to protect the sample to further etching or evaporation process.

The lithography process, which is adopted in this PhD, is divided into three main steps that are going to be discussed below.

1^{st} step

The beginning of the process starts with the sample's coating with the S1813 photoresist (step 2 of **figure A.1**). The S1813 photoresist is a positive photoresist in the way that it becomes soluble in the developer after exposition[1]. A spin-coater is used to spread a homogeneous thickness, which is essential since the exposure time to UV light is linked to the photoresist thickness. The spin-coating is performed during 40s at 10000 rpm, resulting in a homogeneous thickness distribution ($t_{S1813} \approx 850$ nm). The sample is then exposed for 14 s to UV light (around 120 mJ.mm^{-2}) through a photomask that generates the desired patterns (step 3 of **figure A.1**). The development is then done during 40 s at 20 °C to remove the exposed areas (step 4 of **figure A.1**) thanks to the MF-319 developer[2]. The result, in the case of Hall bars, is given in the left part of **figure A.2**. The bars areas are protected by the unexposed photoresist. Everywhere else, the photoresist is gone and the etching can be performed. Ion beam etching is then done to dig the layers (step 5 of **figure A.1**). The etching is realized with a 4Wave ion beam etching system and a mass spectrometer is used to

[1] A negative photoresist is insoluble in the developer after exposition meanwhile the unexposed areas are soluble.

[2] The MF-319 developer is dedicated to the development of S1800 photoresists series.

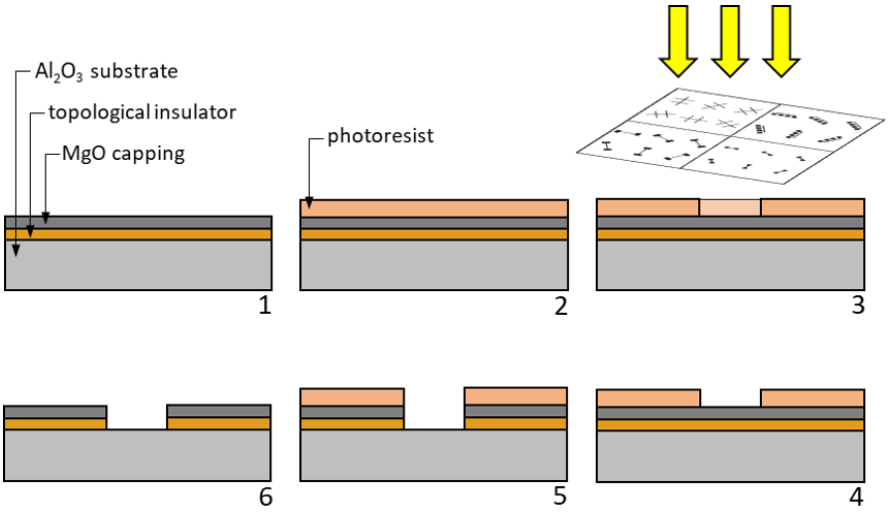

FIGURE A.1: Sketch of the first lithography step. The sample (1) is coated with a photoresist (2). An optical mask is inserted between the UV source and the photoresist layer which changes chemically on the exposed area (3). The development allows to remove the exposed area (4) and an ion beam etching is performed to partially dig the sample (5). Finally, a remover is used to take away all the photoresist (6).

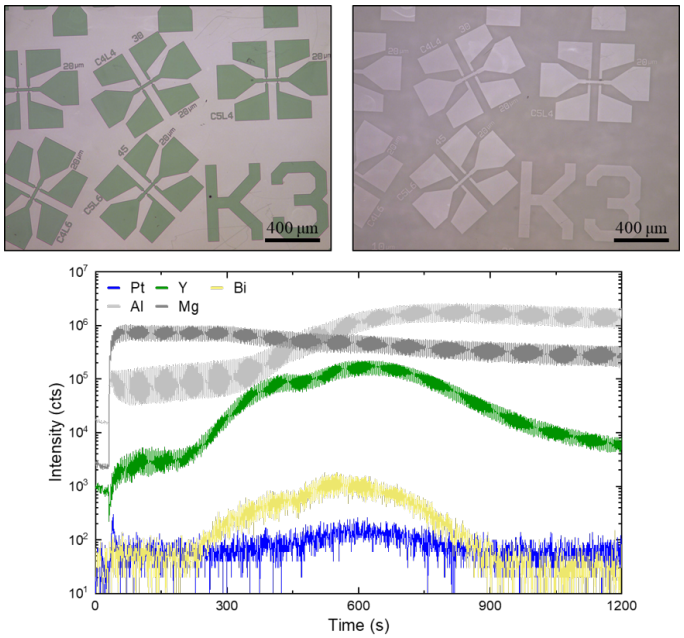

FIGURE A.2: On the left, optical microscope image of the sample patterned in Hall bars geometry. The green areas are protected by unexposed photoresist while the grey ones are naked. The sample is then etched (graph at the bottom) until sapphire substrate is reached. A lift-off is then performed and the result is shown on the right image. The dark grey areas were etched up to sapphire substrate while the initial stack remains in the light grey areas.

follow the etching progress. Thanks to the mass spectrometer, it is possible to analyze the mass of the emitted atoms (graph at the bottom of **figure A.2**) and make sure that the sapphire substrate is reached. For instance, in the graph of **figure A.2**, the end of the PtYBi TI layer is reached around 1000 s since Pt, Y and Bi signals are back to their initial values. Pt (or Pd for PdYBi), Y and Bi are used as reference points even if a slight over-etching is usually done to ensure that sapphire substrate is reached. The mass spectrometer data graph of **figure A.2** presents a double step

for Pt, Y and Bi detection since two samples with different PtYBi layer thicknesses were etched at the same time. The sample is then drowned in the remover 1165 for 1 hour at 80 °C to strip all the photoresist. At this point, the first step is over (step 6 of **figure A.1**). The devices are shaped and they are all separated from each other thanks to the etching stopped in the isolating sapphire substrate. An image of the Hall bars at the end of the first step is given in the left part of **figure A.2**.

2nd step

The second step only applies to heater and spin pumping devices given that it is based on the deposition of an insulating layer. On the one hand, Hall bars and ST-FMR devices are fully covered of unexposed resin that will be used to remove the unwanted SiO_2 layer. On the other hand, some part of the Heaters and the SP-FMR devices are exposed to UV light to develop the resin and form the desired patterns (visible in the images of **figure A.4**). The beginning of the second step is then based on the sample's coating. This time, three spin-coatings are performed. The first one is as a grip layer made of a chemical product named HMDS primer[3] which is annealed afterward on a hot plate at 115 °C for 60 s. The primer layer allows a homogeneous spreading of the second layer named LOR 3A also annealed after deposition at 140 °C during 120 s. The LOR 3A principle is to make the lift-off process easier as sketched in **figure A.3**[4].

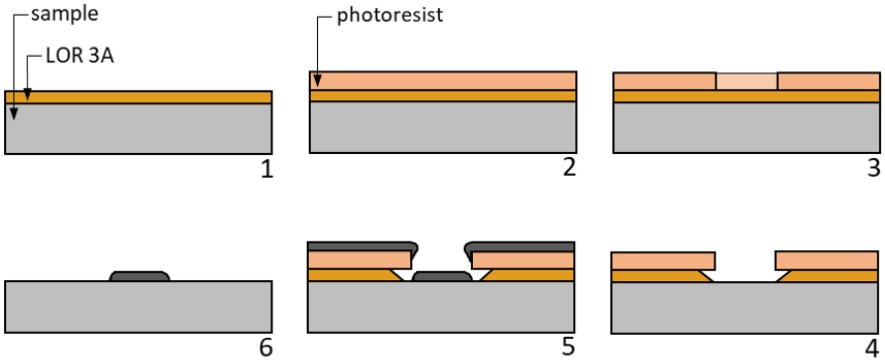

FIGURE A.3: Sketch of the LOR 3A principle. The sample is coated with the LOR 3A (1) and then with the photoresist (2). It is then exposed to UV light (3) and the development is performed (4). The LOR 3A develops isotopically, thus, a cap is formed on top with the unexposed photoresist. The evaporation can be done and the re-entrant profile ensures a discontinuous deposition (5). The lift-off is then done to remove the bi-layer resist (6). The HMDS primer layer is not represented here for the sake of clarity.

Finally, the photoresist is spin-coated on the sample (stage 2 of **figure A.3**), annealed at 115 °C during 60 s and the desired pattern is formed with the help of an optical mask and the UV source (stage 3 of **figure A.3**). The development of the photoresist (only on the exposed area) and of the primer - LOR 3A bilayer (isotropic development) is done by drowning the sample in the MF-319 developer for 55 s (stage 4 of **figure A.3**). At this point, the SiO_2 deposition is performed by sputtering, the sputter used is a ... and a 200 nm thick SiO_2 layer is deposited on top of the sample (stage 5 of **figure A.3**). Finally, the lift-off is carried out. The sample is drowned in the

[3]The HMDS primer is used as an adhesion promoter for the following coating. Indeed, surface oxidation may result in a poor adhesion that is enhanced by the HMDS primer coating.

[4]The Primer layer is not represented here for the sake of clarity but the principle is exactly the same since the Primer behaves like the LOR 3A.

remover 1165 at 80 °C for 1 hour and the desired SiO_2 patterns are obtained (step 6 of **figure A.3** and images of **figure A.4**). Thickness measurements can be performed thanks to a profilometer in order to check the SiO_2 deposition. One of this measurement is given on top of **figure A.4** where the SiO_2 and the sample thicknesses are quickly identified.

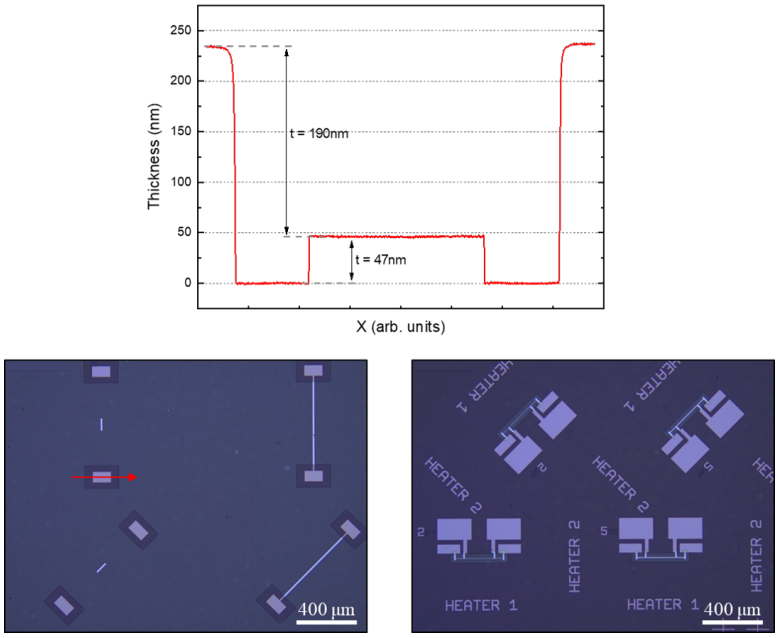

FIGURE A.4: At the top, profilometer measurement performed along the red arrow on the left image. The thicknesses given on the left and at the center are respectively the sample and the SiO2 layer thicknesses. At the bottom, images of SP-FMR (on the left) and Heater (on the right) devices after exposition and development of the patterns. The covered areas will allow to remove the SiO2 deposited during the lift-off. On the left image, only the SPFMR electrodes are covered and thus protected. In the case of heater devices (right image) all the sample is covered except for the rectangles at the devices' center.

3^{rd} step

The last step consists in the electrodes' deposition. In this step, the same spin-coating process described above is performed to pattern the sample by exposing the photoresist and the Primer - LOR 3A bilayer to UV radiations (Steps 1, 2 and 3 of **figure A.3**). **Figure A.5** gives images of the Heater and SP-FMR devices after development. Since the electrodes' positions are in areas where the insulating MgO capping is still present, an etching of the MgO layer has to be done prior to the electrodes' evaporation otherwise current will not flow in the device during transport measurements. Similarly to the first ion beam etching of step 1, the mass spectrometer allows to follow in real time the etching process. The resulting curves are given in **figure A.5**. Here, since only small areas of the sample are dug (most of the sample is protected by photoresist), the signals detected by the mass spectrometer are low and an estimation of the time needed to dig the MgO capping is done according to the first etching[5].

[5]The etching should be stopped when the TI layer is reached. Nonetheless, a slight over-etching in the sapphire substrate is not crippling since the thickness of Ti/Au electrodes allows to still have contact with the TI layer. Most of the time a slight over-etching is done to ensure that no residual MgO capping remains on the surface.

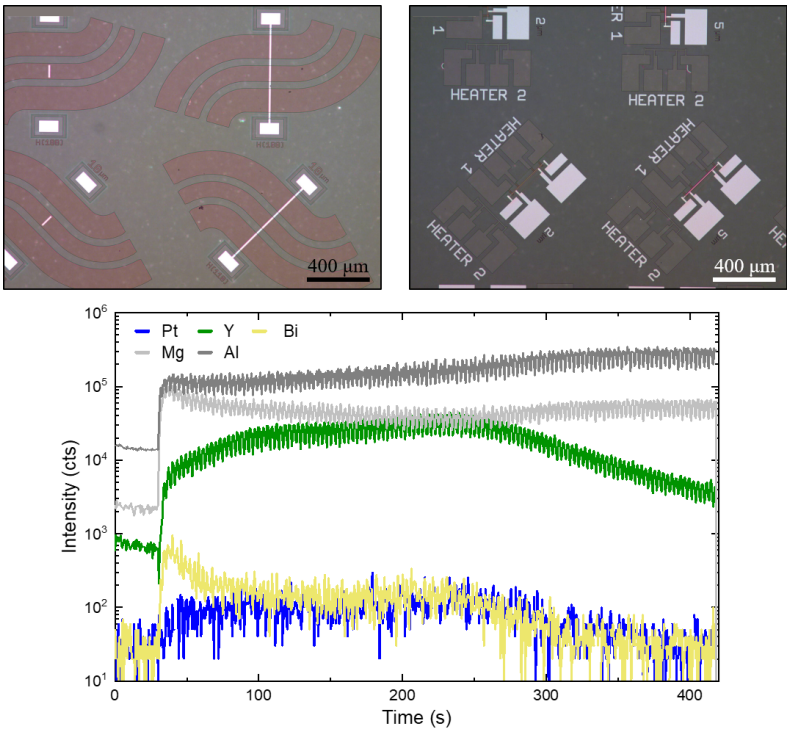

FIGURE A.5: At the top, two images after exposition and development of the patterns for Heater (on the right) and SP-FMR (on the left). The position of the electrodes and the SP-FMR antennas is already visible. The unprotected areas are going to be etched in order to perform Ti/Au electrodes deposition. The etching graph is given at the bottom.

Once the etching done, Ti/Au electrodes are deposited with a Plassys MEB 400S electron beam evaporator. 10 nm of Ti and 150 nm of Au are successively evaporated and cover the sample. The same lift-off performed in the previous step is then done to remove the Ti/Au of the unwanted areas. At this stage, the four types of devices are ready to use. All of them are imaged in **figure A.6**.

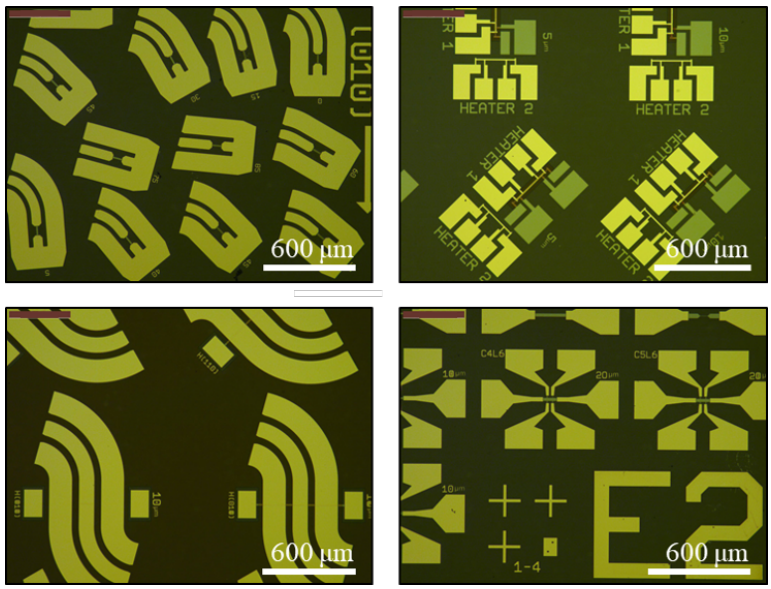

FIGURE A.6: Images of the final four devices made, namely ST-FMR (top left), Heater (top right), SP-FMR (bottom left) and Hall bars (bottom right) devices.

A final step can be carried out in order to enable back gate application on the sample. This step consists of an Au evaporation on the sample's backside. The evaporator is then used to deposit a 150 nm thick Au layer that will allow to apply a voltage back gate on the sample.

Appendix B

RHEED transport samples

Figure B.1 gives the Fe RHEED patterns obtained for each thickness of PdYBi and PtYBi.

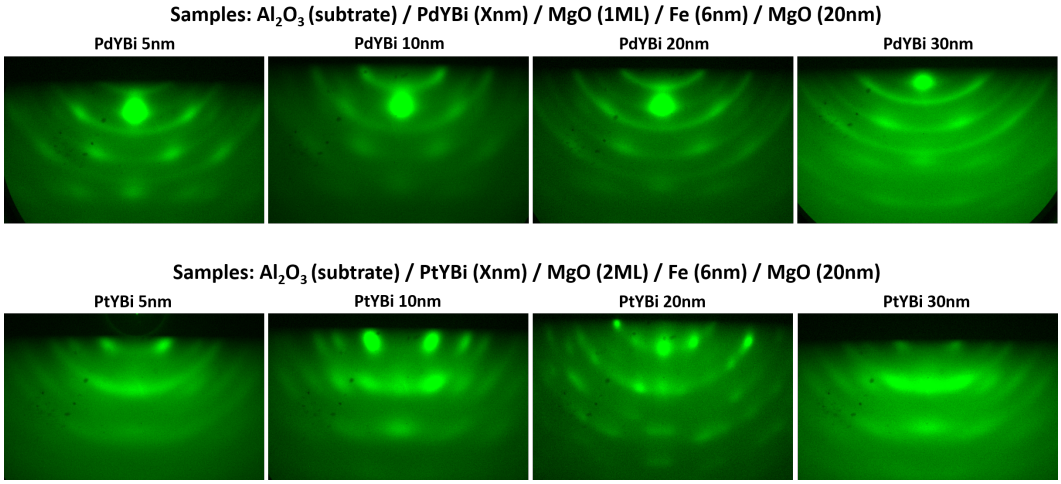

FIGURE B.1: At the top, RHEED patterns of the Fe layer for all PdYBi samples. At the bottom, RHEED patterns of the Fe layer for all PtYBi samples.

Figure B.2 gives the Pt and Fe RHEED patterns obtained for the Pt control and Fe reference samples. The electron beam was applied along the [1$\bar{1}$0] and [11$\bar{2}$] azimuths of platinum.

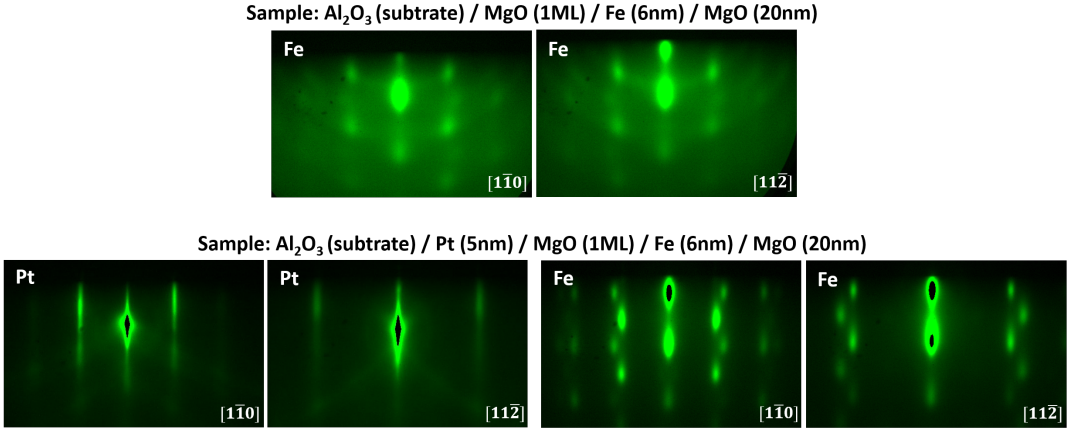

FIGURE B.2: At the top, RHEED patterns of the Fe layer for the Fe reference sample. At the bottom, RHEED patterns of the Pt and Fe layers for the Pt control sample. Electron beam applied along the [1$\bar{1}$0] and [11$\bar{2}$] azimuths of platinum.

Appendix C

X-ray Magnetic Circular Dichroism

All the XMCD measurements shown in this thesis were performed at the Boreas beamline of the ALBA synchrotron under a UHV environment and in total electron yield mode. Boreas beamline is equipped with superconducting coils allowing to apply magnetic field up to 6 T along the beam. A cryostat enables ultra-low temperature studies (4 K to 350 K) and a full polarization control is possible on an extended soft X-ray range going from 80 to 4000 eV.

XMCD is an element sensitive technique that allows to obtain magnetic moments carried by each atom in the cell. Dichroism can be defined as the polarization dependence of the light absorption by a material. An XMCD measurement takes advantage of this property by measuring two X-ray absorption spectra with left and right polarized light. The difference between these two spectra is named the XMCD signal and brings information on the magnetic state of the system. Moreover, the use of synchrotron facilities allows to tune the X-ray to the resonance energy of a core to valence transition making XMCD an element sensitive technique. In the case of transitions metal (for instance Mn, Fe or Co are probed in this thesis) the absorption spectra are usually performed at the L-edges. The 2p core state is divided in two transitions edges L_2 and L_3 due to spin-orbit interaction, namely $2p^{\frac{1}{2}}$ and $2p^{\frac{1}{2}}$. According to the light polarization, different spin-up and spin-down transitions' probabilities happen for the excited electrons. These generated electrons now have to find an empty 3d valence band state with different probabilities of occurrence since spin up and spin down have their own number of unoccupied states in a ferromagnetic material. Spin's conservation is guaranteed by the selection rules imposed by the dipolar electric Hamiltonian which is the origin of this unbalanced spins excitation probability. This phenomenon is summarized in **figure C.1** by the two steps model. The two steps model is a simple picture of the process and more sophisticated explanation can be found elsewhere [155].

A XMCD measurement consists therefore to measure an absorption edge with two circularly polarized lights. Here, σ^-(B) stands for a right polarization of light and a positive applied magnetic field. Thus, σ^+(B) is the absorption edge probed with a left polarization of light and a positive applied magnetic field[1]. The total absorption signal is defined as $\sigma_{XAS} = \frac{\sigma^-(B)+\sigma^+(B)}{2}$. The XMCD signal is the difference between both light polarizations and is defined as σ_{XMCD} = σ^-(B) - σ^-(B). An example of XAS and XMCD signals measured at the Co L edges are given in **figure**

[1]Due to time reversal symmetry, XMCD is the same if the helicity and the magnetic field are reversed; that is to say σ^-(B) = σ^+(-B). Usually, experimenters performed four redundant experiments (σ^-(B), σ^+(-B), σ^-(-B), σ^+(B)) to cancel out potential asymmetry in XAS spectra.

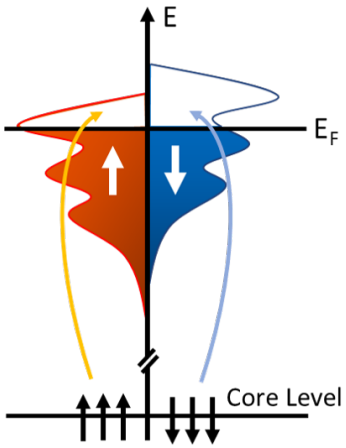

FIGURE C.1: Sketch of the two-step model. A spin polarized electron (up or down) from the 2p level for transition metals is excited by a polarized photon (left or right circularly polarized). The transition weight is not the same for each spin orientation according to the light helicity. The generated electron has to find an empty state in the 3d band which is asymmetric with regards to spin orientation.

C.2 and allow to estimate the orbital, $\langle L_Z \rangle$, and spin, $\langle S_Z \rangle$, magnetic moments separately. In order to perform this analysis, only the transitions to the empty 3d states have to be accounted. A correction (drawn in dash line in the upper graph of **figure C.2**) is done to remove the background due to transitions to higher empty states or directly to the continuum. This correction is based on a two-step function where the steps height takes into account the states degeneracy since two times more electrons are present on $2p^{\frac{3}{2}}$ than $2p^{\frac{1}{2}}$ levels. Once this correction done, σ_{XAS} and σ_{XMCD} can be calculated. The values of r, p and q are extracted after integration of both signals (shown in the graphs at the bottom of **figure 39**) and the sum rules analysis can be done to determine $\langle L_Z \rangle$, $\langle S_Z \rangle$ and the total magnetic moment $\langle M_{tot} \rangle$. An exhaustive demonstration of the sum rules can be found elsewhere [156, 157, 158, 155]. It results in the following equations[2]:

$$\langle L_Z \rangle = \frac{-2q}{3r}.n_h \quad ; \quad \langle S_Z \rangle = \frac{2q-3p}{2r}.n_h \quad and \quad \langle M_{tot} \rangle = \langle L_Z \rangle + 2.\langle S_Z \rangle \tag{C.1}$$

These formulas link the intrinsic magnetic properties of the probed atom with the XAS and XMCD spectra. Nonetheless, one must pay attention to the spin sum rule that can be accurately done only if the L_2 and L_3 edges are well separated. Consequently, the spin-orbit interaction has to be strong enough to isolate the transitions. Usually, p and q extraction for Fe and Co are not problematic but, in the case of Mn, the use of a correction factor is essential to counterbalance the error caused by its low spin-orbit interaction strength. Other sum rules analysis limits (not mentioned here) exist [159, 160] and reveal the significant margin of error generated during the extraction of the magnetic moments values. Moreover, equation C.1 tells us that the number of holes (in the 3d bands for transition metals) has to be known to evaluate the orbital and spin magnetic moments. This estimation is not trivial since a lot of parameters may impact the density of states such as the crystallographic phase, the planes' orientation or if the measurements are performed on a bulk sample or on a

[2]Rigorously, an additional term, called dipolar magnetic interaction (noted $\langle T_Z \rangle$), should be taken into account. In this case, it is assumed to be negligible since the magnetic dipole term in cubic 3d transitions metals is small with regard to the effective spin moment [155].

thin film. In this thesis, the estimation for Mn atom is not done. Indeed, the L_3/L_2 overlapping, the unknown holes number, the strong background in XAS spectra or even the possible complex Mn_3Ge (and Mn_3Ga) magnetic state make the analysis not reliable.

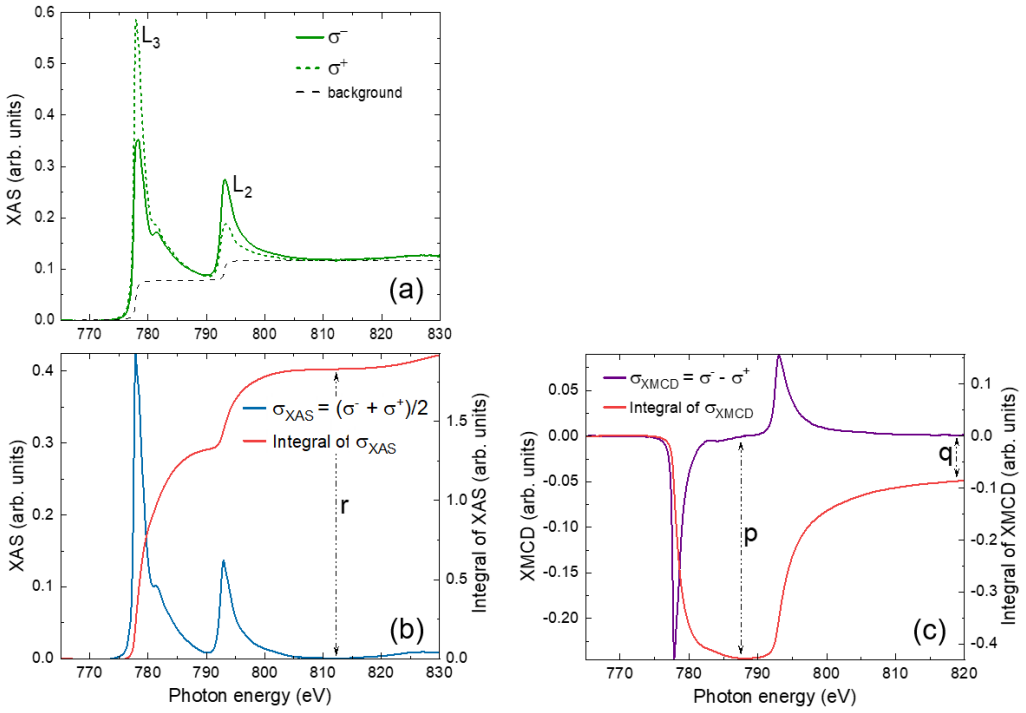

FIGURE C.2: (a), $L_{3,2}$ absorption edges of Co with a right (σ^-) and left (σ^+) circularly polarized light. The dashed line is the background correction. (b) and (c), XAS and XMCD signals along with their integrals after background correction that allows to extract r, p and q values.

Appendix D

Magneto-optical Kerr effect

The Magneto-optical Kerr effect setup is directly connected to the UHV-tube of the Institut Jean Lamour and allows to carry out MOKE measurements without breaking the vacuum. The sample is placed at the center of an electromagnet that allows to apply a magnetic field up to 0.9 T in the direction normal to the sample's surface. The polarized laser beam is produced by a red helium-neon gas laser with a wavelength λ = 632.8 nm. A polarizer is inserted in the optical path of the incoming beam to ensure a perfect polarization of the light in a peculiar direction (the outgoing light has a s polarization in this setup). The beam, then, enters the UHV chamber through a transparent window and is reflected on the magnetic sample. The reflected beam is then pointed at a $\lambda/2$ waveplate. Just next to it, a Wollaston prism splits the beam in two beams of different directions and with orthogonal polarizations. They are then focused on a two-entry photodetector and an output voltage proportional to the difference between the two detected photocurrents is generated. The intensity difference of the two photocurrents is proportional to the polarization rotation. Therefore, the difference between both final beams is adjusted close to zero prior to the measurement with the help of the half-waveplate located in front of the Wollaston prism. The $\lambda/2$ retarder mixes s- and p-waves resulting in an outgoing beam with similar s- and p- light projection that canceled out in the photodiode. The optical path of the photon beam described above is sketched in **figure D.1** and pictures of the set-up are given in **figure D.2**.

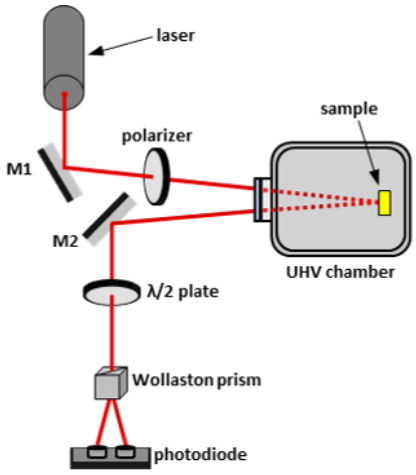

FIGURE D.1: Sketch of the experimental setup used for MOKE measurements. A He-Ne laser emits a beam that is perfectly polarized thanks to a polarizer. The polarized photon beam enters the UHV chamber through a window, is reflected on the sample's surface and goes the other way around. The $\lambda/2$ plate is used to get a similar amount of s and p polarization prior measurement and the Wollaston prism splits the beam in two parts collected by a double entry photodiode to measure the Kerr rotation. The sample is placed at the center of an electromagnet (not represented here for the sake of clarity) which applies an out-of-plane magnetic field up to 0.9 T. M1 and M2 are mirrors.

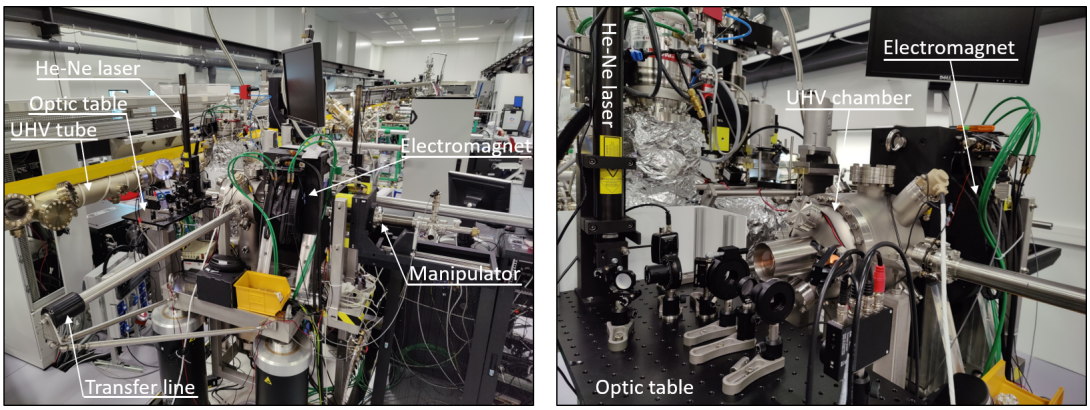

FIGURE D.2: Pictures of the IJL's MOKE set-up connected to the UHV tube.

Bibliography

[1] M.N. Baibich, J.M. Broto, A. Fert, F. Nguyen Van Dau, F. Petroff, P. Eitenne, G. Creuzet, A. Friederich, and J. Chazelas. Giant magnetoresistance of (001)Fe/(001)Cr magnetic superlattices. *Physical Review Letters*, 61(21):2472–2475, 1988.

[2] D.J. Thouless, M. Kohmoto, M.P. Nightingale, and M. den Nijs. Quantized Hall conductance in a two dimensional periodic potential. *Physical Review Letters*, 49(6):405–408, 1982.

[3] L. Fu, C. L. Kane, and E. J. Mele. Topological insulators in three dimensions. *Physical Review Letters*, 98(10):045302, 2007.

[4] V.M. Edelstein. Spin polarization of conduction electrons induced by electric current in two-dimensional asymmetric electron systems. *Solid State Communications*, 73(3):233–235, 1990.

[5] Y. Xia, D. Qian, D. Hsieh, L. Wray, A. Pal, H. Lin, A. Bansil, D. Grauer, Y.S. Hor, R.J. Cava, and M.Z. Hasan. Observation of a large-gap topological-insulator class with a single Dirac cone on the surface. *Nature Physics*, 5(6):398–402, 2009.

[6] Y.L. Chen, J.G. Analytis, J.H. Chu, Z.K. Liu, S.K. Mo, X.L. Qi, H.J. Zhang, P.H. Lu, X. Dai, Z. Fang, S.C. Zhang, I.R. Fisher, Z. Hussain, and Z.X. Shen. Experimental realization of a three-dimensional topological insulator, Bi_2Te_3. *Science*, 325:178–181, 2009.

[7] D. Hsieh, D. Qian, L. Wray, Y. Xia, Y.S. Hor, R.J. Cava, and M.Z. Hasan. A topological Dirac insulator in a quantum spin Hall phase. *Nature*, 452:970–974, 2008.

[8] S. Chadov, X. Qi, J. Kübler, G.H. Fecher, C. Felser, and S.C. Zhang. Tunable multifunctional topological insulators in ternary Heusler compounds. *Nature Materials*, 9(7):541–545, 2010.

[9] R. de Groot, F.M. Mueller, P.G. van Engen, and K.H.J. Buschow. New Class of Materials: Half-Metallic Ferromagnets. *Physical Review Letters*, 50(25):2024–2027, 1983.

[10] A. Neggache. *Propriétés électroniques des alliages d'Heusler $Co_{1.5}Fe_{1.5}Ge$ et Co_2MnSi*. PhD thesis, Université de Lorraine, 2014.

[11] C. Guillemard. *Half-metal magnets Heusler compounds for spintronics*. PhD thesis, Université de Lorraine, 2019.

[12] E. Krén and G. Kádár. Neutron diffraction study of Mn_3Ga. *Journal of Applied Physics*, 8(3):1653–1655, 1970.

[13] B. Balke, G.H. Fecher, J. Winterlik, and C. Felser. Mn_3Ga, a compensated ferrimagnet with high Curie temperature and low magnetic moment for spin torque transfer applications. *Applied Physics Letters*, 90(15):152504, 2007.

[14] J. Winterlik, B. Balke, G.H. Fecher, C. Felser, M.C.M. Alves, F. Bernardi, and J. Morais. Structural, electronic, and magnetic properties of tetragonal $Mn_{3-x}Ga$: Experiments and first-principles calculations. *Physical Review B*, 77(5):054406, 2008.

[15] H. Kurt, N. Baadji, K. Rode, M. Venkatesan, P. Stamenov, S. Sanvito, and J.M.D. Coey. Magnetic and electronic properties of $D0_{22}$-Mn_3Ge (001) films. *Applied Physics Letters*, 101:132410, 2012.

[16] K. Rode, N. Baadji, D. Betto, Y. C. Lau, M. Venkatesan, P. Stamenov, S. Sanvito, J. M. D. Coey, F. Porcher, and G. André. Site-specific order and magnetism in tetragonal Mn_3Ga thin films. *Physical Review B*, 87:184429, 2013.

[17] G. Kádár and E. Krén. Neutron diffraction study of Mn_3Ge. *Int. J. Magn*, 1, 1971.

[18] F. Wu, S. Mizukami, D. Watanabe, H. Naganuma, M. Oogane, Y. Ando, and T. Miyazaki. Epitaxial $Mn_{2.5}Ga$ thin films with giant perpendicular magnetic anisotropy for spintronic devices. *Applied Physics Letters*, 94(12):122503, 2009.

[19] S. Mizukami, T. Kubota, F. Wu, X. Zhang, T. Miyazaki, H. Naganuma, M. Oogane, A. Sakuma, and Y. Ando. Composition dependence of magnetic properties in perpendicularly magnetized epitaxial thin films of Mn-Ga alloys. *Physical Review B*, 85(1):014416, 2012.

[20] M. Julliere. Tunneling between ferromagnetic films. *Physics Letters A*, 54(3):225–226, 1975.

[21] J.C. Slonczewski. Current-driven excitation of magnetic multilayers. *Journal of Magnetism and Magnetic Materials*, 159:L1–L7, 1996.

[22] D.C. Ralph and M.D. Stiles. Spin transfer torques. *Journal of Magnetism and Magnetic Materials*, 320(7):1190–1216, 2009.

[23] J.E. Hirsch. Spin Hall effect. *Physical Review Letters*, 83(9):1834 – 1837, 1999.

[24] J.C. Rojas-Sánchez and A. Fert. Compared Efficiencies of Conversions between Charge and Spin Current by Spin-Orbit Interactions in Two- and Three-Dimensional Systems. *Physical Review Applied*, 11(5):054049, 2019.

[25] K.S. Lee, S.W. Lee, B.C. Min, and K.J. Lee. Threshold current for switching of a perpendicular magnetic layer induced by spin Hall effect. *Applied Physics Letters*, 102(11):112410, 2013.

[26] L. Liu, O.J. Lee, T.J. Gudmundsen, D.C. Ralph, and R.A. Buhrman. Current-induced switching of perpendicularly magnetized magnetic layers using spin torque from the spin Hall effect. *Physical Review Letters*, 109(9):096602, 2012.

[27] C.F. Pai, L. Liu, Y. Li, H.W. Tseng, D.C. Ralph, and R.A. Buhrman. Spin transfer torque devices utilizing the giant spin Hall effect of tungsten. *Applied Physics Letters*, 101(12):122404, 2012.

[28] M.Z. Hasan and C.L. Kane. Colloquium: Topological insulators. *Reviews of Modern Physics*, 82(4):3045–3067, 2010.

[29] B.A. Bernevig, T.L. Hughes, and S.C. Zhang. Quantum spin Hall effect and topological phase transition in HgTe quantum wells. *Science*, 314:1757–1761, 2006.

[30] C. Liu, Y. Lee, T. Kondo, E.D. Mun, M. Caudle, B.N. Harmon, S.L. Bud'Ko, P.L. Canfield, and A. Kaminski. Metallic surface electronic state in half-Heusler compounds RPtBi (R= Lu, Dy, Gd). *Physical Review B - Condensed Matter and Materials Physics*, 83(20):205133, 2011.

[31] J.A. Logan, S.J. Patel, S.D. Harrington, C.M. Polley, B.D. Schultz, T. Balasubramanian, A. Janotti, A. Mikkelsen, and C.J. Palmstrøm. Observation of a topologically non-trivial surface state in half-Heusler PtLuSb (001) thin films. *Nature Communications*, 7:11993, 2016.

[32] Z.K. Liu, L.X. Yang, S.C. Wu, C. Shekhar, J. Jiang, H.F. Yang, Y. Zhang, S.K. Mo, Z. Hussain, B. Yan, C. Felser, and Y.L. Chen. Observation of unusual topological surface states in half-Heusler compounds LnPtBi (Ln=Lu, Y). *Nature Communications*, 7:12924, 2016.

[33] S. Andrieu, A. Neggache, T. Hauet, T. Devolder, A. Hallal, M. Chshiev, A.M. Bataille, P. Le Fèvre, and F. Bertran. Direct evidence for minority spin gap in the Co_2MnSi Heusler compound. *Physical Review B*, 93(9):094417, 2016.

[34] C. Guillemard, S. Petit-Watelot, L. Pasquier, D. Pierre, J. Ghanbaja, J.C. Rojas-Sánchez, A. Bataille, J. Rault, P. Le Fèvre, F. Bertran, and S. Andrieu. Ultralow Magnetic Damping in Co_2Mn-Based Heusler Compounds: Promising Materials for Spintronics. *Physical Review Applied*, 11(6):064009, 2019.

[35] T.L. Gilbert. A phenomenological theory of damping in ferromagnetic materials. *IEEE Transactions on Magnetics*, 40, 1955.

[36] S.V. Faleev, Y. Ferrante, J. Jeong, M.G. Samant, B. Jones, and S.S.P. Parkin. Origin of the Tetragonal Ground State of Heusler Compounds. *Physical Review Applied*, 7(3):034022, 2017.

[37] M.V. Berry. Quantal phase factors accompanying adiabatic changes. *Proceedings of the Royal Society*, 392, 1984.

[38] M. Konig, S. Wiedmann, C. Brune, A. Roth, H. Buhmann, L.W. Molenkamp, X.L. Qi, and S.-C. Zhang. Quantum spin Hall insulator state in HgTe quantum wells. *Science*, 318:766–770, 2007.

[39] A. Barfuss, L. Dudy, M.R. Scholz, H. Roth, P. Höpfner, C. Blumenstein, G. Landolt, J.H. Dil, N.C. Plumb, M. Radovic, A. Bostwick, E. Rotenberg, A. Fleszar, G. Bihlmayer, D. Wortmann, G. Li, W. Hanke, R. Claessen, and J. Schäfer. Elemental topological insulator with tunable Fermi level: Strained α-Sn on InSb(001). *Physical Review Letters*, 111(15):157205, 2013.

[40] Y. Ohtsubo, P. Le Fèvre, F. Bertran, and A. Taleb-Ibrahimi. Dirac cone with helical spin polarization in ultrathin α-Sn(001) films. *Physical Review Letters*, 111(21):216401, 2013.

[41] S. Küfner, M. Fitzner, and F. Bechstedt. Topological α-Sn surface states versus film thickness and strain. *Physical Review B*, 90(12):125312, sep 2014.

[42] J.C. Rojas-Sánchez, S. Oyarzún, Y. Fu, A. Marty, C. Vergnaud, S. Gambarelli, L. Vila, M. Jamet, Y. Ohtsubo, A. Taleb-Ibrahimi, P. Le Fèvre, F. Bertran, N. Reyren, J.M. George, and A. Fert. Spin to charge conversion at room temperature by spin pumping into a new type of topological insulator: α-Sn films. *Physical Review Letters*, 116(9):096602, 2016.

[43] J. Ding, C. Liu, Y. Zhang, V. Kalappattil, R. Yu, U. Erugu, J. Tang, H. Ding, H. Chen, and M. Wu. Large damping enhancement in Dirac-semimetal ferromagnetic-metal layered structures caused by topological surface states. *Advanced Functional Materials*, 31, 2021.

[44] D. Hsieh, Y. Xia, D. Qian, L. Wray, F. Meier, J.H. Dil, J. Osterwalder, L. Patthey, A.V. Fedorov, H. Lin, A. Bansil, D. Grauer, Y.S. Hor, R.J. Cava, and M.Z. Hasan. Observation of time-reversal-protected single-Dirac-cone topological-insulator states in Bi_2Te_3 and Sb_2Te_3. *Physical Review Letters*, 103(14):146401, 2009.

[45] P. Roushan, J. Seo, C.V. Parker, Y.S. Hor, D. Hsieh, D. Qian, A. Richardella, M.Z. Hasan, R.J. Cava, and A. Yazdani. Topological surface states protected from backscattering by chiral spin texture. *Nature*, 460:1106–1109, 2009.

[46] N.H. D. Khang, Y. Ueda, and P.N. Hai. A conductive topological insulator with large spin Hall effect for ultralow power spin–orbit torque switching. *Nature Materials*, 17(9):808–813, 2018.

[47] H. Zhang, C.X. Liu, X.L. Qi, X. Dai, Z. Fang, and S.C. Zhang. Topological insulators in Bi_2Se_3, Bi_2Te_3 and Sb_2Te_3 with a single Dirac cone on the surface. *Nature Physics*, 5(6):438–442, 2009.

[48] D. Hsieh, Y. Xia, D. Qian, L. Wray, J.H. Dil, F. Meier, J. Osterwalder, L. Patthey, J.G. Checkelsky, N.P. Ong, A.V. Fedorov, H. Lin, A. Bansil, D. Grauer, Y.S. Hor, R.J. Cava, and M.Z. Hasan. A tunable topological insulator in the spin helical Dirac transport regime. *Nature*, 460:1101–1105, 2009.

[49] Y. Xia, L. Wray, D. Qian, D. Hsieh, A. Pal, H. Lin, A. Bansil, D. Grauer, Y.S. Hor, R.J. Cava, and M.Z. Hasan. Electrons on the surface of Bi_2Se_3 form a topologically-ordered two dimensional gas with a non-trivial Berry's phase. *arXiv*, 2008.

[50] Y.S. Hor, P. Roushan, H. Beidenkopf, J. Seo, D. Qu, J.G. Checkelsky, L.A. Wray, D. Hsieh, Y. Xia, S.Y. Xu, D. Qian, M.Z. Hasan, N.P. Ong, A. Yazdani, and R.J. Cava. Development of ferromagnetism in the doped topological insulator $Bi_{2-x}Mn_xTe_3$. *Physical Review B*, 81:195203, 2010.

[51] L.A. Wray, S.Y. Xu, Y. Xia, Y.S. Hor, D. Qian, A.V. Fedorov, H. Lin, A. Bansil, R.J. Cava, and M.Z. Hasan. Observation of topological order in a superconducting doped topological insulator. *Nature Physics*, 6(11):NPHYS1762, 2010.

[52] Y. Shiomi, K. Nomura, Y. Kajiwara, K. Eto, M. Novak, K. Segawa, Y. Ando, and E. Saitoh. Spin-electricity conversion induced by spin injection into topological insulators. *Physical Review Letters*, 113(19):196601, 2014.

[53] C.H. Li, O.M.J. Van't Erve, J.T. Robinson, Y. Liu, L. Li, and B.T. Jonker. Electrical detection of charge-current-induced spin polarization due to spin-momentum locking in Bi_2Se_3. *Nature Nanotechnology*, 9(3):218–224, 2014.

[54] A.R. Mellnik, J.S. Lee, A. Richardella, J.L. Grab, P.J. Mintun, M.H. Fischer, A. Vaezi, A. Manchon, E.A. Kim, N. Samarth, and D.C. Ralph. Spin-transfer torque generated by a topological insulator. *Nature*, 511:449–451, 2014.

[55] A.A. Baker, A.I. Figueroa, L.J. Collins-Mcintyre, G. Van Der Laan, and T. Hesjedal. Spin pumping in ferromagnet-topological insulator-ferromagnet heterostructures. *Scientific Reports*, 5:srep07907, 2015.

[56] C.N. Wu, Y.H. Lin, Y.T. Fanchiang, H.Y. Hung, H.Y. Lin, P.H. Lin, J.G. Lin, S.F. Lee, M. Hong, and J. Kwo. Strongly enhanced spin current in topological insulator/ferromagnetic metal heterostructures by spin pumping. *Journal of Applied Physics*, 117(17):17D148, 2015.

[57] H. Wang, J. Kally, J.S. Lee, T. Liu, H. Chang, D.R. Hickey, K.A. Mkhoyan, M. Wu, A. Richardella, and N. Samarth. Surface-state-dominated spin-charge current conversion in topological-insulator-ferromagnetic-insulator heterostructures. *Physical Review Letters*, 117(7):076601, 2016.

[58] Y. Wang, D. Zhu, Y. Wu, Y. Yang, J. Yu, R. Ramaswamy, R. Mishra, S. Shi, M. Elyasi, K.L. Teo, Y. Wu, and H. Yang. Room temperature magnetization switching in topological insulator-ferromagnet heterostructures by spin-orbit torques. *Nature Communications*, 8(1):s41467–017–01583, 2017.

[59] Y. Lv, J. Kally, D. Zhang, J.S. Lee, M. Jamali, N. Samarth, and J.P. Wang. Unidirectional spin-Hall and Rashba-Edelstein magnetoresistance in topological insulator-ferromagnet layer heterostructures. *Nature Communications*, 9(1):s41467–017–02491, 2018.

[60] P. He, S.S.L. Zhang, D. Zhu, Y. Liu, Y. Wang, J. Yu, G. Vignale, and H. Yang. Bilinear magnetoelectric resistance as a probe of three-dimensional spin texture in topological surface states. *Nature Physics*, 14:495–500, 2018.

[61] P. He, H. Isobe, D. Zhu, C.H. Hsu, L. Fu, and H. Yang. Quantum frequency doubling in the topological insulator Bi_2Se_3. *Nature Communications*, 12:s41467–021–20983, 2021.

[62] R. Dey, A. Roy, and L.F. Register. Recent progress on measurement of spin-charge interconversion in topological insulators using ferromagnetic resonance. *APL Materials*, 9:060702, 2021.

[63] H. Lin, L.A. Wray, Y. Xia, S. Xu, S. Jia, R.J. Cava, A. Bansil, and M.Z. Hasan. Half-Heusler ternary compounds as new multifunctional experimental platforms for topological quantum phenomena. *Nature Materials*, 9(7):546–549, 2010.

[64] W. Al-Sawai, H. Lin, R.S. Markiewicz, L.A. Wray, Y. Xia, S.Y. Xu, M.Z. Hasan, and A. Bansil. Topological electronic structure in half-Heusler topological insulators. *Physical Review B - Condensed Matter and Materials Physics*, 82(12):125208, 2010.

[65] M.M. Hosen, G. Dhakal, K. Dimitri, H. Choi, F. Kabir, C. Sims, O. Pavlosiuk, P. Wiśniewski, T. Durakiewicz, J.X. Zhu, D. Kaczorowski, and M. Neupane. Observation of Dirac state in half-Heusler material YPtBi. *Scientific Reports*, 10(1):s41598–020–69284, 2020.

[66] N.P. Butch, P. Syers, K. Kirshenbaum, A.P. Hope, and J. Paglione. Superconductivity in the topological semimetal YPtBi. *Physical Review B - Condensed Matter and Materials Physics*, 84(22):220504(R), 2011.

[67] F.F. Tafti, T. Fujii, A. Juneau-Fecteau, S. René De Cotret, N. Doiron-Leyraud, A. Asamitsu, and L. Taillefer. Superconductivity in the noncentrosymmetric half-Heusler compound LuPtBi: A candidate for topological superconductivity. *Physical Review B*, 87(18):184504, 2013.

[68] O. Pavlosiuk, D. Kaczorowski, and P. Wiśniewski. Superconductivity and Shubnikov-de Haas oscillations in the noncentrosymmetric half-Heusler compound YPtBi. *Physical Review B*, 94(3):035130, 2016.

[69] O. Pavlosiuk, X. Fabreges, A. Gukasov, M. Meven, D. Kaczorowski, and P. Wiśniewski. Magnetic structures of REPdBi half-Heusler bismuthides (RE = Gd, Tb, Dy, Ho, Er). *Physica B: Condensed Matter*, 536:56–59, 2018.

[70] K. Gofryk, D. Kaczorowski, T. Plackowski, A. Leithe-Jasper, and Y. Grin. Magnetic and transport properties of rare-earth-based half-Heusler phases RPdBi: Prospective systems for topological quantum phenomena. *Physical Review B - Condensed Matter and Materials Physics*, 84(3):035208, 2011.

[71] Y. Pan, A.M. Nikitin, T.V. Bay, Y.K. Huang, C. Paulsen, B.H. Yan, and A. De Visser. Superconductivity and magnetic order in the noncentrosymmetric half-Heusler compound ErPdBi. *Epl*, 104(2):27001, 2013.

[72] T.V. Bay, M. Jackson, C. Paulsen, C. Baines, A. Amato, T. Orvis, M.C. Aronson, Y.K. Huang, and A. De Visser. Low field magnetic response of the noncentrosymmetric superconductor YPtBi. *Solid State Communications*, 183:13–17, 2014.

[73] A. Mukhopadhyay and N. Lakshminarasimhan. Multi-functional properties of non- centrosymmetric ternary half-Heuslers, RPdSb (R = Er and Ho). *Journal of Physics D: Applied Physics*, 51(26), 2018.

[74] O. Polat, J.A. Arregi, M. Horák, J. Polčák, K. Bukvišová, J. Zlamal, and T. Sikola. The fabrication and characterization of half-Heusler YPdBi thin films. *Journal of Physics and Chemistry of Solids*, 161:110447, 2022.

[75] V. Bhardwaj, A. Bhattacharya, A.K. Nigam, S.P. Dash, and R. Chatterjee. Observation of surface dominated topological transport in strained semimetallic ErPdBi thin films. *Applied Physics Letters*, 117(13):132406, 2020.

[76] W. Wang, Y. Du, G. Xu, X. Zhang, E. Liu, Z. Liu, Y. Shi, J. Chen, G. Wu, and X.X. Zhang. Large linear magnetoresistance and Shubnikov-de Hass oscillations in single crystals of YPdBi Heusler topological insulators. *Scientific Reports*, 3:srep02181, 2013.

[77] B. Nowak and D. Kaczorowski. Bi NMR in topologically trivial and nontrivial half-Heusler bismuthides. *Journal of Physical Chemistry C*, 120(38):21797–21801, 2016.

[78] F. Shi, L. Jia, M.S. Si, Z. Zhang, J. Xie, C. Xiao, D. Yang, H. Shi, and Q. Luo. Tunable band inversion in half-Heusler topological LuAuSn/LuPtBi superlattices. *Applied Physics Express*, 11(9), 2018.

[79] C. Guillemard, S. Petit-Watelot, T. Devolder, L. Pasquier, P. Boulet, S. Migot, J. Ghanbaja, F. Bertran, and S. Andrieu. Issues in growing Heusler compounds in thin films for spintronic applications. *Journal of Applied Physics*, 128(24):241102, 2020.

[80] S. Hüfner. *Photoelectron Spectroscopy: Principles and Applications*. Springer, 2003.

[81] C.N. Berglund and W.E. Spicer. Photoemission Studies of Copper and Silver: Theory. *Physical Review*, 136(A1030):799–814, 1964.

[82] A. Damascelli, D.H. Lu, and K.M. Shen. Fermi Surface, Surface States, and Surface Seconstruction in Sr_2RuO_4. *Physical Review Letters*, 85(24):5194–5197, 2000.

[83] S.Y. Liu, W.T. Zhang, H.M. Weng, L. Zhao, H.Y. Liu, X.W. Jia, G.D. Liu, X.L. Dong, J. Zhang, Z.Q. Mao, C.T. Chen, Z.Y. Xu, X. Dai, Z. Fang, and X.J. Zhou. Effect of cleaving temperature on the surface and bulk Fermi surface of Sr_2RuO_4 investigated by high resolution angle-resolved photoemission. *Chinese Physics Letters*, 29(6):067401, 2012.

[84] J. Zhang, J.P. Velev, X. Dang, and E.Y. Tsymbal. Band structure and spin texture of Bi_2Se_3 3d ferromagnetic metal interface. *Physical Review B*, 94(1):014435, 2016.

[85] O. Pavlosiuk, P. Fałat, D. Kaczorowski, and P. Wiśniewski. Anomalous Hall effect and negative longitudinal magnetoresistance in half-Heusler topological semimetal candidates TbPtBi and HoPtBi. *APL Materials*, 8(11):111107, 2020.

[86] T.V. Bay, T. Naka, Y.K. Huang, and A. De Visser. Superconductivity in noncentrosymmetric YPtBi under pressure. *Physical Review B - Condensed Matter and Materials Physics*, 86(6):064515, 2012.

[87] V. Bhardwaj, N. Banerjee, and R. Chatterjee. Structural and transport properties of $Y_{1-x}(Dy)_xPdBi$ ($0 \leqslant x \leqslant 1$) topological semi-metallic thin films. *Applied Physics Letters*, 119:122402, 2021.

[88] V. Vlaminck, J.E. Pearson, S.D. Bader, and A. Hoffmann. Dependence of spin-pumping spin Hall effect measurements on layer thicknesses and stacking order. *Physical Review B - Condensed Matter and Materials Physics*, 88(6):064414, 2013.

[89] J.C. Rojas-Sánchez, N. Reyren, P. Laczkowski, W. Savero, J.P. Attané, C. Deranlot, M. Jamet, J.M. George, L. Vila, and H. Jaffrès. Spin pumping and inverse spin hall effect in platinum: The essential role of spin-memory loss at metallic interfaces. *Physical Review Letters*, 112(10):106602, 2014.

[90] Role of transparency of platinum-ferromagnet interfaces in determining the intrinsic magnitude of the spin Hall effect. *Nature Physics*, 11(6):496–502, 2015.

[91] M. Dc, J.Y. Chen, T. Peterson, P. Sahu, B. Ma, N. Mousavi, R. Harjani, and J.P. Wang. Observation of High Spin-to-Charge Conversion by Sputtered Bismuth Selenide Thin Films at Room Temperature. *Nano Letters*, 19(8):4836–4844, 2019.

[92] J. Han and L. Liu. Topological insulators for efficient spin-orbit torques. *APL Materials*, 9:060901, 2021.

[93] E. Longo, L. Locatelli, M. Belli, M. Alia, A. Kumar, M. Longo, M. Fanciulli, and R. Mantovan. Spin-Charge Conversion in Fe/Au/Sb_2Te_3 Heterostructures as Probed By Spin Pumping Ferromagnetic Resonance. *Advanced Materials Interfaces*, 8:2101244.

[94] E. Longo, M. Belli, M. Alia, M. Rimoldi, R. Cecchini, M. Longo, C. Wiemer, L. Locatelli, P. Tsipas, A. Dimoulas, G. Gubbiotti, M. Fanciulli, and R. Mantovan. Large Spin-to-Charge Conversion at Room Temperature in Extended Epitaxial Sb_2Te_3 Topological Insulator Chemically Grown on Silicon. *Advanced Functional Materials*, 32:2109361.

[95] Y. Tserkovnyak, A. Brataas, and G.E.W. Bauer. Spin pumping and magnetization dynamics in metallic multilayers. *Physical Review B - Condensed Matter and Materials Physics*, 66(22):224403, 2002.

[96] Y. Huo, F.L. Zeng, C. Zhou, and Y.Z. Wu. Spin pumping and the inverse spin hall effect in single crystalline Fe/Pt heterostructure. *AIP Advances*, 7(5):056024.

[97] C. Guillemard, S. Petit-Watelot, S. Andrieu, and J.C. Rojas-Sánchez. Charge-spin current conversion in high quality epitaxial Fe/Pt systems: Isotropic spin Hall angle along different in-plane crystalline directions. *Applied Physics Letters*, 113(26):262404, 2018.

[98] J.C. Rojas-Sánchez. *Different spin current sources: from interfaces to bulk materials*. PhD thesis, Université de Lorraine, 2020.

[99] K. Ando, T. Yoshino, and E. Saitoh. Optimum condition for spin-current generation from magnetization precession in thin film systems. *Applied Physics Letters*, 94(15):152509, 2009.

[100] K. Ando and E. Saitoh. Inverse spin-Hall effect in palladium at room temperature. *Journal of Applied Physics*, 108(11):103913, 2011.

[101] F. Bonell, M. Goto, G. Sauthier, J.F. Sierra, A.I. Figueroa, M.V. Costache, S. Miwa, Y. Suzuki, and S.O. Valenzuela. Control of Spin-Orbit Torques by Interface Engineering in Topological Insulator Heterostructures. *Nano Letters*, 20(8):5893–5899, 2020.

[102] O. Rousseau, C. Gorini, F. Ibrahim, J.Y. Chauleau, A. Solignac, A. Hallal, S. Tölle, M. Chshiev, and M. Viret. Spin-charge conversion in ferromagnetic Rashba states. *Physical Review B*, 104(13):134438, 2021.

[103] K. Uchida, M. Ishida, T. Kikkawa, A. Kirihara, T. Murakami, and E. Saitoh. Longitudinal spin Seebeck effect: From fundamentals to applications. *Journal of Physics Condensed Matter*, 26(34):343202, 2014.

[104] R. Ramos, T. Kikkawa, K. Uchida, H. Adachi, I. Lucas, M.H. Aguirre, P. Algarabel, L. Morellón, S. Maekawa, E. Saitoh, and M. R. Ibarra. Observation of the spin Seebeck effect in epitaxial Fe_3O_4 thin films. *Applied Physics Letters*, 102(7), 2013.

[105] T.C. Chuang, P.L. Su, P.H. Wu, and S.Y. Huang. Enhancement of the anomalous Nernst effect in ferromagnetic thin films. *Physical Review B*, 96(17):072413, 2017.

[106] P. J. Webster. Magnetic and chemical order in Heusler alloys containing cobalt and manganese. *Journal of Physics and Chemistry of Solids*, 32(10):1221–1231, 1971.

[107] E. Şaşioğlu, L.M. Sandratskii, P. Bruno, and I. Galanakis. Exchange interactions and temperature dependence of magnetization in half-metallic Heusler alloys. *Physical Review B*, 72(18):184415, 2005.

[108] S. Ishida, S. Fujii, S. Kashiwagi, and S. Asano. Search for Half-Metallic Compounds in Co_2MnZ (Z=IIIb, IVb, Vb Element). *Journal of the Physical Society of Japan*, 64, 1995.

[109] S. Picozzi, A. Continenza, and A. J. Freeman. Co_2MnX (X=Si, Ge, Sn) Heusler compounds: An ab initio study of their structural, electronic, and magnetic properties at zero and elevated pressure. *Physical Review B*, 66(9):094421, 2002.

[110] I. Galanakis, P.H. Dederichs, and N. Papanikolaou. Slater-Pauling behavior and origin of the half-metallicity of the full-Heusler alloys. *Physical Review B - Condensed Matter and Materials Physics*, 66(17):174429, 2002.

[111] H.C. Kandpal, G.H. Fecher, and C. Felser. Calculated electronic and magnetic properties of the half-metallic, transition metal based Heusler compounds. *Journal of Physics D: Applied Physics*, 40(6):1507–1523, 2007.

[112] M. Jourdan, J. Minár, J. Braun, A. Kronenberg, S. Chadov, B. Balke, A. Gloskovskii, M. Kolbe, H.J. Elmers, G. Schönhense, H. Ebert, C. Felser, and M. Kläui. Direct observation of half-metallicity in the Heusler compound Co_2MnSi. *Nature Communications*, 5:ncomms4974, 2014.

[113] J.M. Shaw, E.K. Delczeg-Czirjak, E.R.J. Edwards, Y. Kvashnin, D. Thonig, M.A.W. Schoen, M. Pufall, M.L. Schneider, T.J. Silva, O. Karis, K.P. Rice, O. Eriksson, and H.T. Nembach. Magnetic damping in sputter-deposited Co_2MnGe Heusler compounds with A2, B2, and $L2_1$ orders: Experiment and theory. *Physical Review B*, 97(9):094420, 2018.

[114] A. Sakuma. First-principles study of the Gilbert damping constants of Heusler alloys based on the torque correlation model. *Journal of Physics D: Applied Physics*, 48(16):164011, 2015.

[115] C. Liu, C.K.A. Mewes, M. Chshiev, T. Mewes, and W.H. Butler. Origin of low Gilbert damping in half metals. *Applied Physics Letters*, 95(2):022509, 2009.

[116] B. Pradines, R. Arras, I. Abdallah, N. Biziere, and L. Calmels. First-principles calculation of the effects of partial alloy disorder on the static and dynamic magnetic properties of Co_2MnSi. *Physical Review B*, 95(9):094425, 2017.

[117] T.L. Brown-Heft, J.A. Logan, A.P. McFadden, C. Guillemard, P. Le Fèvre, F. Bertran, S. Andrieu, and C.J. Palmstrøm. Epitaxial Heusler superlattice Co_2MnAl/Fe_2MnAl with perpendicular magnetic anisotropy and termination-dependent half-metallicity. *Physical Review Materials*, 2(3):034402, 2018.

[118] B. Dieny and M. Chshiev. Perpendicular magnetic anisotropy at transition metal/oxide interfaces and applications. *Reviews of Modern Physics*, 89:025008, 2017.

[119] S. Ikeda, K. Miura, H. Yamamoto, K. Mizunuma, H. D. Gan, M. Endo, S. Kanai, J. Hayakawa, F. Matsukura, and H. Ohno. A perpendicular-anisotropy CoFeB-MgO magnetic tunnel junction. *Nature Materials*, 9(9):NMAT2804, 2010.

[120] P.F. Carcia. Perpendicular magnetic anisotropy in Pd/Co and Pt/Co thin-film layered structures. *Journal of Applied Physics*, 63(10):5066–5073, 1988.

[121] J.G. Azadani, K. Munira, J. Romero, J. Ma, C. Sivakumar, A.W. Ghosh, and W.H. Butler. Anisotropy in layered half-metallic Heusler alloy superlattices. *Journal of Applied Physics*, 119(4):043904, 2016.

[122] S. Wurmehl, H.C. Kandpal, G.H. Fecher, and C. Felser. Valence electron rules for prediction of half-metallic compensated- ferrimagnetic behaviour of Heusler compounds with complete spin polarization. *Journal of Physics Condensed Matter*, 18(27):6171–6181, 2006.

[123] D. Zhang, B. Yan, S. C. Wu, J. Kübler, G. Kreiner, S.S.P. Parkin, and C. Felser. First-principles study of the structural stability of cubic, tetragonal and hexagonal phases in Mn_3Z (Z=Ga, Sn and Ge) Heusler compounds. *Journal of Physics Condensed Matter*, 25(20):206006, 2013.

[124] J. T. Holguín-momaca, C. J. Muñoz-carnero, H. Sharma, and C. R. Santillan-Rodriguez. Tuning the ferromagnetism of epitaxial-strained $D0_{19}$-Mn_3Ga thin films. *Journal of Magnetism and Magnetic Materials*, 471:329–333, 2019.

[125] X. Wang, C. Zhang, Q. Yang, L. Liu, D. Pan, X. Chen, J. Deng, T. Zhai, and H.X. Deng. Manipulation of crystalline structure, magnetic performance, and topological feature in Mn_3Ge films. *APL Materials*, 9(11):111107, 2021.

[126] J.M. Taylor, A. Markou, E. Lesne, P.K. Sivakumar, C. Luo, F. Radu, P. Werner, C. Felser, and S.S.P. Parkin. Anomalous and topological Hall effects in epitaxial thin films of the noncollinear antiferromagnet Mn_3Sn. *Physical Review B*, 101(9):094404, 2020.

[127] T. Chen, J. Wang, Z. Cheng, X. Wang, and H. Chen. Structural, electronic and magnetic properties of Mn_xGa-Co_2MnSi (x = 1, 3) bilayers. *Scientific Reports*, 8:s41598–018–34881, 2018.

[128] B. S. Yang, L. N. Jiang, W. Z. Chen, P. Tang, J. Zhang, X. G. Zhang, Y. Yan, and X. F. Han. First-principles study of perpendicular magnetic anisotropy in ferrimagnetic $D0_{22}$-Mn_3X (X = Ga, Ge) on MgO and $SrTiO_3$. *Applied Physics Letters*, 112:142403, 2018.

[129] H. Kurt, K. Rode, M. Venkatesan, P. Stamenov, and J.M.D. Coey. High spin polarization in epitaxial films of ferrimagnetic Mn_3Ga. *Physical Review B*, 83:020405(R), 2011.

[130] H. Lee, H. Sukegawa, J. Liu, S. Mitani, and K. Hono. Tuning the magnetic properties and surface morphology of $D0_{22}$ $Mn_{3-\delta}Ga$ films with high perpendicular magnetic anisotropy by N doping. *Applied Physics Letters*, 109:152402, 2016.

[131] X. P. Zhao, J. Lu, S. W. Mao, Z. F. Yu, D. H. Wei, and J. H. Zhao. Spin-orbit torque induced magnetization switching in ferrimagnetic Heusler alloy $D0_{22}$-Mn_3Ga with large perpendicular magnetic anisotropy. *Applied Physics Letters*, 115:142405, 2019.

[132] A. Sugihara, S. Mizukami, Y. Yamada, K. Koike, and T. Miyazaki. High perpendicular magnetic anisotropy in $D0_{22}$-$Mn_{3+x}Ge$ tetragonal Heusler alloy films. *Applied Physics Letters*, 104, 2014.

[133] A. Sugihara, K. Z. Suzuki, T. Miyazaki, and S. Mizukami. Magnetic properties of ultrathin tetragonal Heusler $D0_{22} - Mn_3Ge$ perpendicular-magnetized films. *Journal of Applied Physics*, 117(17):17B511, 2015.

[134] J. Jeong, Y. Ferrante, S.V. Faleev, M.G. Samant, C. Felser, and S.S.P. Parkin. Termination layer compensated tunnelling magnetoresistance in ferrimagnetic Heusler compounds with high perpendicular magnetic anisotropy. *Nature Communications*, 7:ncomms10276, 2016.

[135] J. Seyd, I. Pilottek, N. Y. Schmidt, O. Caha, M. Urbanek, and M. Albrecht. Mn_3Ge-based tetragonal Heusler alloy thin films with addition of Ni , Pt , and Pd. *Journal of Physics: Condensed Matter*, 32:145801, 2020.

[136] A. Kobayashi, T. Higo, S. Nakatsuji, and Y. Otani. Structural and magnetic properties of Mn_3Ge films with Pt and Ru seed layers. *AIP Advances*, 10:015225, 2020.

[137] L. Ren, L. Liu, X. Shu, W. Lin, P. Yang, J. Chen, and K.L. Teo. Spin Orbit Torque Switching of a High-Quality Perpendicularly Magnetized Ferrimagnetic Heusler Mn_3Ge Film. *ACS Applied Materials Interfaces*, 13:18294–18300, 2021.

[138] Y. Ferrante, J. Jeong, R. Saha, S.V. Faleev, M.G. Samant, T. Topuria, H. Deniz, and S.S.P. Parkin. Tetragonal Mn_3Sn Heusler films with large perpendicular magnetic anisotropy deposited on metallic MnN underlayers using amorphous substrates. *APL Materials*, 7(3):031103, 2019.

[139] E. Arras, D. Caliste, and T. Deutsch. Phase diagram , structure , and magnetic properties of the Ge-Mn system : A first-principles study. *Physical Review B*, 83:174103, 2011.

[140] T. Ohoyama, K. Yasukochi, and K. Kanematsu. A New Phase of an Intermetallic Compound $Mn_{3.4}Ge$ and its Magnetism. *Journal of the Physycal Society of Japan*, 16:352–353, 1961.

[141] S. Mizukami, A. Sakuma, A. Sugihara, T. Kubota, Y. Kondo, H. Tsuchiura, and T. Miyazaki. Tetragonal $D0_{22}$ $Mn_{3+x}Ge$ Epitaxial Films Grown on MgO(100) with a Large Perpendicular Magnetic Anisotropy. *Applied Physics Express*, 6:123002, 2013.

[142] T. Kubota, Y. Miura, D. Watanabe, S. Mizukami, F. Wu, H. Naganuma, X. Zhang, M. Oogane, M. Shirai, Y. Ando, and T. Miyazaki. Magnetoresistance Effect in Tunnel Junctions with Perpendicularly Magnetized $D0_{22} - Mn_{3-\delta}Ga$ Electrode and MgO Barrier. *Applied Physics Express*, 4:043002, 2011.

[143] R. Ranjbar, K. Suzuki, A. Sugihara, Q. L. Ma, X. M. Zhang, T. Miyazaki, Y. Ando, and S. Mizukami. Interfacial exchange coupling in cubic Heusler Co_2FeZ (Z = Al and Si) tetragonal Mn_3Ga bilayers. *Journal of Applied Physics*, 117:17A332, 2015.

[144] R. Ranjbar, K. Suzuki, A. Sugihara, Q.L. Ma, X.M. Zhang, T. Miyazaki, Y. Ando, and S. Mizukami. Antiferromagnetic coupling in perpendicularly magnetized cubic and tetragonal Heusler bilayers. *Materials Letters*, 160:88–91, 2015.

[145] R. Ranjbar, K. Suzuki, A. Sugihara, Q.L. Ma, X.M. Zhang, Y. Ando, T. Miyazaki, and S. Mizukami. Structural and magnetic properties of cubic and tetragonal Heusler alloy bilayers. *Materials and Design*, 96:490–498, 2016.

[146] R. Ranjbar, K.Z. Suzuki, A. Sugihara, Y. Ando, T. Miyazaki, and S. Mizukami. Thickness dependencies of structural and magnetic properties of cubic and tetragonal Heusler alloy bilayer films. *Journal of Magnetism and Magnetic Materials*, 433:195–201, 2017.

[147] S. Mao, J. Lu, X. Zhao, X. Wang, D. Wei, J. Liu, J. Xia, and J. Zhao. MnGa-based fully perpendicular magnetic tunnel junctions with ultrathin Co_2MnSi interlayers. *Scientific Reports*, 7:srep43064, 2017.

[148] Q. L. Ma, X. M. Zhang, T. Miyazaki, and S. Mizukami. Artificially engineered Heusler ferrimagnetic superlattice exhibiting perpendicular magnetic anisotropy. *Scientific Reports*, 5:srep07863, 2015.

[149] L. You, R.C. Sousa, S. Bandiera, B. Rodmacq, and B. Dieny. Co/Ni multilayers with perpendicular anisotropy for spintronic device applications. *Applied Physics Letters*, 100:172411, 2012.

[150] M. Itoh. Relation between surface reconstructions and RHEED intensity oscillations. *Physical Review B*, 58(11):6716–6719, 1998.

[151] T. Graf, C. Felser, and S.S.P. Parkin. Simple rules for the understanding of Heusler compounds. *Progress in Solid State Chemistry*, 39(1):1–50, 2011.

[152] S. Seong, E. Lee, H.Y. Kim, Y. Kim, J. Baik, and J.S. Kang. XMCD and PES study of a compensated-ferrimagnetic half-metal Mn_3Ga. *Current Applied Physics*, 18(11):1190–1195, 2018.

[153] J. Okabayashi, Y. Miura, Y. Kota, K. Z. Suzuki, A. Sakuma, and S. Mizukami. Detecting quadrupole: a hidden source of magnetic anisotropy for Manganese alloys. *Scientific Reports*, 10:9744, 2020.

[154] N.V. Uvarov, Y.V. Kudryavtsev, A.F. Kravets, A.Y. Vovk, R.P. Borges, M. Godinho, and V. Korenivski. Electronic structure, optical and magnetic properties of Co_2FeGe Heusler alloy films. *Journal of Applied Physics*, 112(6):063909, 2012.

[155] G. van der Laan and A.I. Figueroa. X-ray magnetic circular dichroism - A versatile tool to study magnetism. *Coordination Chemistry Reviews*, 277:95–129, 2014.

[156] B.T. Thole, P. Carra, P. Sette, and G. van der Laan. X-ray circular dichroism as a probe of orbital magnetization. *Physical Review Letters*, 68, 1992.

[157] P. Carra, B.T. Thole, M. Altarelli, and X. Wang. X-ray circular dichroism and local magnetic fields. *Physical Review Letters*, 70, 1993.

[158] S. Andrieu and P. Müller. *Les surfaces solides : concepts et méthodes*. EDP Sciences, 2005.

[159] G. Van Der Laan. Sum rule practice. *Journal of Synchrotron Radiation*, 6(3):694–695, 1999.

[160] A. Scherz, H. Wende, C. Sorg, K. Baberschke, J. Minr, D. Benea, and H. Ebert. Limitations of integral XMCD sum-rules for the early 3d elements. *Physica Scripta*, T115:586–588, 2005.

Acknowledgements

Je tiens à remercier l'ensemble des personnes qui ont pu contribuer, de près ou de loin, à la réalisation de ce travail de thèse.

Tout d'abord, je souhaite remercier mes deux directeurs François et Stéphane qui m'ont tout appris et sans qui ce travail de thèse aurait été impossible.

Je tiens également à remercier l'ensemble de l'équipe 101. Notamment Carlos et Sébastien qui m'ont beaucoup aidé pour les expériences de transports. Enfin Alberto, qui m'a formé sur les différentes techniques de transports, qui a réalisé les expériences spin Seebeck présentées dans cette thèse et qui m'a permis d'améliorer mon anglais.

Je tiens à remercier l'ensemble des centres de compétences dans lesquels j'ai eu la chance de travailler et d'échanger :
- le CC DAUM avec Ludovic, Daniel, Alexandre, Olivier, Oleg qui a réalisé les images STM présentes dans cette thèse et tout particulièrement Claudia avec qui j'ai énormément échangé et qui a grandement contribué à la partie croissance de cette thèse.
- le CC Minalor avec Demba, Gwladys et particulièrement Laurent qui m'a formé au processus de lithographie et ce toujours dans la bonne humeur.
- le CC 3M avec Sylvie et Jaafar qui m'ont permis d'obtenir de très belles images de microscopie.
- le CC X-Gamma avec Pascal et Sylvie.
- le CC MagCryo avec Stéphane et Luc.

Je tiens à remercier Charles, avec qui j'ai pu échanger depuis mon stage, au cours de ma thèse et avec qui j'ai réalisé les mesures XMCD présentées dans cette thèse. Enfin Yannick et Luc, qui m'ont aidé à prendre en main le setup de photoémission de l'IJJ.

Je tiens à remercier l'ensemble de la ligne de photoémission CASSIOPEE du synchrotron Soleil avec notamment Patrick et William mais également les doctorants avec lesquels j'ai pu échanger lors de mes séjours.

Je tiens à remercier Julian et Benoît d'avoir accepté de faire partie de mon comité de suivi et de suivre les travaux réalisés au cours de ces 3 ans.

Je tiens à remercier l'ensemble des doctorants et post doctorants avec qui j'ai pu échanger lors de cette thèse et tout particulièrement mes camarades de bureau, mais aussi mes anciens camarades de master et l'ensemble des doctorants de l'équipe 101.

Ma famille et mes amis, loin du monde de la physique mais tout aussi important. Enfin, ma petite amie, qui a eu la lourde tâche de relire mon manuscrit rédigé en anglais et de supporter mes retours tardifs les soirs.

Merci à toutes et à tous pour ces 3 années.

Abstract:

Over the last decades, the needs in storage capacity has shot up with computing development. The energy crisis that we are going through in the 21^{th} century requires to develop new fundamental materials for data storage. It was with this purpose that physicists develop new ways of storing information in order to reduce devices' scale, energy consumption and manufacturing cost while memories' size and information's speed has shot up. The research conducted in this thesis make use of two different ways to improve data storage:

- The first one is by using emerging materials in science, called topological insulators, that host peculiar spin texture predicted to generate very high spin-to-charge interconversion. This non-trivial state of matter can be complex to stabilize and image. This is the goal of the first part of this thesis where topological insulators coming from the half-Heusler family are engineered by molecular beam epitaxy. Structural characterization are carried out by X-ray and electronic diffraction along with scanning tunneling microscopy and transmission electron microscopy that confirm an epitaxial growth in the desired structure predicted to host a non-trivial topology. Angle resolved photoemission spectroscopy is performed and reveals the presence of linear states around the $\overline{\Gamma}$ point of the Brillouin zone. Nonetheless, the complex Fermi surfaces imaged do not allow to draw clear conclusions on the non-trivial nature of both alloys. Transport measurements were performed to test the potential interconversion efficiency of our compounds and spin Seebeck experiments revealed a spin-to-charge conversion two to three times higher in our TIs compared to a Pt control sample.

- The second way chosen to improve conventional magnetic memories is by playing with magnetic anisotropy. Here again, the Heusler family offers a vast variety of compounds allowing to fulfill this goal. The Mn_3Z family compounds has attracted a lot of attention owing to their tetragonalized unit cell that allows to stabilize perpendicular magnetic anisotropy (PMA) even in a thin film geometry. In this thesis, we investigate $Mn_{100-x}Ga_x$ and $Mn_{100-x}Ge_x$ alloys and manage to stabilize them in their $D0_{22}$ structure that offers PMA. A peculiar zoom is then done on Mn_3Ge-based stacks composed of a second Heusler alloy with remarkable properties, the Co_2MnZ' alloys (Z' = Si, Ge). Co_2MnZ' compounds have a half-metallic behavior making them very suitable for spin transfer torque related applications due to their low magnetic damping and full spin polarization at the Fermi level. Here we develop Mn_3Ge/Co_2MnZ' heterostructures (bilayers and superlattices) and manage to grow both compounds in the desired structures. The overall system is perpendicularly magnetized (thanks to Mn_3Ge), terminated with a half-metal magnet (thanks to Co_2MnZ') and the thicknesses used for both layers allow to tune the magnetic properties and obtained 100% of remanence.

Résumé :

Au cours des dernières décennies, les besoins en capacité de stockage ont explosé avec l'avènement de l'ordinateur. La crise énergétique que nous traversons au 21^{eme} siècle nécessite le développement de nouveaux matériaux pour le stockage de l' information. C'est dans ce but que les physiciens ont développé de nouvelles façons de stocker l'information de façon à réduire la taille, la consommation énergétique et le coût de fabrication des mémoires tout en augmentant leurs capacités et la vitesse de traitement de l'information. Les recherches réalisées au cours de cette thèse visent à améliorer le stockage de l'information à l'aide des deux champs de recherches suivants :

- Le premier se base sur l'utilisation de matériaux émergents dans le domaine de la recherche scientifique : les isolants topologiques. Ces matériaux possèdent des textures de spin particulières susceptibles de générer une conversion très élevée entre courant de spin et courant de charge. Cet état de la matière (non trivial topologiquement) peut s'avérer complexe à stabiliser et à imager. C'est l'objectif de la première partie de cette thèse où des isolants topologiques provenant de la famille des demi-Heusler sont fabriqués par épitaxie par jets moléculaires. La caractérisation structurale par diffraction des rayons X et électroniques ainsi que par microscopie à effet tunnel et microscopie électronique à transmission confirme la croissance épitaxiale dans la structure désirée prédite comme ayant une topologie non triviale. La spectroscopie photoélectronique résolue en angle révèle la présence d'états linéaires autour du point $\overline{\Gamma}$ de la zone de Brillouin. Néanmoins, les surfaces de Fermi obtenues sont complexes et ne permettent pas de tirer des conclusions claires sur la nature non triviale des composés. Des mesures de transport ont été effectuées pour tester l'efficacité potentielle d'interconversion de nos composés et les expériences de spin Seebeck révèlent une conversion spin/charge deux à trois fois plus élevée dans nos isolants topologiques comparés à un échantillon référence de Pt.

- La seconde étude réalisée afin d'améliorer les mémoires magnétiques conventionnelles porte sur l'anisotropie magnétique. Ici encore les alliages d'Heusler offrent une grande variété de composés permettant de répondre à ce but. La famille de composés Mn_3Z (Z = Ge, Ga) a beaucoup attiré l'attention du fait de sa maille élémentaire tetragonalisée permettant de stabiliser une aimantation perpendiculaire et cela même dans une géométrie de film mince. Dans cette thèse, nous étudions les alliages $Mn_{100-x}Ga_x$ et $Mn_{100-x}Ge_x$ et parvenons à les stabiliser dans leur structure $D0_{22}$ offrant une aimantation perpendiculaire. Une attention particulière est ensuite portée sur des empilements (bicouches et super-réseaux) à base de Mn_3Ge et composés d'un second alliage d'Heusler aux propriétés remarquables, les alliages Co_2MnZ' (Z' = Si, Ge). Les composés Co_2MnZ' ont un comportement semi-métallique leur conférant un faible amortissement magnétique et une polarisation en spin de 100% au niveau de Fermi, deux propriétés très souhaitées pour des applications basées sur le couple de transfert de spin. Nous développons donc ici des hétérostructures Mn_3Ge/Co_2MnZ' (bicouches et super-réseaux) et parvenons à faire croître les deux composés dans les structures souhaitées. Le système global possède une aimantation perpendiculaire (amenée par Mn_3Ge), la dernière couche de l'empilement est un demi-métal magnétique (amené par Co_2MnZ') et les épaisseurs utilisées pour les deux couches permet d'accorder les propriétés magnétiques et d'obtenir 100% de rémanence.